Localized Patterns in the Gray-Scott Model

An Asymptotic and Numerical Study of Dynamics and Stability

by

Wan Chen

B.Sc., Wuhan University, China, 2003
Ph.D, The University of British Columbia, Canada, 2009

A THESIS SUBMITTED IN PARTIAL FULFILLMENT OF
THE REQUIREMENTS FOR THE DEGREE OF

DOCTOR OF PHILOSOPHY

in

The Faculty of Graduate Studies

(Mathematics)

THE UNIVERSITY OF BRITISH COLUMBIA

(Vancouver)

May, 2009

Abstract

Localized patterns have been observed in many reaction-diffusion systems. One well-known such system is the two-component Gray-Scott model, which has been shown numerically to exhibit a rich variety of localized spatio-temporal patterns including, standing spots, oscillating spots, self-replicating spots, etc. This thesis concentrates on analyzing the localized pattern formation in this model that occurs in the semi-strong interaction regime where the diffusivity ratio of the two solution components is asymptotically small.

In a one-dimensional spatial domain, two distinct types of oscillatory instabilities of multi-spike solutions to the Gray-Scott model that occur in different parameter regimes are analyzed. These two instabilities relate to either an oscillatory instability in the amplitudes of the spikes, or an oscillatory instability in the spatial locations of the spikes. In the latter case a novel Stefan-type problem, with moving Dirac source terms, is shown to characterize the dynamics of a collection of spikes. From a numerical and analytical study of this problem, it is shown that an oscillatory motion in the spike locations can be initiated through a Hopf bifurcation. In a subregime of the parameters it is shown that this Stefan-type problem is quasi-steady, allowing for the derivation of an explicit set of ODE's for the spike dynamics. In this subregime, a nonlocal eigenvalue problem analysis shows that spike amplitude oscillations can occur from another Hopf bifurcation.

In a two-dimensional domain, the method of matched asymptotic expansions is used to construct multi-spot solutions by effectively summing an infinite-order logarithmic expansion in terms of a small parameter. An asymptotic differential algebraic system of ODE's for the spot locations is derived to characterize the slow dynamics of a collection of spots. Furthermore, it is shown theoretically and from the numerical computation of certain eigenvalue problems that there are three main types of fast instabilities for a multi-spot solution. These instabilities are spot self-replication, spot annihilation due to overcrowding, and an oscillatory instability in the spot amplitudes. These instability mechanisms are studied in detail and phase diagrams in parameter space where they occur are computed and illustrated for various spatial configurations of spots and several domain geometries.

Table of Contents

List of Tables

List of Figures

Acknowledgements

This thesis presents the work under the supervision of Dr. Michael Ward, I would like to thank him for his great guidance, support and encouragement. Also I would like to thank Dr. Brian Wetton for his useful suggestions and help. Finally, I would like to thank Prof. Juncheng Wei of the Chinese University of Hong Kong for some helpful discussions on the theory of nonlocal eigenvalue problems.

To my dear parents and my husband

Chapter 1

Introduction

Various patterns have been observed in the physical world, such as spot or stripe patterns on animal skins, spiral waves in the Belousov-Zhabotinsky (BT) reaction, among many others. In 1952, the British mathematician Alan Turing [90] first proposed a simple reaction-diffusion system describing chemical reaction and diffusion to account for morphogenesis, i.e. the development of patterns in biological systems. This study is the foundation of modern pattern formation. In [90], Turing employed linear analysis to determine the threshold for the instability of spatially homogeneous equilibrium solutions of general two-component reaction-diffusion systems; a more specific summary of his work is discussed in §1.1. Turing's original study has stimulated numerous theoretical and numerical studies of reaction-diffusion systems, which focus on pattern formation from a spatially uniform state that is near the transition from linear stability to linear instability. It was suggested in 1972 by Gierer et. al. [31] and Segel et.al. [83] that two key ingredients for localization are *positive feedback of the activator*, which results in a self-production of activator substance, and a *long-range inhibiting substance*, which suppresses the growth of activator. It is these two competing processes that give rise to different patterns.

In 1993, Pearson [77] observed that for parameter values far from the Turing instability regime, the Gray-Scott model (cf. [35]) in a two-dimensional spatial domain can exhibit a rich variety of spatio-temporal patterns including, stationary spots, traveling spots, spot self-replication, spot-annihilation, growing stripes, labyrinthian patterns , stripe filaments, and spatial-temporal chaos, etc. The common feature in all of these patterns is that each consists of two distinct states of solutions: some localized regions where the chemical concentrations are very large, and a background ambient spatially homogeneous state. As time evolves, the localized regions of elevated chemical concentrations can remain stable, or develop very complicated structures through drifting, splitting, breaking, etc., driven by intricate and unknown mechanisms that depend on the range of parameters in the reaction-diffusion model. The stability and dynamics of these localized patterns can not be analyzed by Turing's approach based on a linearization around a spatially homogeneous equilibrium state.

A detailed mathematical study of these localized structures could have significant applications in controlling chemical reactions for certain purposes, and in understanding and classifying patterns in biological systems. One example is the self-organized formation of either labyrinths, spots, or stripe patterns in the calcification and mineralization of cardiovascular stem cells, described by a prototype Gierer-Meinhardt model (cf. [105]). Another example is the stable or oscillatory spots arising in the BZ reaction in a closed system in which the reactants are mixed with octane and the surfactant aerosol OT (BZ-AOT) (cf. [41]). This reaction can be fabricated to design a re-writable memory device (cf. [41]).

Over the past decade there has been a more systematic effort to undertake detailed numerical and theoretical studies of the dynamics and stability of localized patterns in reaction-diffusion systems. In this introductory chapter, in §1.1 we first review the pioneering work of Turing on stationary, spatially periodic patterns, resulting from the interplay between pure diffusion and nonlinear reaction kinetics. Some experimental and numerical evidence of spot patterns and spot self-replication behavior are provided in §1.2. A brief history of the Gray-Scott model is given in §1.3. The various theoretical approaches for analyzing pattern formation are outlined in §1.4. Previous theoretical work for the existence, stability, and dynamics for one- and two-dimensional reaction-diffusion models are surveyed in §1.5. Finally in §1.6, we give an outline of this thesis and briefly highlight the analytical and numerical approaches that we have employed.

1.1 Turing Patterns

A typical two-component reaction-diffusion (RD) system has the form

$$\tau_A A_t = D_A \Delta A + F(A,H)\,, \quad \mathbf{x} \in \Omega\,; \quad \partial_n A = 0\,, \quad \mathbf{x} \in \partial\Omega\,, \tag{1.1a}$$

$$\tau_H H_t = D_H \Delta H + G(A,H)\,, \quad \mathbf{x} \in \Omega\,; \quad \partial_n H = 0\,, \quad \mathbf{x} \in \partial\Omega\,. \tag{1.1b}$$

Such two-component, and even multi-component, systems arise in many physical applications including, chemical reaction theory with autocatalysis, solid combustion theory, biological morphogenesis, population dynamics with spatial segregation, semiconductor gas-discharge systems, etc..

In many specific systems, A and H are the concentrations of activator and inhibitor, respectively; D_A and D_H are the corresponding diffusion coefficients; τ_A and τ_H represent the corresponding reaction-time constants; F

and G are the nonlinear reaction kinetics. This system has a spatially homogeneous equilibrium solution A_E, H_E when $F(A_E, H_E) = G(A_E, H_E) = 0$. If we ignore the diffusion terms, and only consider the temporal evolution of A and H, then the Jacobian matrix of the kinetics determines the linear stability of this spatially homogeneous solution A_E and H_E. However, in the presence of diffusion, the criteria for instability becomes more complicated.

In 1952, Alan Turing (cf. [90]) studied (1.1) mathematically, and proposed that spatial concentration patterns could arise from an initial arbitrary configuration due to the interaction of reaction and diffusion, which are now known as *Turing patterns*. Then he hypothesized that such structures could play a role in the formation of patterns of leaf buds, skin markings and limbs, etc.

The first experimental observation of Turing patterns occurred almost 40 years later. In [75] it was reported that a chlorite-iodide-malonic acid (CIMA) reaction can support either hexagonal, striped, or mixed, patterns that emerge spontaneously from an initially uniform background, and then remain stationary after propagating for a period of time. These results provided experimental evidence of Turing patterns that can be maintained indefinitely in a well-defined non-equilibrium state. In 1995, Kondo and Asai [58] identified that the skin pattern of a certain species of angelfish also developed according to Turing's instability mechanism.

1.2 Experimental and Numerical Evidence of Spot Patterns in Reaction-Diffusion Systems

The motivation behind much theoretical work on localized pattern formation arises from the diverse laboratory and physical applications where localized patterns occur, and from the many supporting numerical simulations of various RD systems. A survey of experimental and theoretical studies of localized spot patterns through reaction-diffusion modeling in various physical or chemical contexts is given in [92]. Since we are particularly interested in spot patterns (or spike patterns in a one-dimensional spatial domain) and the phenomena of self-replicating spots, the following examples in this section are carefully chosen to demonstrate the existence of spot patterns in various models.

One example of localized spot patterns is for a certain semiconductor gas-discharge system (cf. [3] [4] [5]), which is modeled by a three-component reaction-diffusion system by Schenk et. al. (cf. [80]). In the laboratory experiment, when the current exceeds a certain critical value, the differential resistance of the gas discharge domain becomes negative, and the homogeneous state is then destabilized, which leads to spatio-temporal structures such as the birth, death, and scattering of localized regions of high current density. The experimental figures can be found in [4] and [5].

Our second example concerns *in vitro* experiments that show that vascular-derived mesenchymal stem cells can display self-organized calcified patterns such as labyrinths, stripes, and spots (cf. [30] [105]). In these experiments, the bone morphogenetic protein 2 (BMP-2) acts as an activator, and the matrix GLA protein (MGP) acts as the inhibitor, which is altered by external addition of MGP.

Spot-replication patterns are also observed in numerical simulations of a wide range of RD systems. Muratov and Osipov [61] have performed an extensive numerical study of a prototype two-dimensional system with cubic nonlinearity. The activator nullcline has an 'N'-shape, which determines the properties of patterns and self-organization scenarios. When the ratio of diffusion coefficients and reaction-time constants satisfy $D_A/D_H \ll 1$ and $\tau_A/\tau_H \ll 1$, the self-replication event of a single spot is numerically studied in Fig. 10 of [61]. In addition, it has been shown numerically that above a critical temperature, a certain mathematical model of a diblock copolymer melt can exhibit localized patterns including spots, filaments, and spot self-replication phenomena (cf. [32]).

1.3 A Brief History of the Gray-Scott Model

In this thesis, we concentrate on one specific RD model, the Gray-Scott model, which over the past ten years has been one of the most intensely studied RD system. It was first introduced to model an irreversible chemical reaction $u + 2v \rightarrow 3v, v \rightarrow p$, by Gray and Scott in [35]. It qualitatively models a chemical experiment that is set up in a thin transparent gel reactor, whose bottom surface is in contact with a well-stirred reservoir that is continuously fed by all reagents.

In 1993, Pearson [77] discovered a large variety of spatio-temporal patterns by numerically computing solutions to the two-dimensional Gray-Scott (GS) model. This numerical study stimulated much interest in exploring new non-Turing type localized patterns in other RD systems. In [77] the following GS model with periodic boundary conditions was computed in a square of size 2.5×2.5:

$$U_t = D_U \Delta U - UV^2 + F(1-U)\,, \tag{1.2a}$$

$$V_t = D_V \Delta V + UV^2 - (F+k)V\,. \tag{1.2b}$$

Here k is the dimensionless rate of the second reaction and F is the dimensionless feed rate. The diffusion coefficients are $D_v = 2D_u = 2.0 \times 10^{-5}$. For this ratio of diffusion coefficients used in [77] there are no stable Turing patterns. Clearly, this system has a trivial steady state at $U = 1$ and $V = 0$, which is linearly stable for any F and k. Initially the system was placed at this trivial state, then certain localized regions located symmetrically about the center of the grid were perturbed to $U = 1/2$ and $V = 1/4$. These initial conditions were further perturbed with $\pm 1\%$ random noise to break the symmetry. The system was then integrated for $200,000$ time steps and an image was saved.

In this way, the numerical study of [77] revealed a variety of new and intricate spatial-temporal localized patterns in various regions of the two-dimensional (F, k) parameter space, which had not been seen previously in other RD systems. These patterns include stable spots, traveling spots, a mixture of spots and stripes, growing labyrinths, chaotic dynamics, and a continuous process of spot-birth through replication and spot-death through over-crowding etc. The corresponding phase diagram in the parameter space F vs. k for all patterns was plotted in [77]. Of all the new types of patterns observed, the spot self-replication process was considered the most qualitatively interesting.

Later in 1994, an autocatalytic ferrocyanide-iodate-sulphite (FIS) reaction experiment (cf. [59]) was performed to exhibit spot self-replication in the laboratory. In this experiment the control parameter was the concentration of ferrocyanide input in the reservoir. The repeated growth, self-replication, and annihilation, of spots was observed in this laboratory setting for a wide range of experimental parameters. The chemical reaction kinetics in this experimental reaction, although much more involved, are qualitatively similar to that for a modified Gray-Scott model of the form

$$U_t = D_U \Delta U - UV^2 + A(U_0 - U)\,, \tag{1.3a}$$

$$V_t = D_V \Delta V + UV^2 + B(V_0 - V)\,. \tag{1.3b}$$

Here U and V are the concentrations of the two chemical species, the reagents in the reservoir are at fixed concentrations (U_0, V_0) with $U_0 = V_0 = 1$, while A and B represent the strengths of the coupling between the two chemical species.

Fig. 1.1 shows the time evolution of spot patterns as copied from [59] (with permission). The top row is from the laboratory experiment, with blue (red) representing a state of high (low) pH level. The spot in the middle on the frame $t = 0$ develops a peanut shape at $t = 4$, and eventually

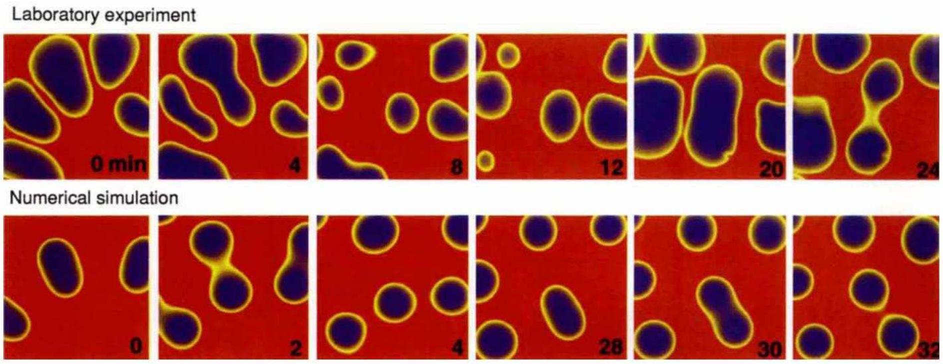

Figure 1.1: *From [59] (with permission). The top row of figures are taken by video camera for the FIS reaction, with the blue (red) area representing high (low) pH levels. The bottom row are figures from the numerical simulation of the Gray-Scott model* (1.3) *(with permission). Similar spot self-replication processes are observed.*

splits. The same phenomena is observed for the spot in the middle of the last two frames. This behavior continues indefinitely, as long as the reactor conditions are maintained. The bottom row of Fig. 1.1 is from the numerical simulation of the dimensionless Gray-Scott model (1.3), with the parameters $A = 0.02, B = 0.079$ and $D_U = 2D_V = 2.0 \times 10^{-5}$. The spots correspond to a region of high concentration V and low concentration U. It is obvious that the self-replication behaviors in the experiment and numerical computation are similar, which also suggests that replicating spots can also occur in other RD systems.

In §1.5 we give a detailed summary of some more recent analytical and numerical studies of localized pattern formation in the GS model in various parameter regimes and from different mathematical viewpoints.

1.4 Methodology

Theoretical approaches for the analysis of spatial-temporal pattern formation have been developed over the past half century. Comprehensive surveys and examples of weakly nonlinear theory for various physical and chemical systems are given in [15], [14], [94], [66], and [95]. In this section, we describe some general analytic approaches that are applicable to many RD systems.

1.4.1 Turing Stability Analysis

For the finite domain problem, a Turing instability is determined by linearizing (1.1) around a spatially homogeneous steady state (A_E, H_E), and then examining the behavior of discrete spatial Fourier modes as a function of a dimensionless bifurcation parameter (cf. [90]).

For (1.1) posed in the one-dimensional interval $0 < x < 1$ with homogeneous Neumann boundary conditions at both endpoints, we perturb the spatially homogeneous state (A_E, H_E) by introducing in (1.1) a sinusoidal perturbation of the form $A = A_E + a\cos(\omega_j x)e^{\lambda t/\tau_A}$ and $H = H_E + h\cos(\omega_j x)e^{\lambda t/\tau_H}$, where $\omega_j = \pi\, j$. By linearizing the resulting system, we obtain the eigenvalue problem

$$\lambda \begin{pmatrix} a \\ h \end{pmatrix} = \begin{pmatrix} -\omega_j^2 D_A + K_1 & K_2 \\ K_3 & -\omega_j^2 D_H + K_4 \end{pmatrix} \begin{pmatrix} a \\ h \end{pmatrix}.$$

Here $K_1 = F_A(A_E, H_E)$, $K_2 = F_H(A_E, H_E)$, $K_3 = G_A(A_E, H_E)$, and $K_4 = G_H(A_E, H_E)$. Assume that the spatially homogeneous equilibrium state is always stable, so that $K_1 + K_4 < 0$ and $K_1K_4 - K_2K_3 > 0$. In the presence of diffusion, the spatially homogeneous equilibrium state is stable when the following two conditions hold:

$$-\omega_j^2(D_A + D_H) + K_1 + K_4 < 0\,, \quad (K_1 - \omega_j^2 D_A)(K_3 - \omega_j^2 D_H) - K_2K_3 > 0\,.$$

When these conditions are not satisfied, the spatially homogeneous equilibrium state loses its stability to a spatially periodic Turing pattern of a certain wavelength. This type of diffusion-driven instability is well-known to occur when the ratio of inhibitor to activator diffusivity, i.e. D_H/D_A, is sufficiently large (cf. [90]). Many examples of this type of linear Turing stability theory are given in [66].

There are several common classifications of RD systems. If A is an activator it means that for some parameters the amplitudes of localized structures of A will grow when H is fixed. Mathematically this requires that $\partial_A F < 0$ for certain values of A and H (cf. [42] [44] [43]). Moreover, if H is an inhibitor it means that H diffuses over a wide range to damp elevated regions of the activator A. These conditions are expressed mathematically in [42], [44], and [43], by $\partial_H G > 0$ and $\partial_A G \cdot \partial_H F < 0$ for all values of A and H. Then, according to the sign of $\partial_A G$, the RD system (1.1) is classified into two categories: the *activator-substrate* model with a Jacobian matrix with sign structure $\begin{pmatrix} + & + \\ - & - \end{pmatrix}$, and the *activator-inhibitor* model with a Jacobian matrix with sign structure $\begin{pmatrix} + & - \\ + & - \end{pmatrix}$.

It follows readily that the GS system (1.2) is an *activator-substrate* model. The activator V increases the rate of a catalyzed reaction, while the chemical U is the substance acted upon by a catalyst, which is referred to as a *substrate*. The inhibitory effect results from the depletion of the substrate required to produce the activator.

1.4.2 Weakly Nonlinear Theory

Perturbation Method

For nonlinear differential equations, finding an analytical solution is impossible in general. However, when some parameters take extreme values, the original model can often be reduced to a simpler one for which the solution can be calculated analytically. In the 1960's and early 1970's, many asymptotic and perturbation methods were developed and studied. The importance of these methods is that they can often greatly reduce the intricate mathematical models into a form that is more amenable to analyze (cf. [81]). Many formal asymptotic and perturbation methods are discussed and illustrated in [45].

One method, called the method of *multiple scales*, applies to wave-type problems where there are two time or space scales; a fast oscillation together with a slow modulation of the envelope of the fast oscillation. Usually it is difficult to represent all physical scales analytically, but this method allows for an accurate solution over asymptotically long time or space intervals.

When the nonlinearities are weak and for the slow spatial and temporal solution behavior generic to parameter values near instability thresholds, the method of *amplitude equations* is often used to describe weakly nonlinear effects for the envelope function associated with the basic state (cf. [82] [67]). The derivation of these amplitude equations, which evolve over an asymptotically long time interval, is based on a formal multiple-scale method. The analysis incorporates projections of the nonlinear terms on the discrete unstable Fourier modes in a perturbative way. For many infinite domain problems, the resulting amplitude equation characterizing a weakly nonlinear instability near a bifurcation point is the complex Ginzburg-Landau model (CGL) partial differential equation

$$\partial_t A = \mu A - (1 + i\alpha)|A|^2 A + \gamma(1 + i\beta)\partial_{xx} A \,. \tag{1.4}$$

Here $i = \sqrt{-1}$, while $\alpha, \beta, \mu, \gamma$ are real constants with numerical values determined by the kinetics and diffusivities of each specific RD system. This CGL model provides a general and simple framework to address various

RD models in a unified manner, and thus it plays an important role in analyzing weakly nonlinear instabilities. However, the CGL model is only valid in a small region near instability thresholds of the base state, and may provide qualitatively misleading information if it is applied to explain pattern formation scenarios far from the instability threshold.

Formal Method of Bifurcation Theory

Another general method of analysis of RD systems uses qualitative *bifurcation theory* of differential equations to find general features of the solutions. Starting in the late 1960s there was an increased focus on the development of a *bifurcation theory* to describe the branching behavior of solutions to differential equations as a function of dimensionless parameters, and to determine mathematical principles governing the exchange of stability of intersecting solution branches. This approach is geometrical and topological, and can be applied either at the level of fast oscillations, or to analyze the amplitude equations that are difficult to solve.

An expansion scheme known as *normal form* theory (cf. [33]) is often considered to preserve the essential features of the original model and it represents a universal description of dynamics near bifurcation points. This theoretical framework is very useful in complicated situations with degenerate or symmetric bifurcations, but it is usually restricted to ideal, spatially periodic solutions.

A related approach is to derive a reduced dynamical description near a bifurcation point by projecting the dynamics onto a lower dimensional space (the *center manifold*). For finite domain problems, *center manifold theory* (cf. [9]) allows for the rigorous analysis of ODE amplitude equations.

1.4.3 Techniques for Localized Spike and Spot Patterns

In contrast to the extensive development and successful use of weakly nonlinear theory to characterize small-amplitude pattern formation near bifurcation points in the 1970's and 1980's, there are few general theoretical results addressing the dynamics and stability of spatially localized patterns for RD models, such as those described in §1.2. The role of analytical theories to explain the dynamics and stability of localized patterns, including localized spikes and spots, stripes, spiral waves and interfacial patterns etc., for which the singular perturbation method is essential, has gained increasing interest since the mid-1980s.

With regards to the rich collection of localized patterns computed for the GS model by him in [77], Pearson comments: "*Most work in this field has focused on pattern formation from a spatially uniform state that is near the transition from linear stability to linear instability. With this restriction, standard bifurcation-theoretic tools such as amplitude equations have been used with considerable success. It is unclear whether the patterns presented here will yield to these standard technologies.*" Further emphasizing this point, Knobloch in his survey [47] remarks that "*The question of the stability of finite amplitude structures, be they periodic or localized, and their bifurcation properties is a major topic that requires new insights.*"

In particular, to characterize localized spike and spot patterns the method of *matched asymptotic expansions* must be used to incorporate the two distinct spatial scales, and to resolve localized regions or boundary layers where solution behavior changes rapidly. Similar singular perturbation techniques often allow for the reduction of an RD system to a finite-dimensional dynamical system for certain *collective coordinates* that evolve slowly in time. The evolution of these coordinates often characterize the dynamics of certain features of quasi-equilibrium localized patterns, such as slowly drifting spots. In order to analyze the stability of spatially localized quasi-equilibrium solutions, one typically must analyze the spectrum of certain singularly perturbed eigenvalue problems. These eigenvalue problems, with two distinct spatial scales, are often very challenging to investigate analytically. In certain limiting cases, a class of nonlocal eigenvalue problems determines the threshold for the instability of localized patterns. This general theoretical framework is the one used in this thesis to investigate some specific aspects of localized pattern formation in the GS model.

1.5 Literature Review: Localized Spot Patterns for Reaction-Diffusion Systems

The experimental and numerical evidence highlighted above for the occurrence of spot patterns and various spatio-temporal structures have, over the past decade, been the motivation for many theoretical investigations concerning the existence, stability, and dynamics of localized patterns in reaction-diffusion systems.

For the study of localized pattern formation, there are two main asymptotic regimes of the diffusion coefficients in (1.1) that can be distinguished: the weak interaction regime with $D_A \ll 1$, $D_A/D_H = O(1)$ where the original numerical simulation of the Gray-Scott model (cf. [77]) was performed, and the semi-strong interaction regime $D_A/D_H \ll 1$, where many analytical studies, such as those described below, have been focused.

In the semi-strong interaction regime, a prototypical reaction-diffusion system of *activator-substrate* type is the Gray-Scott (GS) model (1.2) where the chemical u is a fast-diffusing substrate, and is consumed by a slowly-diffusing activator v. This mechanism drives sharply localized spatial spikes (or spots) of activator coupled with nearby shallow dips of substrate. In contrast, the Gierer-Meinhardt (GM) model was suggested in [31] as a typical *activator-inhibitor* reaction-diffusion system. For this model the reaction terms in (1.1) have the form

$$F(A,H) = -A + \frac{A^p}{H^q}, \quad G(A,H) = -H + \frac{A^r}{H^s}, \quad 1 < \frac{qr}{(p-1)(s+1)}, \quad 1 < p\,.$$

In the semi-strong interaction regime, the time-dependent solutions to the GM model are characterized by sharply localized spatial spikes (or spots) of activator coupled with nearby shallow peaks of inhibitor. The inhibitor has a long range interaction and mediates the creation of additional spikes (or spots) of activator concentration.

Over the past decade there have been many theoretical studies relating to the existence, stability, and dynamics, of localized structures for (1.1) in the semi-strong interaction regime, for various choices of the kinetics. Most of these previous studies have been focused on pattern formation in a one-dimensional domain. In contrast, owing to the significantly increased mathematical complexity of higher dimensional analysis, there have been relatively few analytical studies of localized pattern formation in more realistic two-dimensional domains. In §1.3.1 we give a literature survey of some analytical studies of spike-type pattern formation in one-dimensional domains, while in §1.3.2 we highlight some analytical work for spot-type pattern formation in two-dimensional domains.

1.5.1 Analysis in a One-Dimensional Domain

Since early 1990s, there have been many analytical studies for spike patterns of the Gray-Scott (GS) model (1.2). A convenient alternative dimensionless form of the GS model was put forth in [64], by introducing $v = V/\sqrt{F}$, $x = -1 + 2X/L$ and $t = (F+k)T$, where L is the length of the spatial interval, i.e. $X \in [0, L]$. Then, on $|x| < 1$, (1.2) becomes

$$\begin{aligned} v_t &= \varepsilon^2 v_{xx} - v + Auv^2, \quad v_x(\pm 1, t) = 0\,, && \text{(1.5a)} \\ \tau u_t &= D\, u_{xx} + (1-u) - uv^2, \quad u_x(\pm 1, t) = 0\,, && \text{(1.5b)} \end{aligned}$$

where the positive parameters A, τ, D, and $0 < \varepsilon \ll 1$, are defined in terms of the positive parameters F, k, D_U, D_V, L of (1.2) as

$$D \equiv \frac{4D_U}{FL^2}, \quad \varepsilon^2 \equiv \frac{4D_V}{L^2(F+k)}, \quad \tau \equiv \frac{F+k}{k}, \quad A \equiv \frac{\sqrt{F}}{F+k}.$$

The new system (1.5) is particularly convenient in that it shows that the asymptotic construction of equilibrium solutions in the semi-strong limit $\varepsilon \to 0$ with $D = O(1)$ depends only on the so-called feed-rate parameter A and the diffusion coefficient D. Alternatively, the reaction-time constant τ only influences the stability of the solutions. The effect of the finite domain and the strength of inter-spike interactions is mediated by the diffusivity D. The problem (1.5) for a one-spike solution with $D \ll 1$ and the spike interior to $(-1, 1)$ is essentially equivalent to the problem for a one-spike solution on the infinite line $x \in (-\infty, \infty)$. For $k-$spike patterns, the effect of the finite domain and inter-spike interactions are significant only when $k\sqrt{D} = O(1)$. When $k\sqrt{D} \ll 1$, an equilibrium $k-$spike solution is closely approximated by a solution consisting of k identical copies of a one-spike equilibrium for the infinite line problem.

In the weak interaction regime where $D/\varepsilon^2 = O(1)$, Nishiura et. al [72] have studied self-replicating patterns in (1.2) for the specific diffusivity values $D_U = 2 \times 10^{-5}$ and $D_V = 10^{-5}$. Starting from a localized initial pattern of one spike, self-replication was viewed as a complicated transient process leading to a stable stationary or oscillating Turing pattern. The mechanism underlying spike self-replication suggested in [72] was based on a hierarchical saddle-node bifurcation structure for the global bifurcation branches of multi-spike solutions to (1.2). The saddle-node bifurcation values for multi-spike solution branches were found to nearly coincide. When the parameters in the GS model were chosen to be near this saddle-node bifurcation value, a single initial spike was found to undergo a self-replication process, whereby the two spikes at the extremities of the spike pattern underwent repeated replication. This edge-splitting self-replication process terminated with a stable spatially periodic Turing pattern. Some necessary conditions for the occurrence of self-replicating spike patterns were formulated in [72]. See [72] for further details.

The related investigations of [68] and [73] for the GS model in the weak interaction regime gave a qualitative explanation for the occurrence of spatio-temporal chaos of spikes based on the inter-relationship of global bifurcation branches of ordered patterns with respect to supply (feed-rate parameter F) and removal rates (reaction time constant k). As a result, the chaotic dynamics in the GS model were suggested to be driven by at least two mechanisms. One is the heteroclinic cycle built up by three different processes; long wave instability (the unstable homogeneous state to background state $(1,0)$ with small perturbation), self-replication, and self-destruction (from stationary spike patterns to the homogeneous state). The other possible mechanism was the combination of replication and annihilation (two spikes collide and generate a new one).

In the semi-strong interaction regime $D \gg O(\varepsilon^2)$, the substrate u in the GS model varies globally over the domain. In contrast, the activator v is localized and consists of a a sequence of spikes, each of which is localized within a narrow layer of order $O(\varepsilon)$ around some point interior to the interval. In this semi-strong regime, there are many results from formal asymptotic analysis for spike solutions for the GS model, including, the construction of single spike solutions and pulse-splitting instability [78] [19] [55], the slow dynamics of traveling spikes [22] [16] [17] [64] [86] [53], and the oscillatory instability of the spike amplitudes [54], etc. We now describe some of this work in terms of the different parameter regimes for the dimensionless system (1.5).

In terms of feed-rate parameter A, three distinct regimes for the GS model (1.5) in a one-dimensional domain, each with very different solution behavior, have been identified in [63]. They are the high feed-rate regime $A = O(1)$ (also called the pulse-splitting regime), the low feed-rate regime $A = O(\varepsilon^{1/2})$, and the intermediate regime $O(\varepsilon^{1/2}) \ll A \ll 1$, which separates the former two regimes in A.

In the high feed-rate regime $A = O(1)$, the central phenomena is *pulse-splitting*, as shown in Fig. 1.2(a). Referring to Fig. 1.2(a), there is initially one spike as depicted by the blue curve, whose peak gradually deforms and splits into two spikes as shown by the green curve. The resulting spikes then slowly drift towards their equilibrium location (shown at some later instant by the red curve) as time evolves. Another possible instability that can occur in the high feed-rate regime is the *oscillatory drift instability*. This instability relates to the oscillatory motion of spot locations, as seen in Fig. 1.2(b), where the blue spike keeps its basic shape, but oscillates repeatedly about its equilibrium location at $x = 0$. The realization of either type of instability in a numerical simulation depends on the actual parameter values of $A = O(1)$, D, and τ.

In the high feed-rate regime, the asymptotic study of [55] constructed a certain core problem for k-spike equilibria in a finite domain. The far-field conditions for this core problem were derived from the asymptotic matching of outer and inner expansions for the global variable u. An alternative

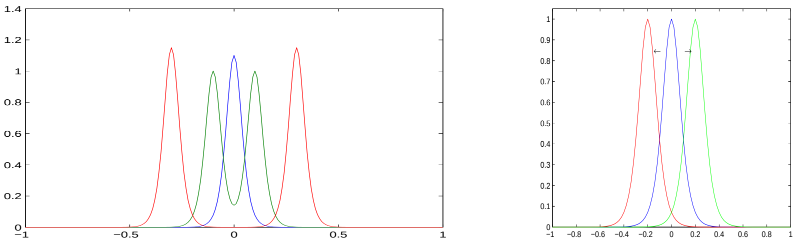

(a) Splitting (b) Drift

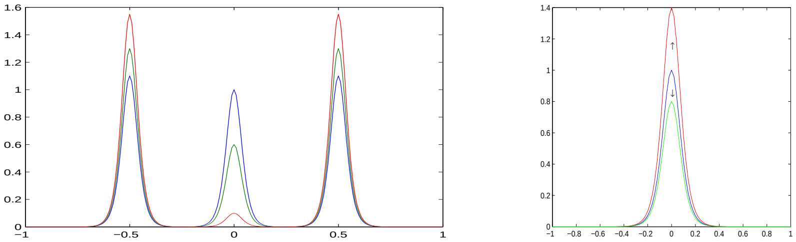

(c) Competition (d) Profile

Figure 1.2: *An illustration of different instabilities of spike solutions* v *vs.* x*. As time evolves, each spike pattern is plotted first by the blue curve, then the green curve and finally the red curve. (a) Splitting instability: one initial spike (in blue) splits into two and the resulting two spikes slowly drift toward their equilibrium locations; (b) Oscillatory drift instability: the location of the spike oscillates about the equilibrium location at* $x = 0$*; (c) Competition instability: the amplitude of the center spike decays as a result of the overcrowding effect; (d) Oscillatory profile instability: the amplitude of a spike oscillates repeatedly.*

analysis, based on geometric singular perturbation theory, was given in [19]. It is shown in [55] that there are no k-spike equilibria to (1.5) when $A > A_{pk}$ with $A_{pk} = 1.347\coth(1/(k\sqrt{D}))$, and that a pulse-splitting process will be initiated in an $O(1)$ time when $A > A_{pk}$. A conjecture based on these critical values A_{pk} was used in [55] to predict the the final number of equilibrium spikes. In addition, in [55] the stability of k-spike equilibria with respect to the small eigenvalues of $O(\varepsilon)$ associated with the oscillatory drift instability was studied. The instability leads to the oscillation of spike locations as shown in Fig. 1.2(b). The scaling law for the Hopf bifurcation value associated with the oscillatory drift instability was found to be $\tau_{TW} = O(\varepsilon^{-1}A^{-2})$, with the exact value for τ_{TW} depending on A, D, ε, k.

In the low feed-rate regime $A = O(\varepsilon^{1/2})$, there are two possible mechanisms for instabilities of spike patterns. One is the *competition instability*, whereby the interaction between spikes may annihilate some of them due to an overcrowding effect. One example of this is given in Fig. 1.2(c), where for an initial pattern of three spikes (in blue), the center spike gradually decays (in green), and eventually is annihilated (in red). Alternatively, the amplitude of a spike may oscillate repeatedly, which is referred to as an *oscillatory profile instability.* This instability is depicted in Fig. 1.2(d). For equilibrium spike solutions, these instabilities were analyzed in [54].

In the low feed-rate regime, with new parameter $\mathcal{A} = \varepsilon^{-1/2}A = O(1)$ and variable $\nu = \varepsilon^{1/2}v$, we reformulate the GS model (1.5) on $|x| < 1$ as

$$\nu_t = \varepsilon^2\nu_{xx} - v + \mathcal{A}u\nu^2\,, \quad v_x(\pm1,t) = 0\,, \tag{1.6a}$$

$$\tau u_t = Du_{xx} + (1-u) - \varepsilon^{-1}u\nu^2\,, \quad u_x(\pm1,t) = 0\,. \tag{1.6b}$$

It was shown in [54] (see also [22]), that there exists a saddle-node bifurcation structure of k-spike equilibria. In addition, a nonlocal eigenvalue problem (NLEP) for the large eigenvalues with $\lambda = O(1)$ was analyzed in [54], which showed that these large eigenvalues can enter the unstable right half-plane either along the real axis or through a Hopf bifurcation leading, respectively, to either a competition instability (also called an overcrowding or annihilation instability) as shown in Fig. 1.2(c)), or to an oscillatory profile instability respectively (as shown in Fig. 1.2(d)). The type of instability obtained depends on the values of $\mathcal{A}$, τ, and D. Other related work for a one-spike solution for the infinite line problem in the low feed-rate regime was given in [63]. An alternative analysis, based on geometric singular perturbation theory, for a periodic spike pattern on the infinite line was given in [93].

In [86], the dynamics and instabilities of quasi-equilibrium two-spike solutions were studied in the low feed-rate regime on a finite domain. The spikes were found to slowly drift towards there equilibrium locations on a finite interval with speed $O(\varepsilon^2)$. It was also shown the parameter thresholds for competition and oscillatory profile instabilities for the two-spike pattern depend on the parameters $\mathcal{A}$, D, and τ, as well as the instantaneous locations of the two spikes. This dependence of the stability thresholds on the spike locations suggests that, for a two-spike pattern that is initially stable, the pattern can be de-stabilized at some later time if, as a result of the spike motion, the stability boundary is crossed before the spikes reach their equilibrium locations. Such an intrinsic dynamically triggered instability was studied in [86]. The companion study [53] analyzed the stability problem of k-spike equilibria with respect to the small eigenvalues $\lambda = O(\varepsilon^2)$, which are associated with slow oscillatory drift instabilities of the equilibrium spike locations. An oscillatory drift instability refers to an oscillatory behavior of the location of a spike around its equilibrium value on a finite domain.

In the intermediate regime, $O(1) \ll \mathcal{A} \ll O(\varepsilon^{-1/2})$, it was shown in [54] that no competition instabilities can occur for a k-spike equilibrium solution when the spikes are separated by $O(1)$ distances. In addition, a single universal NLEP problem independent of D and k was derived to provide a scaling law for the stability of a symmetric k-spike equilibrium solution with respect to oscillatory profile instabilities. The critical value of τ where such profile instabilities occur has the scaling law $\tau_H = O(\mathcal{A}^4) \gg 1$. In contrast, in [53] it was shown that the Hopf bifurcation value associated with the small eigenvalues $\lambda = O(\varepsilon^2)$, governing oscillatory drift instabilities, has the scaling law $\tau_{TW} = O(\varepsilon^{-2}\mathcal{A}^{-2})$. By comparing these two scaling laws, we conclude that there are the following two subregimes in the intermediate regime for $\mathcal{A}$ where different solution behavior occur:

$$O(1) \ll \mathcal{A} \ll O(\varepsilon^{-1/3}), \quad \tau_H \ll \tau_{TW}, \quad \text{profile instability dominates;}$$
$$O(\varepsilon^{-1/3}) \ll \mathcal{A} \ll O(\varepsilon^{-1/2}), \quad \tau_{TW} \ll \tau_H, \quad \text{drift instability dominates.}$$

In the first subregime, an oscillatory profile instability occurs before the onset of an oscillatory drift instability as τ is increased. In contrast, the drift instability dominates in the second subregime as τ is increased. For the infinite-line problem, this result was also observed in [65]. In this thesis, our contribution to the study of spike solutions for the one-dimensional problem focuses on analyzing these two distinct oscillatory instabilities in the intermediate regime for the evolution of multi-spike patterns on a finite interval.

In a more general context, there have been many formal asymptotic studies of spike motion for other two-component reaction-diffusion singularly perturbed reaction-diffusion systems including, $k-$spike dynamics for an elliptic-parabolic limit of the Gierer-Meinhardt (GM) model (cf. [39]), two-spike dynamics for a class of problems including a regularized GM model on the infinite line (cf. [20]), and two-spike dynamics for the GM and GS models (cf. [86]).

In addition to the largely formal asymptotic studies outlined above, there are only a few rigorous theories for spike solutions to two-component reaction-diffusion systems. The existence and stability of single-spike and multi-spike stationary state on the infinite line was studied in [22] and [18]. Recently, in [21] a renormalization method was used to rigorously analyze two-spike dynamics for a regularized GM model on the infinite line.

1.5.2 Analysis in a Two-Dimensional Domain

For a two-dimensional spatial domain, there are only a few analytical results characterizing spot dynamics of reaction-diffusion systems, such as [13], [52] and [88] for a one-spot solution of the GM model, and [26] [27] and [28] for exponentially weakly interacting spots in various contexts.

With regards to the stability of equilibrium multi-spot patterns for singularly perturbed two-component reaction diffusion systems, an analytical theory based on the rigorous derivation and analysis of certain nonlocal eigenvalue problems (NLEP) has been developed in [103] [102] [99] [101] [100] for the GM and GS models.

In [99], the existence and stability of a one-spot solution was analyzed in the infinite domain $\Omega = \mathbb{R}^2$ for the following GS model:

$$v_t = \varepsilon^2 \Delta v - v + Auv^2, \qquad \mathbf{x} \in \Omega, \tag{1.7a}$$

$$\tau u_t = D\,\Delta u + (1-u) - uv^2, \quad \partial_n u = \partial_n v = 0, \quad \mathbf{x} \in \partial\Omega. \tag{1.7b}$$

In [101] the one-spot analysis was extended to treat the case of a $k-$spot patterns on a bounded domain. In [101] it was shown that there is a saddle-node bifurcation for equilibrium solution branches, similar to that for multi-spike patterns for the GS model in one space dimension. This saddle-node bifurcation was found to occur in the low feed-rate regime, characterized by the scaling $A = O(\varepsilon(-\ln\varepsilon)^{1/2})$. In this regime for A, in [101] a leading order asymptotic theory in powers of $\nu \equiv -1/\ln\varepsilon$ was developed to characterize the stability of a k-spot pattern for a fixed τ independent of ε. This leading order theory predicts that the stability threshold for the spot pattern is independent of the spot locations and that there are no oscillatory instabilities in the spot amplitudes for fixed τ independent of ε. Rigorous results of the existence and stability of asymmetric multiple spot patterns for the GS model in $\mathbb{R}^2$ were given in [100]. Finally, a survey of this theory, together with a further application of it to the Schnakenburg model, is described in [104].

However, these previous theoretical results based on the leading order theory in powers of ν have been found not to agree rather closely with stability thresholds computed from full numerical simulations of the GS model. This discrepancy between the previous theoretical results and full numerical results occurs since $\nu = -1/\ln \varepsilon$ is not very small unless ε is extremely small, for which numerical computations are extremely stiff. Therefore, a stability theory for multiple spot solutions that accounts for all terms in powers of ν is required. In addition, since the scaling regime $A = O(\varepsilon(-\ln \varepsilon))$ where a spot-replication instability can occur (cf. [63]) is logarithmically close to the low feed-rate regime $A = O(\varepsilon(-\ln \varepsilon)^{1/2})$ where competition instabilities can occur, it is highly desirable to develop an asymptotic theory that incorporates these two slightly different scaling regimes into a single parameter regime where both types of instabilities be studied simultaneously. The leading order theory in [101] is not sufficiently accurate to treat both types of instabilities in a single parameter regime.

To our knowledge, the first attempt to asymptotically analyze the mechanism of self-replicating spot patterns in a two-dimensional domain is [56] for the Schnakenburg model. In the semi-strong diffusion limit of this model, a differential algebraic (DAE) system of ODE's was derived to describe the dynamical behavior of multi-spot patterns. This asymptotic analysis is based on constructing a quasi-equilibrium solution that has the effect, in the outer region, of representing the spots as logarithmic singularities of certain unknown source strengths at unknown spot locations. Asymptotic matching, based on summing all of the logarithmic terms in the asymptotic expansion, is then used to derive a DAE system for the spot locations and source strengths. Related methods to account for all logarithmic terms in singularly perturbed elliptic problems have been formulated previously for eigenvalue problems in [96] and for other related problems in [85].

With regards to spot self-replication, in [56] the numerical computation of an eigenvalue problem, which was derived by matched asymptotic analysis, was performed to determine the source strength value for the onset of a spot-replication event. This critical value of the source strength was found to depend on the the parameters in the Schnakenburg model, together with the domain geometry and the spot locations through a certain Neumann Green's function.

1.6 Objectives And Outline

The overall general objective of this thesis is to characterize quantitatively the dynamics and instability mechanisms of spatio-temporal localized patterns for the GS model in various parameter regimes. The main analytical method that we use here is a formal matched asymptotic analysis, which is a very powerful tool for problems involving disparate spatial scales, such as those for localized patterns in reaction-diffusion systems. This method provides a way to reduce intricate mathematical models into a form more amenable to analysis. The central role of this asymptotic method in applied mathematics was emphasized by Segel in [81], and in his later paper [84] on quasi-steady state analysis.

More specifically, this thesis consists of certain analytical and numerical results for the GS model in one-dimensional and two-dimensional domains. For a one-dimensional domain, we study the open problem of analyzing the two distinct types of oscillatory instabilities discussed previously together with the dynamics of multi-spike patterns in the intermediate feed-rate regime $O(1) \ll \mathcal{A} \ll O(\varepsilon^{-1/2})$ for the semi-strong interaction limit $D = O(1)$ with $\varepsilon \to 0$. In a two-dimensional domain, we analyze the dynamics, self-replication behavior, and competition and oscillatory profile instabilities of spot patterns in the semi-strong interaction regime $D = O(1)$ and $\varepsilon \to 0$ for the GS model. Phase diagrams in parameter space highlighting where these diverse instabilities can occur are constructed through a combination of analytical and numerical methods from the spectrum of certain eigenvalue problems. The objectives and structure of the thesis are given below in greater detail.

1.6.1 Thesis Outline: the GS Model in a 1-D Domain

In Chapter §2 we analyze the dynamics and oscillatory instabilities of multi-spike solutions to the GS model (1.6) in the intermediate regime $O(1) \ll \mathcal{A} \ll O(\varepsilon^{-1/2})$ of the feed-rate parameter $\mathcal{A}$. The novelty and significance of this intermediate parameter regime is that, in terms of the reaction-time parameter τ, there are two distinct subregimes in $\mathcal{A}$ where qualitatively different types of spike dynamics and instabilities occur. These instabilities are either a breathing instability in the spike amplitude, or a breathing instability in the spike location. In addition, in the intermediate parameter regime a formal singular perturbation analysis, as summarized in Principal Result 2.1, reveals that an ODE-PDE coupled Stefan-type problem with moving Dirac source terms determines the time-dependent locations of the spike trajectories. The derivation and study of this Stefan problem is a new result for spike dynamics in the GS model. Finally, in contrast to previous studies, our study is not limited to the special case of two-spike dynamics. In our analysis we can readily treat an arbitrary number of spikes for (1.6) in the regime $O(1) \ll \mathcal{A} \ll O(\varepsilon^{-1/2})$.

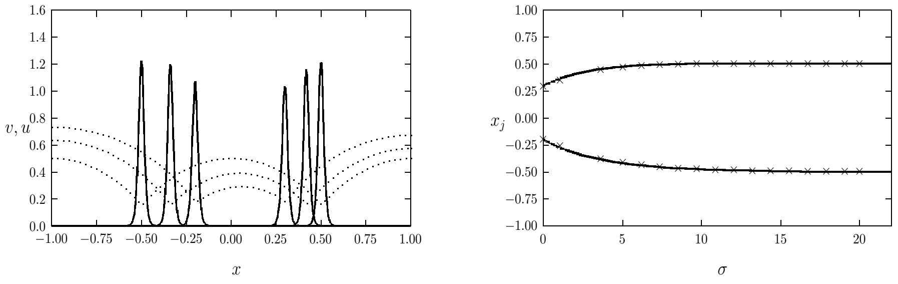

(a) v and u vs. x

(b) x_j vs. σ

Figure 1.3: *Slow dynamics, for* $\varepsilon = 0.01$*,* $\mathcal{A} = 8$*, and* $D = 0.2$*, of a two-spike quasi-equilibrium solution with* $x_1(0) = -0.2$ *and* $x_2(0) = 0.3$*. Left figure: plot of* v *(solid curves) and* u *(dotted curves) vs.* x *at* $\sigma = 0$*,* $\sigma = 2.5$*, and* $\sigma = 30$*. Right figure: plot of* x_j *vs.* $\sigma = \varepsilon^2\mathcal{A}^2 t$*. As* σ *increases, the spikes drift to their steady state limits at* $x = \pm 1/2$*. The solid curves are the asymptotic results and the crosses indicate full numerical results computed from (1.6) using the software of [8].*

In the subregime $O(1) \ll \mathcal{A} \ll O(\varepsilon^{-1/3})$ with $\tau \ll O(\varepsilon^{-2}\mathcal{A}^{-2})$, the Stefan problem is quasi-steady and we derive an explicit differential-algebraic (DAE) system for the spike trajectories. The result is given in Principal Result 2.2. For the case of a two-spike evolution, in Fig. 1.3 we illustrate our result by plotting the quasi-equilibrium solution for u and v together with the spike trajectories for a particular set of the parameter values. In this figure the asymptotic DAE system results for the spike trajectories are shown to compare very favorably with full numerical results computed from (1.6) using the method of [8]. In this subregime, where the speed of the spikes is $O(\varepsilon^2\mathcal{A}^2) \ll 1$, we show from the analysis of a nonlocal eigenvalue problem (NLEP) that the instantaneous quasi-equilibrium spike solution first loses its stability to a Hopf bifurcation in the spike amplitudes when $\tau = \tau_H = O(\mathcal{A}^4)$. This bifurcation leads to oscillations on an $O(1)$ time scale in the amplitudes of the spikes. Our stability results are given in Principal

Results 2.3 and 2.4. These NLEP stability results are the first such results for multi-spike quasi-equilibrium patterns for the GS model on a finite domain with an arbitrary number of spikes. An important remark is that our NLEP stability analysis in the intermediate regime for a multi-spike pattern with $O(1)$ inter-spike distances can be reduced to the study of a *single* NLEP. This feature, which greatly simplifies the stability analysis, is in distinct contrast to the stability analysis of [86] and [54] for the GS model in the low feed-rate regime $\mathcal{A} = O(1)$, and for the corresponding Gierer-Meinhardt model (see [39], [21], [97]), where k distinct NLEP's govern the stability of k-spike patterns.

Next, we study spike dynamics in the subregime $O(\varepsilon^{-1/3}) \ll \mathcal{A} \ll O(\varepsilon^{-1/2})$ with $\tau = \tau_0 \varepsilon^{-2} \mathcal{A}^{-2}$, for some $O(1)$ bifurcation parameter τ_0. In this regime, the time-dependent spike locations are determined from the full numerical solution of a Stefan-type problem with moving Dirac source terms concentrated at the unknown spike locations. Similar moving boundary problems arise in the study of the immersed boundary method (see [6] and [89]). The numerical method that we use for our Stefan problem relies on the approach of [89] involving a high-order spatial discretization of singular Dirac source terms. Such high spatial accuracy is needed in our problem in order to accurately calculate the average flux for u at each source point, which determines the speed of each spike. An explicit time integration scheme is then used to advance the spike trajectories each time step. With this numerical approach we compute large-scale time-dependent oscillatory motion in the spike locations when the reaction-time parameter τ_0 exceeds some critical bifurcation value. Although the overall scheme has a high spatial order of accuracy, the explicit time integration step renders our numerical scheme not particularly suitable for studying large-scale drift instabilities over very long time intervals.

By linearizing the Stefan problem around an equilibrium spike solution, we analytically calculate a critical value of τ_0 at which the equilibrium solution becomes unstable to small-scale oscillations in the equilibrium spike location. This bifurcation value of τ_0, given in Proposition 2.5 below, sets the threshold value for an oscillatory drift instability. The result for τ_0, based on a linearization of the Stefan problem, agrees with the result derived in [53] using the singular limit eigenvalue problem (SLEP) method of [69].

The SLEP method has been extensively used to study similar oscillatory drift instabilities that lead to the destabilization of equilibrium transition layer solutions for Fitzhugh-Nagumo type systems (cf. [70], [38]). With this method, Hopf bifurcation values for the onset of the instability can be calculated and the dominant translation instability, either zigzag or breather, can be identified (cf. [70]). For spatially extended systems on the infinite line, it is then often possible to perform a center manifold reduction, valid near the Hopf bifurcation point, to develop a weakly nonlinear normal form theory for large-scale oscillatory drift instabilities (see [25], [24] and the references therein). In contrast to this normal form theory, we emphasize that our Stefan problem with moving sources provides a description of large-scale oscillatory drift instabilities for values of τ_0 not necessarily close to the Hopf bifurcation point.

Similar Stefan problems with moving Dirac source terms have appeared in a few other contexts. In particular, such a problem determines a flame-front interface in the thin reaction zone limit of a certain PDE model of solid fuel combustion on the infinite line (cf. [76]). By using the heat kernel, this Stefan problem was reformulated in [76] into a nonlinear integro-differential equation for the moving flame-front interface. By solving this integro-differential equation numerically, a periodic doubling cascade and highly irregular relaxation oscillations of the flame-front interface were computed in [76]. For a related Stefan problem arising from solid combustion theory, a three-term Galerkin type-truncation was used in [29] to qualitatively approximate the Stefan problem by a more tractable finite dimensional dynamical system, which can then be readily analyzed. Finally, we remark that in [46] a time-dependent moving source with prescribed speed was shown to prevent blowup behavior for a certain class of nonlinear heat equation.

An outline of Chapter §2 is as follows. In §2.1 we derive the Stefan problem governing spike dynamics in the intermediate regime $O(1) \ll \mathcal{A} \ll O(\varepsilon^{-1/2})$. In §2.1.1 we analyze the quasi-steady limit of this problem. In §2.2 we analyze the stability of the quasi-equilibrium spike patterns of §2.1.1 in the subregime $O(1) \ll \mathcal{A} \ll O(\varepsilon^{-1/3})$. In §2.3 we compute numerical solutions to the Stefan problem showing large-scale oscillatory drift instabilities in the subregime $O(\varepsilon^{-1/3}) \ll \mathcal{A} \ll O(\varepsilon^{-1/2})$. In addition, a critical value of τ_0 for the onset of this instability is determined analytically. Concluding remarks are made in §2.4.

1.6.2 Thesis Outline: the GS Model in a 2-D Domain

In Chapter §3 we construct quasi-equilibrium spot patterns to the GS model in a two-dimensional domain. In addition, we derive a DAE system for the evolution of a k-spot pattern and we study self-replicating instabilities for this pattern.

In §3.1, the method of matched asymptotic expansions is used to construct a $k-$spot quasi-equilibrium solution to the GS model in an arbitrary bounded 2-D spatial domain. Let the j^{th} spot be centered at $\mathbf{x}_j$ for $j = 1, \cdots, k$. The local solution in the vicinity of each spot is, to leading order, radially symmetric. Upon introducing a new local spatial variable, and by rescaling u and v, we derive the following radially symmetric *core* problem that holds in the inner, or local, region near the j^{th} spot:

$$\Delta_\rho V_j - V_j + U_j V_j^2 = 0, \quad \Delta_\rho U_j - U_j V_j^2 = 0, \quad 0 < \rho < \infty, \tag{1.8a}$$

$$V_j \to 0, \quad U_j \to S_j \ln \rho + \chi(S_j) + O(\rho^{-1}), \quad \text{as } \rho \to \infty. \tag{1.8b}$$

Here U_j, V_j are inner variables corresponding to u, v, and Δ_ρ is the radially symmetric part of the Laplacian. In (1.8), the local solution U_j has a logarithmic growth in the far-field, where the unknown *source strength* $S_j > 0$ is introduced to measure the logarithmic growth of the j^{th} spot. This far-field logarithmic behavior for U_j must asymptotically match with a logarithmic singularity of the Green's function for the reduced-wave equation in the 2-D spatial domain. Recall that this Green's function in 2-D can be decomposed as $G(\mathbf{x}; \mathbf{x}_j) \sim -\frac{1}{2\pi} \ln |\mathbf{x} - \mathbf{x}_j| + R_{jj}$, where R_{jj} is the regular, or self-interaction, part of G. The *core* problem, without the explicit far-field condition in (1.8b), was first identified in [64] in the context of the GS model in $\mathbb{R}^2$, and later in the study [56] of the Schnakenburg model. The boundary value problem (1.8) is then solved by using the collocation software COLSYS (cf. [2]), for a range of values of the source strength S_j.

In the outer region, the nonlinear terms in (1.7b) can be represented as the sum of singular Dirac source terms, which results from the localization of the activator v near each x_j. Therefore, in the quasi-steady limit, the outer variable u can be explicitly expressed in terms of the Green's function of the reduced-wave equation. By asymptotically matching the inner and outer solutions for u, a system of algebraic equations for the source strengths S_j for $j = 1, \cdots, k$ is obtained. This system depends on the parameters A, D, and ε together with the spot locations and domain geometry through the Green's function. Analytically, we show that this nonlinear algebraic system has a saddle node bifurcation in terms of the parameter A. After calculating the source strengths, the quasi-equilibrium solution can then be explicitly represented in terms of A, D, ε and the core solution $U_j, V_j, S_j,\ j = 1, \cdots, k$ valid near each spot.

In §3.3 we asymptotically match higher order terms in the asymptotic expansion of the inner and outer solutions to derive an ODE system governing the dynamics of a collection of spots. This ODE system is coupled to the nonlinear algebraic system for the source strengths. The resulting DAE system for the spot locations shows that the speed of each spot is slow on the order $O(\varepsilon^2)$, and that the motion of each spot is proportional to a linear combination of the gradients of a certain Green's function at the other spot locations. This DAE system is asymptotically valid for any quasi-equilibrium spot pattern for parameter values away from the instability thresholds for spot-splitting, spot-oscillation, and spot-annihilation.

In §3.2 we study the stability of the core solution near the j^{th} spot to a local perturbation with angular dependence $e^{im\theta}$, where m is a non-negative integer. Assuming that $\tau\lambda \ll O(\varepsilon^{-2})$, we then derive a radially symmetric eigenvalue problem in which $m \geq 0$ appears as a parameter. The angular mode $m = 1$ corresponds to translation, which trivially has a zero eigenvalue with multiplicity two for any source strength S_j. In contrast, spot-splitting instabilities are associated with modes $m \geq 2$, whereas instabilities in the spot amplitudes correspond to $m = 0$. In §3, we only consider the eigenvalue problem with $m \geq 2$, which corresponds to spot self-replication behavior. For this mode, the local eigenvalue problems near each spot are coupled together only through the nonlinear algebraic system that determine the source strengths S_j for $j = 1, \ldots, k$.

For a given source strength S_j the solution to the core problem (1.8) for the inner variables U_j and V_j is computed. We then compute the spectrum of the local eigenvalue problem near the j^{th} spot in terms of the parameters $m \geq 0$ and S_j. The quasi-equilibrium solution is unstable to spot-replication with mode m when the principal eigenvalue λ_0 of this problem satisfies $\text{Re}(\lambda_0) > 0$. From a numerical computation of the spectrum of this eigenvalue problem, obtained by using the linear algebra package LAPACK (cf. [1]), we determine the splitting threshold by seeking the critical value Σ_m of the source strength S_j for mode m for which the real part of the first eigenvalue λ_0 enters the positive half-plane (i.e. $Re(\lambda_0) = 0$). We compute that $\Sigma_2 < \Sigma_3 < \Sigma_4$, where $\Sigma_2 \approx 4.31$. Therefore, we predict that when S_j satisfies $\Sigma_2 < S_j < \Sigma_3$, a peanut-splitting instability with mode $m = 2$ for the j^{th} spot is initiated through a linear instability. This initial instability is found numerically to be the precursor to a nonlinear spot self-replication event. This self-replication instability occurs in the high feed-rate regime, characterized by $A = O\left(-\varepsilon \ln \varepsilon / \sqrt{D}\right)$.

In §3.4 we determine the direction of spot-splitting relative to the direction of spot motion. In §3.5 we analyze the motion and spot self-replication instability for a two-spot pattern in $\mathbb{R}^2$. In order to obtain an explicit analytical theory for certain bounded domains, in §3.6 we give analytical expressions for the required Green's function for the unit circle and for a rectangular domain, which is valid for the two relevant asymptotic limits $D = O(1)$ and $D \gg 1$. For these specific domains where the Green's function is readily available, we illustrate our asymptotic theory by taking different initial spot patterns, and we compare the asymptotic results for the spot trajectories with corresponding full numerical results computed from (1.7). For instance in Fig. 1.6.2, we show numerical solutions to (1.7) in a square domain $[0, 1] \times [0, 1]$ for the parameter values $A = 2.35$, $D = 1$, and $\varepsilon = 0.02$, starting from an initial 4-spot pattern with spots equally spaced on a ring of radius 0.2 centered at $(0.6, 0.6)$. The initial coordinates of the spots are $\mathbf{x}_1 = (0.8, 0.6)$, $\mathbf{x}_2 = (0.6, 0.8)$, $\mathbf{x}_3 = (0.4, 0.6)$, and $\mathbf{x}_4 = (0.6, 0.4)$. For this domain and parameter set, the numerical computation of the nonlinear algebraic system for the source strengths give $S_1 = S_2 = 2.82$, and $S_3 = S_4 = 5.69 > \Sigma_2$. Based on our stability criterion, the two spots with the larger source strengths are predicted to undergo splitting. The full numerical results show that the spots $\mathbf{x}_1$ and $\mathbf{x}_2$ begin to deform at $t = 11$, undergo self-replication after $t = 21$, and then ultimately approach a steady state $6-$spot pattern when $t \approx 581$. This numerical experiment confirms our asymptotic spot-replication criterion. Many further numerical experiments are done in §3.7.

In Chapter §4, we consider two different types of instabilities of multi-spot quasi-equilibrium solutions to the GS model that occur in different parameter regions. In contrast to the spot-splitting instability occurring in the high feed-rate regime, as considered in Chapter §3, in Chapter §4 we formulate a certain eigenvalue problem associated with the angular mode $m = 0$ in order to study competition and oscillatory profile instabilities of multi-spot patterns in the low feed-rate regime $A = O(\varepsilon(-\ln\varepsilon)^{1/2})$. Recall that in the low feed-rate regime $A = O(\varepsilon^{1/2})$ in a one-dimensional domain unstable eigenvalues can enter the right half-plane either along the $\text{Im}(\lambda) = 0$ axis or through a Hopf-bifurcation, resulting in either a competition instability or an oscillatory profile instability of the spike amplitudes, respectively (cf. [54] and [86]).

Some theoretical instability thresholds for the 2-D GS model for the low feed-rate regime $A = O(\varepsilon(-\ln\varepsilon)^{1/2})$ have been derived previously from a rigorous analysis of a nonlocal eigenvalue problem in [99], [101], and [100]. With a different scaling of the parameters, and to leading order in ν, this previous NLEP theory relies on certain properties of the solution of the radially symmetric scalar ground state problem $w'' + \rho^{-1}w' - w + w^2 = 0$ for the fast variable from (1.7b), together with a constant leading order approximation for the slow variable u in the inner region. With this approximation for

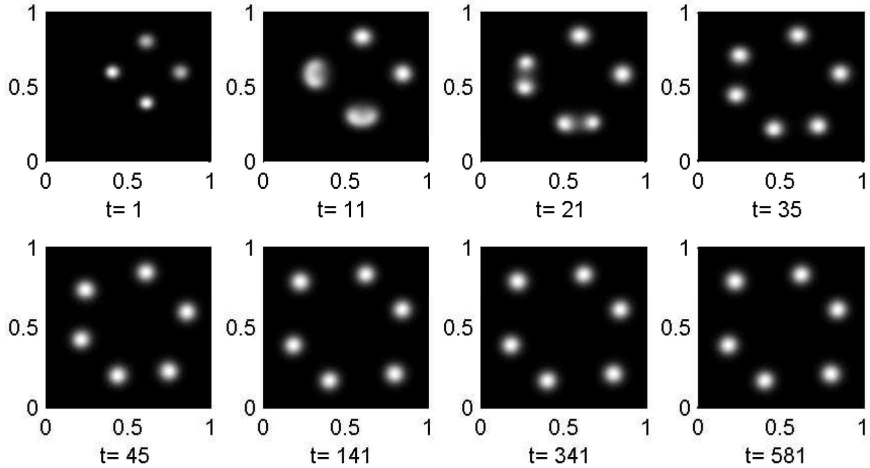

Figure 1.4: *With* $A = 2.35$, $D = 1$, $\varepsilon = 0.02$, *in a square domain* $[0,1]\times[0,1]$, *we compute numerical solutions to* (1.7) *from an initial 4-spot pattern with spots initially equally spaced on a ring of radius* 0.2 *centered at* $(0.6, 0.6)$. *The asymptotic theory yields the source strengths* $S_1 = S_2 = 2.82$ *(two dull spots), and* $S_3 = S_4 = 5.69 > \Sigma_2$ *(two bright spots). The two spots with larger source strengths are predicted to split. The numerical solutions are plotted as time evolves. At* $t = 11$ *the two spots begin to deform, and undergo replication after* $t = 21$. *When* $t = 581$, *a steady state* $6-$*spot pattern is approached. The numerical simulation confirms our asymptotic spot-replication criterion.*

the inner solution near each spot, a nonlocal eigenvalue problem is derived and analyzed to leading order accuracy in ν. This NLEP theory provides a qualitative way to understand the mechanisms for competition and oscillatory instabilities. However, since the instability thresholds from this NLEP theory are only accurate to leading order in ν, our higher order stability theory based on accounting for all logarithmic correction terms in ν is essential for providing accurate instability thresholds for moderately small values of ε.

By studying our eigenvalue problem for $m = 0$ numerically we show that, similar to the one-dimensional case, eigenvalues can enter the right half-plane $\mathrm{Re}(\lambda) > 0$ through either a Hopf bifurcation, leading to an oscillatory profile instability, or along the real axis $\mathrm{Im}(\lambda) = 0$, leading to a competition instability. The eigenvalue problem corresponding to the mode $m = 0$ consists of k separate local eigenvalue problems that are coupled together through a homogeneous linear algebraic system and a nonlinear algebraic system for the source strengths. A numerical method to compute instability thresholds from this non-standard eigenvalue formulation is proposed and implemented. Finally, by combining the profile instability results with the self-replication threshold results of Chapter §3, we plot phase diagrams for certain multi-spot patterns in simple domains that illustrate specific parameter ranges where each instability occurs. The predictions from these phase diagrams are compared with full numerical simulations of the GS model.

The outline of Chapter §4 is as follows. In §4.1, we briefly review the analysis of Chapter §3 that constructed a quasi-equilibrium k-spot pattern with an error smaller than any power of $\nu = -1/\ln\varepsilon$. In addition, we state the eigenvalue problem corresponding to $m = 0$, and discuss the two distinct instability types associated with this problem. Then, we develop a numerical algorithm that efficiently calculates the threshold conditions for the two types of profile instabilities. In §4.2, some analytical results from [99] and [101] for both one-spot and multi-spot patterns, which were obtained from a leading order in $\nu = -1/\ln\varepsilon$ NLEP theory, are summarized. From a perturbation calculation for $\nu \ll 1$, we show that to leading order our constructions of the quasi-equilibrium solution and the eigenvalue problem reproduce those results obtained previously in the NLEP theory of [99] and [101]. From our eigenvalue problem that accounts for all logarithmic correction terms in ν, in §4.3 we numerically calculate the oscillatory instability threshold for a one-spot solution, Moreover, we also compute competition and oscillatory instability thresholds for two-spot patterns in $\mathbb{R}^2$. Then, in §4.4 and §4.5 we consider finite domains such as the unit circle and square for both one-spot or certain symmetric multi-spot patterns. The resulting theoretical instability thresholds are again confirmed from full numerical simulations of the GS model (1.7). Finally in §4.6, we conclude with a short discussion and a list of some open problems.

Chapter 2

Dynamics and Oscillatory Instabilities of Spikes in the One-Dimensional Gray-Scott Model

2.1 The Dynamics of k-Spike Quasi-Equilibria: A Stefan Problem

In this section we first derive the ODE-PDE Stefan-type problem that determines the time-dependent trajectories of the spike locations for (1.6) in the intermediate regime $O(1) \ll \mathcal{A} \ll O(\varepsilon^{-1/2})$.

To do so we first motivate the scalings of u, v, and the slow time that are needed for describing spike dynamics when $O(1) \ll \mathcal{A} \ll O(\varepsilon^{-1/2})$. In the inner region, we introduce a scaling such that $\mathcal{A}uv = O(1)$, with $v = O(\mathcal{A})$ as suggested by the equilibrium theory of §4 of [54] We also introduce the slow time $\sigma = \sigma_0 t$, with $\sigma_0 \ll 1$. With $v = \mathcal{A}v_j$, $u = u_j/\mathcal{A}^2$, and $y = \varepsilon^{-1}\left[x - x_j(\sigma)\right]$, where $\sigma = \sigma_0 t$, (1.6) becomes

$$-\varepsilon^{-1}\sigma_0 \frac{dx_j}{d\sigma} v_j' = v_j'' - v_j + u_j v_j^2 \,, \tag{2.1a}$$

$$-\frac{\sigma_0 \tau}{\mathcal{A}^2}\left(\frac{dx_j}{d\sigma}\right) u_j' = \frac{D}{\varepsilon \mathcal{A}^2} u_j'' + \varepsilon\left(1 - \frac{u_j}{\mathcal{A}^2}\right) - u_j v_j^2 \,, \tag{2.1b}$$

where the primes on u_j and v_j indicate derivatives in y. Multiplying both sides of (2.1b) by $\varepsilon\mathcal{A}^2$, we have the leading order equation $Du_{j0}'' = 0$, and the next order term is $\varepsilon\mathcal{A}^2 u_j v_j^2$ with $u_j v_j^2 = O(1)$, which suggests that $u_j = u_{j0} + O(\varepsilon\mathcal{A}^2)$, where u_{j0} is a constant. This enforces from the equation for v_j that $v_j = v_{j0} + O(\varepsilon\mathcal{A}^2)$, and $\sigma_0 = \varepsilon^2\mathcal{A}^2$. Since u_j is independent of y to leading order, the left-hand side of the equation for u_j can be neglected only when $\sigma_0 \tau \varepsilon \mathcal{A}^2/\mathcal{A}^2 \ll 1$. When $\sigma_0 = \varepsilon^2\mathcal{A}^2$, this condition is satisfied only when $\tau\varepsilon^3\mathcal{A}^2 \ll 1$.

This simple scaling argument suggests that we expand the solution in the j^{th} inner region as

$$u = \frac{1}{\mathcal{A}^2}\left[u_{0j} + \varepsilon\mathcal{A}^2 u_{1j} + \cdots\right] , \qquad v = \mathcal{A}\left[v_{0j} + \varepsilon\mathcal{A}^2 v_{1j} + \cdots\right] , \tag{2.2a}$$

where $u_{mj} = u_{mj}(y,\sigma)$ and $v_{mj}(y,\sigma)$ depend on the inner variable y, and the slow time σ is defined by

$$y \equiv \varepsilon^{-1}\left[x - x_j(\sigma)\right] , \qquad \sigma \equiv \varepsilon^2\mathcal{A}^2 t\,. \tag{2.2b}$$

Upon substituting (2.2) into (1.6), and assuming that $\tau\varepsilon^3\mathcal{A}^2 \ll 1$, we obtain the leading-order problem

$$v_{0j}'' - v_{0j} + u_{0j}v_{0j}^2 = 0\,, \qquad u_{0j}'' = 0\,, \qquad -\infty < y < \infty\,. \tag{2.3}$$

At next order, we obtain on $-\infty < y < \infty$ that

$$v_{1j}'' - v_{1j} + 2u_{0j}v_{0j}v_{1j} = -u_{1j}v_{0j}^2 - x_j'v_{0j}'\,, \qquad Du_{1j}'' = u_{0j}v_{0j}^2\,. \tag{2.4}$$

From (2.3) we take u_{0j} to be independent of y. The leading-order solution is then written as

$$u_{0j} = \frac{1}{\gamma_j}\,, \qquad v_{0j} = \gamma_j w\,, \tag{2.5}$$

where $\gamma_j = \gamma_j(\sigma)$, referred to as the amplitude of the j^{th} spike, is to be found. Here $w(y)$ on $-\infty < y < \infty$ satisfies

$$w'' - w + w^2 = 0\,; \quad w(\pm\infty) = 0\,, \quad w(0) > 0\,, \quad w'(0) = 0\,. \tag{2.6}$$

The unique homoclinic of (2.6) is $w = \frac{3}{2}\text{sech}^2(y/2)$. Therefore, from (2.4), we get on $-\infty < y < \infty$ that

$$\mathcal{L}v_{1j} \equiv v_{1j}'' - v_{1j} + 2wv_{1j} = -\gamma_j^2 w^2 u_{1j} - x_j'\gamma_j w' \qquad Du_{1j}'' = \gamma_j w^2\,. \tag{2.7}$$

Since $\mathcal{L}w' = 0$, the solvability condition for v_{ij} in (2.7) yields that

$$x_j'\int_{-\infty}^{\infty}\left(w'\right)^2\,dy = -\frac{\gamma_j}{3}\int_{-\infty}^{\infty}u_{1j}\frac{d}{dy}\left(w^3\right)\,dy\,. \tag{2.8}$$

Upon integrating (2.8) by parts twice, and noting that w and u_{1j}'' are even functions of y, we obtain

$$x_j'\int_{-\infty}^{\infty}\left(w'\right)^2\,dy = \frac{\gamma_j}{6}\left[u_{1j}'(+\infty) + u_{1j}'(-\infty)\right]\int_{-\infty}^{\infty}w^3\,dy\,. \tag{2.9}$$

The explicit form of w is then used to evaluate the integrals in (2.9) to get

$$x_j' = \gamma_j \left[u_{1j}'(+\infty) + u_{1j}'(-\infty) \right] \,, \qquad j = 1, \cdots, k \,. \tag{2.10}$$

Now consider the outer region defined where $|x - x_j| = O(1)$ for $j = 1, \cdots, k$. Since the term $\varepsilon^{-1} u v^2$ in (1.6) is localized near each $x = x_j$, its effect on the outer solution for u can be calculated in the sense of distributions. From (2.2a), and $\int_{-\infty}^{\infty} w^2 \, dy = 6$, we obtain that $\varepsilon^{-1} u v^2 \to \sum_{j=1}^{k} \gamma_j \left(\int_{-\infty}^{\infty} w^2 \, dy \right) \delta(x - x_j) = \sum_{j=1}^{k} 6\gamma_j \delta(x - x_j)$. This leads to the outer problem for $u(x, \sigma)$ given by

$$\tau \varepsilon^2 \mathcal{A}^2 u_\sigma = D u_{xx} + (1 - u) - \sum_{j=1}^{k} 6\gamma_j \, \delta(x - x_j) \,, \qquad |x| \leq 1 \,,$$

with $u_x = 0$ at $x = \pm 1$. The matching condition between the inner and outer solutions for u yields

$$u(x_j(\sigma), \sigma) = \frac{1}{\gamma_j \mathcal{A}^2} \ll 1 \,, \qquad u_x(x_j^{\pm}(\sigma), \sigma) = u_{1j}'(\pm\infty) \,. \tag{2.11}$$

We summarize our asymptotic construction as follows:
Principal Result 2.1: *Assume that* $\tau \varepsilon^3 \mathcal{A}^2 \ll 1$. *Then, in the intermediate regime* $O(1) \ll \mathcal{A} \ll O(\varepsilon^{-1/2})$, *the GS model (1.6) can be reduced to the coupled ODE-PDE Stefan-type problem*

$$\tau \varepsilon^2 \mathcal{A}^2 u_\sigma = D u_{xx} + (1 - u) - \sum_{j=1}^{k} 6\gamma_j \, \delta(x - x_j) \,, \qquad |x| \leq 1 \,, \tag{2.12a}$$

$$\frac{dx_j}{d\sigma} = \gamma_j \left[u_x(x_j^+, \sigma) + u_x(x_j^-, \sigma) \right] \,, \qquad j = 1, \cdots, k \,, \tag{2.12b}$$

$$u(x_j(\sigma), \sigma) = \frac{1}{\gamma_j \mathcal{A}^2} \,, \qquad j = 1, \cdots, k \,, \tag{2.12c}$$

with $u_x(\pm 1, \sigma) = 0$. *Here* $\sigma = \varepsilon^2 \mathcal{A}^2 t$ *is the slow time scale, and* $x_j(\sigma)$ *is the center of the* j^{th} *spike.*

We observe that (2.12a) is a heat equation with singular Dirac source terms, and that (2.12b) become explicit ODE's only when we can determine $u_x(x_j^{\pm}, \sigma)$ analytically. Finally, the constraints in (2.12c) implicitly determine the spike amplitudes $\gamma_j(\sigma)$, for $j = 1, \cdots, k$. As a remark, the interface motion in (2.12b) resulting from the average of the flux of u_x across the interface differs from that of the classic Stefan moving boundary problem (cf. [74]) from mathematical theories of phase change that involve the difference in the flux of u_x across the interface.

2.1.1 Multi-Spike Quasi-Equilibria: The Quasi-Steady Limit $\tau\varepsilon^2\mathcal{A}^2 \ll 1$

We suppose that $\tau \ll \varepsilon^{-2}\mathcal{A}^{-2}$ so that u in (2.12a) is quasi-steady. With this assumption, we readily calculate from (2.12a), together with $u_x = 0$ at $x = \pm 1$, that

$$u = \begin{cases} 1 - g_1 \frac{\cosh(\theta(x+1))}{\cosh(\theta(x_1+1))}\,, & -1 \le x < x_1 \\ 1 - g_j \frac{\sinh(\theta(x_{j+1}-x))}{\sinh(\theta(x_{j+1}-x_j))} - g_{j+1} \frac{\sinh(\theta(x-x_j))}{\sinh(\theta(x_{j+1}-x_j))}\,, & x_j \le x \le x_{j+1}\,, \\ 1 - g_k \frac{\cosh(\theta(1-x))}{\cosh(\theta(1-x_k))}\,, & x_k < x \le 1\,. \end{cases} \tag{2.13}$$

In the middle expression above the index j ranges from $j = 1, \dots, k-1$. Here $\theta \equiv D^{-1/2}$ and $u = 1 - g_j$ at $x = x_j$. From this solution we calculate u_x as $x \to x_j^{\pm}$, and we impose the required jump conditions $[Du_x]_j = 6\gamma_j$ for $j = 1, \cdots, k$ as seen from (2.12a). Here $[\zeta]_j \equiv \zeta(x_j^+) - \zeta(x_j^-)$. This leads to the matrix problem

$$\mathcal{B}\,\mathbf{g} = \frac{6}{\sqrt{D}}\,\Gamma\,\mathbf{e}\,, \tag{2.14}$$

where the matrices $\mathcal{B}$ and Γ are defined by

$$\mathcal{B} \equiv \begin{pmatrix} c_1 & d_1 & 0 & \cdots & 0 \\ d_1 & c_2 & d_2 & \cdots & 0 \\ \vdots & \ddots & \ddots & \ddots & \vdots \\ 0 & \cdots & d_{k-2} & c_{k-1} & d_{k-1} \\ 0 & \cdots & 0 & d_{k-1} & c_k \end{pmatrix}, \quad \Gamma \equiv \begin{pmatrix} \gamma_1 & \cdots & 0 \\ \vdots & \ddots & \vdots \\ 0 & \cdots & \gamma_k \end{pmatrix}. \tag{2.15}$$

The vectors $\mathbf{g}$ and $\mathbf{e}$ are $\mathbf{g}^T \equiv (g_1, \cdots, g_k)$, $\mathbf{e}^T \equiv (1, \cdots, 1)$. The matrix entries of $\mathcal{B}$ are given explicitly by

$$\begin{gathered} c_1 = \coth(\theta(x_2 - x_1)) + \tanh(\theta(1 + x_1))\,, \\ c_k = \coth(\theta(x_k - x_{k-1})) + \tanh(\theta(1 - x_k))\,, \\ c_j = \coth(\theta(x_{j+1} - x_j)) + \coth(\theta(x_j - x_{j-1}))\,, \quad j = 2, \cdots, k-1\,, \\ d_j = -\operatorname{csch}(\theta(x_{j+1} - x_j))\,, \quad j = 1, \cdots, k-1\,. \end{gathered} \tag{2.16}$$

Next, we write the constraint (2.12c) in matrix form and combine it with (2.14) to get

$$\mathbf{g} = \mathbf{e} - \frac{1}{\mathcal{A}^2}\Gamma^{-1}\mathbf{e}\,. \qquad \gamma = \frac{\sqrt{D}}{6}\left(\mathcal{B}\mathbf{e} - \frac{1}{\mathcal{A}^2}\mathcal{B}\Gamma^{-1}\mathbf{e}\right)\,, \tag{2.17}$$

where $\gamma \equiv (\gamma_1, \cdots, \gamma_k)^t$. Since Γ^{-1} depends on γ, (2.17) is a nonlinear algebraic system for the spike amplitudes γ_j for $j = 1, \cdots, k$. For $\mathcal{A} \gg 1$, (2.17) reduces asymptotically to the two-term result

$$\gamma = \frac{\sqrt{D}}{6}\mathcal{B}\left(I - \frac{6}{\mathcal{A}^2\sqrt{D}}\Gamma_0^{-1}\right)\mathbf{e} + O(\mathcal{A}^{-4}), \tag{2.18}$$

where I is the identity matrix. Here Γ_0^{-1} is the inverse of the diagonal matrix Γ_0 defined by

$$\Gamma_0 \equiv \begin{pmatrix} (\mathcal{B}\mathbf{e})_1 & \cdots & 0 \\ \vdots & \ddots & \vdots \\ 0 & \cdots & (\mathcal{B}\mathbf{e})_k \end{pmatrix}, \tag{2.19}$$

where $(\mathcal{B}\mathbf{e})_j$ denotes the j^{th} component of the vector $\mathcal{B}\mathbf{e}$. Upon using the identity $\coth\mu - \text{csch}\mu = \tanh(\mu/2)$, we can write (2.18) component-wise as

$$\gamma_j = \frac{\sqrt{D}}{6}(\mathcal{B}\mathbf{e})_j\left(1 - \frac{6}{\mathcal{A}^2\sqrt{D}}r_j\right) + O(\mathcal{A}^{-4}), \qquad r_j \equiv \frac{\left(\mathcal{B}\Gamma_0^{-1}\mathbf{e}\right)_j}{(\mathcal{B}\mathbf{e})_j}, \tag{2.20a}$$

where

$$(\mathcal{B}\mathbf{e}) = \begin{pmatrix} \tanh\left(\frac{\theta}{2}(x_2 - x_1)\right) + \tanh\left(\theta(1 + x_1)\right) \\ \vdots \\ \tanh\left(\frac{\theta}{2}(x_j - x_{j-1})\right) + \tanh\left(\frac{\theta}{2}(x_{j+1} - x_j)\right) \\ \vdots \\ \tanh\left(\frac{\theta}{2}(x_k - x_{k-1})\right) + \tanh\left(\theta(1 - x_k)\right) \end{pmatrix}. \tag{2.20b}$$

With this approximation, and since $\Gamma^{-1} \sim \frac{6}{\sqrt{D}}\Gamma_0^{-1}$ for $\mathcal{A} \gg 1$, (2.17) for $\mathbf{g}$ reduces asymptotically to

$$\mathbf{g} = \mathbf{e} - \frac{6}{\mathcal{A}^2\sqrt{D}}\,\Gamma_0^{-1}\mathbf{e} + O(\mathcal{A}^{-4}). \tag{2.21}$$

This asymptotically determines the unknown constants g_j for $j = 1, \cdots, k$ in (2.13) with an error $O(\mathcal{A}^{-4})$.

Next, we derive an explicit form for the ODE's in (2.12b). By calculating $u_x(x_j^{\pm})$ from (2.13), we readily derive that $\mathbf{x}' = (x_1', \cdots, x_k')^t$ satisfies

$$\mathbf{x}' = -\frac{1}{\sqrt{D}}\Gamma\mathcal{Q}\,\mathbf{g}, \tag{2.22}$$

where $\mathcal{Q}$ is the tridiagonal matrix defined by

$$\mathcal{Q} \equiv \begin{pmatrix} e_1 & f_1 & 0 & \cdots & 0 \\ -f_1 & e_2 & f_2 & \cdots & 0 \\ \vdots & \ddots & \ddots & \ddots & \vdots \\ 0 & \cdots & -f_{k-2} & e_{k-1} & f_{k-1} \\ 0 & \cdots & 0 & -f_{k-1} & e_k \end{pmatrix}, \tag{2.23a}$$

with matrix entries

$$\begin{gathered} e_1 = -\coth(\theta(x_2 - x_1)) + \tanh(\theta(1 + x_1)) \,, \\ e_k = \coth(\theta(x_k - x_{k-1})) - \tanh(\theta(1 - x_k)) \,, \\ e_j = -\coth(\theta(x_{j+1} - x_j)) + \coth(\theta(x_j - x_{j-1})) \,, \quad j = 2, \cdots, k-1 \,, \\ f_j = \operatorname{csch}(\theta(x_{j+1} - x_j)) \,, \quad j = 1, \cdots, k-1 \,. \end{gathered} \tag{2.23b}$$

Finally, by combining (2.22) and (2.17), we obtain the following asymptotic result for the dynamics of k-spike quasi-equilibria:

<u>Principal Result 2.2:</u> *Assume that $O(1) \ll \mathcal{A} \ll O(\varepsilon^{-1/2})$ and that τ satisfies $\tau\varepsilon^2\mathcal{A}^2 \ll 1$. Then, the quasi-equilibrium solution for $v(x,\sigma)$ satisfies*

$$v(x,\sigma) \sim \mathcal{A} \sum_{j=1}^{k} \gamma_j w \left[\varepsilon^{-1}(x - x_j(\sigma))\right] \,, \tag{2.24}$$

where $w(y) = \frac{3}{2}\text{sech}^2(y/2)$. The corresponding outer approximation for u is given in (2.13) where the coefficients g_j in (2.13) for $j = 1, \cdots, k$ are given asymptotically in (2.21). For $\mathcal{A} \gg 1$, the spike amplitudes $\gamma_j(\sigma)$ are given asymptotically in terms of the instantaneous spike locations x_j by (2.20a). Finally, the vector of spike locations satisfy the ODE system

$$\frac{d\mathbf{x}}{d\sigma} \sim -\frac{1}{\sqrt{D}} \Gamma \mathcal{Q} \left(I - \frac{6}{\mathcal{A}^2\sqrt{D}} \Gamma_0^{-1} \right) \mathbf{e} \,, \tag{2.25}$$

with $\sigma = \varepsilon^2\mathcal{A}^2 t$. Here Γ_0 is defined in (2.19) and Γ is defined in (2.15).

The equilibrium positions of the spikes satisfy $\Gamma\,\mathcal{Q}\,\mathbf{g} = 0$. In equilibrium, γ_j is a constant independent of j, and hence $\mathbf{g} = c\mathbf{e}$ where c is some constant. Consequently, the equilibrium spike locations satisfy $\mathcal{Q}\mathbf{e} = \mathbf{0}$. By using (2.23), this leads to $x_j = -1 + (2j-1)/k$ for $j = 1, \cdots, k$.

The leading-order approximation for the ODE's in (2.25) is obtained by using $\Gamma \sim \frac{\sqrt{D}}{6}\Gamma_0 + O(\mathcal{A}^{-2})$, and $\mathbf{g} \sim \mathbf{e} + O(\mathcal{A}^{-2})$. With this approximation, which neglects the $O(\mathcal{A}^2)$ terms, (2.25) reduces to

$$\begin{aligned}
x_1' &\sim -\frac{1}{6}\left(\tanh^2\left[\theta(1+x_1)\right] - \tanh^2\left[\frac{\theta}{2}(x_2-x_1)\right]\right) \,, \\
x_j' &\sim -\frac{1}{6}\left(\tanh^2\left[\frac{\theta}{2}(x_j-x_{j-1})\right] - \tanh^2\left[\frac{\theta}{2}(x_{j+1}-x_j)\right]\right) \,, \\
&\qquad\qquad\qquad\qquad \text{for} \quad j=1,\cdots,k-1 \,, \qquad (2.26) \\
x_k' &\sim -\frac{1}{6}\left(\tanh^2\left[\frac{\theta}{2}(x_k-x_{k-1})\right] - \tanh^2\left[\theta(1-x_k)\right]\right) \,.
\end{aligned}$$

2.2 Oscillatory Profile Instabilities of k-Spike Quasi-Equilibria

We now analyze the stability of the k-spike quasi-equilibrium solution of §2.1 to instabilities occurring on a fast $O(1)$ time scale. Since the spike locations drift slowly with speed $O(\varepsilon^2\mathcal{A}^2)$ (cf. (2.25)), in our stability analysis we make the asymptotic approximation that the spikes are at some fixed locations $x_1, \cdots, x_k$. This asymptotic separation of time scales with "frozen" spike locations allows for the derivation of an NLEP governing fast instabilities.

Let u_e and v_e be the quasi-equilibrium solution constructed in §2.1. We substitute $u(x,t) = u_e + e^{\lambda t}\eta(x)$ and $v(x,t) = v_e + e^{\lambda t}\phi(x)$ into (1.6), and then linearize to obtain

$$\varepsilon^2\phi_{xx} - \phi + 2\mathcal{A}u_e v_e\phi + \mathcal{A}v_e^2\eta = \lambda\phi \,, \quad |x| \leq 1 \,; \quad \phi_x(\pm 1) = 0 \,, \qquad (2.27\text{a})$$

$$D\eta_{xx} - (1+\tau\lambda)\,\eta - \varepsilon^{-1}v_e^2\eta = 2\varepsilon^{-1}u_e v_e\phi \,, \quad |x| \leq 1 \,; \quad \eta_x(\pm 1) = 0 \,. \qquad (2.27\text{b})$$

We then look for a localized eigenfunction for ϕ in the form

$$\phi(x) = \sum_{j=1}^{k} \phi_j\left[\varepsilon^{-1}(x-x_j)\right] \,, \qquad (2.28)$$

with $\phi_j \to 0$ as $|y| \to \infty$. Since $v_e \sim \mathcal{A}\gamma_j w$ and $u_e \sim 1/(\gamma_j\mathcal{A}^2)$ near $x = x_j$, we obtain from (2.27a) that $\phi_j(y)$ satisfies

$$\phi_j'' - \phi_j + 2w\phi_j + \mathcal{A}^3\gamma_j^2 w^2\eta(x_j) = \lambda\phi_j \,, \qquad -\infty < y < \infty \,. \qquad (2.29)$$

Next, we consider (2.27b). Since ϕ_j is localized near each spike, the spatially inhomogeneous coefficients in (2.27b) can be approximated by

Dirac masses. In this way, and by using $v_e \sim \mathcal{A}\gamma_j w$, $u_e \sim 1/(\gamma_j \mathcal{A}^2)$, and $\int_{-\infty}^{\infty} w^2\, dy = 6$, we obtain for x near x_j that, in a distributional sense, $2\varepsilon^{-1} u_e v_e \phi \sim \frac{2}{\mathcal{A}} \left(\int_{-\infty}^{\infty} w\phi_j\, dy \right) \delta(x - x_j)$ and $\varepsilon^{-1} v_e^2 \sim 6\mathcal{A}^2 \gamma_j^2 \delta(x - x_j)$. Therefore, the outer problem for η in (2.27b) becomes

$$D\eta_{xx} - \left[1 + \tau\lambda + 6\mathcal{A}^2 \sum_{j=1}^{k} \gamma_j^2\, \delta(x - x_j) \right] \eta = \sum_{j=1}^{k} \frac{2}{\mathcal{A}} \left(\int_{-\infty}^{+\infty} w\phi_j\, dy \right) \delta(x - x_j)\,, \tag{2.30}$$

with $\eta_x = 0$ at $x = \pm 1$. Defining $[\xi]_j$ by $[\xi]_j \equiv \xi(x_{j+}) - \xi(x_{j-})$, we obtain the following equivalent problem for η:

$$D\eta_{xx} - (1 + \tau\lambda)\,\eta = 0\,, \quad |x| \leq 1\,; \qquad \eta_x(\pm 1) = 0\,, \tag{2.31a}$$

$$[\eta]_j = 0\,, \quad [D\eta_x]_j = -6\omega_j + 6\mathcal{A}^2\gamma_j^2 \eta(x_j)\,, \quad j = 1, .., k\,;$$
$$\omega_j \equiv -\frac{2}{\mathcal{A}} \left(\frac{\int_{-\infty}^{\infty} w\phi_j\, dy}{\int_{-\infty}^{\infty} w^2\, dy} \right). \tag{2.31b}$$

Next, we calculate $\eta_j \equiv \eta(x_j)$ from (2.31), which is needed in (2.29). To do so, we solve (2.31a) on each subinterval and then use the jump conditions in (2.31b). This leads to the matrix problem

$$\mathcal{E}_\lambda \boldsymbol{\eta} = \frac{6}{[D(1+\tau\lambda)]^{1/2}} \boldsymbol{\omega}\,, \tag{2.32}$$

where the vectors $\boldsymbol{\omega}$ and $\boldsymbol{\eta}$ are defined by $\boldsymbol{\omega}^t = (\omega_1, \cdots, \omega_k)$ and $\boldsymbol{\eta}^t = (\eta_1, \cdots, \eta_k)$, and where t denotes transpose. The matrix $\mathcal{E}_\lambda$ in (2.32) is defined in terms of a tridiagonal matrix $\mathcal{B}_\lambda$ by

$$\mathcal{E}_\lambda \equiv \mathcal{B}_\lambda + \frac{6\mathcal{A}^2}{\sqrt{D(1+\tau\lambda)}}\,\Gamma^2\,, \quad \mathcal{B}_\lambda \equiv \begin{pmatrix} c_{1,\lambda} & d_{1,\lambda} & 0 & \cdots & 0 \\ d_{1,\lambda} & \ddots & \ddots & \ddots & \vdots \\ 0 & \ddots & \ddots & \ddots & 0 \\ \vdots & \ddots & \ddots & \ddots & d_{k-1,\lambda} \\ 0 & \cdots & 0 & d_{k-1,\lambda} & c_{k,\lambda} \end{pmatrix}. \tag{2.33}$$

Here Γ is the diagonal matrix of spike amplitudes defined in (2.15). The matrix entries of $\mathcal{B}_\lambda$ are

$$\begin{aligned} c_{1,\lambda} &= \coth(\theta_\lambda(x_2 - x_1)) + \tanh(\theta_\lambda(1 + x_1)) \,, \\ c_{k,\lambda} &= \coth(\theta_\lambda(x_k - x_{k-1}) + \tanh(\theta_\lambda(1 - x_k)) \,, \\ c_{j,\lambda} &= \coth\left(\theta_\lambda(x_{j+1} - x_j)\right) + \coth\left(\theta_\lambda(x_j - x_{j-1})\right) \,, \quad j = 2, \cdots, k-1 \,, \\ d_{j,\lambda} &= -\operatorname{csch}\left(\theta_\lambda(x_{j+1} - x_j)\right) \,, \quad j = 1, \cdots, k-1 \,. \end{aligned} \tag{2.34}$$

In (2.34), θ_λ is the principal branch of the square root for $\theta_\lambda \equiv \theta_0\sqrt{1+\tau\lambda}$, with $\theta_0 \equiv D^{-1/2}$. Notice that when $\lambda = 0$, $\mathcal{B}_\lambda = \mathcal{B}$, where $\mathcal{B}$ was defined in (2.15).

Next, we invert (2.32) to obtain

$$\boldsymbol{\eta} = \frac{1}{[D(1+\tau\lambda)]^{1/2}} \mathcal{E}_\lambda^{-1} \boldsymbol{\omega} = -\frac{12}{\mathcal{A}\sqrt{D(1+\tau\lambda)}} \left(\frac{\int_{-\infty}^{\infty} w \left(\mathcal{E}_\lambda^{-1} \boldsymbol{\phi}\right) \, dy}{\int_{-\infty}^{\infty} w^2 \, dy} \right) , \tag{2.35}$$

where $\boldsymbol{\phi}^t = (\phi_1, \cdots, \phi_k)$. Substituting (2.35) into (2.29), we obtain the following NLEP in terms of a new matrix $\mathcal{C}_\lambda$:

$$\boldsymbol{\phi}'' - \boldsymbol{\phi} + 2w\boldsymbol{\phi} - w^2 \left(\frac{\int_{-\infty}^{\infty} w \left(\mathcal{C}_\lambda \boldsymbol{\phi}\right) \, dy}{\int_{-\infty}^{\infty} w^2 \, dy} \right) = \lambda \boldsymbol{\phi} \, ; \quad \mathcal{C}_\lambda \equiv \frac{12\mathcal{A}^2}{\sqrt{D(1+\tau\lambda)}} \Gamma^2 \mathcal{E}_\lambda^{-1} \, . \tag{2.36}$$

Since Γ is a positive definite diagonal matrix and $\mathcal{E}_\lambda$ is symmetric, we can decompose $\mathcal{C}_\lambda$ as

$$\mathcal{C}_\lambda = \mathcal{S} \mathcal{X} \mathcal{S}^{-1} \,, \tag{2.37}$$

where $\mathcal{X}$ is the diagonal matrix of eigenvalues χ_j of $\mathcal{C}_\lambda$ and $\mathcal{S}$ is the matrix of its eigenvectors $\boldsymbol{s}_j$. We then set $\boldsymbol{\psi} = \mathcal{S}^{-1}\boldsymbol{\phi}$ to diagonalize (2.36), and we rewrite $\mathcal{C}_\lambda$ in terms of $\mathcal{B}_\lambda$ by using (2.33). This leads to the following stability criterion for $O(1)$ time scale instabilities:

Principal Result 2.3: *The k-spike quasi-equilibrium solution of §2.1 with fixed spike locations is stable on a fast $O(1)$ time scale if the following k NLEP's on $-\infty < y < \infty$, given by*

$$\psi'' - \psi + 2w\psi - \chi_j(\tau\lambda) w^2 \left(\frac{\int_{-\infty}^{\infty} w\psi \, dy}{\int_{-\infty}^{\infty} w^2 \, dy} \right) = \lambda\psi \, ; \qquad \psi \to 0 \quad \text{as} \quad |y| \to \infty \,, \tag{2.38}$$

only have eigenvalues with Re$(\lambda) < 0$. Here $\chi_j(\tau\lambda)$ for $j = 1, \cdots, k$ are the eigenvalues of the matrix C_λ defined by

$$\mathcal{C}_\lambda = 2 \left[I + \frac{\sqrt{D(1+\tau\lambda)}}{6\mathcal{A}^2} \mathcal{B}_\lambda \Gamma^{-2} \right]^{-1} \, . \tag{2.39}$$

We now analyze (2.38). Let $\tau = O(1)$ and assume that the inter-spike distances $d_j = x_{j+1} - x_j$ for $j = 0, \cdots, k$ are $O(1)$. Here, for $j = 0$ and $j = k$ we define $d_0 = x_1 + 1$ and $d_k = 1 - x_k$, respectively. Then, for $\mathcal{A} \gg 1$, (2.39) yields $C_\lambda \sim 2I$ so that $\chi_j \sim 2$ for $j = 1, \cdots, k$. Since χ_j is a constant with $\chi_j > 1$ in this limit, the result of Theorem 1.4 of [98] proves that $\text{Re}(\lambda) < 0$. This guarantees stability for $\mathcal{A} \gg 1$ when $\tau = O(1)$ and $d_j = x_{j+1} - x_j = O(1)$.

Next, we consider the limit $\mathcal{A} \gg 1$, $\tau = O(1)$, but we will allow for the inter-spike distances $d_j = x_{j+1} - x_j$ to be small but with $d_j \gg O(\varepsilon)$. Recall that the analysis above and in §2.1 leading to Principal Result 2.3 required that $d_j \gg O(\varepsilon)$. We will show that for the scaling regime $d_j = O(\mathcal{A}^{-2/3}) \gg O(\varepsilon)$ of closely spaced spikes, and with $O(1) \ll \mathcal{A} \ll O(\varepsilon^{-1/2})$, the NLEP (2.38) can have an unstable eigenvalue for any $\tau > 0$. For simplicity we will only consider a closely spaced equilibrium configuration with $j = 1, \cdots, k-1$, and $d_0 = d_k = L/2$. In this limit it is readily shown from (2.34) that

$$\mathcal{B}_\lambda \sim \frac{1}{\theta_\lambda L}\mathcal{B}_0 \,, \qquad \mathcal{B}_0 \equiv \begin{pmatrix} 1 & -1 & 0 & \cdots & 0 \\ -1 & 2 & -1 & \cdots & 0 \\ \vdots & \ddots & \ddots & \ddots & \vdots \\ 0 & \cdots & -1 & 2 & -1 \\ 0 & \cdots & 0 & -1 & 1 \end{pmatrix} . \tag{2.40}$$

Moreover, for $\mathcal{A} \gg 1$ and with spikes of a uniform spacing $L \ll 1$, we obtain from (2.20) that the spikes have a common amplitude given by

$$\gamma_j \sim \frac{\sqrt{D}}{6} \left(\mathcal{B}e\right)_j = \frac{\sqrt{D}}{3} \tanh\left(\frac{\theta_0 L}{2}\right) \sim \frac{L}{6} \,. \tag{2.41}$$

Substituting (2.40) and (2.41) into (2.39), we obtain that the eigenvalues χ_j of C_λ are given by

$$\chi_j \sim 2\left[1 + \frac{\sqrt{D(1+\tau\lambda)}}{6\mathcal{A}^2}\left(\frac{36}{L^2}\right)\left(\frac{r_j}{\theta_\lambda L}\right)\right]^{-1} = 2\left[1 + \frac{6Dr_j}{\mathcal{A}^2 L^3}\right]^{-1} , \tag{2.42}$$

where r_j for $j = 1, \cdots, k$ are the eigenvalues of the matrix $\mathcal{B}_0$ defined in (2.40). Appendix E of [40] and Theorem 1.4 of [98] prove that when χ_j is constant, then $\text{Re}(\lambda) > 0$ if and only if $\chi_j < 1$ for $j = 1, \cdots, k$.

The stability threshold is determined by $\chi_m \equiv \min_{j=1,\cdots,k}(\chi_j) = 1$, which depends on the largest eigenvalue $r_m \equiv \max_{j=1,\cdots k}(r_j)$ of $\mathcal{B}_0$. By calculating r_m and setting $\chi_m = 1$, we obtain that the k-spike equilibrium solution is unstable for any $\tau > 0$ on the regime $O(1) \ll \mathcal{A} \ll O(\varepsilon^{-1/2})$ when $L < L_*$, where

$$L_* \equiv \left(\frac{6Dr_m}{\mathcal{A}^2} \right)^{1/3} , \qquad r_m \equiv 2 \left[1 + \cos(\pi/k) \right] . \tag{2.43}$$

The result (2.43) shows that competition instabilities in the intermediate regime $O(1) \ll \mathcal{A} \ll O(\varepsilon^{-1/2})$ can only occur if the spikes are sufficiently close with inter-spike separation $O(\mathcal{A}^{-2/3})$. If we did set $\mathcal{A} = O(1)$ in (2.43), then $L_* = O(1)$ is consistent with the scalings in [54] and [86] for competition instabilities of equilibrium and quasi-equilibrium spike patterns in the low feed-rate regime $\mathcal{A} = O(1)$.

Next, we obtain our main instability result that oscillatory instabilities of k-spike quasi-equilibria can occur when $\tau = O(\mathcal{A}^4) \gg 1$ and with $O(1)$ inter-spike separation distances. From the choice of the principal value of the square root, we obtain that $\text{Re}(\theta_\lambda) = \theta_0 \text{Re}(\sqrt{1+\tau\lambda}) \to +\infty$ on $|\arg(\lambda)| < \pi$ as $\tau \to \infty$. Therefore, for $\tau \gg 1$, and for $x_{j+1} - x_j = O(1)$, we calculate from the matrix entries of $\mathcal{B}_\lambda$ in (2.34) that $\mathcal{B}_\lambda \to 2I$ in $|\arg(\lambda)| < \pi$. Therefore, with $\tau = \tilde{\tau}\mathcal{A}^4$, where $\tilde{\tau} = O(1)$, we get from (2.39) that C_λ and its eigenvalues χ_j are given asymptotically by

$$\mathcal{C}_\lambda \sim 2 \left[I + \frac{\sqrt{D\tilde{\tau}\lambda}}{3} \Gamma^{-2} \right]^{-1} ; \quad \chi_j \sim 2 \left[1 + \frac{\sqrt{D\tilde{\tau}\lambda}}{3} \gamma_j^{-2} \right]^{-1} \qquad j = 1, \cdots, k . \tag{2.44}$$

This limiting expression for χ_j suggests that we define τ_H by $\tilde{\tau} = 9D^{-1}\gamma_j^4 \tau_H$, so that $\mathcal{C} \sim 2 \left[1 + \sqrt{\tau_H \lambda} \, \right]^{-1} I$. Therefore, in the scaling regime $\tau = O(\mathcal{A}^4)$, the stability of k-spike quasi-equilibria is determined by the NLEP (2.38) with the single multiplier

$$\chi_\infty = \frac{2}{1 + \sqrt{\tau_H \lambda}} , \qquad \text{when} \quad \tau = \frac{9\mathcal{A}^4 \tau_H \gamma_j^4}{D} \gg 1 . \tag{2.45}$$

This limiting NLEP was derived for equilibrium spike solutions in [19], [18], [63], and [54] in the intermediate regime. From the rigorous analysis of [18] and [54], this NLEP has a Hopf bifurcation at some $\tau_H = \tau_{H0}$. From numerical computations, $\tau_{H0} \approx 1.748$, and $\text{Re}(\lambda) < 0$ only when $\tau_H < \tau_{H0}$ (cf. [19], [54]). Although this limiting NLEP has a continuous spectrum on the non-negative real axis $\text{Re}(\lambda) \leq 0$, there are no edge bifurcations arising from the end-point $\lambda = 0$ (cf. [18], [54]).

The scaling law for τ in (2.45) shows that there are k distinct values of τ where complex conjugate eigenvalues appear on the imaginary axis. The minimum of these values determines the instability threshold for τ. Finally, by using (2.20) to calculate the spike amplitudes asymptotically for $\mathcal{A} \gg 1$, we obtain the following main instability result:

Principal Result 2.4: *Let* $\tau = O(\mathcal{A}^4)$ *with* $x_{j+1} - x_j = O(1)$ *and* $O(1) \ll \mathcal{A} \ll O(\varepsilon^{-1/2})$. *Then, the frozen k-spike quasi-equilibrium solution of §2.1 develops an oscillatory instability due to a Hopf bifurcation when* τ *increases past* τ_h*, where*

$$\tau_h = \min_{j=1,\cdots,k} (\tau_{hj}) \, , \quad \tau_{hj} \sim \frac{D\mathcal{A}^4}{144} \tau_{H0} \, (\mathcal{B}\mathbf{e})_j^4 \left(1 - \frac{6}{\mathcal{A}^2 \sqrt{D}} r_j \right)^4 \, , \quad j = 1, \cdots, k \, . \tag{2.46}$$

Here $\tau_{H0} \approx 1.748$*, while* $(\mathcal{B}\mathbf{e})_j$ *and* r_j *are defined in terms of the spike locations by (2.20).*

For an equilibrium k-spike pattern where $x_j = -1 + (2j-1)/k$ for $j = 1, \cdots, k$, we calculate from (2.20b) that $(\mathcal{B}\mathbf{e})_j = 2\tanh(\theta_0/k)$ and $r_j = [2\tanh(\theta_0/k)]^{-1}$ for $j = 1, \cdots, k$. This leads to the following equilibrium stability threshold, which agrees asymptotically with the following result given in Proposition 4.3 of [54]:

$$\tau_h \sim \frac{D\mathcal{A}^4}{9} \tau_{H0} \tanh^4\left(\frac{\theta_0}{k}\right) \left(1 - \frac{3}{\mathcal{A}^2 \sqrt{D} \tanh(\theta_0/k)} \right)^4 \, . \tag{2.47}$$

An important remark concerns the range of validity of Principal Result 2.4 with respect to τ. The derivation of (2.46) assumed that $\tau\varepsilon^2\mathcal{A}^2 \ll 1$, while the scaling law for instabilities predicts that $\tau = O(\mathcal{A}^4)$. Therefore, (2.46) only holds in the subregime $O(1) \ll \mathcal{A} \ll O(\varepsilon^{-1/3})$ of the intermediate regime.

2.2.1 Numerical Experiments of Quasi-Equilibrium Spike Layer Motion

We now give two examples illustrating our results of §2.1 for slow spike dynamics.

Experiment 2.1: A two-spike evolution

Consider a two-spike evolution with parameter values $D = 1.0$, $\mathcal{A} = 10.0$, $\tau = 5.0$, and $\varepsilon = 0.005$. The initial spike locations are $x_1(0) = -0.20$ and $x_2(0) = 0.80$. In Fig 2.1(a) we plot the spike layer trajectories versus the slow time σ, computed numerically from (2.25), which shows the gradual approach to the equilibrium values at $x_1 = -1/2$ and $x_2 = 1/2$. In Fig. 2.1(c) we plot the spike amplitudes versus σ. A plot of the quasi-equilibrium solution at several instants in time is shown in Fig. 2.1(d). In Fig. 2.1(b) we plot the two Hopf bifurcation values τ_{hj}, for $j = 1, 2$, versus σ calculated from (2.46). In these figures the solid curves were obtained when computing for the spike amplitudes from the nonlinear algebraic system (2.17), while the dotted curves correspond to using the two-term approximation (2.18). For the spike trajectories shown in Fig. 2.1(a) these two curves are indistinguishable. In the plots of the spike locations and spike amplitudes in Fig. 2.1(a) and Fig. 2.1(c) the marked points are the full numerical results computed from (1.6) using the adaptive-grid software of [8]. From these figures we observe that the asymptotic and full numerical results agree very closely. An important observation from Fig. 2.1(b) is that the stability threshold $\tau_h(\sigma)$, defined by $\tau_h(\sigma) \equiv \min_{j=1,2}[\tau_{hj}(\sigma)]$, is an increasing function of σ with $\tau_h(0) \approx 12.5$ and $\tau_h(\infty) \approx 67.7$. This monotone behavior of $\tau_h(\sigma)$, together with the initial value $\tau_h(0) > \tau = 5.0$, implies that there is no dynamic triggering of an oscillatory instability in the spike amplitudes before the equilibrium two-spike pattern is reached.

More generally, for a k-spike pattern, we have been unable to prove analytically from the DAE system (2.25) and (2.18) that the stability threshold for τ, given by $\tau_h(\sigma) \equiv \min_{j=1,\cdots,k}(\tau_{hj}(\sigma))$ of (2.46), must always be an increasing function of σ. However, we have performed many numerical experiments to examine this condition, and in each case we have found numerically that $\tau_h(\sigma)$ is a monotonically increasing function of σ. This leads to the conjecture that there are no dynamically triggered oscillatory instabilities of multi-spike quasi-equilibria in the intermediate regime $O(1) \ll \mathcal{A} \ll O(\varepsilon^{-1/2})$. In other words, $\tau < \tau_h(0)$ is a sufficient condition for stability of the quasi-equilibrium multi-spike pattern for all $\sigma > 0$. In contrast, for the simple case of symmetric two-spike quasi-equilibria in the low feed-rate regime $\mathcal{A} = O(1)$, dynamically triggered instabilities due to either Hopf bifurcations or from the creation of a real positive eigenvalue were established analytically in [86].

Experiment 2.2: A three-spike evolution

Next, we consider a three-spike evolution with parameter values $D = 1.0$, $\mathcal{A} = 10.0$, $\tau = 2.0$, and $\varepsilon = 0.005$. The initial spike locations are $x_1(0) = -0.50$, $x_2(0) = 0.20$, and $x_3(0) = 0.80$. In Fig 2.2(a) an Fig 2.2(c) we plot the spike layer trajectories and spike amplitudes, respectively, computed from (2.25) and the two-term approximation (2.18). Snapshots of the quasi-equilibrium solution are shown in Fig. 2.2(d). In Fig. 2.2(b) we plot the three Hopf bifurcation values τ_{hj}, for $j = 1, \cdots, 3$, versus σ calculated from

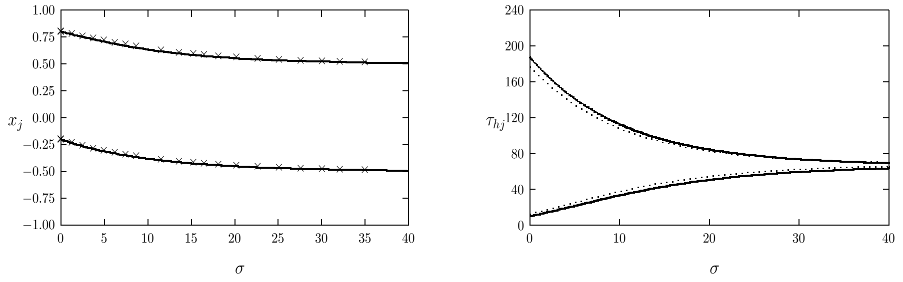

(a) x_j vs. σ

(b) τ_{hj} vs. σ

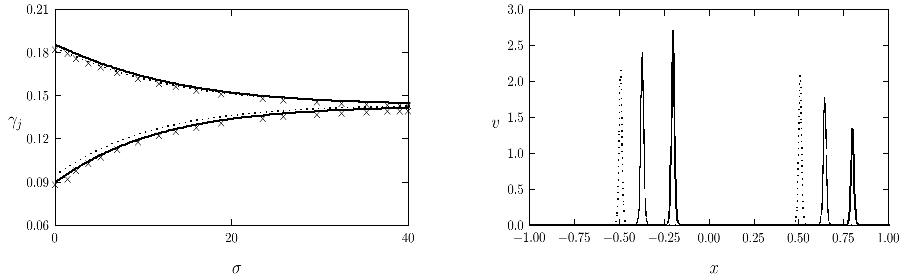

(c) γ_j vs. σ

(d) v vs. x

Figure 2.1: *Experiment 2.1: Slow evolution of a two-spike quasi-equilibrium solution for* $\varepsilon = 0.005$, $\mathcal{A} = 10$, *and* $D = 1.0$, *with* $x_1(0) = -0.2$ *and* $x_2(0) = 0.8$. *Top Left:* x_j *vs.* σ. *Top Right:* τ_{hj} *vs.* σ. *Bottom Left:* γ_j *vs.* σ. *Bottom Right:* v *vs.* x *at* $\sigma = 0$ *(heavy solid curve),* $\sigma = 10$ *(solid curve), and* $\sigma = 50$ *(dotted curve). Except for the plot of* v *vs.* x*, the solid curves correspond to computing the spike amplitudes from (2.17), while the dotted curves correspond to the two-term approximation (2.18). The crosses in the plots of* x_j *and* γ_j *vs.* σ *are the full numerical results computed from (1.6).*

(2.46). In the plots of τ_{hj}, γ_j and x_j versus σ the solid curves correspond to computing the spike amplitudes from the nonlinear algebraic system (2.17), while the dotted curves correspond to the two-term approximation (2.18). In the plots of x_j and γ_j the marked points are the full numerical results computed from (1.6) using the software of [8]. As in Experiment 2.1, the asymptotic and full numerical results agree rather closely.

From Fig. 2.1(b) we again observe that the stability threshold for τ, given by $\tau_h(\sigma) \equiv \min_{j=1,2,3}[\tau_{hj}(\sigma)]$, is an increasing function of σ with $\tau_h(0) \approx 2.6$ and $\tau_h(\infty) \approx 14.0$. This monotonicity of $\tau_h(\sigma)$, together with $\tau_h(0) > \tau = 2.0$, precludes the occurrence of a dynamically triggered Hopf bifurcation in the spike amplitudes.

2.3 Oscillatory Drift Instabilities of k-Spike Patterns

In this section we compute numerical solutions to the Stefan problem (2.12) when $\tau\varepsilon^2\mathcal{A}^2 = O(1)$ and $O(\varepsilon^{-1/3}) \ll \mathcal{A} \ll O(\varepsilon^{-1/2})$. For notational convenience, so as not to confuse spike locations with gridpoints of the discretization, we re-label the spike trajectories as $\xi_j(\sigma)$, for $j = 1, \cdots, k$. Then, defining $\tau_0 \equiv \varepsilon^{-2}\mathcal{A}^{-2}\tau = O(1)$ to be the key bifurcation parameter, (2.12) on $|x| \leq 1$ becomes

$$\tau_0 u_\sigma = D u_{xx} + (1-u) - \sum_{j=1}^{k} 6\gamma_j\, \delta(x-\xi_j)\,; \quad u_x(\pm 1,\sigma) = 0\,, \tag{2.48a}$$

$$\xi_j' = \gamma_j \left[u_x(\xi_j^+,\sigma) + u_x(\xi_j^-,\sigma) \right]\,, \qquad j = 1,\cdots,k\,, \tag{2.48b}$$

$$u(\xi_j(\sigma),\sigma) = 1/(\gamma_j \mathcal{A}^2)\,, \qquad j = 1,\cdots,k\,. \tag{2.48c}$$

By using a SLEP approach, which is related to the method pioneered in [69], it was shown in [53] that a one-spike equilibrium solution will become unstable at some critical value of τ_0 to an oscillatory drift instability associated with a pure imaginary small eigenvalue $\lambda \ll 1$ of the linearization. As τ_0 increases above this critical value a complex conjugate pair of eigenvalues crosses into the right half-plane $\mathrm{Re}(\lambda) > 0$, leading to the initiation of a small-scale oscillatory motion of the spike location. This oscillatory drift instability is the dominant instability mechanism in the subregime $O(\varepsilon^{-1/3}) \ll \mathcal{A} \ll O(\varepsilon^{-1/2})$ of the intermediate regime.

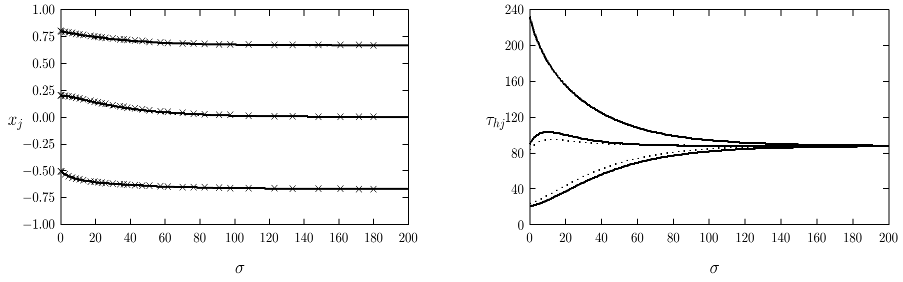

(a) x_j vs. σ (b) τ_{hj} vs. σ

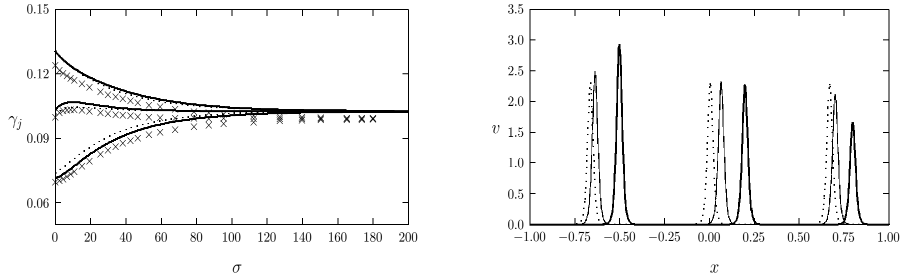

(c) γ_j vs. σ (d) v vs. x

Figure 2.2: *Experiment 2.2: Slow evolution of a three-spike quasi-equilibrium solution for* $\varepsilon = 0.005$*,* $\mathcal{A} = 10$*, and* $D = 1.0$*, with* $x_1(0) = -0.5$*,* $x_2(0) = 0.2$*, and* $x_3(0) = 0.80$*, obtained from the two-term asymptotic result (2.18) for the spike amplitudes. Top Left:* x_j *vs.* σ*. Top Right:* τ_{hj} *vs.* σ*. Bottom Left:* γ_j *vs.* σ*. Bottom Right:* v *vs.* x *at* $\sigma = 0$ *(heavy solid curve),* $\sigma = 40$ *(solid curve), and* $\sigma = 140$*. Except for the plot of* v *vs.* x*, the solid curves correspond to computing the spike amplitudes from (2.17), while the dotted curves correspond to the two-term approximation (2.18). The crosses in the plots of* x_j *and* γ_j *vs.* σ *are the full numerical results computed from (1.6).*

For the one-spike case where $k = 1$ we now show that the condition for the stability of the equilibrium solution to the Stefan problem (2.48) is equivalent to that obtained in [53] using the SLEP method. We let $U \equiv U(x)$ and $\gamma_1 = \gamma_{1e}$ denote the equilibrium solution to (2.48) with $\xi_1 = 0$. Then, U satisfies

$$DU_{xx} + (1 - U) = 0\,, \quad |x| < 1\,; \quad U_x(\pm 1) = 0\,, \tag{2.49a}$$

$$[DU_x]_0 = 6\gamma_{1e}\,; \quad U(0) = \frac{1}{\gamma_e \mathcal{A}^2}\,. \tag{2.49b}$$

Here we have defined $[v]_0 \equiv v(0^+) - v(0^-)$. We readily calculate that

$$U = \begin{cases} 1 - B\frac{\cosh(\theta_0(1+x))}{\cosh\theta_0}\,, & -1 \le x < 0\,; \\ 1 - B\frac{\cosh(\theta_0(1-x))}{\cosh\theta_0}\,, & 0 < x \le 1\,, \end{cases} \tag{2.50a}$$

where $\theta_0 \equiv D^{-1/2}$, and

$$\gamma_{1e} \equiv \frac{B\sqrt{D}}{3}\tanh\theta_0\,, \qquad B \equiv 1 - \frac{1}{\gamma_{1e}\mathcal{A}^2}\,. \tag{2.50b}$$

By solving the quadratic equation for γ_{1e} we get

$$\gamma_{1e} = \frac{\sqrt{D}}{6}\tanh\theta_0\left[1 + \sqrt{1 - \frac{\mathcal{A}_{1e}^2}{\mathcal{A}^2}}\right]\,, \quad \mathcal{A}_{1e} \equiv \sqrt{\frac{12\theta_0}{\tanh\theta_0}}\,. \tag{2.50c}$$

For $\mathcal{A} \gg 1$, this expression reduces to

$$\gamma_{1e} = \frac{\sqrt{D}}{3}\tanh\theta_0 - \frac{1}{\mathcal{A}^2} + O(\mathcal{A}^{-4})\,, \quad B = 1 - \frac{3}{\mathcal{A}^2\sqrt{D}\tanh\theta_0} + O(\mathcal{A}^{-4})\,. \tag{2.50d}$$

For $\delta \ll 1$, we perturb the equilibrium solution as

$$u(x,\sigma) = U(x) + \delta e^{\lambda\sigma}\phi(x)\,, \qquad \gamma_1 = \gamma_{1e} + \delta\beta e^{\lambda\sigma}\,, \qquad \xi_1 = \delta e^{\lambda\sigma}\,. \tag{2.51}$$

We substitute (2.51) into (2.48a), and collect $O(\delta)$ terms to get $D\phi_{xx} - (1 + \tau_0\lambda)\phi = 0$ on $|x| \le 1$. From the linearization of the ODE (2.48b), we obtain

$$\begin{aligned} \delta\lambda e^{\lambda\sigma} = \Big(\gamma_{1e} + \delta\beta e^{\lambda\sigma}\Big)\Big(&U_x(0^+) + U_x(0^-) + \delta e^{\lambda\sigma} \\ &\left[\phi_x(0^+) + \phi_x(0^-) + U_{xx}(0^+) + U_{xx}(0^-)\right]\Big)\,. \end{aligned} \tag{2.52a}$$

In addition, the conditions $[Du_x]_{\xi_1} = 6\gamma_1$ and $u(\xi_1) = 1/(\gamma_1 \mathcal{A}^2)$ become

$$D\left(U_x(0^+) - U_x(0^-) + \delta e^{\lambda\sigma}\left[U_{xx}(0^+) - U_{xx}(0^+) + \phi_x(0^+) - \phi_x(0^-)\right]\right)$$
$$= 6\left(\gamma_{1e} + \varepsilon\delta e^{\lambda\sigma}\right), \tag{2.52b}$$
$$U(0^\pm) + \delta e^{\lambda t}\left(U_x(0^\pm) + \phi(0^\pm)\right) = \frac{1}{\gamma_{1e}\mathcal{A}^2} - \frac{\delta\beta}{\gamma_{1e}^2\mathcal{A}^2}e^{\lambda\sigma}. \tag{2.52c}$$

Since $U_x(0^+) + U_x(0^-) = 0$, $U_{xx}(0^+) = U_{xx}(0^-)$, and $U_x(0^+) = \pm 3\gamma_{1e}/D$, we collect the $O(\delta)$ terms in (2.52) to obtain the following problem for ϕ:

$$D\phi_{xx} - (1 + \tau_0\lambda)\,\phi = 0, \quad |x| \le 1; \quad \phi_x(\pm 1) = 0, \tag{2.53a}$$
$$[D\phi_x]_0 = 6\beta; \qquad \phi(0^\pm) = \mp\frac{3\gamma_{1e}}{D} - \frac{\beta}{\gamma_{1e}^2\mathcal{A}^2}, \tag{2.53b}$$
$$\lambda = 2\gamma_{1e}\left(U_{xx}(0) + \frac{1}{2}\left[\phi_x(0^+) + \phi_x(0^-)\right]\right). \tag{2.53c}$$

The solution to (2.53a) satisfying the prescribed values for $\phi(0^\pm)$ is

$$\phi = C_-\frac{\cosh(\theta_\lambda(x+1))}{\cosh\theta_\lambda}, \quad -1 \le x < 0; \tag{2.54a}$$
$$\phi = C_+\frac{\cosh(\theta_\lambda(1-x))}{\cosh\theta_\lambda}, \quad 0 < x \le 1, \tag{2.54b}$$

where $\theta_\lambda \equiv \theta_0\sqrt{1+\tau_0\lambda}$, and

$$C_\pm = \mp\frac{3\gamma_{1e}}{D} - \frac{\beta}{\gamma_{1e}^2\mathcal{A}^2}. \tag{2.55}$$

The jump condition $[D\phi_x]_0 = 6\beta$, then yields that $\beta = 0$. Then, we substitute values for $\phi_x(0^\pm)$ and $U_{xx}(0) = -D^{-1}\left(1 - 1/(\gamma_{1e}\mathcal{A}^2)\right)$ into (2.53c) to obtain

$$\lambda = 2\gamma_{1e}\left[\frac{3\gamma_{1e}}{D}\theta_\lambda\tanh\theta_\lambda - \frac{1}{D}\left(1 - \frac{1}{\gamma_{1e}\mathcal{A}^2}\right)\right]. \tag{2.56}$$

Finally, by using (2.50c) for γ_{1e}, we readily derive that λ satisfies the transcendental equation

$$\lambda = \mu\left[\sqrt{1+\tau_0\lambda}\tanh\theta_0\tanh\theta_\lambda - 1\right], \quad \mu \equiv \frac{\theta_0}{6}\tanh\theta_0\left[1 + \sqrt{1 - \frac{\mathcal{A}_{1e}^2}{\mathcal{A}^2}}\right]^2. \tag{2.57}$$

Here $\theta_\lambda \equiv \theta_0\sqrt{1+\tau_0\lambda}$, $\theta_0 \equiv D^{-1/2}$, while $\mathcal{A}_{1e}$ is defined in (2.50c). Equation (2.57) is identical to that derived in equation (5.5) of [53] from using the SLEP method based on a linearization of (1.6) around a one-spike equilibrium solution.

We introduce ω, τ_d, and ζ, by $\lambda = \mu\omega$, $\tau_0 = \tau_d/\mu$, and $\zeta = \tau_d\omega$. Then, from (2.57), ζ is a root of

$$F(\zeta) \equiv \frac{\zeta}{\tau_d} - G(\zeta) = 0\,, \quad G(\zeta) \equiv \sqrt{1+\zeta}\tanh\theta_0 \tanh\left[\theta_0\sqrt{1+\zeta}\right] - 1\,. \tag{2.58}$$

By examining the roots of (2.58) in the complex ζ plane, the following result was proved in §5 of [53].

Proposition 2.5: *There is a complex conjugate pair of pure imaginary eigenvalues to (2.57) at some unique value $\tau_d = \tau_{dh}$ depending on D. For any $\tau_d > \tau_{dh}$ there are exactly two eigenvalues in the right half-plane. These eigenvalues have nonzero imaginary parts when $\tau_{dh} < \tau_d < \tau_{dm}$, and they merge onto the positive real axis at $\tau_d = \tau_{dm}$. They remain on the positive real axis for all $\tau_d > \tau_{dm}$.*

The numerically computed Hopf bifurcation value τ_{dh} is plotted versus D in Fig. 2.3(a). In Fig. 2.3(a) we also plot the magnitude $|\omega_h|$ of the pure imaginary eigenvalues $\omega_h = \pm i|\omega_h|$ at $\tau_d = \tau_{dh}$. Since $\tau_0 = \tau_d/\mu$ and $\tau = \varepsilon^{-2}\mathcal{A}^{-2}\tau_0$, the Hopf bifurcation value for the onset of an oscillatory drift instability for a one-spike solution is

$$\tau_{tw} \sim \varepsilon^{-2}\mathcal{A}^{-2}\tau_{0d}\,, \quad \tau_{0d} \equiv \frac{\tau_{dh}}{\mu}\,, \quad \mu \equiv \frac{\theta_0}{6}\tanh\theta_0\left[1+\sqrt{1-\frac{\mathcal{A}_{1e}^2}{\mathcal{A}^2}}\right]^2\,. \tag{2.59}$$

Recall from (2.47) that there is an oscillatory instability in the amplitude of an equilibrium spike when $\tau = \tau_h = O(\mathcal{A}^4)$. Thus, $\tau_h \ll \tau_{tw}$ when $O(1) \ll \mathcal{A} \ll O(\varepsilon^{-1/3})$ and $\tau_{tw} \ll \tau_h$ when $O(\varepsilon^{-1/3}) \ll \mathcal{A} \ll O(\varepsilon^{-1/2})$. In Fig. 2.3(b) we plot $\log_{10}(\tau_{tw})$ and $\log_{10}(\tau_h)$ versus $\mathcal{A}$, $\log_{10}(\tau_h)$ versus $\mathcal{A}$, showing the exchange in the intermediate regime. For the equilibrium problem on the infinite line this exchange in the dominant instability mechanism was also noted in [65] and [19]. As a remark, we notice that ω_h, representing the (scaled) temporal frequency of small oscillations, satisfies $\omega_h \to 0$ in the infinitely long domain limit $D \to 0$. Therefore, the existence of an oscillatory instability requires a finite domain.

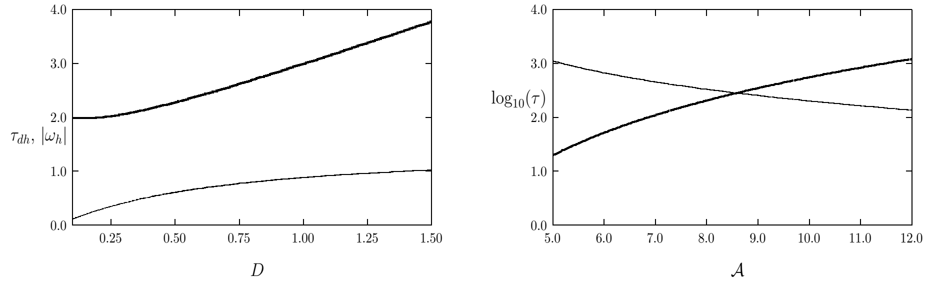

(a) τ_{dh} and $|\omega_h|$ vs. D

(b) $\log_{10}(\tau_{tw})$ and $\log_{10}(\tau_h)$ vs. $\mathcal{A}$

Figure 2.3: *Left Figure: The drift instability thresholds* τ_{dh} *(heavy solid curve) and* $|\omega_h|$ *(solid curve) versus* D*. Right figure: Plots of* $\log_{10}(\tau_h)$ *(heavy solid curve) from (2.47) with* $k = 1$ *and* $\log_{10}(\tau_{tw})$ *(solid curve) from (2.59) versus* $\mathcal{A}$ *for* $D = 0.75$ *and* $\varepsilon = 0.015$*. This shows the exchange in the dominant instability mechanism in the intermediate regime.*

2.3.1 Numerical Solution of the Coupled ODE-PDE Stefan Problem

To compute numerical solutions to the Stefan problem (2.48) we adapt the numerical method of [89] for computing solutions to a heat equation with a moving singular Dirac source term. We use a Crank-Nicolson scheme to discretize (2.48a) together with a forward Euler scheme for the ODE (2.48b).

For simplicity we first consider (2.48a) for one spike where $k = 1$. Let h and Δt denote the space step and time step, respectively. We set $\Delta t = h^2/2$ to satisfy the stability requirement of the forward Euler scheme. The number of grid points is $M = 1 + 2/h$, and we label the j^{th} grid point by $x_j = -1 + (j-1)h$ for $j = 1, \cdots, M$. The total time period is T_m, and we label $\sigma_n = n\Delta t$ for $n = 1, \cdots, T_m/\Delta t$. At time σ_n, the solution $u(x_j, \sigma_n)$ at the j^{th} grid point is approximated by U_j^n, and we label $\mathbf{U}^n = (U_1^n, \cdots, U_M^n)^T$. Also, the spike location $\xi_1(\sigma_n)$ and spike amplitude $\gamma_1(\sigma_n)$ are approximated by ξ_1^n and γ_1^n, respectively.

As in [89] we approximate the delta function $\delta(x - \xi_1)$ in (2.48a) with the discrete delta function $d^{(1)}(x - \xi_1)$, where $d^{(1)}(y)$ is given by

$$d^{(1)}(y) = \begin{cases} (2h - |y|)/(4h^2)\,, & |y| \le 2h\,, \\ 0\,, & \text{otherwise}\,. \end{cases} \tag{2.60}$$

The numerical approximation $d^{(1)}$ of the delta function in (2.48a) spreads the singular force to the neighboring grid points within its support. Next, we write the constraint of (2.48c), given by $u(\xi_1(\sigma),\sigma) = 1/(\gamma_1\mathcal{A}^2)$, in the form

$$u(\xi_1(\sigma),\sigma) = \int_{-\infty}^{\infty} u(x,\sigma)\delta(x-\xi_1(\sigma))\,dx = \frac{1}{\gamma_1\mathcal{A}^2}\,. \tag{2.61}$$

With $U_j^n \approx u(x_j,\sigma_n)$, $\xi_1^n \approx \xi_1(\sigma_n)$, and $\gamma_1^n \approx \gamma_1(\sigma_n)$, the discrete version of (2.61) is

$$u(\xi_1^n,\sigma_n) \approx h\sum_j U_j^n d^{(2)}(x_j-\xi_1^n) = \frac{1}{\gamma_1^n\mathcal{A}^2}\,, \tag{2.62}$$

where $d^{(2)}(y)$ is a further numerical approximation to the delta function given explicitly by

$$d^{(2)}(y) = \frac{1}{h}\begin{cases} 1-(y/h)^2\,, & |y|\le h\,,\\ 2-3|y|/h+(y/h)^2\,, & h\le |y|\le 2h\,,\\ 0\,, & \text{otherwise}\,. \end{cases} \tag{2.63}$$

The function $d^{(2)}$ interpolates grid values U_j^n to approximate the requirement $u(\xi_1^n,\sigma_n) = 1/(\gamma_1^n\mathcal{A}^2)$ at the spike location. A rough outline of the algorithm for the numerical solution to (2.48) to advance from the n^{th} to the $(n+1)^{\text{th}}$ time-step is as follows: We first use (2.48b) to take a forward Euler step to get the new location ξ_1^{n+1} given $\mathbf{U}^n$ and γ_1^n. Then, we use the approximate condition

$$u(\xi_1^{n+1},\sigma_{n+1}) \approx \frac{1}{2\mathcal{A}^2}\left(\frac{1}{\gamma_1^n}+\frac{1}{\gamma_1^{n+1}}\right)\,, \tag{2.64}$$

on the right-hand side of (2.62) together with the Crank-Nicolson discretization of (2.48a) to solve for γ_1^{n+1}. Then, we calculate $\mathbf{U}^{n+1}$ from the discretization of (2.48a) using the value of γ_1^{n+1}. Finally, we set $n=n+1$, and repeat the iteration.

In order to obtain higher accuracy, we use a fourth order accurate scheme as suggested in [89] to approximate the second order differential operator u_{xx} as $u_{xx}(x_j,\sigma_n)\approx \mathcal{D}_{2j}^n$, where

$$\mathcal{D}_{2j}^n \equiv \begin{cases} \frac{1}{12h^2}(U_{j+4}^n - 6U_{j+3}^n + 14U_{j+2}^n - 4U_{j+1}^n - 15U_j^n + 10U_{j-1}^n)\,, & j=1\,,\\ \frac{1}{12h^2}(-U_{j+2}^n + 16U_{j+1}^n - 30U_j^n + 16U_{j-1}^n - U_{j-2}^n)\,, & 2\le j\le N\,,\\ \frac{1}{12h^2}(U_{j-4}^n - 6U_{j-3}^n + 14U_{j-2}^n - 4U_{j-1}^n - 15U_j^n + 10U_{j+1}^n)\,, & j=M\,. \end{cases}$$

Here U_0^n and U_{M+1}^n are ghost points outside each end of the boundaries at $x = \pm 1$. The Neumann condition $u_x(\pm 1, t) = 0$ is also discretized as

$$\begin{aligned} u_x(x_1, \sigma_n) &\approx (-3U_0^n - 10U_1^n + 18U_2^n - 6U_3^n + U_4^n)/(12h)\,, \\ u_x(x_M, \sigma_n) &\approx (3U_{M+1}^n + 10U_M^n - 18U_{M-1}^n + 6U_{M-2}^n - U_{M-3}^n)/(12h)\,. \end{aligned}$$

Eliminating the ghost points from the discretization of u_{xx}, we obtain the $M \times M$ coefficient matrix $\mathbf{T} = \mathbf{T}_0/(12h^2)$, where

$$\mathbf{T}_0 \equiv \begin{pmatrix} -145/3 & 56 & -6 & -8/3 & 1 & 0 & 0 & 0 & \cdots & 0 \\ 58/3 & -36 & 18 & -4/3 & 0 & 0 & 0 & 0 & \cdots & 0 \\ -1 & 16 & -30 & 16 & -1 & 0 & 0 & 0 & \cdots & 0 \\ 0 & -1 & 16 & -30 & 16 & -1 & 0 & 0 & \cdots & 0 \\ 0 & 0 & -1 & 16 & -30 & 16 & -1 & 0 & \cdots & 0 \\ & & & \ddots & \ddots & \ddots & \ddots & \ddots & & \\ 0 & \cdots & 0 & 0 & -1 & 16 & -30 & 16 & -1 & 0 \\ 0 & \cdots & 0 & 0 & 0 & -1 & 16 & -30 & 16 & -1 \\ 0 & \cdots & 0 & 0 & 0 & 0 & -4/3 & 18 & -36 & 58/3 \\ 0 & \cdots & 0 & 0 & 0 & 1 & -8/3 & -6 & 56 & -145/3 \end{pmatrix}.$$

Next, we outline how we calculate the fluxes in (2.48b). For convenience, in the notation of this paragraph we omit the superscript n at time σ_n. In order to approximate the one-sided first order derivatives $u_x(\xi_1^{\pm}, \sigma_n)$ in (2.48b), we first use the solution values at gridpoints on each side of ξ_1 to interpolate the values at points that are equally distributed near ξ_1. Then, we approximate $u_x(\xi_1^{\pm}, \sigma_n)$ by differencing values at these points. For instance, assuming that the closest grid point on the left-hand side of the spike is x_j, we use six point values $(\bar{u}, U_j, U_{j-1}, U_{j-2}, U_{j-3}, U_{j-4})$ with $\bar{u} = u(\xi_1, \sigma_n) = 1/(\gamma_1 \mathcal{A}^2)$ to interpolate the solution at $x = (\xi_1 - 3h, \xi_1 - 2h, \xi_1 - h, \xi_1)$. Denoting the results to be $(U_1^-, U_2^-, U_3^-, U_4^-)$ with $U_4^- = u(\xi_1, \sigma_n) = 1/(\gamma_1 \mathcal{A}^2)$, we can use them for estimating $u_x(\xi_1^-, \sigma_n)$ as

$$u_x(\xi_1^-, t) \approx (-3U_3^- + \frac{3}{2}U_2^- - \frac{1}{3}U_1^-)/h\,. \tag{2.65a}$$

Similarly, we obtain $(U_1^+, U_2^+, U_3^+, U_4^+)$ at $x = (\xi_1, \xi_1 + h, \xi_1 + 2h, \xi_1 + 3h)$ by interpolation, and we then discretize to obtain

$$u_x(\xi_1^+, t) \approx (3U_2^+ - \frac{3}{2}U_3^+ + \frac{1}{3}U_4^+)/h\,. \tag{2.65b}$$

Next, we discretize (2.48a) by the Crank-Nicolson scheme to get

$$\left[(1+\frac{1}{2}\mu)\mathbf{I}-\frac{\mu D}{2}\mathbf{T}\right]\mathbf{U}^{n+1}=\left[(1-\frac{1}{2}\mu)\mathbf{I}+\frac{\mu D}{2}\mathbf{T}\right]\mathbf{U}^{n} \\ -3\mu\left(\mathbf{d}^{n+1}\gamma_1^{n+1}+\mathbf{d}^{n}\gamma_1^{n}\right)+\mathbf{p}\,, \quad (2.66)$$

where $\mu \equiv \Delta t/\tau_0$ and $\mathbf{p}^t \equiv (\mu,\, \mu,\, \cdots,\, \mu)$. Here $\mathbf{d}^{n+1}$ denotes the discretization of the delta function by $d^{(1)}$ at time σ_{n+1}. Denoting the coefficient matrix of $\mathbf{U}^{n+1}$ to be $\mathbf{A}$ and that of $\mathbf{U}^{n}$ to be $\mathbf{B}$, the system above can be written in the simpler form

$$\mathbf{A}\mathbf{U}^{n+1}=\mathbf{B}\mathbf{U}^{n}-3\mu\left(\mathbf{d}^{n+1}\gamma_1^{n+1}+\mathbf{d}^{n}\gamma_1^{n}\right)+\mathbf{p}\,. \quad (2.67)$$

In (2.67), only the boldface variables are matrices and vectors. We then approximate (2.48c) by the discrete form (2.62). We write this interpolation as a dot product $\mathbf{N}^{n+1}\mathbf{U}^{n+1}$, where

$$\mathbf{N}^{n+1}\mathbf{U}^{n+1}=\frac{1}{2\mathcal{A}^2}\left(\frac{1}{\gamma_1^{n}}+\frac{1}{\gamma_1^{n+1}}\right). \quad (2.68)$$

Since $\mathbf{A}$ has full rank, we then left multiply (2.67) by $\mathbf{N}^{n+1}\mathbf{A}^{-1}$ to get a quadratic equation for γ_1^{n+1} given by

$$3\mu\mathbf{N}^{n+1}\mathbf{A}^{-1}\mathbf{d}^{n+1}\gamma_1^{n+1}-\Big[\mathbf{N}^{n+1}\mathbf{A}^{-1}(\mathbf{B}\mathbf{U}^{n}-3\mu\mathbf{d}^{n}\gamma_1^{n}+\mathbf{p}) \\ -\frac{1}{2\mathcal{A}^2}\frac{1}{\gamma_1^{n}}\Big]+\frac{1}{2\mathcal{A}^2}\frac{1}{\gamma_1^{n+1}}=0\,. \quad (2.69)$$

Since $\mathcal{A}\gg 1$, we can solve (2.69) for the correct root γ_1^{n+1}. We then calculate $\mathbf{U}^{n+1}$ using (2.67) and start the next iteration by using a forward Euler step on (2.48b) to advance the spike location.

This numerical method can be readily extended to treat (2.48) for two or more spikes. For instance, consider the case of two spikes. With the same Crank-Nicolson scheme, we let $\mathbf{d}_1$ and $\mathbf{d}_2$ be the discrete approximations of $\delta(x-\xi_1)$ and $\delta(x-\xi_2)$ in (2.48a), respectively, with the discrete delta function $d^{(1)}$. Define the row vectors $\mathbf{N}_1^{n+1}$ and $\mathbf{N}_2^{n+1}$ to the discrete versions of $d^{(2)}$ near ξ_1 and ξ_2, respectively. The conditions $u(\xi_j^{n+1},\sigma^{n+1})=1/(\gamma_j^{n+1}\mathcal{A}^2)$, can then be approximated by the two discrete constraints

$$\mathbf{N}_j^{n+1}\mathbf{U}^{n+1}=\frac{1}{2\mathcal{A}^2}\left(\frac{1}{\gamma_j^{n}}+\frac{1}{\gamma_j^{n+1}}\right), \quad j=1,2\,. \quad (2.70)$$

The Crank-Nicolson discretization of (2.48a) with $k = 2$ is written as

$$\mathbf{A}\mathbf{U}^{n+1} = \mathbf{B}\mathbf{U}^{n} - 3\mu(\mathbf{d}_1^{n+1}\gamma_1^{n+1} + \mathbf{d}_2^{n+1}\gamma_2^{n+1}) - 3\mu(\mathbf{d}_1^{n}\gamma_1^{n} + \mathbf{d}_2^{n}\gamma_2^{n}) + \mathbf{p} \,. \quad (2.71)$$

Upon imposing the constraints (2.70) we obtain the following system for γ_1^{n+1} and γ_2^{n+1}:

$$\begin{aligned} &3\mu\mathbf{N}_j^{n+1}\mathbf{A}^{-1}(\mathbf{d}_1^{n+1}\gamma_1^{n+1} + \mathbf{d}_2^{n+1}\gamma_2^{n+1}) + \frac{1}{2\mathcal{A}^2}\frac{1}{\gamma_j^{n+1}} \\ &- \left[\mathbf{N}_j^{n+1}\mathbf{A}^{-1}(\mathbf{B}\mathbf{U}^{n} - 3\mu(\mathbf{d}_1^{n}\gamma_1^{n} + \mathbf{d}_2^{n}\gamma_2^{n}) + \mathbf{p}) - \frac{1}{2\mathcal{A}^2}\frac{1}{\gamma_j^{n}}\right] = 0 \,, \quad j = 1, 2 \,. \end{aligned} \quad (2.72)$$

After calculating γ_1^{n+1} and γ_2^{n+1} from this system, we then compute $\mathbf{U}^{n+1}$ from (2.72), and update the locations of the spikes.

2.3.2 Numerical Experiments of Oscillatory Drift Instabilities

We now perform some numerical experiments on (2.48) to verify the drift instability threshold of a one-spike solution given in (2.59). We also use the numerical scheme of §2.3.1 to compute large-scale oscillatory motion for some one- and two-spike patterns.

For each of the numerical experiments below we give initial spike locations $\xi_j(0) = \xi_{j0}$, for $j = 1, \cdots, k$, and we choose the initial condition $u(x, 0)$ for (2.48) to be the quasi-equilibrium solution (2.13) with $g_j = 1$ and $x_j = \xi_{j0}$ for $j = 1, \cdots, k$ in (2.13). In all of the numerical computations below we chose the mesh size $h = 0.01$ and the diffusivity $D = 0.75$. For $D = 0.75$, the stability threshold from Proposition 2.5 is computed numerically as $\tau_{dh} = 2.617$.

Experiment 2.3: A one-spike solution near equilibrium: Testing the instability threshold

Let $D = 0.75$ and $\mathcal{A} = 28.5$. Then, from (2.59) we calculate $\tau_{0d} \approx 4.19$. For an initial spike location at $\xi_1(0) = 0.1$, in Fig 2.4 we plot the numerically computed spike layer trajectory ξ_1 versus σ for six values of τ_0. Comparing Fig. 2.4(d) with Fig. 2.4(e) we see that the amplitude of the oscillation grows slowly when $\tau_0 = 4.22$, and decays slowly when $\tau_0 = 4.20$. From Fig. 2.4(f) we observe that the drift Hopf bifurcation value is $\tau_{0d} \approx 4.21$, which compares favorably with the theoretical prediction of $\tau_{0d} \approx 4.19$ from (2.59). With regards to the convergence of the numerical scheme for (2.48), we estimate numerically that $\tau_{0d} \approx 4.23$ with the coarser meshsize $h = 0.02$,

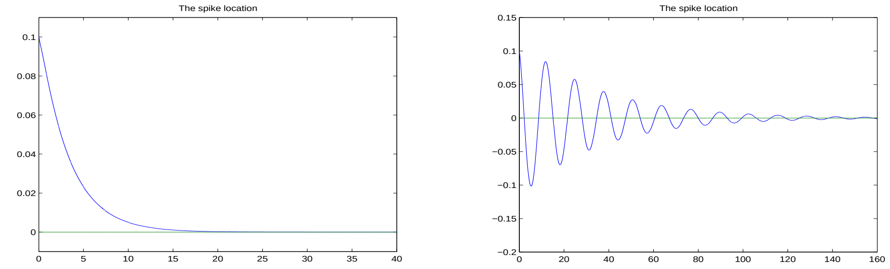

(a) ξ_1 vs. σ for $\tau_0 = 1.0$ (b) ξ_1 vs. σ for $\tau_0 = 4.0$

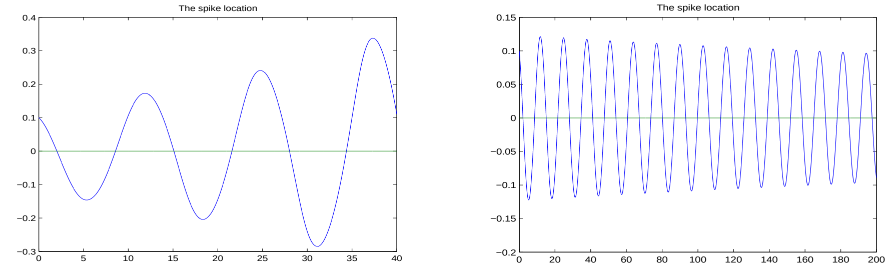

(c) ξ_1 vs. σ for $\tau_0 = 4.4$ (d) ξ_1 vs. σ for $\tau_0 = 4.20$

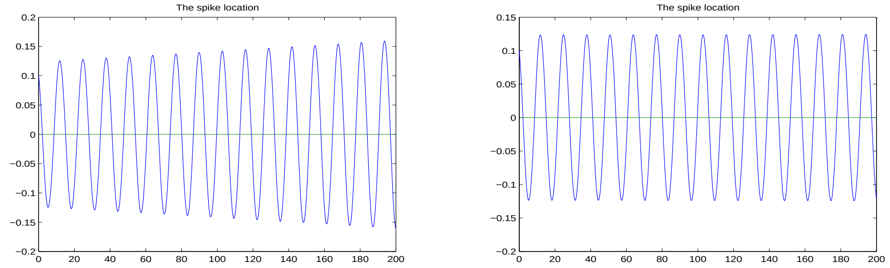

(e) ξ_1 vs. σ for $\tau_0 = 4.22$ (f) ξ_1 vs. σ for $\tau_0 = 4.21$

Figure 2.4: *Experiment 2.3: Testing the stability threshold for initial values near the equilibrium value. Plots of* ξ_1 *versus* σ *with* $\xi_1(0) = 0.1$, $D = 0.75$, *and* $\mathcal{A} = 28.5$, *for different values of* τ_0. *The numerical threshold* $\tau_{0d} \approx 4.21$ *in the plot (f) compares well with the theoretical prediction* $\tau_{0d} \approx 4.19$.

and that $\tau_{0d} \approx 4.20$ for the very fine meshsize $h = 0.005$. As a trade-off between accuracy and computational expense, we chose $h = 0.01$ in our computations.

Experiment 2.4: A one-spike solution: Large-scale oscillatory dynamics

We again let $D = 0.75$ and $\mathcal{A} = 28.5$. However, we now choose the initial spike location $\xi_1(0) = 0.3$, which is not near its equilibrium value. In Fig. 2.5 we plot the numerically computed spike layer trajectory ξ_1 versus σ for $\tau_0 = 4.20$ and $\tau_0 = 4.22$. For the smaller value of τ_0 the spike slowly approaches its steady state at $\xi_1 = 0$. However, for $\tau_0 = 4.22$, the spike location exhibits a sustained large-scale oscillation.

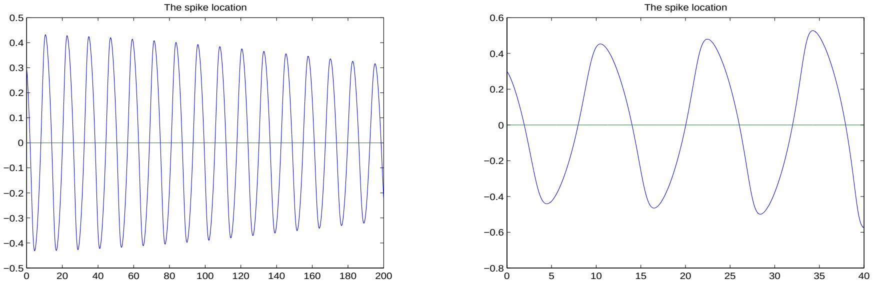

(a) ξ_1 vs. σ for $\tau_0 = 4.20$

(b) ξ_1 vs. σ for $\tau_0 = 4.22$

Figure 2.5: *Experiment 2.4: Plots of* ξ_1 *versus* σ *with* $\xi_1(0) = 0.3$, $D = 0.75$, *and* $\mathcal{A} = 28.5$. *(a)* $\tau_0 = 4.20$*; (b)* $\tau_0 = 4.22$.

Experiment 2.5: A two-spike pattern: Oscillatory drift instabilities and the breather mode

We now compute two-spike solutions. For $D = 0.75$ and $\mathcal{A} = 63.6$, in Fig. 2.6(a) and Fig. 2.6(b) we plot the numerically computed spike trajectories with initial values $\xi_1(0) = -0.38$ and $\xi_2(0) = 0.42$ for two values of τ_0. For $\tau_0 = 16$ the spike trajectories develop a large-scale sustained oscillatory motion. In each case, the observed oscillation is of breather type, characterized by a 180° out of phase oscillation in the spike locations. A breather instability was shown in [38] to be the dominant instability mode for instabilities of equilibrium transition layer patterns for a Fitzhugh-Nagumo type model. It is also the dominant instability mode for equilibrium spike patterns of the GS model in the high feed-rate regime $\mathcal{A} = O(\varepsilon^{-1/2})$ (see [55]).

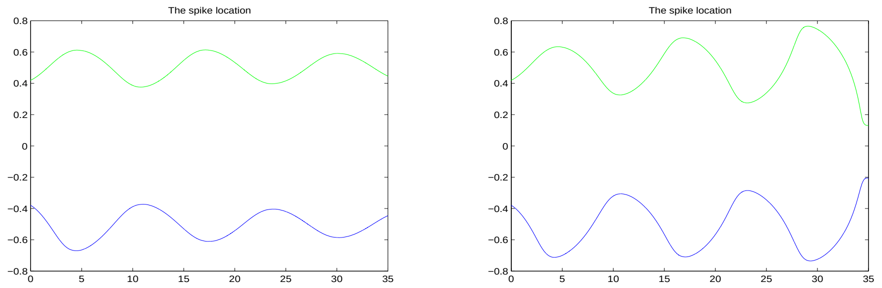

(a) ξ_j vs. σ for $\tau_0 = 15$ (b) ξ_j vs. σ for $\tau_0 = 16$

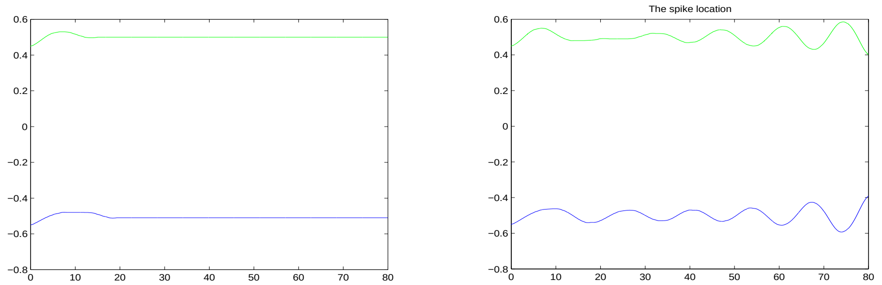

(c) ξ_j vs. σ for $\tau_0 = 15$ (d) ξ_j vs. σ for $\tau_0 = 17$

Figure 2.6: *Experiment 2.5: Spike trajectories* ξ_j *versus* σ *for a two-spike pattern with* $D = 0.75$ *and* $\mathcal{A} = 63.6$*. Top row: the initial values* $\xi_1(0) = -0.38$ *and* $\xi_2(0) = 0.42$ *with* $\tau_0 = 15$ *and* $\tau_0 = 16$*. Bottom Row: the initial values* $\xi_1(0) = -0.55$ *and* $\xi_2(0) = 0.45$ *with* $\tau_0 = 15$ *and* $\tau_0 = 17$*.*

For the same values of D and $\mathcal{A}$, in Fig. 2.6(c) and Fig. 2.6(d) we plot the numerically computed spike trajectories with initial values $\xi_1(0) = -0.55$ and $\xi_2(0) = 0.45$ for $\tau_0 = 15$ and $\tau_0 = 17$, respectively.

2.3.3 Integral Equation Formulation

In this subsection we show how to cast the Stefan problem (2.48) for a one-spike solution into an equivalent integral equation formulation. We let $K(x, \sigma; \eta, s)$ to be the Green's function satisfying

$$\tau_0 \, K_\sigma = D K_{xx} - K + \delta(x - \eta)\delta(\sigma - s) \,, \quad |x| < 1 \,; \quad K_x(\pm 1, \sigma) = 0 \,, \tag{2.73}$$

with initial value $K = 0$ for $0 < \sigma < s$. The solution for K is represented as an eigenfunction expansion as

$$\begin{aligned} K(x,\sigma;\eta,s) =& \frac{H(\sigma - s)}{\tau_0} e^{-(\sigma-s)/\tau_0} \Big[\frac{1}{2} + \sum_{n=1}^{\infty} \exp\left(-\frac{Dn^2\pi^2}{4} \frac{(\sigma - s)}{\tau_0} \right) \\ & \cos\left(\frac{n\pi}{2}(\xi + 1) \right) \cos\left(\frac{n\pi}{2}(\eta + 1) \right) \Big] . \end{aligned} \tag{2.74}$$

By using Green's identity, a straightforward calculation shows that the solution $u(x,\sigma)$ to (2.48) with one spike can be written in terms of K as

$$\begin{aligned} u(x,\sigma) = 1 + \tau_0 \int_{-1}^{1} [u(\eta,0) - 1]\, K(x,\sigma;\eta,0)\, d\eta & \\ - 6 \int_0^{\sigma} \gamma_1(s) K(x,\sigma;\xi_1(s),s)\, ds \,, & \end{aligned} \tag{2.75}$$

where $\xi_1(s)$ is the spike trajectory. By imposing the constraint condition $u = 1/(\gamma_1 \mathcal{A}^2)$ at $x = \xi_1(\sigma)$, we obtain an integral equation for $\gamma_1(\sigma)$ in terms of the unknown spike location as

$$\begin{aligned} \frac{1}{\gamma_1(\sigma)\mathcal{A}^2} = 1 + \tau_0 \int_{-1}^{1} [u(\eta,0) - 1]\, K(\xi_1(\sigma),\sigma;\eta,0)\, d\eta & \\ - 6 \int_0^{\sigma} \gamma_1(s) K(\xi_1(\sigma),\sigma;\xi_1(s),s)\, ds \,. & \end{aligned} \tag{2.76}$$

Then, by calculating u_x as $x \to \xi_1(\sigma)$ from above and from below, we calculate

$$\begin{aligned} u_x(\xi_1^{\pm}(\sigma),\sigma) = \tau_0 \int_{-1}^{1} [u(\eta,0) - 1]\, K_x(\xi_1^{\pm}(\sigma),\sigma;\eta,0)\, d\eta & \\ - 6 \int_0^{\sigma} \gamma_1(s) K_x(\xi_1^{\pm}(\sigma),\sigma;\xi_1(s),s)\, ds \,. & \end{aligned} \tag{2.77}$$

Finally, by substituting (2.77) into (2.48c), we obtain the integro-differential equation

$$\begin{aligned} \frac{d\xi_1}{d\sigma} = \gamma_1(\sigma) \Big(\tau_0 \int_{-1}^{1} [u(\eta,0) - 1] \left(K_x(\xi_1^{+}(\sigma),\sigma;\eta,0) + K_x(\xi_1^{-}(\sigma),\sigma;\eta,0) \right) d\eta & \\ -6 \int_0^{\sigma} \gamma_1(s) \left(K_x(\xi_1^{+}(\sigma),\sigma;\xi_1(s),s) + K_x(\xi_1^{-}(\sigma),\sigma;\xi_1(s),s) \right) ds \Big) . & \end{aligned} \tag{2.78}$$

Here $u(\eta, 0)$ is the initial condition for (2.48). This shows that the speed of the spike layer at time σ depends on its entire past history. Therefore, $\xi_1(\sigma)$ is determined, essentially, by a continuously distributed delay model. Such problems typically lead to oscillatory behavior when τ_0 is large enough. This suggests the mechanism underlying the oscillatory dynamics computed in §2.3.2.

We remark that as a result of the infinite series representation of K in (2.74), together with the constraint (2.76) for γ_1, the integro-differential equation (2.78) is significantly more complicated in form than a related integro-differential equation modeling a flame-front on the infinite line that was studied numerically in [76].

2.4 Discussion

We have studied the dynamics and oscillatory instabilities of spike solutions to the one-dimensional GS model (1.6) in the intermediate regime $O(1) \ll \mathcal{A} \ll O(\varepsilon^{-1/2})$ of the feed-rate parameter $\mathcal{A}$. In the subregime $O(1) \ll \mathcal{A} \ll O(\varepsilon^{-1/3})$, and for $\tau \ll O(\varepsilon^{-2}\mathcal{A}^2)$, we have derived an explicit DAE system for the spike trajectories from the quasi-steady limit of the Stefan problem (2.12). From the analysis of a certain nonlocal eigenvalue problem, it was shown that the instantaneous spike pattern in this regime will become unstable to a Hopf bifurcation in the spike amplitudes at some critical value critical value $\tau = \tau_H = O(\mathcal{A}^4)$. Alternatively, in the subregime $O(\varepsilon^{-1/3}) \ll \mathcal{A} \ll O(\varepsilon^{-1/2})$, and with $\tau = O(\varepsilon^{-2}\mathcal{A}^{-2})$, oscillatory drift instabilities for the spike locations were computed numerically from time-dependent Stefan problem (2.48) with moving sources. In this subregime, the onset of such drift instabilities occur at occur at some critical value $\tau = \tau_{TW} = O(\varepsilon^{-2}\mathcal{A}^{-2})$ be calculated analytically. An open technical problem is to study the codimension-two bifurcation problem that occurs when $\mathcal{A} = O(\varepsilon^{-1/3})$ where both types of oscillatory instability can occur simultaneously at some critical value of $\tau = O(\varepsilon^{-4/3})$.

There are two key open problems. The first problem is to extend the numerical approach of [76], used for a flame-front integro-differential equation model, to compute long-time solutions to the integro-differential equation formulation (2.78) of the Stefan problem (2.48). With such an approach, one could compute numerical solutions to (2.48) over very long time intervals to study whether irregular, or even chaotic, large-scale oscillatory drift behavior of the spike trajectories is possible for the GS model in the subregime $O(\varepsilon^{-1/3}) \ll \mathcal{A} \ll O(\varepsilon^{-1/2})$. A second direction of inquiry is to derive Stefan-type problems with moving sources from an asymptotic reduction of related reaction-diffusion systems with localized solutions such as the Gierer-Meinhardt model with saturation [50], the combustion-reaction model of [60], the Brusselator model of [49], and the GS model in two spatial dimensions. The derivation of such Stefan problems would allow for the study of large-scale drift instabilities of localized structures for parameter values far from their bifurcation values at which a normal form reduction, such as in [25] and [24], can be applied.

Chapter 3

Dynamics and the Spot-Replication Instability for the Two-Dimensional Gray-Scott Model

3.1 k-spot Quasi-Equilibrium Solutions

We first construct a quasi-equilibrium solution to (1.7) for a k-spot pattern in a two-dimensional domain. The stability of this quasi-equilibrium solution with respect to spot self-replication is then studied.

For each $j = 1, \ldots, k$, we denote the center of the j^{th} spot by $\mathbf{x}_j = (x_j, y_j)$ where $\mathbf{x}_j \in \Omega$. We assume that the spots are well-separated in the sense that $\text{dist}(\mathbf{x}_i, \mathbf{x}_j) = O(1)$ for $i \neq j$ and $\text{dist}(\mathbf{x}_i, \partial\Omega) = O(1)$ for $i = 1, \ldots, k$. We then use the method of matched asymptotic expansions to construct the quasi-equilibrium solution. In an $O(\varepsilon)$ neighborhood near each spot, the solution v is large and has a sharp gradient. In this inner region for the j^{th} spot, we introduce the new local variables U_j, V_j, and $\mathbf{y}$ by

$$u = \frac{\varepsilon}{A\sqrt{D}} U_j \,, \qquad v = \frac{\sqrt{D}}{\varepsilon} V_j \,, \qquad \mathbf{y} = \varepsilon^{-1}(\mathbf{x} - \mathbf{x}_j) \,.$$

In terms of these local variables, (1.7) transforms to leading order to

$$\Delta_{\mathbf{y}} V_j - V_j + U_j V_j^2 = 0 \,, \qquad \Delta_{\mathbf{y}} U_j - U_j V_j^2 = 0 \,, \quad \mathbf{y} \in \mathbb{R}^2 \,. \tag{3.1}$$

This leading order inner problem, referred to as the *core* problem, is the same as that derived in [56] for the Schnakenburg model. We look for a radially symmetric solution to this core problem of the form $U_j = U_j(\rho)$ and $V_j = V_j(\rho)$, where $\rho \equiv |y|$ and $\Delta_{\mathbf{y}} = \partial_{\rho\rho} + \rho^{-1}\partial_\rho$ denotes the radially symmetric part of the Laplacian. The radially symmetric core problem is to solve the coupled BVP system

$$U_{j\rho\rho} + \frac{1}{\rho} U_{j\rho} - U_j V_j^2 = 0 \,, \quad 0 < \rho < \infty \tag{3.2a}$$

$$V_{j\rho\rho} + \frac{1}{\rho} V_{j\rho} - V_j + U_j V_j^2 = 0 \,, \quad 0 < \rho < \infty \,, \tag{3.2b}$$

subject to the the boundary conditions

$$V_j'(0) = 0 \,, \qquad U_j'(0) = 0 \,, \tag{3.2c}$$

$$V_j(\rho) \to 0 \,, \qquad U_j(\rho) \sim S_j \ln \rho + \chi(S_j) + o(1) \,, \quad \text{as} \quad \rho \to \infty \,. \tag{3.2d}$$

We refer to S_j as the *source strength* of the j^{th} spot. From the divergence theorem, it follows from the U_j equation that $S_j = \int_0^\infty U_j V_j^2 \rho \, d\rho > 0$. In the far-field behavior (3.2d) for U_j, the constant χ is a nonlinear function of the source strength S_j. This function must be computed from the solution to (3.2).

The solution to (3.2) is calculated numerically for a range of values of $S_j > 0$ by using the BVP solver COLSYS (cf. [2]). In Fig. 3.1, we plot $\chi = \chi(S_j)$ in the left subfigure, $V_j(0)$ vs. S_j in the middle subfigure, and $V_j(\rho)$ for different values of S_j in the right subfigure. For $S_j > S_v \approx 4.78$, the profile $V_j(\rho)$ develops a volcano shape, whereby the maximum of V_j occurs at some $\rho > 0$. These computations give numerical evidence to support the claim that there is a unique solution to (3.2) for each $S_j > 0$.

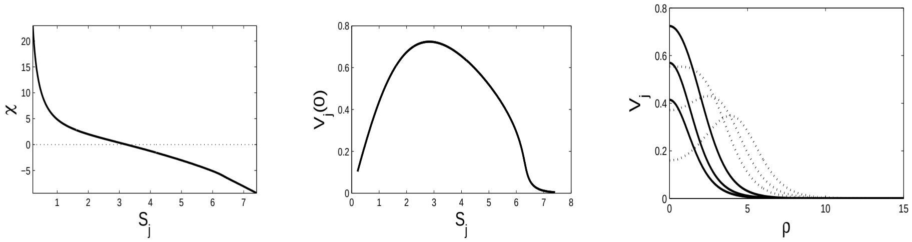

(a) χ vs. S_j (b) $V_j(0)$ vs. S_j (c) V_j vs. ρ

Figure 3.1: *Numerical results for the core problem* (3.2) *computed by COLSYS ([2]). (a) The function* χ *vs.* S_j*; (b)* $V_j(0)$ *vs.* S_j*; (c) The spot profile* $V_j(\rho)$ *for* $S_j = 0.94,\ 1.45,\ 2.79$ *(solid curves from bottom to top at* $\rho = 0$*), and the volcano profile* $V_j(\rho)$ *for* $S_j = 4.79,\ 5.73,\ 6.29$ *(dotted curves from top to bottom at* $\rho = 0$*).*

Since v is localized near each $\mathbf{x}_j$ for $j = 1, \ldots, k$, and is exponentially small in the outer region away from the spot centers, the effect of the nonlinear term uv^2 in the outer region can be calculated in the sense of distributions as

$$uv^2 \sim \varepsilon^2 \sum_{j=1}^{k} \left(\int_{\mathbb{R}^2} \frac{\sqrt{D}}{A\varepsilon} U_j V_j^2 \, dy \right) \delta(\mathbf{x} - \mathbf{x}_j) \sim \frac{2\pi\varepsilon\sqrt{D}}{A} \sum_{j=1}^{k} S_j \, \delta(\mathbf{x} - \mathbf{x}_j) \, .$$

Therefore, in the quasi-steady limit, the outer problem for u is

$$D\Delta u + (1-u) = \frac{2\pi\sqrt{D}\,\varepsilon}{A} \sum_{j=1}^{k} S_j \, \delta(\mathbf{x} - \mathbf{x}_j) \, , \quad \mathbf{x} \in \Omega \, , \tag{3.3a}$$

$$\partial_n u = 0 \, , \quad \mathbf{x} \in \partial\Omega \, , \tag{3.3b}$$

$$u \sim \frac{\varepsilon}{A\sqrt{D}} \Big(S_j \ln|\mathbf{x} - \mathbf{x}_j| - S_j \ln \varepsilon + \chi(S_j) \Big) \, , \quad \text{as } \mathbf{x} \to \mathbf{x}_j \, , \quad j = 1 \ldots, k \, . \tag{3.3c}$$

The singularity condition above as $\mathbf{x} \to \mathbf{x}_j$ was derived by matching the outer solution for u to the far-field behavior (3.2d) of the core solution and by recalling $u = \varepsilon/(A\sqrt{D})U_j$. The problem (3.3) suggests that we introduce new variables $\mathcal{A} = O(1)$ and $\nu \ll 1$, defined by

$$\nu = -1/\ln\varepsilon \, , \qquad \mathcal{A} = \nu A \sqrt{D}/\varepsilon \, . \tag{3.4}$$

In terms of these new variables, (3.3) transforms to

$$\Delta u + \frac{(1-u)}{D} = \frac{2\pi\nu}{\mathcal{A}} \sum_{j=1}^{k} S_j \, \delta(\mathbf{x} - \mathbf{x}_j) \, , \quad \mathbf{x} \in \Omega \, , \tag{3.5a}$$

$$\partial_n u = 0 \, , \quad \mathbf{x} \in \partial\Omega \, , \tag{3.5b}$$

$$u \sim \frac{1}{\mathcal{A}} \Big(S_j \nu \ln|\mathbf{x} - \mathbf{x}_j| + S_j + \chi(S_j)\nu \Big) \, , \quad \text{as } \mathbf{x} \to \mathbf{x}_j \, , \quad j = 1 \ldots, k \, . \tag{3.5c}$$

It is important to emphasize that the singularity behavior in (3.5c) specifies both the strength of the logarithmic singularity for u and the regular, or non-singular, part of this behavior. This pre-specification of the regular part of this singularity behavior at each $\mathbf{x}_j$ will yield a nonlinear algebraic system for the source strengths $S_1, \ldots, S_k$.

To solve (3.5), we introduce the reduced-wave Green's function $G(\mathbf{x}; \mathbf{x}_j)$, which satisfies

$$\Delta G - \frac{1}{D} G = -\delta(\mathbf{x} - \mathbf{x}_j) \, , \quad \mathbf{x} \in \Omega \, ; \qquad \partial_n G = 0 \, , \quad \mathbf{x} \in \partial\Omega \, . \tag{3.6}$$

As $\mathbf{x} \to \mathbf{x}_j$, this Green's function has the local behavior

$$G(\mathbf{x};\mathbf{x}_j) \sim -\frac{1}{2\pi} \ln |\mathbf{x}-\mathbf{x}_j| + R_{jj} + o(1)\,, \quad \text{as} \quad \mathbf{x} \to \mathbf{x}_j\,, \tag{3.7}$$

where R_{jj} is referred to as the regular part of G at $\mathbf{x} = \mathbf{x}_j$. In terms of $G(\mathbf{x};\mathbf{x}_j)$ we can represent the outer solution for u in (3.5) as

$$u = 1 - \sum_{i=1}^{k} \frac{2\pi\nu S_i}{\mathcal{A}} G(\mathbf{x};\mathbf{x}_i)\,.$$

Finally, by expanding this representation for u as $\mathbf{x} \to \mathbf{x}_j$ and equating the resulting expression with the required singularity behavior (3.5c), we obtain the following nonlinear algebraic system for $S_1, \ldots, S_k$:

$$\mathcal{A} = S_j(1+2\pi\nu R_{jj}) + \nu\chi(S_j) + 2\pi\nu \sum_{i=1, i\neq j}^{k} S_i G(\mathbf{x}_i;\mathbf{x}_j)\,, \quad j = 1, \ldots, k\,. \tag{3.8}$$

Since $\nu = -1/\ln\varepsilon \ll 1$, it follows that the geometry of the domain Ω and the spatial configuration $(\mathbf{x}_1, \ldots, \mathbf{x}_k)$ of the spot pattern has a weak, but not insignificant, influence on the source strengths $S_1, \ldots, S_k$ through the Green's function and its regular part. The nonlinear algebraic system (3.8) incorporates all logarithmic correction terms in ν involved in the determination of the source strengths. Given values for the GS parameters A, ε and D, we first calculate $\mathcal{A}$ and ν from (3.4) and then solve (3.8) numerically for the source strengths $S_1, \ldots, S_k$, which determines the quasi-equilibrium in each inner region. The result is summarized as follows:

Principal Result 3.1: *Assume that* $\varepsilon \ll 1$ *and define* $\nu = -1/\ln\varepsilon$ *and* $\mathcal{A} = \nu A\sqrt{D}/\varepsilon$, *with* $\mathcal{A} = O(1)$. *Then, the solution* v *and the outer solution for* u *corresponding to a* k*-spot quasi-equilibrium solution of* (1.7) *are given by*

$$u \sim 1 - \frac{2\pi\nu}{\mathcal{A}} \sum_{j=1}^{k} S_j G(\mathbf{x};\mathbf{x}_j)\,, \qquad v \sim \frac{\sqrt{D}}{\varepsilon} \sum_{j=1}^{k} V_j\left(\varepsilon^{-1}|\mathbf{x}-\mathbf{x}_j|\right)\,, \tag{3.9}$$

where $(\mathbf{x}_1, \cdots, \mathbf{x}_k)$ *are the centers of the spots, and* $G(\mathbf{x};\mathbf{x}_j)$ *is the reduced-wave Green's function satisfying* (3.6). *In* (3.9), *each spot profile* $V_j(\rho)$ *for* $j = 1, \ldots, k$ *satisfies the BVP system* (3.2) *where the source strength* S_j *in* (3.2d) *is to be calculated from the nonlinear algebraic system* (3.8).

We emphasize that the nonlinear algebraic system (3.8) is the mechanism through which spots interact with each other and sense the presence of the domain Ω. This global coupling mechanism is rather significant since $\nu = -1/\ln\varepsilon$ is not very small unless ε is extremely small.

We briefly illustrate this construction of a quasi-equilibrium pattern for the special case of a one-spot solution centered at the midpoint of the unit square. Many further illustrations of the theory are given in subsequent sections.

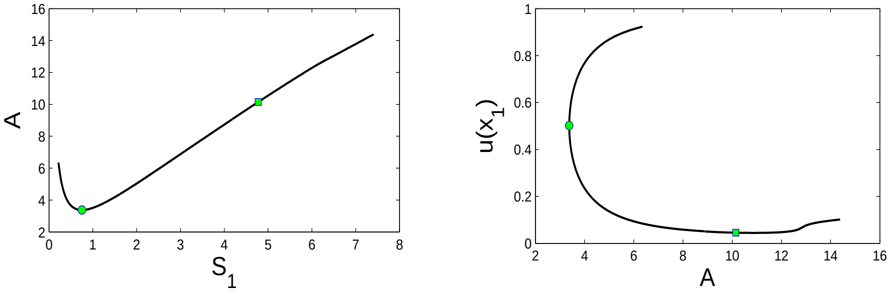

(a) $\mathcal{A}$ vs. S_1

(b) $u(\mathbf{x}_1)$ vs. $\mathcal{A}$

Figure 3.2: *Experiment 3.1: Let* $\Omega = [0,1]\times[0,1]$, *and set* $\varepsilon = 0.02, D = 1$, *and* $\mathbf{x}_1 = (0.5, 0.5)$. *(a)* $\mathcal{A}$ *vs.* S_1*; the square marks the volcano threshold* $S_v = 4.78$, *and the circle marks the fold point* $\mathcal{A}_f = 3.3756$ *corresponding to* $S_f = 0.7499$. *(b)* $u(\mathbf{x}_1)$ *vs.* $\mathcal{A}$, *the square marks* $S_v = 4.78$, *and the circle marks the fold point* $S_f = 0.7499$. *The upper branch is for* $S_1 < S_f$, *while the lower branch is for* $S_1 > S_f$.

Experiment 3.1: One spot in a square: The fold point for $\mathcal{A}$

To illustrate the asymptotic theory, suppose that there is one spot centered at $\mathbf{x}_1$ with source strength S_1 inside the unit square $\Omega = [0,1]\times[0,1]$. Then, (3.8) reduces to the scalar nonlinear algebraic equation

$$\mathcal{A} = S_1\left(1 + 2\pi\nu R_{11}\right) + \nu\chi(S_1). \tag{3.10}$$

We fix $\varepsilon = 0.02$ and $D = 1$, so that $\nu = 0.2556$, and we let $\mathbf{x}_1 = (0.5, 0.5)$. Then, by using (3.59) for the Green's function as given below in §3.6, we obtain that $R_{11} = 0.7876$. In the left subfigure of Fig. 3.2 we plot $\mathcal{A}$ vs. S_1, showing the existence of a fold point at $\mathcal{A}_f = 3.3756$ corresponding to $S_f = 0.7499$. Thus, $\mathcal{A} \geq \mathcal{A}_f$ is required for the existence of a one-spot quasi-equilibrium solution centered at the midpoint of the square. In the right subfigure of Fig. 3.2 we plot $u(\mathbf{x}_1) = \nu\, U(0)/\mathcal{A}$ with respect to $\mathcal{A}$. For $\mathcal{A} > \mathcal{A}_f$, u has two solution branches. The upper branch corresponds to $S_1 < S_f$, while the lower branch is for the range $S_1 > S_f$.

In the remainder of this section we derive analytical approximations for the solution to the nonlinear algebraic system (3.8) for the source strengths. To do so, it is convenient to first re-write (3.8) in matrix form. For a k-spot pattern we define the Green's matrix $\mathcal{G}$, the vector of source strengths $\mathbf{s}$, and the identity vector $\mathbf{e}$ by

$$\mathcal{G} \equiv \begin{pmatrix} R_{11} & G_{12} & G_{13} & \cdots & G_{1k} \\ G_{21} & R_{22} & G_{23} & \cdots & G_{2k} \\ G_{31} & G_{32} & R_{33} & \cdots & G_{3k} \\ \vdots & \vdots & \vdots & \ddots & \vdots \\ G_{k1} & G_{k2} & G_{k3} & \cdots & R_{kk} \end{pmatrix}, \quad \mathbf{s} \equiv \begin{pmatrix} S_1 \\ S_2 \\ S_3 \\ \vdots \\ S_k \end{pmatrix}, \quad \mathbf{e} \equiv \begin{pmatrix} 1 \\ 1 \\ 1 \\ \vdots \\ 1 \end{pmatrix}. \tag{3.11}$$

Here $G_{ij} \equiv G(\mathbf{x}_i; \mathbf{x}_j)$, and $G_{ij} = G_{ji}$ by reciprocity, so that $\mathcal{G}$ is a symmetric matrix. Then, (3.8) is written in matrix form as

$$\mathcal{A}\, \mathbf{e} = \mathbf{s} + 2\pi\nu \mathcal{G}\, \mathbf{s} + \nu \chi(\mathbf{s}), \tag{3.12}$$

where $\chi(\mathbf{s})$ is defined by $\chi(\mathbf{s}) = (\chi(S_1), \ldots, \chi(S_k))^t$ and t denotes transpose.

We will consider (3.12) for two ranges of D. For $D = O(1)$, we can obtain a two-term approximation of the source strengths in terms of $\nu \ll 1$ by expanding $\mathbf{s} = \mathbf{s}_0 + \nu \mathbf{s}_1 + \cdots$. Upon substituting this expansion into (3.12) and collecting powers of ν, we readily obtain the two-term expansion

$$\mathbf{s} = \mathcal{A}\mathbf{e} - \nu \left[2\pi \mathcal{A}\, \mathcal{G}\, \mathbf{e} + \chi(\mathcal{A})\mathbf{e} \right] + O(\nu^2). \tag{3.13}$$

This shows that, for $\nu \ll 1$, the leading order approximation for $\mathbf{s}$ is the same for all of the spots, but that the next order term depends on the spot locations and the domain geometry.

An interesting special case for multi-spot patterns is when the spatial configuration $(\mathbf{x}_1, \ldots, \mathbf{x}_k)$ of spots is such that the Green's matrix $\mathcal{G}$ is a circulant matrix. For instance, this occurs when k spots are equally spaced on a circular ring that is concentric within a circular disk. When $\mathcal{G}$ is circulant, then it has the eigenpair $\mathcal{G}\mathbf{e} = \theta \mathbf{e}$, where $\theta = k^{-1} \sum_{i=1}^{k} \sum_{j=1}^{k} G_{ij}$. For this special case, (3.12) shows that the spots have a common source strength $S_j = S_c$ for $j = 1, \ldots, k$ to all orders in ν, where S_c is the solution to the single nonlinear algebraic equation

$$\mathcal{A} = S_c + 2\pi\nu\theta S_c + \nu \chi(S_c). \tag{3.14}$$

For $\nu \ll 1$, a two-term approximation for this common source strength is

$$S_c = \mathcal{A} - \nu \left[2\pi\theta\mathcal{A} + \chi(\mathcal{A}) \right] + O(\nu^2) \,.$$

Next, we consider (3.12) for the distinguished limit where D is logarithmically large in ε, given by $D = D_0/\nu$ with $D_0 = O(1)$. Since the reduced-wave Green's function depends on D, we first must approximate it for D large. Assuming that Ω is a bounded domain, we expand G and its regular part R for $D \gg 1$ as

$$G \sim DG_{-1} + G_0 + \frac{1}{D} G_1 + \cdots \,, \qquad R \sim DR_{-1} + R_0 + \frac{1}{D} R_1 + \cdots \,.$$

Substituting this expansion into (3.6), and collecting powers of D, we obtain that G_{-1} is constant and that G_0 satisfies

$$\Delta G_0 = G_{-1} - \delta(\mathbf{x} - \mathbf{x}_j) \,, \quad \mathbf{x} \in \Omega \,; \qquad \partial_n G_0 = 0 \,, \quad \mathbf{x} \in \partial\Omega \,.$$

The divergence theorem then shows that $G_{-1} = |\Omega|^{-1}$, where $|\Omega|$ denotes the area of Ω. In addition, the divergence theorem imposed on the G_1 problem enforces that $\int_\Omega G_0 \, d\mathbf{x} = 0$, which makes G_0 unique. Next, from the singularity condition (3.7) for G we obtain for $\mathbf{x} \approx \mathbf{x}_j$ that

$$DG_{-1} + G_0(\mathbf{x};\mathbf{x}_j) + \cdots \sim -\frac{1}{2\pi} \ln |\mathbf{x} - \mathbf{x}_j| + DR_{-1} + R_0(\mathbf{x};\mathbf{x}_j) + \cdots \,.$$

Since $G_{-1} = |\Omega|^{-1}$, we conclude that $R_{-1} = G_{-1} = 1/|\Omega|$. In this way, we obtain the following two-term expansion for the reduced-wave Green's function and its regular part in the limit $D \gg 1$:

$$R_{jj} \sim \frac{D}{|\Omega|} + R_{jj}^{(N)} + \cdots \,, \qquad G(\mathbf{x};\mathbf{x}_j) \sim \frac{D}{|\Omega|} + G^{(N)}(\mathbf{x};\mathbf{x}_j) + \cdots \,. \tag{3.15}$$

Here $G^{(N)}(\mathbf{x};\mathbf{x}_j)$ is the Neumann Green's function with regular part $R_{jj}^{(N)}$, determined from the unique solution to

$$\Delta G^{(N)} = \frac{1}{|\Omega|} - \delta(\mathbf{x} - \mathbf{x}_j) \,, \quad \mathbf{x} \in \Omega \,, \tag{3.16a}$$

$$\partial_n G^{(N)} = 0 \,, \quad \mathbf{x} \in \partial\Omega \,; \qquad \int_\Omega G^{(N)} \, d\mathbf{x} = 0 \,, \tag{3.16b}$$

$$G^{(N)}(\mathbf{x};\mathbf{x}_j) \sim -\frac{1}{2\pi} \ln |\mathbf{x} - \mathbf{x}_j| + R_{jj}^{(N)} \,, \quad \text{as} \quad \mathbf{x} \to \mathbf{x}_j \,. \tag{3.16c}$$

We now use this approximation to find approximate solutions to the nonlinear algebraic system (3.12) in the limit $D = D_0/\nu \gg 1$ with $D_0 = O(1)$ and $\nu \ll 1$. Substituting (3.15) into (3.12) we obtain

$$\mathcal{A}\mathbf{e} = \mathbf{s} + \frac{2\pi D_0}{|\Omega|}\mathbf{e}\,\mathbf{e}^t\mathbf{s} + 2\pi\nu\mathcal{G}^{(N)}\mathbf{s} + \nu\chi(\mathbf{s})\,,$$

where $\mathcal{G}^{(N)}$ is the Green's matrix associated with the Neumann Green's function, i.e. $\mathcal{G}^{(N)}_{ij} = G^{(N)}(\mathbf{x}_i;\mathbf{x}_j)$ for $i \neq j$, and $\mathcal{G}^{(N)}_{jj} = R^{(N)}_{jj}$. By expanding $\mathbf{s}$ as $\mathbf{s} = \mathbf{s}_0 + \nu\mathbf{s}_1 + \cdots$ for $\nu \ll 1$, we then obtain that $\mathbf{s}_0$ and $\mathbf{s}_1$ satisfy

$$\left(\mathcal{I} + \frac{2\pi D_0}{|\Omega|}\mathbf{e}\mathbf{e}^t\right)\mathbf{s}_0 = \mathcal{A}\mathbf{e}\,, \tag{3.17a}$$

$$\left(\mathcal{I} + \frac{2\pi D_0}{|\Omega|}\mathbf{e}\mathbf{e}^t\right)\mathbf{s}_1 = -2\pi\mathcal{G}^{(N)}\mathbf{s}_0 - \chi(\mathbf{s}_0)\,, \tag{3.17b}$$

where $\mathcal{I}$ is the $k \times k$ identity matrix. Since $\mathbf{e}^t\mathbf{e} = k$, the leading order approximation $\mathbf{s}_0$ shows that the source strengths have an asymptotically common value S_c given by

$$\mathbf{s}_0 = S_c\mathbf{e}\,, \qquad S_c \equiv \mathcal{A}\left[1 + \frac{2\pi k D_0}{|\Omega|}\right]^{-1}\,.$$

This shows that decreasing the area of the domain or increasing the diffusion parameter D_0 both have the same effect of decreasing S_c. The next order approximation $\mathbf{s}_1$ from (3.17) yields

$$\mathbf{s}_1 = -\left(\mathcal{I} + \frac{2\pi D_0}{|\Omega|}\mathbf{e}\mathbf{e}^t\right)^{-1}\Big(2\pi S_c\mathcal{G}^{(N)} + \chi(S_c)\Big)\mathbf{e}\,. \tag{3.18}$$

Since the matrix $\mathcal{I} + \frac{2\pi D_0}{|\Omega|}\mathbf{e}\mathbf{e}^t$ is a rank-one perturbation of the identity, its inverse is readily calculated explicitly from the Shermann-Woodbury-Morrison formula as

$$(\mathcal{I} + \mu\mathbf{e}\mathbf{e}^t)^{-1} = \mathcal{I} - \frac{\mu\mathbf{e}\mathbf{e}^t}{1 + \mu\mathbf{e}^t e}\,, \qquad \mu = \frac{2\pi D_0}{|\Omega|}\,,$$

which determines $\mathbf{s}_1$ from (3.18). In this way, we obtain for $D = D_0/\nu$ and $\nu \ll 1$ that the source strengths have the two-term expansion

$$\mathbf{s} = S_c\mathbf{e} - \left(\frac{\chi(S_c)}{1+\mu k}\mathbf{e} + \frac{2\pi\mathcal{A}}{1+\mu k}\Big(\mathcal{G}^{(N)} - \frac{\mu\,F}{1+\mu k}\mathcal{I}\Big)\,\mathbf{e}\right)\nu + O(\nu^2)\,. \tag{3.19}$$

Here $S_c \equiv \mathcal{A}/(1+\mu k)$, $\mu \equiv 2\pi D_0/|\Omega|$, and $F((\mathbf{x}_1, \ldots, \mathbf{x}_k)$ is a scalar function denoting the sum of all of the entries of $\mathcal{G}^{(N)}$, i.e.

$$F(\mathbf{x}_1, \ldots, \mathbf{x}_k) = \mathbf{e}^t \mathcal{G}^{(N)}\, \mathbf{e} = \sum_{i=1}^{K} \sum_{j=1}^{k} \mathcal{G}_{ij}^{(N)} \, . \tag{3.20}$$

The k-components of the $O(\nu)$ correction to $\mathbf{s}$ have, in general, different values owing to the term involving $\mathcal{G}^{(N)}\, \mathbf{e}$. A simple calculation shows that the sum of $\mathbf{s}$ is

$$\mathbf{e}^t \mathbf{s} \sim \frac{\mathcal{A} k}{1+\mu k} - \nu \left[\frac{k\, \chi(S_c)}{1+\mu k} + \frac{2\pi \mathcal{A} F}{(1+\mu k)^2} \right] . \tag{3.21}$$

From this expression, we note that $\mathbf{e}^t s$ is minimized when $F(\mathbf{x}_1, \ldots, \mathbf{x}_k)$ is maximized.

Finally, we remark that if the Neumann Green's matrix $\mathcal{G}^{(N)}$ is a circulant matrix, then it must have the eigenpair $\mathcal{G}^{(N)}\mathbf{e} = \theta^{(N)}\mathbf{e}$, where $\theta^{(N)} = F/k$. In this case, (3.19) shows that the spots have the common source strength given asymptotically by

$$\mathbf{s} = \Big[\frac{\mathcal{A}}{1+\mu k} - \nu \left(\frac{\chi(S_c)}{1+\mu k} + \frac{2\pi \mathcal{A}}{1+\mu k} \left(\frac{F}{k} - \frac{\mu F}{1+\mu k} \right) \right) \Big] \mathbf{e} + O(\nu^2) \, . \tag{3.22}$$

Owing to the rather simple structure of the nonlinear algebraic system (3.12) when the Green's matrix is circulant, in many of our numerical experiments in the sections below we will focus on k-spot quasi-equilibrium patterns that lead to this special matrix structure.

3.2 The Spot-Splitting Instability

We now study the stability of a quasi-equilibrium spot pattern to a spot self-replicating instability that can occur on a fast $O(1)$ time-scale relative to the slow motion of speed $O(\varepsilon^2)$ of the spot locations. The slow motion of spots is studied later in Section 3.3. The stability analysis in this section is similar to that done in [56] for the Schnakenburg model.

We first perturb the quasi-equilibrium solution u_e, v_e as

$$u(\mathbf{x}, t) = u_e + e^{\lambda\, t} \eta(\mathbf{x}) \, , \quad v(\mathbf{x}, t) = v_e + e^{\lambda\, t} \phi(\mathbf{x}) \, ,$$

for a given and fixed spatial configuration $(\mathbf{x}_1, \ldots, \mathbf{x}_k)$ of spots. Substituting this perturbation into (1.7) and linearizing, we obtain the eigenvalue problem

$$\begin{aligned} \varepsilon^2\Delta\phi - (1+\lambda)\phi + 2Au_e v_e\phi + Av_e^2\eta &= 0\,, & (3.23a)\\ D\Delta\eta - (1+\tau\lambda)\eta - 2u_e v_e\phi - v_e^2\eta &= 0\,. & (3.23b)\end{aligned}$$

In the inner region near the j^{th} spot, we recall that $u_e \sim \frac{\varepsilon}{A\sqrt{D}}U_j$ and $v_e \sim \frac{\sqrt{D}}{\varepsilon}V_j$, where U_j, V_j is the solution of the core problem (3.2). We then let $\mathbf{y} = \varepsilon^{-1}(\mathbf{x}-\mathbf{x}_j)$, and define N_j and Φ_j by $\eta = \frac{\varepsilon}{A\sqrt{D}}N_j$ and $\phi = \frac{\sqrt{D}}{\varepsilon}\Phi_j$. Then, upon neglecting algebraic terms in ε, (3.23) reduces to

$$\begin{aligned} \Delta_{\mathbf{y}}\Phi_j - (1+\lambda)\Phi_j + 2U_jV_j\Phi_j + V_j^2N_j &= 0\,, & (3.24a)\\ \Delta_{\mathbf{y}}N_j - V_j^2N_j - 2U_jV_j\Phi_j &= 0\,, & (3.24b)\end{aligned}$$

under the assumption that $\tau \ll O(\varepsilon^{-2})$. Next we look for angular perturbations of the form $\Phi_j = e^{im\psi}\hat{\Phi}_j(\rho)\,,\ N_j = e^{im\psi}\hat{N}_j(\rho)$, where $\hat{\Phi}_j$ and $\hat{N}_j$ are radially symmetric in the inner variable $\rho = |\mathbf{y}|$. Then, from (3.24), $\hat{N}_j(\rho)$ and $\hat{\Phi}_j(\rho)$ on $0<\rho<\infty$ satisfy

$$\hat{\Phi}_{j\rho\rho} + \frac{1}{\rho}\hat{\Phi}_{j\rho} - \frac{m^2}{\rho^2}\hat{\Phi}_j - (1+\lambda)\hat{\Phi}_j + 2U_jV_j\hat{\Phi}_j + V_j^2\hat{N}_j = 0\,, \qquad (3.25a)$$

$$\hat{N}_{j\rho\rho} + \frac{1}{\rho}\hat{N}_{j\rho} - \frac{m^2}{\rho^2}\hat{N}_j - V_j^2\hat{N}_j - 2U_jV_j\hat{\Phi}_j = 0\,, \qquad (3.25b)$$

with boundary conditions

$$\hat{\Phi}_j'(0) = 0, \quad \hat{N}_j'(0) = 0, \quad \hat{\Phi}_j(\rho)\to 0, \ \text{as} \ \ \rho\to\infty\,. \qquad (3.25c)$$

The specific form for the far-field behavior of $\hat{N}_j$ will be different for the two cases $m=0$ and $m\geq 2$. For the case $m=1$, which corresponds to translation invariance, it follows trivially that $\lambda = 0$. Since this case $m=1$ is accounted for by the analysis of Section 3.3 for the slow spot dynamics it is not considered here.

An instability of (3.25) for the mode $m=2$ is associated with the initiation of a peanut-splitting instability. This initial instability is found numerically to lead to a spot self-replication event, whereby a single spot splits into two identical spots. Instabilities for the higher modes $m\geq 3$ suggest the possibility of more spatially intricate spot self-replication events. Thus, the eigenvalue problem (3.25) with angular mode $m\geq 2$ determines spot-splitting instabilities. For this range of m, the linear operator for N_j in (3.25b) allows for decay as $\rho\to\infty$ owing to the $m^2\hat{N}_j/\rho^2$ term. As such, for the modes $m \geq 2$ we impose the far-field boundary condition that $\hat{N}_j' \to 0$ as $\rho \to \infty$.

The eigenvalue problem (3.25) is coupled to the core problem (3.2) for U_j and V_j, and can only be solved numerically. To do so, we first solve (3.2) numerically by using COLSYS (cf. [2]). Then, we discretize (3.25) by a centered difference scheme to obtain a matrix eigenvalue problem. By using the linear algebra package LAPACK [1] to compute the spectrum of this matrix eigenvalue problem, we estimate the eigenvalue λ_0 of (3.25) with the largest real part as a function of the source strength S_j for different angular modes $m \geq 2$. The instability threshold occurs when $\text{Re}(\lambda_0) = 0$. We find numerically that λ_0 is real when S_j is large enough. In the left subfigure of Fig. 3.3, we plot $\text{Re}(\lambda_0)$ as a function of the source strength S_j for $m = 2, 3, 4$. Our computational results show that the instability threshold for the modes $m \geq 2$ occurs at $S_j = \Sigma_m$, where $\Sigma_2 \approx 4.31$, $\Sigma_3 \approx 5.44$, and $\Sigma_4 \approx 6.14$. In the right subfigure of Fig. 3.3, we plot the eigenfunction $(\hat{\Phi}_j, \hat{N}_j)$ corresponding to $\lambda_0 = 0$ with $m = 2$ at $S_j = \Sigma_2$. In this subfigure we have scaled the maximum value of $\hat{\Phi}_j$ to unity.

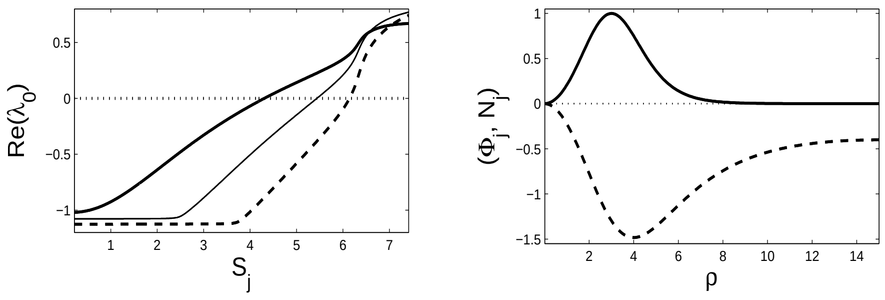

(a) $\text{Re}(\lambda_0)$ vs. S_j (b) $(\hat{\Phi}_j, \hat{N}_j)$ vs. ρ

Figure 3.3: *Numerical results for the principal eigenvalue of* (3.25) *with mode* $m \geq 2$. *(a) Re*(λ_0) *vs.* S_j*; heavy solid curve is for* $m = 2$ *with* $\Sigma_2 = 4.31$*, the solid curve is for* $m = 3$ *with* $\Sigma_3 = 5.44$*, and the dashed curve is for* $m = 4$ *with* $\Sigma_4 = 6.14$*. (b) For* $m = 2$*, the eigenfunctions* $(\hat{\Phi}_j(\rho), \hat{N}_j(\rho))$ *near* $\lambda_0 = 0$ *with* $S_j = \Sigma_2 \approx 4.31$ *are shown. The solid curve is* $\hat{\Phi}_j(\rho)$*, and the dashed curve is* $\hat{N}_j(\rho)$*.*

Principal Result 3.2: *Consider the 2-D Gray Scott model* (1.7) *with given parameters* A, D, ε*, and* $\tau \ll O(\varepsilon^{-2})$*, on a fixed domain. Calculate* $\mathcal{A}$ *and* ν *from* (3.4)*. In terms of* $\mathcal{A}$*,* D*, and* ν*, calculate the source strengths* $S_1, \ldots, S_k$

for a k-spot quasi-equilibrium pattern from the nonlinear algebraic system (3.8)*. Then, if $S_j < \Sigma_2 \approx 4.31$, the j^{th} spot is linearly stable to a spot deformation instability for modes $m \geq 2$. Alternatively, for $S_j > \Sigma_2$, it is linearly unstable to the mode $m = 2$ associated with peanut-splitting.*

We remark that in our stability analysis we linearized the GS model around a quasi-equilibrium solution, where the spots were assumed to be at fixed locations $\mathbf{x}_1, \ldots, \mathbf{x}_k$, independent of time. However, as shown below in Section 3.3, the spots have a speed $O(\varepsilon^2)$, so that the source strengths S_j for $j = 1, \ldots, k$ also vary slowly in time. As a result, there can be a triggered, or dynamically induced, spot-replication instability due to the slow evolution of S_j. More specifically, for a spot pattern that is initially stable to self-replication at $t = 0$ in the sense that $S_j < \Sigma_2$ at $t = 0$ for $j = 1, \ldots, k$, it is possible that as the J^{th} spot moves toward its equilibrium location in the domain that $S_J > \Sigma_2$ after a sufficiently long time. Thus, the source strength of a particular spot (i.e. the J^{th} spot) may drift above the instability threshold for peanut-splitting as a result of the intrinsic slow dynamics of the collection of spots. This scenario is similar to other ODE and PDE problems that have triggered instabilities generated from slowly varying external bifurcation, or control, parameters. The key difference here, is that the spot self-replication instability can be triggered from the intrinsic motion of the collection of spots, and is not due to an externally imposed control parameter.

Our second remark is that the eigenvalue problem (3.25) with mode $m = 0$ corresponds to instabilities in the amplitudes of the spots. For this mode, we cannot impose that the eigenfunction $\hat{N}_j$ is bounded at infinity. Instead, we must impose that $\hat{N}_j \to C_j \ln \rho + B_j$ as $\rho \to \infty$. This type of spot profile instability is discussed in detail in Chapter §4.

3.3 The Slow Dynamics of Spots

Next we derive the slow dynamics for the spot locations for a k-spot quasi-equilibrium solution to the GS model. The analysis is similar to that in [56].

In the inner region near the j^{th} spot, we introduce $\mathbf{y} = \varepsilon^{-1}(\mathbf{x} - \mathbf{x}_j)$ and we expand

$$u = \frac{\varepsilon}{A\sqrt{D}}(U_{0j}(\rho) + \varepsilon U_{1j}(\mathbf{y}) + \cdots), \quad v = \frac{\sqrt{D}}{\varepsilon}(V_{0j}(\rho) + \varepsilon V_{1j}(\mathbf{y}) + \cdots).$$

Note that the subscript 0 in U_{0j}, V_{0j} denotes the order of expansion, and j denotes that the variables are near the j^{th} spot. In the analysis below we omit the subscript j if there is no confusion in the notation. The expansions above for u and v yield the same core problem for U_{0j} and V_{0j} as in (3.2). At next order, we get that U_1 and V_1 satisfy

$$\begin{aligned} \Delta_{\mathbf{y}} V_1 - V_1 + 2U_0V_0V_1 + V_0^2U_1 &= V_0' \frac{d}{d\varsigma}|\mathbf{x}-\mathbf{x}_j|\,, \\ \Delta_{\mathbf{y}} U_1 - 2U_0V_0V_1 - V_0^2U_1 &= 0\,, \end{aligned} \tag{3.26}$$

where we have introduced $\varsigma = \varepsilon^2 t$ as the slow time variable. We define θ to be the polar angle for the vector $(\mathbf{x}-\mathbf{x}_j)$, with $\mathbf{x}_j = \mathbf{x}_j(\varepsilon^2 t)$, so that $\frac{d|\mathbf{x}-\mathbf{x}_j|}{d\varsigma} = -\mathbf{x}_j' \cdot \mathbf{e}_\theta$, where $\mathbf{e}_\theta = (\cos\theta, \sin\theta)^t$, $\mathbf{x}_j = (x_1, x_2)^t$, and t denotes transpose. The system (3.26) for U_1 and V_1 can be written in matrix form as

$$\Delta_{\mathbf{y}} \mathbf{w}_j + \mathcal{M}_j \mathbf{w}_j = \mathbf{f}_j\,, \qquad \mathbf{y} \in \mathbb{R}^2, \tag{3.27}$$

where

$$\mathcal{M}_j = \begin{pmatrix} -1+2U_0V_0 & V_0^2 \\ -2U_0V_0 & -V_0^2 \end{pmatrix}, \quad \mathbf{w}_j = \begin{pmatrix} V_1 \\ U_1 \end{pmatrix}, \quad \mathbf{f}_j = \begin{pmatrix} -V_0'\mathbf{x}_j' \cdot \mathbf{e}_\theta \\ 0 \end{pmatrix}. \tag{3.28}$$

Recall that the outer solution for u is

$$u = 1 - \sum_{j=1}^{k} \frac{2\pi\nu S_j}{\mathcal{A}} G(\mathbf{x};\mathbf{x}_j)\,.$$

The local behavior of the reduced-wave Green's function as $\mathbf{x} \to \mathbf{x}_j$, written in terms of the inner variable $\mathbf{y}$, is

$$G(\mathbf{x};\mathbf{x}_j) \sim -\frac{1}{2\pi}\ln|\mathbf{x}-\mathbf{x}_j| + R_{jj} + \varepsilon\nabla R(\mathbf{x}_j;\mathbf{x}_j)\cdot\mathbf{y} + \cdots\,,$$

where ∇f denotes the gradient of the function f. Upon matching the inner and outer solutions for u near the j^{th} spot, we obtain the far-field behavior of the inner solution U_{1j} given by

$$U_{ij} \sim -2\pi\Big[S_j\nabla R(\mathbf{x}_j;\mathbf{x}_j) + \sum_{i=1,\,i\neq j}^{k} S_i \nabla G(\mathbf{x}_i;\mathbf{x}_j)\Big]\cdot\mathbf{y}\,, \quad \text{as} \quad \mathbf{y} \to \infty\,.$$

Therefore, the required far-field behavior for (3.27) is that

$$\mathbf{w}_j \to \begin{pmatrix} 0 \\ -\vec{\alpha}_j \cdot \mathbf{y} \end{pmatrix}, \quad \text{as } \mathbf{y} \ \to \ \infty\,, \tag{3.29a}$$

$$\vec{\alpha}_j = \begin{pmatrix} \alpha_1 \\ \alpha_2 \end{pmatrix} \equiv 2\pi (S_j \nabla R_{jj} + \sum_{i=1,\, i\neq j}^{k} S_i \nabla G_{ij})\,. \tag{3.29b}$$

Here α_1, α_2 are the first and second components of the vector $\vec{\alpha}_j$, respectively. We define $\hat{P}_j^*(\rho) = (\hat{\phi}_j^*(\rho), \hat{\psi}_j^*(\rho))^t$ to be the radially symmetric solution of the adjoint problem

$$\Delta_\rho \hat{P}_j^* + \mathcal{M}_j^t \hat{P}_j^* = 0\,, \tag{3.30}$$

subject to the far-field condition that $\hat{P}_j^* \to (0, 1/\rho)^t$ as $\rho \to \infty$, where $\Delta_\rho \equiv \partial_{\rho\rho} + \rho^{-1}\partial_\rho - \rho^{-2}$. We look for solutions P_j^c and P_j^s of the adjoint problem $\Delta_{\mathbf{y}} P_j + \mathcal{M}_j^t P_j = 0$ in the form $P_j^c = \hat{P}_j^* \cos\theta$ and $P_j^s = \hat{P}_j^* \sin\theta$, where $\hat{P}_j^*$ is a radially symmetric function. In terms of the adjoint solution P_j^c, the solvability condition for (3.27), subject to (3.29a), is that

$$\lim_{\sigma\to\infty} \int_{B_\sigma} P_j^c \cdot \mathbf{f}\, d\mathbf{y} = \lim_{\sigma\to\infty} \int_{\partial B_\sigma} \left[P_j^c \cdot \partial_\rho \mathbf{w}_j - \mathbf{w}_j \cdot \partial_\rho P_j^c \right]\Big|_{\rho=\sigma} d\rho\,. \tag{3.31}$$

Here B_σ is a ball of radius σ, i.e $|\mathbf{y}| = \sigma$. Upon using the far-field condition (3.29a), we reduce (3.31) to

$$\begin{aligned} x_1^{'} \int_0^{2\pi} \int_0^\infty \hat{\phi}_j^* V_0' \cos^2\theta \rho\, d\rho\, d\theta \, - x_2^{'} \int_0^{2\pi} \int_0^\infty \hat{\phi}_j^* V_0' \cos\theta \sin\theta \rho\, d\rho\, d\theta \\ = \lim_{\sigma\to\infty} \int_0^{2\pi} \left[\frac{\cos\theta}{\sigma} \vec{\alpha}_j \cdot \mathbf{e}_\theta - \sigma \vec{\alpha}_j \cdot \mathbf{e}_\theta \left(-\frac{1}{\sigma^2} \right) \cos\theta \right] \sigma\, d\theta\,. \end{aligned} \tag{3.32}$$

Since $\int_0^{2\pi} \cos\theta \sin\theta\, d\theta = 0$, we obtain

$$\frac{\partial x_1}{\partial \varsigma} = \frac{2\alpha_1}{\int_0^\infty \hat{\phi}_j^* V_0' \rho\, d\rho}\,. \tag{3.33}$$

Similarly, the solvability condition for (3.27), subject to (3.29a), with respect to the homogeneous adjoint solution P_j^s, yields

$$\frac{\partial x_2}{\partial \varsigma} = \frac{2\alpha_2}{\int_0^\infty \hat{\phi}_j^* V_0' \rho d\rho}\,. \tag{3.34}$$

We summarize the result for the dynamics as follows:

Principal Result 3.3: *Consider the 2-D GS model* (1.7) *for* $\varepsilon \to 0$ *with* $\tau \ll O(\varepsilon^{-2})$. *Then, the slow dynamics of a collection* $(\mathbf{x}_1, \dots, \mathbf{x}_k)$ *of spots that are stable to spot profile instabilities are governed by the differential-algebraic (DAE) system*

$$\frac{d\mathbf{x}_j}{dt} \sim -2\pi\varepsilon^2\gamma(S_j)\left(S_j\nabla R(\mathbf{x}_j;\mathbf{x}_j) + \sum_{i=1,\, i\neq j}^{k} S_i\nabla G(\mathbf{x}_j;\mathbf{x}_i)\right)\,, \quad j=1,\dots,k\,, \tag{3.35}$$

where $\gamma(S_j) \equiv \left(-2/\int_0^\infty \hat{\phi}_j^* V_0'\rho\, d\rho\right)$. *Here the source strengths* S_j, *for* $j = 1,\dots,k$, *are determined in terms of the instantaneous spot locations and the parameters* $\mathcal{A}$, D, *and* $\nu = -1/\ln\varepsilon$ *by the nonlinear algebraic system* (3.8). *In addition,* V_0 *satisfies the core problem* (3.2), *and* $\hat{\phi}_j^*$ *is the radially symmetric solution of the adjoint problem* (3.30).

The ODE system (3.35) coupled to the nonlinear algebraic system (3.8) comprises a DAE system for the time-dependent spot locations $\mathbf{x}_j$ and source strengths S_j for $j = 1,\dots,k$. These collective coordinates evolve slowly over a long time-scale of order $t = O(\varepsilon^{-2})$. The function $\gamma(S_j)$ in (3.35) was previously computed numerically in Fig. 3 of [56], where it was shown that $\gamma(S_j)$ is positive for a wide range of S_j. This plot is re-computed below in Fig. 3.4(f). In Section §3.7, we will compare the dynamics (3.35) with full numerical results for different patterns.

It is important to emphasize that the DAE system in Principal Result 3.3 for the slow spot evolution is only valid if each spot profile is stable to any spot profile instability that occurs on a fast $O(1)$ time-scale. Such instabilities are the spot-splitting instability studied in Section §3.2 and the competition and oscillatory profile instabilities studied later in Chapter 4.

The equilibrium or steady-state locations of a collection $(\mathbf{x}_1, \dots, \mathbf{x}_k)$ of spots satisfies $d\mathbf{x}_j/dt = 0$ for $j = 1,\dots,k$, where the dynamics was given as in Principal Result 3.3. This leads to the following equilibrium result:

Principal Result 3.4: *Consider the 2-D GS model* (1.7) *with given parameters* $\mathcal{A}, D, \varepsilon$. *Then, the equilibrium spot locations* $\mathbf{x}_{je}$ *and corresponding equilibrium source strengths* S_{je} *for* $j = 1,\dots,k$ *satisfy*

$$S_j\nabla R_{jj} + \sum_{i=1,\, i\neq j}^{k} S_i\nabla G_{ij} = 0\,, \quad j = 1,\dots,k\,, \tag{3.36}$$

subject to the nonlinear algebraic system (3.8)*, which relates the source strengths to the spot locations. In* (3.36) *we have labeled* $\nabla = (\partial_{x_j}, \partial_{y_j})$.

In general it is intractable to determine analytically all possible equilibrium solution branches for k-spot patterns in an arbitrary 2-D domain as the parameters $\mathcal{A}$ and D are varied. However, some partial results are obtained in Section 3.7 for the special case of k spots equally spaced on a circular ring that lies within and is concentric with a circular disk domain. For this special case, the Green's matrix is circulant, and the equilibrium problem is reduced to determining the equilibrium ring radius for the pattern.

3.4 The Direction of Splitting

Next we determine the direction in which a spot splits, relative to the direction of its motion, if its source strength is slightly above the threshold value $\Sigma_2 \approx 4.31$. When $S_j = \Sigma_2$, the eigenspace for $\lambda = 0$ is four-dimensional; there are two eigenfunctions associated with the peanut-splitting mode $m = 2$, and there are two translation eigenfunctions associated with the mode $m = 1$. For $S_j - \Sigma_2 = O(\varepsilon)$, we have $\lambda = 0(\varepsilon)$. Therefore, we will expand $\lambda = \varepsilon\lambda_1 + \cdots$, and calculate both λ_1 and its unstable eigenfunction, which will determine the direction for which a spot will split. The calculation below is similar to that in [56].

To analyze the direction of splitting, we must calculate a two-term expansion for the solution of the core problem in addition to its associated eigenvalue problem near the j^{th} spot. Throughout the calculation below, we omit the index j if there is no confusion. We first introduce

$$U = U_0(\rho) + \varepsilon U_1(\mathbf{y}) + \cdots , \quad V = V_0(\rho) + \varepsilon V_1(\mathbf{y}) + \cdots , \quad \rho = |\mathbf{y}| .$$

Then, as in the analysis of the slow dynamics in Section §3.3, the perturbation $\mathbf{w} = (V_1, U_1)^t$ satisfies (3.27) with

$$\mathbf{x}_j' = -\gamma(S_j)\vec{\alpha}_j , \qquad \vec{\alpha}_j = 2\pi\Big(S_j \nabla R_{jj} + \sum_{i=1,\, i\neq j}^{k} S_i \nabla G_{ij}\Big) .$$

Next, we introduce a complex constant g defined by $g \equiv \alpha_1 - i\alpha_2$, so that in (3.28) the vector $\mathbf{f}$ can be written as

$$\mathbf{f} = \gamma(S_j) \begin{pmatrix} \mathrm{Re}(g e^{i\theta}) V_0' \\ 0 \end{pmatrix} ,$$

where $\vec{\alpha}_j = (\alpha_1, \alpha_2)^t$, and $\text{Re}(A)$ is the real part of A. Then, $\mathbf{w}(\mathbf{y})$ can be written in terms of a real-valued radially symmetric function $\hat{\mathbf{w}}(\rho)$ as

$$\mathbf{w}(\mathbf{y}) = \frac{1}{2} g e^{i\theta} \hat{\mathbf{w}}(\rho) + c.c., \quad \hat{\mathbf{w}}(\rho) = (\hat{V}_1(\rho), \hat{U}_1(\rho))^t,$$

where $c.c.$ denotes the complex conjugate, and $\hat{\mathbf{w}}(\rho)$ on $0 \le \rho < \infty$ satisfies

$$\Delta_\rho \hat{\mathbf{w}} + \mathcal{M}\hat{\mathbf{w}} = \gamma(S_j) \begin{pmatrix} V_0' \\ 0 \end{pmatrix}, \qquad \hat{\mathbf{w}} \to \begin{pmatrix} 0 \\ -\rho \end{pmatrix} \quad \text{as } \rho \to \infty \,. \tag{3.37}$$

For the eigenvalue problem (3.24), we expand

$$\Phi = \hat{\Phi}_0(\rho) + \varepsilon \Phi_1(\mathbf{y}) + \cdots, \quad N = \hat{N}_0(\rho) + \varepsilon N_1(\mathbf{y}) + \cdots, \quad \lambda = \varepsilon\lambda_1 + \cdots.$$

Upon substituting these expansions into (3.24), we obtain the leading order approximation $\mathbf{P}_0 = (\hat{\Phi}_0, \hat{N}_0)^t$ as before, and obtain an equation for the next order terms $\mathbf{P}_1 = (\Phi_1, N_1)^t$. In this way, we get

$$\Delta_\rho \mathbf{P}_0 + \mathcal{M}\mathbf{P}_0 = 0\,, \tag{3.38a}$$

$$\Delta_{\mathbf{y}} \mathbf{P}_1 + \mathcal{M}\mathbf{P}_1 = \Lambda_1 \mathbf{P}_0 - \mathcal{M}_1 \mathbf{P}_0 - \mathcal{F}\mathbf{P}_0\,, \tag{3.38b}$$

where $\mathcal{M}$ and $\mathcal{M}_1$ are defined by

$$\mathcal{M} = \begin{pmatrix} -1 + 2U_0V_0 & V_0^2 \\ -2U_0V_0 & -V_0^2 \end{pmatrix}, \quad \mathcal{M}_1 = \begin{pmatrix} 2U_1V_0 + 2U_0V_1 & 2V_0V_1 \\ -U_1V_0 - 2U_0V_1 & -2V_0V_1 \end{pmatrix}.$$

In addition, we have defined Λ_1 and $\mathcal{F}$ by

$$\Lambda_1 = \begin{pmatrix} \lambda_1 & 0 \\ 0 & 0 \end{pmatrix} \qquad \mathcal{F} = \begin{pmatrix} \mathbf{x}_j' \cdot \nabla & 0 \\ 0 & 0 \end{pmatrix}.$$

Since $\mathbf{x}_j' \cdot \nabla = -\gamma(S_j)\text{Re}(g e^{i\theta})\partial_\rho$, we can write $\mathcal{M}_1$ and $\mathcal{F}$ as

$$\mathcal{M}_1 = \frac{1}{2} g e^{i\theta} \hat{\mathcal{M}}_1 + c.c.\,, \quad \mathcal{F} = -\frac{1}{2}\gamma(S_j)(g e^{i\theta} + c.c.)\hat{\mathcal{F}}, \quad \hat{\mathcal{F}} = \begin{pmatrix} \partial_\rho & 0 \\ 0 & 0 \end{pmatrix},$$

where $\hat{\mathcal{M}}_1$ is obtained by replacing V_1, U_1 with the radially symmetric solution $\hat{V}_1, \hat{U}_1$ in every component of $\mathcal{M}_1$. For the leading order equation (3.38a), the solution consists of the eigenfunctions associated with the zero eigenvalue, so that

$$\mathbf{P}_0 = A\hat{\mathbf{P}}_{01}(\rho)e^{i\theta} + B\hat{\mathbf{P}}_{02}(\rho)e^{2i\theta} + c.c.$$

For $m = 1$, the eigenfunctions are $\hat{\mathbf{P}}_{01} = (V_0', U_0')^t$, and for $m = 2$ with $S_j \approx \Sigma_2$, the eigenfunctions $\hat{\mathbf{P}}_{02}$ are plotted in Fig. 3.3(b). The corresponding homogeneous adjoint problem has four independent solutions, which we write in complex form as

$$\begin{aligned} \mathbf{P}_{11}^* &\equiv \hat{\mathbf{P}}_1^*(\rho) e^{i\theta} + c.c.\,, \qquad \mathbf{P}_{12}^* \equiv \hat{\mathbf{P}}_1^*(\rho)\, ie^{i\theta} + c.c.\,, \\ \mathbf{P}_{21}^* &\equiv \hat{\mathbf{P}}_2^*(\rho) e^{2i\theta} + c.c.\,, \qquad \mathbf{P}_{22}^* \equiv \hat{\mathbf{P}}_2^*(\rho)\, i\, e^{2i\theta} + c.c.\,, \end{aligned} \tag{3.39}$$

where $\hat{\mathbf{P}}_m^*(\rho) = (\hat{\mathbf{\Phi}}_m^*(\rho), \hat{\mathbf{N}}_m^*(\rho))^t$ for $m = 1, 2$ is the radially symmetric solution on $0 < \rho < \infty$ satisfying

$$(\hat{\mathbf{P}}_m^*)_{\rho\rho} + \frac{1}{\rho}(\hat{\mathbf{P}}_m^*)_\rho - \frac{m^2}{\rho^2}\hat{\mathbf{P}}_m^* + \mathcal{M}^t \hat{\mathbf{P}}_m^* = 0\,, \quad \hat{\mathbf{P}}_m^* \to 0 \ \text{ as } \ \rho \to \infty. \tag{3.40}$$

Then, the four solvability conditions for (3.38b) give the four equations

$$\int_{\mathbb{R}^2} (\mathbf{P}_{ml}^*)^t \Big(\Lambda_1 - \mathcal{M}_1 - \mathcal{F} \Big) \mathbf{P}_0 \, d\mathbf{y} = 0\,, \qquad l, m = 1, 2\,. \tag{3.41}$$

We introduce the integrals J_{ml}, I_{ml}, and F_{ml}, defined by

$$J_{ml} = \int_{\mathbb{R}^2} (\mathbf{P}_{ml}^*)^t \Lambda_1 \mathbf{P}_0 \, d\mathbf{y}\,, \quad I_{ml} = \int_{\mathbb{R}^2} (\mathbf{P}_{ml}^*)^t \mathcal{M}_1 \mathbf{P}_0 \, d\mathbf{y}\,, \qquad F_{ml} = \int_{\mathbb{R}^2} (\mathbf{P}_{ml}^*)^t \mathcal{F} \mathbf{P}_0 \, d\mathbf{y}\,.$$

To calculate the integral I_{11} we write it as

$$\begin{aligned} I_{11} = \frac{1}{2} \int_{\mathbb{R}^2} & \Big(\hat{\mathbf{P}}_1^*(\rho) e^{i\theta} + c.c. \Big)^t \Big(g e^{i\theta} \hat{\mathcal{M}}_1 + c.c. \Big) \\ & \Big(A \hat{\mathbf{P}}_{01}(\rho) e^{i\theta} + B \hat{\mathbf{P}}_{02}(\rho) e^{2i\theta} + c.c. \Big) \, d\mathbf{y}\,, \\ = \frac{1}{2} \int_0^{2\pi} & (e^{i\theta} + e^{-i\theta})(g e^{i\theta} + \overline{g e^{i\theta}})(A e^{i\theta} + \overline{A e^{i\theta}})\, d\theta \int_0^\infty (\hat{\mathbf{P}}_1^*)^t \hat{\mathcal{M}}_1 \hat{\mathbf{P}}_{01} \rho \, d\rho \\ + \frac{1}{2} \int_0^{2\pi} & (e^{i\theta} + e^{-i\theta})(g e^{i\theta} + \overline{g e^{i\theta}})(B e^{2i\theta} + \overline{B e^{2i\theta}})\, d\theta \int_0^\infty (\hat{\mathbf{P}}_1^*)^t \hat{\mathcal{M}}_1 \hat{\mathbf{P}}_{02} \rho \, d\rho\,, \end{aligned}$$

where $\bar{g}$ is the complex conjugate of g. Since $\int_0^{2\pi} e^{ij\theta} d\theta = 0$ for any integer $j \neq 0$, only a constant integrand in the integral over θ gives a nonzero contribution to I_{11}. The other integrals are calculated similarly. In this way, we obtain

$$
\begin{aligned}
I_{11} &= 2\pi \mathrm{Re}(g\bar{B}) \int_0^\infty (\hat{\mathbf{P}}_1^*)^t \hat{\mathcal{M}}_1 \hat{\mathbf{P}}_{02} \rho d\rho \,, \\
I_{12} &= 2\pi \mathrm{Re}(ig\bar{B}) \int_0^\infty (\hat{\mathbf{P}}_1^*)^t \hat{\mathcal{M}}_1 \hat{\mathbf{P}}_{02} \rho \, d\rho \,, \\
I_{21} &= 2\pi \mathrm{Re}(gA) \int_0^\infty (\hat{\mathbf{P}}_2^*)^t \hat{\mathcal{M}}_1 \hat{\mathbf{P}}_{01} \rho \, d\rho \,, \\
I_{22} &= 2\pi \mathrm{Re}(-igA) \int_0^\infty (\hat{\mathbf{P}}_2^*)^t \hat{\mathcal{M}}_1 \hat{\mathbf{P}}_{01} \rho \, d\rho \,.
\end{aligned}
$$

In a similar way, we calculate

$$
\begin{aligned}
J_{11} &= 2\pi \mathrm{Re}(A)\lambda_1 \int_0^\infty \hat{\mathbf{\Phi}}_1^* \hat{\mathbf{\Phi}}_{01} \rho \, d\rho \,, \quad & J_{12} &= 2\pi \mathrm{Re}(i\bar{A})\lambda_1 \int_0^\infty \hat{\mathbf{\Phi}}_1^* \hat{\mathbf{\Phi}}_{01} \rho \, d\rho \,, \\
J_{21} &= 2\pi \mathrm{Re}(B)\lambda_1 \int_0^\infty \hat{\mathbf{\Phi}}_2^* \hat{\mathbf{\Phi}}_{02} \rho \, d\rho \,, \quad & J_{22} &= 2\pi \mathrm{Re}(i\bar{B})\lambda_1 \int_0^\infty \hat{\mathbf{\Phi}}_2^* \hat{\mathbf{\Phi}}_{02} \rho \, d\rho \,,
\end{aligned}
$$

and

$$
\begin{aligned}
F_{11} &= 2\pi \mathrm{Re}(g\bar{B})\gamma(S_j) \int_0^\infty (\hat{\mathbf{P}}_1^*)^t \hat{\mathcal{F}} \hat{\mathbf{P}}_{02} \rho \, d\rho \,, \\
F_{12} &= 2\pi \mathrm{Re}(ig\bar{B})\gamma(S_j) \int_0^\infty (\hat{\mathbf{P}}_1^*)^t \hat{\mathcal{F}} \hat{\mathbf{P}}_{02} \rho \, d\rho \,, \\
F_{21} &= 2\pi \mathrm{Re}(gA)\gamma(S_j) \int_0^\infty (\hat{\mathbf{P}}_2^*)^t \hat{\mathcal{F}} \hat{\mathbf{P}}_{01} \rho \, d\rho \,, \\
F_{22} &= 2\pi \mathrm{Re}(-igA)\gamma(S_j) \int_0^\infty (\hat{\mathbf{P}}_2^*)^t \hat{\mathcal{F}} \hat{\mathbf{P}}_{01} \rho \, d\rho \,.
\end{aligned}
$$

Substituting these formulae into the solvability conditions (3.41), we obtain

$$
\begin{aligned}
\lambda_1 \mathrm{Re}(A)\kappa_1 &= \mathrm{Re}(g\bar{B}) \,, \qquad & \lambda_1 \mathrm{Re}(i\bar{A})\kappa_1 &= \mathrm{Re}(ig\bar{B}) \,, \\
\lambda_1 \mathrm{Re}(B)\kappa_2 &= \mathrm{Re}(gA) \,, \qquad & \lambda_2 \mathrm{Re}(i\bar{B})\kappa_2 &= \mathrm{Re}(-igA) \,,
\end{aligned}
\tag{3.42}
$$

where the constants κ_1 and κ_2 are defined by

$$
\begin{aligned}
\kappa_1 &= \frac{\int_0^\infty \hat{\mathbf{\Phi}}_1^* \hat{\mathbf{\Phi}}_{01} \rho d\rho}{\int_0^\infty (\hat{\mathbf{P}}_1^*)^t [\hat{\mathcal{M}}_1 - \gamma(S_j)\hat{\mathcal{F}}] \hat{\mathbf{P}}_{02} \rho \, d\rho} \,, \\
\kappa_2 &= \frac{\int_0^\infty \hat{\mathbf{\Phi}}_2^* \hat{\mathbf{\Phi}}_{02} \rho d\rho}{\int_0^\infty (\hat{\mathbf{P}}_2^*)^t [\hat{\mathcal{M}}_1 - \gamma(S_j)\hat{\mathcal{F}}] \hat{\mathbf{P}}_{01} \rho \, d\rho} \,.
\end{aligned}
\tag{3.43}
$$

For $S_j = 4.31$, we calculate that $\gamma(S_j) \approx 1.703$. The solutions $\hat{\mathbf{P}}_m^*$ of the adjoint problem (3.40) are plotted in Fig. 5 of [56]. Numerical values for the constants κ_1 and κ_2 are also computed in §2.4 of [56] as $\kappa_1 = -0.926$ and $\kappa_2 = -1.800$.

We define $A = A_r + iA_i$, $B = B_r + iB_i$, and recall that $g = \alpha_1 - i\alpha_2$. Then, from (3.42) we obtain that

$$\begin{pmatrix} 0 & 0 & \frac{\alpha_1}{\kappa_1} & -\frac{\alpha_2}{\kappa_1} \\ 0 & 0 & \frac{\alpha_2}{\kappa_1} & \frac{\alpha_1}{\kappa_1} \\ \frac{\alpha_1}{\kappa_2} & \frac{\alpha_2}{\kappa_2} & 0 & 0 \\ -\frac{\alpha_2}{\kappa_2} & \frac{\alpha_1}{\kappa_2} & 0 & 0 \end{pmatrix} \begin{pmatrix} A_r \\ A_i \\ B_r \\ B_i \end{pmatrix} = \lambda_1 \begin{pmatrix} A_r \\ A_i \\ B_r \\ B_i \end{pmatrix} . \tag{3.44}$$

The eigenvalues λ_1 of this problem are degenerate and satisfy

$$\lambda_1^2 = \left(\frac{\alpha_1}{\kappa_1}\frac{\alpha_1}{\kappa_2} + \frac{\alpha_2}{\kappa_1}\frac{\alpha_2}{\kappa_2} \right) \pm i \left(\frac{\alpha_1}{\kappa_1}\frac{\alpha_2}{\kappa_2} - \frac{\alpha_1}{\kappa_2}\frac{\alpha_2}{\kappa_1} \right) = \frac{\alpha_1^2 + \alpha_2^2}{\kappa_1 \kappa_2} .$$

Since $\kappa_1 < 0$ and $\kappa_2 < 0$, the eigenvalues and eigenvectors are, respectively,

$$\lambda_1^{\pm} = \pm\frac{\sqrt{\alpha_1^2 + \alpha_2^2}}{\sqrt{\kappa_1 \kappa_2}} , \qquad \begin{pmatrix} B_r \\ B_i \end{pmatrix} = \frac{\lambda_1^{\pm} \kappa_1}{\alpha_1 \pm i\alpha_2} \begin{pmatrix} A_r \\ A_i \end{pmatrix} . \tag{3.45}$$

The unstable eigenvalue is λ_1^+ and its corresponding eigenvector is

$$\lambda_1^+ = \frac{\sqrt{\alpha_1^2 + \alpha_2^2}}{\sqrt{\kappa_1 \kappa_2}}, \qquad B = -\sqrt{\frac{\kappa_1}{\kappa_2}} \frac{\alpha_1 - i\alpha_2}{\sqrt{\alpha_1^2 + \alpha_2^2}} A = -\sqrt{\frac{\kappa_1}{\kappa_2}} \frac{g}{|g|} A.$$

Therefore, we conclude that the leading order eigenfunction $\mathbf{P}_0$ has the form

$$\mathbf{P}_0 = 2A\Big(\cos\theta \hat{\mathbf{P}}_{01} + \kappa \frac{\mathrm{Re}(g e^{2i\theta})}{|g|} \hat{\mathbf{P}}_{02} \Big) , \qquad \kappa = -\sqrt{\frac{\kappa_1}{\kappa_2}}.$$

The first term corresponds to the direction of motion of the j^{th} spot, which is (α_1, α_2), while the second term controls the direction of the splitting of the spot. Since $\kappa < 0$ this splitting direction is orthogonal to the direction of spot motion.

We remark that this analysis of the direction of spot-splitting is, largely, a local analysis based on a linearization of the core problem and the eigenvalue problem associated with the inner region. The only coupling to the other spots is through the determination of the source strength S_j from (3.8) and the vector $\vec{\alpha}_j$, defined in (3.29a), representing the "force" exerted by the other spots and the domain geometry. As a consequence, we conclude that for any spot that slightly exceeds the instability threshold condition $S_j = \Sigma_2$ it will split in a direction orthogonal to the direction of its motion.

3.5 Two-Spot Patterns in an Infinite Domain

We first illustrate our asymptotic theory for the simple case of a two-spot pattern in $\mathbb{R}^2$ when $D = O(1)$. For this infinite plane, the reduced-wave Green's function and its regular part are readily available. Therefore, for this infinite domain problem it is rather straightforward to explicitly determine the spot dynamics and to characterize the self-replication instability.

Without loss of generality, we assume that the centers of the two spots are at $\mathbf{x}_1 = (\alpha, 0)$ and $\mathbf{x}_2 = (-\alpha, 0)$ where $\alpha > 0$ and $\alpha \gg O(\varepsilon)$. In addition, by a coordinate re-scaling it is readily shown that we can set $D = 1$ without loss of generality. The reduced-wave Green's function for the infinite plane satisfies $\Delta G - G = -\delta(\mathbf{x} - \mathbf{x}_j)$, with $G \to 0$ as $|\mathbf{x}| \to \infty$. The solution is simply

$$G(\mathbf{x}; \mathbf{x}_j) = \frac{1}{2\pi} K_0 \left(|\mathbf{x} - \mathbf{x}_j| \right) ,$$

where $K_0(r)$ is the modified Bessel function of the second kind of order zero. The asymptotic behavior of $K_0(r)$ as $r \to 0$ is $K_0(r) \sim -(\ln r - \ln 2 + \gamma_e)$, where $\gamma_e \approx 0.5772$ is Euler's constant. Therefore, the entries of the Green's matrix, consisting of $G_{12} \equiv G(\mathbf{x}_1; \mathbf{x}_2)$ and its regular part $R_{jj} = R(\mathbf{x}_j; \mathbf{x}_j)$, are simply

$$G_{12} = G_{21} = \frac{1}{2\pi} K_0 \left(2\alpha \right) , \quad R_{11} = R_{22} = \frac{1}{2\pi} (\ln 2 - \gamma_e) .$$

Thus, the Green's matrix $\mathcal{G}$ in (3.12) is a symmetric circulant matrix. Consequently, it follows from (3.14) of Section 3.1, that there is a common source strength $S_c = S_1 = S_2$, which satisfies the scalar nonlinear algebraic equation

$$\mathcal{A} = S_c \left[1 + \nu (\ln 2 - \gamma_e) + \nu K_0 \left(2\alpha \right) \right] + \nu \, \chi(S_c) , \qquad \nu = -1/\ln \varepsilon . \quad (3.46)$$

From this equation, we now numerically determine the relationship between S_c, the half-distance α between the two spots on the x-axis, and the feed-rate parameter $\mathcal{A}$.

Experiment 3.2: Two spots in the infinite plane

We fix $\varepsilon = 0.02$ in the computational results below. In Fig. 3.4(a) we plot $\mathcal{A}$ versus S_c for three different values of α. From this plot we observe that the graph of $\mathcal{A}$ versus S_c has a fold point $\mathcal{A}_f$, which depends on α. This fold point $\mathcal{A}_f(\alpha)$ is shown in Fig. 3.4(b) by the dotted curve. The solid curve in Fig. 3.4(b) is the corresponding two-term asymptotic result for $\mathcal{A}_f$ obtained by expanding (3.46) in powers of ν. This result shows that a quasi-equilibrium two-spot pattern exists for a spot separation 2α only when the feed-rate parameter $\mathcal{A}$ is larger than the existence threshold $\mathcal{A}_f(\alpha)$, i.e. $\mathcal{A} > \mathcal{A}_f(\alpha)$.

Next, we discuss the possibility of self-replicating instabilities for an inter-spot separation of 2α. In Fig. 3.4(c), we plot S_c vs. α for $\mathcal{A} = 3.5$ (solid curve), $\mathcal{A} = 4.0$ (dashed curve) and $\mathcal{A} = 4.5$ (heavy solid curve). Notice that for a fixed $\mathcal{A} > \mathcal{A}_f$, there could be two solutions of S_c for a given α. As such, we only plot the large solution branch for S_c in this figure. This figure shows that for a fixed distance 2α between the spots, the source strength S_c is an increasing function of the feed-rate $\mathcal{A}$. In addition, for a fixed feed-rate $\mathcal{A}$, the source strength S_c increases as α increases. For the solid curve in Fig. 3.4(c) with $\mathcal{A} = 3.5$, the source strength S_c is always below the spot-replication threshold Σ_2, so that the spots never split for any inter-separation distance. Alternatively, the dashed curve for $\mathcal{A} = 4.0$ and the heavy solid curve for $\mathcal{A} = 4.5$ in Fig. 3.4(c) intersect the spot self-replication threshold $S_c = \Sigma_2$ at $\alpha \approx 1.81$ and $\alpha \approx 0.46$, respectively. This threshold initiates a spot-replication event.

In Fig. 3.4(d), we plot $\mathcal{A}$ vs. α corresponding to the different spot-deformation thresholds $S_c = \Sigma_2 \approx 4.31$ (solid curve), $S_c = \Sigma_3 \approx 5.44$ (dashed curve) and $S_c = \Sigma_4 \approx 6.14$ (heavy solid curve). For the solid curve in this figure, which corresponds to $S_c = \Sigma_2$, we observe that $\mathcal{A}$ decreases with α but asymptotes to its minimum value $\mathcal{A}_s = 3.98$ as $\alpha \to \infty$. This minimum value is obtained by setting $S_c = \Sigma_2$ and $K_0(2\alpha) \to 0$ in (3.46). We conclude that for any $\mathcal{A} > \mathcal{A}_s$, a two-spot pattern in an infinite domain will be linearly unstable to a peanut-splitting instability if the inter-spot separation distance 2α is taken to be sufficiently large.

Next we derive the ODE system that determines the slow dynamics of the two-spot pattern when $S_c < \Sigma_2$. A simple application of the general result in Principal Result 3.3 shows that

$$\alpha_c \equiv \frac{d\alpha}{d\varsigma} = -4\varepsilon^2 \gamma(S_c) S_c K_0'(2\alpha) \,, \quad \gamma(S_c) \equiv \frac{-2}{\int_0^\infty \phi^* V_0' \rho \, d\rho,} \,, \quad \varsigma = \varepsilon^2 t \,. \tag{3.47}$$

Since $K_0'(r) < 0$ for any $r > 0$ and $|K_0'(r)|$ a decreasing function of r, it follows that the two spots repel each other along the x-axis for all time and that their common speed $\alpha_c = |\frac{d\alpha}{d\varsigma}|$ is a decreasing function of inter-separation distance 2α. This is shown in Fig. 3.4(e) for three different values of $\mathcal{A}$. In Fig. 3.4(f) we plot the curve $\gamma(S_c)$ versus S_c used in the numerical computation of the ODE (3.47).

Since the two spots are repelling and S_c is a monotonically increasing

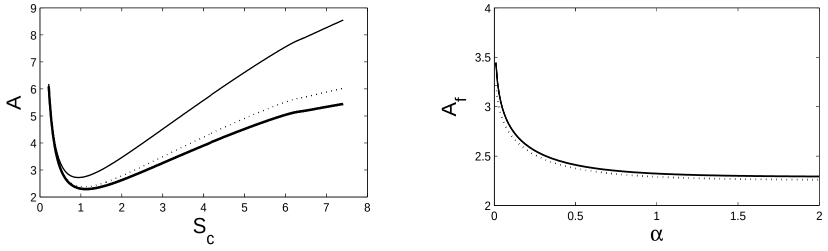

(a) $\mathcal{A}$ vs. S_c (b) $\mathcal{A}_f$ vs. α

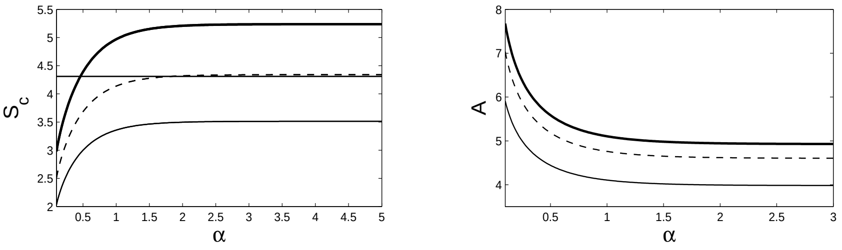

(c) S_c vs. α (d) $\mathcal{A}$ vs. α

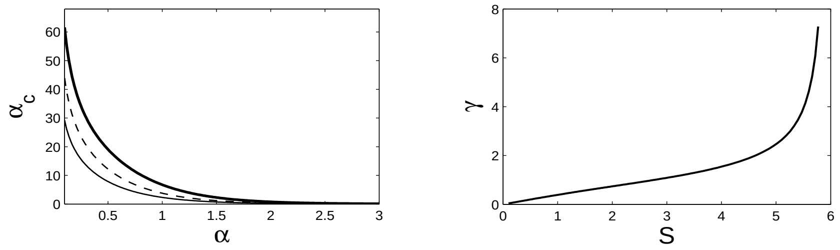

(e) α_c vs. α (f) γ vs. S

Figure 3.4: *Experiment 3.2: Two spots at* $(\pm\alpha, 0)$ *in the infinite plane, with* $\varepsilon = 0.02$. *(a)* $\mathcal{A}$ *vs.* S_c *for* $\alpha = 0.1$ *(solid curve),* $\alpha = 0.5$ *(dashed curve) and* $\alpha = 1.0$ *(heavy solid curve). (b) The fold point* $\mathcal{A}_f$ *vs.* α*; two-term asymptotic result (solid curve), and numerical result from* (3.46) *(dotted curve). (c)* S_c *vs.* α *for* $\mathcal{A} = 3.5$ *(solid curve),* $\mathcal{A} = 4.0$ *(dashed curve) and* $\mathcal{A} = 4.5$ *(heavy solid curve). (d)* $\mathcal{A}$ *vs.* α *with* $S_c = \Sigma_2$ *(solid curve),* $S_c = \Sigma_3$ *(dashed curve) and* $S_c = \Sigma_4$ *(heavy solid curve). (e)* α_c *vs.* α *for* $\mathcal{A} = 3.5$ *(solid curve),* $\mathcal{A} = 4.0$ *(dashed curve) and* $\mathcal{A} = 4.5$ *(heavy solid curve). (f)* γ *vs.* S *defined in the ODE* (3.47) .

function of α it follows that a dynamically triggered spot-replicating instability will occur when $\mathcal{A} > \mathcal{A}_s \approx 3.98$. In particular, suppose that $\mathcal{A} = 4.0$. Then, the graph of S_c versus α is shown by the dashed curve in Fig. 3.4(c). This curve shows that $S_c > \Sigma_2$ if and only if $\alpha \geq 1.81$. Now consider an initial two-spot quasi-equilibrium solution with $\alpha = 1$ at $t = 0$. For this initial value of α, $\mathcal{A}$ exceeds the existence threshold $\mathcal{A}_f$ of Fig. 3.4(b). Then, since the ODE (3.47) predicts that $\alpha \to \infty$ as $t \to \infty$, it follows that $\alpha = 1.81$ at some sufficiently long time $t = O(\varepsilon^{-2})$, which initiates the spot self-replication instability. Based on the theory in Section 3.2, the spots should split in a direction perpendicular to the x-axis. In summary, two spots on the infinite plane can readily undergo dynamically triggered spot self-replication events that are induced by their collective motion.

3.6 The Reduced-Wave and Neumann Green's Functions

In order to implement the asymptotic theory in the previous sections we require some detailed analytical results for the reduced-wave Green's function for a given domain. In addition, for $D = O(\nu^{-1}) \gg 1$, this Green's function can be approximated by the Neumann Green's function $G^{(N)}$, as was discussed in Section 3.1. In this section we give analytical formulae for both the reduced-wave and Neumann Green's functions for the unit disk and the rectangle for a given source point at $\mathbf{x_0}$.

3.6.1 Green's Function for a Unit Disk

Let Ω be the unit disk $\Omega = \{\mathbf{x} : |\mathbf{x}| \leq 1\}$. Introducing polar coordinates, $(x_0, y_0) = (\rho_0 \cos\theta_0, \rho_0 \sin\theta_0)$, the reduced-wave Green's function satisfies

$$G_{\rho\rho} + \frac{1}{\rho} G_\rho + \frac{1}{\rho^2} G_{\theta\theta} - \frac{1}{D} G = -\frac{1}{\rho}\, \delta(\rho - \rho_0)\delta(\theta - \theta_0)\,, \quad \text{in } \Omega\,, \tag{3.48}$$

with boundary conditions $G(\rho, \theta + 2\pi) = G(\rho, \theta)$ and $G_\rho(1, \theta) = 0$.

To determine G we extract the θ dependence in a complex Fourier series by introducing

$$G(\rho, \rho_0; \theta, \theta_0) = \frac{1}{2\pi} \sum_{n=-\infty}^{\infty} \tilde{G}_n(\rho, \rho_0; \theta_0) e^{-in\theta}\,, \tag{3.49}$$

so that

$$\tilde{G}_n(\rho, \rho_0; \theta_0) = \int_0^{2\pi} e^{in\theta} G(\rho, \rho_0; \theta, \theta_0)\, d\theta\,.$$

In the usual way, we derive from (3.48) that

$$\tilde{G}_{n\rho\rho} + \frac{1}{\rho}\tilde{G}_{n\rho} - \frac{n^2}{\rho^2}\tilde{G}_{n\theta\theta} - \frac{1}{D}\tilde{G}_n = -\frac{\delta(\rho-\rho_0)}{\rho}e^{in\theta_0}\,, \quad 0<\rho<1\,,$$

with boundary conditions

$$\tilde{G}_{n\rho}(1,\rho_0;\theta_0) = 0\,, \quad \tilde{G}_n(0,\rho_0;\theta_0) < \infty\,.$$

The solution to this problem is given by

$$\tilde{G}_n = \begin{cases} A_1 I_n\left(\frac{\rho}{\sqrt{D}}\right), & 0<\rho<\rho_0\,, \\ A_2\left[I_n\left(\frac{\rho}{\sqrt{D}}\right) - \frac{I_n'\left(\frac{1}{\sqrt{D}}\right)}{K_n'\left(\frac{1}{\sqrt{D}}\right)}K_n\left(\frac{\rho}{\sqrt{D}}\right)\right], & \rho_0<\rho<1\,, \end{cases} \tag{3.50}$$

where $I_n(r)$ and $K_n(r)$ are modified Bessel functions of the second kind of order n. In (3.50), the coefficients A_1 and A_2 are obtained by making $\tilde{G}_n$ continuous at ρ_0 and by requiring that the jump in the derivative of $\tilde{G}_n$ at ρ_0 is $[\tilde{G}_{n\rho}]_{\rho_0} = -\frac{e^{in\theta_0}}{\rho_0}$. Upon using the Wronskian determinant

$$K_n\left(\frac{\rho_0}{\sqrt{D}}\right)I_n'\left(\frac{\rho_0}{\sqrt{D}}\right) - K_n'\left(\frac{\rho_0}{\sqrt{D}}\right)I_n\left(\frac{\rho_0}{\sqrt{D}}\right) = \frac{\sqrt{D}}{\rho_0}\,,$$

we calculate A_1 and A_2 as

$$A_1 = -e^{in\theta_0}\left[\frac{K_n'\left(\frac{1}{\sqrt{D}}\right)}{I_n'\left(\frac{1}{\sqrt{D}}\right)}I_n\left(\frac{\rho_0}{\sqrt{D}}\right) - K_n\left(\frac{\rho_0}{\sqrt{D}}\right)\right]\,,$$

$$A_2 = -e^{in\theta_0}\,I_n\left(\frac{\rho_0}{\sqrt{D}}\right)\frac{K_n'\left(\frac{1}{\sqrt{D}}\right)}{I_n'\left(\frac{1}{\sqrt{D}}\right)}\,.$$

Upon substituting these expressions into (3.50), we obtain

$$\tilde{G}_n = \begin{cases} \left[K_n\left(\frac{\rho_0}{\sqrt{D}}\right) - \frac{K_n'\left(\frac{1}{\sqrt{D}}\right)}{I_n'\left(\frac{1}{\sqrt{D}}\right)}I_n\left(\frac{\rho_0}{\sqrt{D}}\right)\right]e^{in\theta_0}I_n\left(\frac{\rho}{\sqrt{D}}\right), & 0<\rho<\rho_0 \\ \left[K_n\left(\frac{\rho}{\sqrt{D}}\right) - \frac{K_n'\left(\frac{1}{\sqrt{D}}\right)}{I_n'\left(\frac{1}{\sqrt{D}}\right)}I_n\left(\frac{\rho}{\sqrt{D}}\right)\right]e^{in\theta_0}I_n\left(\frac{\rho_0}{\sqrt{D}}\right), & \rho_0<\rho<1. \end{cases} \tag{3.51}$$

Therefore, the Fourier expansion for the reduced-wave Green's function for (3.48) is

$$G(\rho,\rho_0;\theta,\theta_0) = \frac{1}{2\pi}\sum_{n=-\infty}^{\infty} e^{-in(\theta-\theta_0)}\mathcal{F}_n(\rho)\,, \qquad 0<\rho<\rho_0\,, \tag{3.52a}$$

$$\mathcal{F}_n(\rho) \equiv \left[K_n\left(\frac{\rho_0}{\sqrt{D}}\right) - \frac{K_n'\left(\frac{1}{\sqrt{D}}\right)}{I_n'\left(\frac{1}{\sqrt{D}}\right)} I_n\left(\frac{\rho_0}{\sqrt{D}}\right)\right] I_n\left(\frac{\rho}{\sqrt{D}}\right)\,. \tag{3.52b}$$

Alternatively, for the range $\rho_0 < \rho < 1$ we can simply interchange ρ and ρ_0 in (3.52). Next, we identify the free-space Green's function G_f, which is given by

$$G_f(\rho,\rho_0;\theta,\theta_0) = \frac{1}{2\pi}\sum_{n=-\infty}^{\infty} e^{-in(\theta-\theta_0)} K_n\left(\frac{\rho_0}{\sqrt{D}}\right) I_n\left(\frac{\rho}{\sqrt{D}}\right)\,, \quad 0<\rho<\rho_0\,. \tag{3.53}$$

For the range $\rho_0 < \rho < \infty$ we interchange ρ and ρ_0 in the formula above. Then, by the well-known addition formula

$$K_0\left(\frac{R}{\sqrt{D}}\right) = \sum_{n=-\infty}^{\infty} e^{-in(\theta-\theta_0)} K_n\left(\frac{\rho_0}{\sqrt{D}}\right) I_n\left(\frac{\rho}{\sqrt{D}}\right)\,, \tag{3.54}$$

with $R = \sqrt{\rho^2+\rho_0^2-2\rho\rho_0\cos(\theta-\theta_0)}$, we can decompose (3.52) as

$$G = \frac{1}{2\pi}K_0\left(\frac{R}{\sqrt{D}}\right) - \frac{1}{2\pi}\sum_{n=-\infty}^{\infty} e^{-in(\theta-\theta_0)} \frac{K_n'\left(\frac{1}{\sqrt{D}}\right)}{I_n'\left(\frac{1}{\sqrt{D}}\right)} I_n\left(\frac{\rho_0}{\sqrt{D}}\right) I_n\left(\frac{\rho}{\sqrt{D}}\right)\,. \tag{3.55}$$

In (3.55), the first term arises from the source at (ρ_0,θ_0), while the Fourier series term represents the effects of the boundary conditions. Since n is an integer, we can use $K_{-n}(z) = K_n(z)$ and $I_{-n}(z) = I_n(z)$, to further simplify (3.55) to

$$\begin{aligned} G = {} & \frac{1}{2\pi}K_0\left(\frac{R}{\sqrt{D}}\right) - \frac{1}{2\pi}\frac{K_0'\left(\frac{1}{\sqrt{D}}\right)}{I_0'\left(\frac{1}{\sqrt{D}}\right)} I_0\left(\frac{\rho_0}{\sqrt{D}}\right) I_0\left(\frac{\rho}{\sqrt{D}}\right) + \delta_M \\ & - \frac{1}{\pi}\sum_{n=1}^{M}\cos(n(\theta-\theta_0)) \frac{K_n'\left(\frac{1}{\sqrt{D}}\right)}{I_n'\left(\frac{1}{\sqrt{D}}\right)} I_n\left(\frac{\rho_0}{\sqrt{D}}\right) I_n\left(\frac{\rho}{\sqrt{D}}\right)\,. \end{aligned} \tag{3.56}$$

Since $K_n'\left(\frac{1}{\sqrt{D}}\right) < 0$, and $I_n'\left(\frac{1}{\sqrt{D}}\right) > 0$ for any integer $n \geq 0$, then δ_M is a small error term bounded by P_M, where

$$|\delta_M| \leq P_M \equiv -\sum_{n=M+1}^{\infty} \frac{K_n'\left(\frac{1}{\sqrt{D}}\right)}{I_n'\left(\frac{1}{\sqrt{D}}\right)} I_n\left(\frac{\rho_0}{\sqrt{D}}\right) I_n\left(\frac{\rho}{\sqrt{D}}\right) .$$

The expression (3.56) for G is the one used in the numerical simulations in Section 3.7. From (3.56) we can readily extract the regular part R of the reduced-wave Green's function. The gradients of R and G that are needed in Principal Result 3.3 to determine the motion of a collection of spots is determined numerically from (3.56).

In Table 3.1, we give the number M of Fourier terms in (3.56) that are required in order to calculate the Green's function within a tolerance of 10^{-8}. The series for P_M is found to converge fairly fast, especially when the spots are not close to the boundary of the unit circle and D is not too large.

ρ_0	ρ	M	P_M
0.8	0.8	31	8.1737e-009
0.8	0.5	16	6.7405e-009
0.8	0.2	8	9.5562e-009
0.5	0.5	11	4.3285e-009

Table 3.1: The number of Fourier terms needed to determine the reduced-wave Green's function within a tolerance 10^{-8} for $D = 1$.

3.6.2 Neumann Green's Function for a Unit Disk

Next for $D = O(\nu^{-1}) \gg O(1)$, we recall from (3.15) that the reduced-wave Green's function and its regular part can be approximated by the Neumann Green's function $G^{(N)}(\mathbf{x}; \mathbf{x}_0)$ and its regular part $R^{(N)}(\mathbf{x}; \mathbf{x}_0)$ satisfying (3.16). From equation (4.3) of [51], this Neumann Green's function and its regular part for the unit disk are given in terms of Cartesian coordinates by

$$G^{(N)} = \frac{1}{2\pi}\left(-\ln|\mathbf{x}-\mathbf{x}_0| - \ln\left|\mathbf{x}|\mathbf{x}_0| - \frac{\mathbf{x}_0}{|\mathbf{x}_0|}\right| + \frac{1}{2}(|\mathbf{x}|^2 + |\mathbf{x}_0|^2) - \frac{3}{4}\right)\,, \tag{3.57}$$

$$R^{(N)} = \frac{1}{2\pi}\left(-\ln\left|\mathbf{x}_0|\mathbf{x}_0| - \frac{\mathbf{x}_0}{|\mathbf{x}_0|}\right| + |\mathbf{x}_0|^2 - \frac{3}{4}\right)\,. \tag{3.58}$$

The gradients of these quantities can be obtained by a simple calculation as

$$\nabla G^{(N)}(\mathbf{x};\mathbf{x}_0) = -\frac{1}{2\pi}\left[-\frac{\mathbf{x}-\mathbf{x}_0}{|\mathbf{x}-\mathbf{x}_0|^2} + \frac{|\mathbf{x}_0|^2}{\bar{\mathbf{x}}|\mathbf{x}_0|^2 - \bar{\mathbf{x}}_0} - \mathbf{x}\right]\,,$$

$$\nabla R^{(N)}(\mathbf{x}_0;\mathbf{x}_0) = \frac{1}{2\pi}\left(\frac{2-|\mathbf{x}_0|^2}{1-|\mathbf{x}_0|^2}\right)\mathbf{x}_0\,.$$

These results allow us to explicitly determine the dynamics of a collection of spots when D is large, as described in Principal Result 3.3.

3.6.3 Green's Function for a Rectangle

Next, we calculate the reduced-wave Green's function $G(x, y; x_0, y_0)$ in the rectangular domain $\Omega = [0, L] \times [0, d]$. The free-space Green's function G_f is given by

$$G_f = \frac{1}{2\pi} K_0\left(\frac{|\mathbf{x}-\mathbf{x_0}|}{\sqrt{D}}\right)\,.$$

Therefore, using the method of images, we can write the Green's function satisfying (3.6) as

$$G(\mathbf{x};\mathbf{x_0}) = \frac{1}{2\pi}\sum_{n=-\infty}^{\infty}\sum_{m=-\infty}^{\infty}\sum_{l=1}^{4} K_0\left(\frac{|\mathbf{x}-\mathbf{x}_{mn}^{(l)}|}{\sqrt{D}}\right)\,, \tag{3.59}$$

where

$$\mathbf{x}_{mn}^{(1)} = (x_0 + 2nL, y_0 + 2md)\,, \quad \mathbf{x}_{mn}^{(2)} = (-x_0 + 2nL, y_0 + 2md)\,,$$
$$\mathbf{x}_{mn}^{(3)} = (x_0 + 2nL, -y_0 + 2md)\,, \quad \mathbf{x}_{mn}^{(4)} = (-x_0 + 2nL, -y_0 + 2md)\,.$$

The modified Bessel function $K_0(r)$ decays exponentially as $r \to \infty$. For example when $r > 22$, then $K_0(r) < 7.5\times 10^{-11}$. Therefore, provided that D is not too large, the infinite series in (3.59) converges fairly fast. The regular part of the reduced-wave Green's function together with the gradients of G and R, as required in Principal Result 3.3, are readily evaluated numerically from (3.59).

3.6.4 Neumann Green's Function for a Rectangle

If $D = O(\nu^{-1})$ is large, we can approximate the reduced-wave Green's function and its regular part by the corresponding Neumann Green's function $G^{(N)}$ and its regular part $R^{(N)}$, as given by the expansion in (3.15). This latter Green's function was given analytically in formula (4.13) of [56] as

$$G^{(N)}(\mathbf{x};\mathbf{x}_0) = -\frac{1}{2\pi}\ln|\mathbf{x}-\mathbf{x}_0| + R^{(N)}(\mathbf{x};\mathbf{x}_0)\,,$$

where $R^{(N)}(\mathbf{x};\mathbf{x}_0)$ is given explicitly by

$$\begin{aligned} R^{(N)}(\mathbf{x};\mathbf{x}_0) = -\frac{1}{2\pi}\sum_{n=0}^{\infty} \ln(&|1-q^n z_{+,+}||1-q^n z_{+,-}||1-q^n z_{-,+}||1-q^n \zeta_{+,+}| \\ &|1-q^n \zeta_{+,-}||1-q^n \zeta_{-,+}||1-q^n \zeta_{-,-}|) + \frac{L}{d}\left[\frac{1}{3} - \frac{x}{L} + \frac{1}{2}\left(\frac{x_0^2+x^2}{L^2}\right)\right] \\ &- \frac{1}{2\pi}\ln\left(\frac{|1-z_{-,-}|}{|r_{-,-}|}\right) - \frac{1}{2\pi}\sum_{n=1}^{\infty}\ln|1-q^n z_{-,-}|\,. \end{aligned} \tag{3.60}$$

Here points in the rectangle are written as complex coordinates. In (3.60), $q \equiv e^{-2L\pi/d}$, while $z_{\pm,\pm}$ and $\zeta_{\pm,\pm}$ are given by

$$\begin{aligned} z_{+,\pm} &\equiv \exp(\mu(-|x+x_0| + i(y \pm y_0))/2)\,, \\ z_{-,\pm} &\equiv \exp(\mu(-|x-x_0| + i(y \pm y_0))/2)\,, \\ \zeta_{+,\pm} &\equiv \exp(\mu(|x+x_0| - 2L + i(y \pm y_0))/2)\,, \\ \zeta_{-,\pm} &\equiv \exp(\mu(|x-x_0| - 2L + i(y \pm y_0))/2)\,, \end{aligned}$$

where μ is defined by $\mu = 2\pi/d$.

3.7 Comparison of Asymptotic Results and Full Numerical Results

In this section we compare our asymptotic results for spot dynamics, the spot self-replication threshold, and the equilibrium positions of spot patterns with full numerical simulations of (1.7). The comparisons are made for the unit disk and square, since for these two specific domains the required Green's functions are analytically known as given in the previous section.

In all of the numerical simulations below we have set $\varepsilon = 0.02$ so that $\nu = -1/\ln\varepsilon = 0.2556$. In each numerical experiment, we first fix the parameters

$\mathcal{A}$ and D. Then, for an initial configuration of spot locations $(\mathbf{x}_1, \ldots, \mathbf{x}_k)$, we compute the source strengths $(S_1, \ldots, S_k)$ from the nonlinear algebraic system (3.8). The initial condition for the full numerical simulations is taken to be the quasi-equilibrium solution (3.9) with the values for $V_j(0)$ as plotted in Fig. 3.1(b), corresponding to the computed values of S_j. Since this initial condition provides a decent, but not sufficiently precise, initial $k-$spot pattern, we only begin to track the spot locations from the full numerical simulations after the completion of a short transient period. To numerically identify the locations of the spots at any time, we determine all local maxima of the computed solution v by identifying the maximal grid values. This simple procedure is done since it is expensive to interpolate the grid values to obtain more accurate spot locations every time step. In this way, the trajectories of the spots are obtained from the full numerical results, and are then compared with the asymptotic dynamics of the spots as predicted by Principal Result 3.3.

3.7.1 The Unit Square

In this subsection, we consider the unit square domain $\Omega = [0, 1] \times [0, 1]$. The numerical simulations in this domain are done by solving (1.7) using the PDE solver VLUGR (cf. [7]), with a minimum step size 0.005. In each of the experiments below, we plot the contour map of the numerical solution v in a gray-scale form. The bright (white) regions correspond to the spot regions where v has a large amplitude, while the dark region is where v is asymptotically zero.

Experiment 3.3: A three-spot pattern: Slowly drifting spots

Let $\mathcal{A} = 20$ and $D = 1$, and consider an initial three-spot pattern with spots equally spaced on a ring of radius $r = 0.2$ centered at $(0.5, 0.5)$. The initial coordinates for the spots locations are at x_j, y_j, as given in Table 3.2. For this pattern, the Green's matrix $\mathcal{G}$ is not strictly circulant, but from (3.12) we compute that all three spots share a common source strength $S_c \approx 3.71$. Since $S_c < \Sigma_2$, we predict that there is no spot self-replication initiated at $t = 0$. In Fig. 3.5 we plot v at $t = 1, 21, 106, 581$, where we observe that all three spots drift outwards, and approach equilibrium locations x_{jn}, y_{jn} for $j = 1, \ldots, 3$ after a sufficiently long time. During this evolution, the source strengths never exceed the threshold Σ_2, and so there is no triggered dynamical spot-replication instability.

In Fig. 3.6 the solid curves are the spot trajectories obtained from the asymptotic result of Principal Result 3.3. The green, blue, and red curves, in this figure correspond, respectively, to the 1^{st}, 2^{nd}, and 3^{rd} spots. Since the initial locations of the 1^{st} and 2^{nd} spots are exactly symmetric, it follows that $G_{13} = G_{23}$, $R_{11} = R_{22}$, and $G_{12} = G_{21}$ in the Green's matrix. Therefore, from Principal Result 3.3, these two spots move at the same speed and their trajectories in the $x-$direction exactly overlap, as plotted by the green curve in Fig. 3.6(a). The spot locations as predicted from the full numerical solution are indicated by circles in Fig. 3.6. We observe that the asymptotic and numerical results for the spot dynamics agree very closely, which confirms that the asymptotic result in Principal Result 3.3 closely predicts the slow evolution of spots when there is no spot self-replication.

In addition, from the asymptotic result in Principal Result 3.4, we calculate the equilibrium location x_{je}, y_{je} and the equilibrium source strength S_{je} for $j = 1, \ldots, 3$. These values are given in Table 3.2, and our equilibrium result is found to closely predict the final equilibrium state x_{jn}, y_{jn}, S_{jn} obtained by numerically computing solutions to the full system (1.7) for a sufficiently long time.

j	x_j	y_j	S_j	$V_j(0)$	x_{jn}	y_{jn}	S_{jn}	x_{je}	y_{je}	S_{je}
1	0.40	0.67	3.71	34.2	0.33	0.77	3.68	0.33	0.77	3.68
2	0.40	0.33	3.71	34.2	0.33	0.23	3.68	0.33	0.23	3.68
3	0.70	0.50	3.71	34.2	0.79	0.50	3.95	0.79	0.50	3.95

Table 3.2: Data for Experiment 3.3: The columns of x_j, y_j, S_j and $V_j(0)$ correspond to the initial condition. The remaining data is with regards to the asymptotic and numerical results for the equilibrium state.

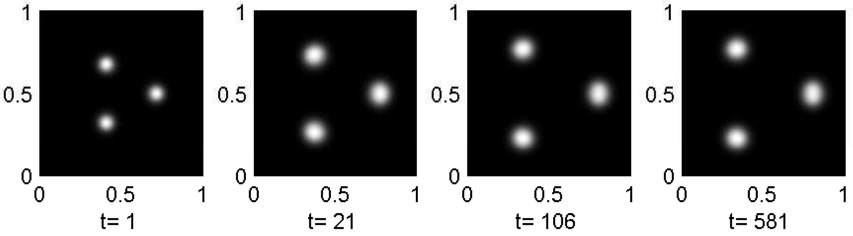

Figure 3.5: *Experiment 3.3: Fix* $\mathcal{A} = 20$ *and* $D = 1$*, and consider a three-spot initial pattern with spots equally spaced on a ring of radius* $r = 0.2$ *centered at* $(0.5, 0.5)$*. The initial common source strength is* $S_c = 3.71$*, as given in Table. 3.2. The numerical solution* v *is shown at* $t = 1, 21, 106, 581$*, and all spots drift slowly outwards.*

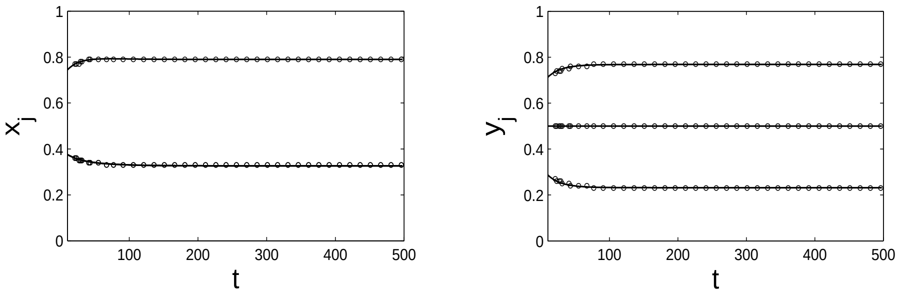

(a) x_j vs. t (b) y_j vs. t

Figure 3.6: *Experiment 3.3: Fix* $\mathcal{A} = 20$ *and* $D = 1$. *We compare the dynamics of a* $3-$*spot pattern (solid curves) with full numerical results (discrete markers) starting from* $t = 10$. *(a)* x_j *vs.* t*; (b)* y_j *vs.* t.

Experiment 3.4: A three-spot pattern: Spot-splitting and dynamics after splitting

We fix $\mathcal{A} = 20$ and $D = 1$, and consider an initial three-spot pattern on a ring of radius $r = 0.3$ centered at $(0.4, 0.4)$. Note that this experiment has the same parameters as in the previous experiment, except now the initial spot configuration is different. The initial data are given on the left side of Table 3.3. Since the source strength for the 3^{rd} spot now exceeds the spot-splitting threshold, i.e. $S_3 > \Sigma_2$, the asymptotic theory predicts that the 3^{rd} spot will undergo splitting beginning at $t = 0$. In Fig. 3.7, we plot the numerical solution v at $t = 1, 10, 31, 46,\ 61, 91, 121, 421$. From this figure we observe that the 3^{rd} spot (the brightest one at $t = 1$) deforms into a peanut shape at $t = 31$, and then splits into two spots at $t = 46$ in a direction perpendicular to its motion. Subsequently, the four spots interact and slowly drift to a symmetric four-spot equilibrium state when $t = 421$.

After the splitting event, we use the new $4-$spot pattern x_{jt}, y_{jt} for $j = 1, \ldots, 4$ at $t = 61$, as given in Table 3.3, as the initial conditions for the asymptotic ODE's in Principal Result 3.3. At $t = 61$, the source strengths $S_{1t}, \cdots, S_{4t}$ are below the splitting threshold, and so there is no further spot-splitting at this time. In Fig. 3.8, the subsequent asymptotic trajectories of the spots for $t \geq 61$ are shown by the solid curves. The $x-$coordinates of the 1^{st} and 2^{nd} spots, as well as the 3^{rd} and 4^{th} spots, essentially overlap in Fig. 3.8(b), as a result of their almost symmetric locations. The discrete markers on the spot trajectory curves in Fig. 3.8 are the full numerical results as computed from the GS model (1.7). From this figure, we observe that there is a very close agreement between the asymptotic and full numerical results for the dynamics. Thus, Principal Result 3.3 can also be used to predict the motion of a collection of spots after a spot self-replication event.

From Principal Result 3.4, we calculate the asymptotic result for the symmetric equilibrium locations x_{je}, y_{je} and the equilibrium source strengths S_{je}, for $j = 1, \ldots, 4$. These results are given in Table. 3.3, and compare almost exactly with the results from the full numerical simulations at $t = 421$ (not shown).

j	x_j	y_j	S_j	$V_j(0)$	x_{jt}	y_{jt}	S_{jt}	x_{je}	y_{je}	S_{je}
1	0.25	0.66	4.05	32.54	0.30	0.75	3.44	0.25	0.75	2.87
2	0.25	0.14	2.37	35.48	0.28	0.20	3.01	0.25	0.25	2.87
3	0.70	0.40	4.79	27.65	0.76	0.36	2.40	0.75	0.25	2.87
4	-	-	-	-	0.77	0.59	2.55	0.75	0.75	2.87

Table 3.3: Data for Experiment 3.4: The columns of x_j, y_j, S_j and $V_j(0)$ correspond to the initial condition. The data x_{jt}, y_{jt}, and S_{jt} correspond to the initial conditions used for the asymptotic dynamics at $t = 61$ after the spot-splitting event. The final columns are the equilibrium results for the 4-spot pattern obtained from the asymptotic theory.

Experiment 3.5: An asymmetric four-spot pattern

We fix $\mathcal{A} = 30$ and $D = 1$, and consider an initial $4-$spot pattern with equally spaced spots on a ring of radius 0.2 centered at $(0.6, 0.6)$. The initial spot locations x_j, y_j for $j = 1, \ldots, 4$ and initial source strengths are given on the left side of Table 3.4. For this case, the two source strengths S_3 and S_4 satisfy $S_3 > \Sigma_2$ and $S_4 > \Sigma_2$, so that our asymptotic theory predicts that the 3^{rd} and 4^{th} spots undergo spot-splitting events starting at $t = 0$. The full numerical results for this pattern are given in Fig. 3.9, where we observe that the 3^{rd} and 4^{th} spots split in a direction perpendicular to their motion. The resulting $6-$spot pattern, with initial locations x_{jt}, y_{jt} for $j = 1, \ldots, 6$ at $t = 21$, as given in Table 3.4, are used as initial conditions for the asymptotic ODE's in Principal Result 3.3. These six spots evolve outwards as t increases and eventually approach their equilibrium states x_{je}, y_{je}, and S_{je}, for $j = 1, \ldots, 6$, as given in Table 3.4, when $t = 581$. The asymptotic result obtained from Principal Result 3.4 for the $6-$spot equilibrium state is found to compare very favorably with the full numerical

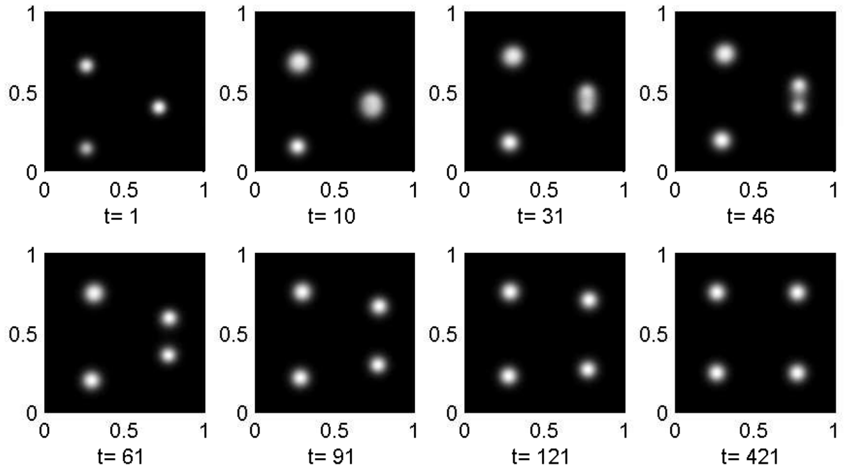

Figure 3.7: *Experiment 3.4: Fix* $\mathcal{A} = 20$ *and* $D = 1$*, and consider a three-spot initial pattern with spots equally spaced on a ring of radius* $r = 0.3$ *centered at* $(0.4, 0.4)$*. The initial source strengths* S_j *for* $j = 1, \ldots, 3$ *are given in Table. 3.3, for which* $S_3 > \Sigma_2$*. We plot the full numerical solution* v *as time evolves, and observe that the* 3^{rd} *spot undergoes self-replication. Subsequently, all four spots drift slowly towards a symmetric equilibrium* $4-$*spot pattern.*

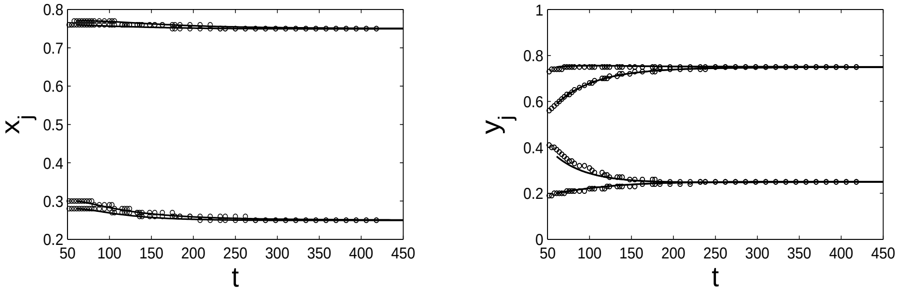

(a) x_j vs. t

(b) y_j vs. t

Figure 3.8: *Experiment 3.4: Fix* $\mathcal{A} = 20$ *and* $D = 1$*. Starting from* $t = 61$ *after the spot-replication event, we compare the dynamics of the* $4-$*spot pattern from asymptotic analysis (solid curves) with full numerical results (discrete markers). (a)* x_j *vs. t; (b)* y_j *vs. t.*

results at $t = 581$. We remark that this parameter set corresponds to the numerical experiment given in Chapter 1 in Fig. 1.4.

A very favorable comparison of analytical (solid curves) and full numerical results (discrete markers) for the spot locations after $t = 21$ is shown in Fig. 3.10. This agreement further validates our main asymptotic result in Principal Result 3.3.

j	x_j	y_j	S_j	V_j	x_{jt}	y_{jt}	S_{jt}	x_{je}	y_{je}	S_{je}
1	0.80	0.60	2.82	36.21	0.84	0.58	3.13	0.83	0.61	2.91
2	0.60	0.80	2.82	36.21	0.58	0.84	3.13	0.61	0.83	2.91
3	0.40	0.60	5.69	19.07	0.25	0.49	2.93	0.17	0.39	2.91
4	0.60	0.40	5.69	19.07	0.26	0.66	2.73	0.21	0.79	3.07
5	-	-	-	-	0.49	0.25	2.93	0.39	0.17	2.91
6	-	-	-	-	0.66	0.26	2.73	0.79	0.21	3.07

Table 3.4: Data for Experiment 3.5: The columns of x_j, y_j, S_j and $V_j(0)$ correspond to the initial condition. The data x_{jt}, y_{jt}, and S_{jt} correspond to the initial conditions used for the asymptotic dynamics at $t = 21$ after the two spot-splitting events. The final columns are the equilibrium results for the 6-spot pattern.

3.7.2 The Unit Disk

In this subsection we compare results from our asymptotic theory for spot patterns in the unit disk $\Omega = \{\mathbf{x} : |\mathbf{x}| \leq 1\}$, with corresponding full numerical results. For the unit disk, numerical solutions to the GS model (1.7) are computed by using the finite element code developed by W. Sun in [50].

We first consider the special case when k spots are equally distributed on a ring of radius r centered at the origin of the unit disk. The centers of the spots are at

$$\mathbf{x}_j = re^{2\pi ij/k}, \quad j = 1, 2, \cdots, k,$$

where $i = \sqrt{-1}$. For this symmetric arrangement of spots, the Green's matrix in (3.12) is circulant and is a function of the ring radius r. Hence, it follows that $\mathcal{G}\mathbf{e} = \theta\mathbf{e}$ with $\mathbf{e} = (1, \ldots, 1)^t$, where $\theta = p_k(r)/k$ and $p_k(r)$ is defined by $p_k(r) \equiv \sum_{i=1}^{k} \sum_{j=1}^{k} \mathcal{G}_{ij}$. Since the Green's matrix $\mathcal{G}$ is circulant, the source strengths S_j for $j = 1, \ldots, k$ have a common value S_c. From (3.14) of Section §3.1, it follows that the source strength S_c satisfies the

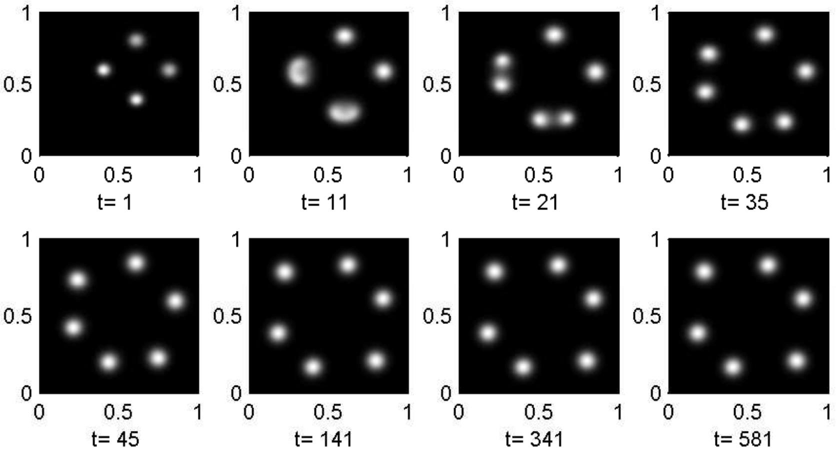

Figure 3.9: *Experiment 3.5: Fix* $\mathcal{A} = 30$ *and* $D = 1$, *and consider a four-spot initial pattern with spots equally spaced on a ring of radius* $r = 0.2$ *centered at* $(0.6, 0.6)$. *The initial source strengths* S_j *for* $j = 1, \ldots, 4$ *are given in Table 3.4, for which* $S_3 > \Sigma_2$ *and* $S_4 > \Sigma_2$. *We plot the full numerical solution* v *as time evolves, and observe that the* 3^{rd} *and* 4^{th} *spots undergo self-replication. Subsequently, all six spots move towards a symmetric* $6-$*spot equilibrium pattern.*

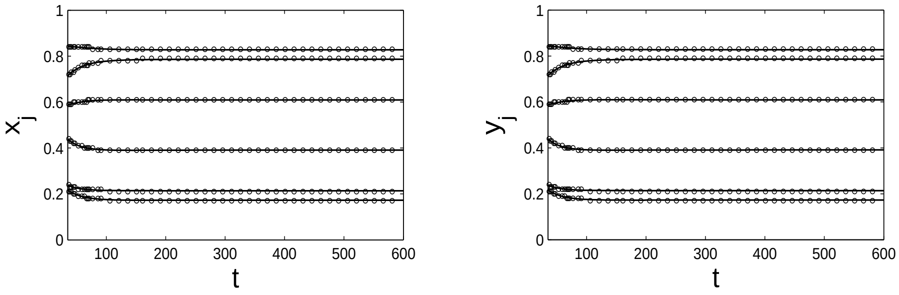

(a) x_j vs. t

(b) y_j vs. t

Figure 3.10: *Experiment 3.5: Fix* $\mathcal{A} = 30$ *and* $D = 1$. *Starting from* $t = 21$ *after the two spot-replication events, we compare the asymptotic dynamics of the* $6-$*spot (solid curves) with full numerical results (discrete markers). (a)* x_j *vs.* t*; (b)* y_j *vs.* t*.*

scalar nonlinear algebraic equation

$$\mathcal{A} = S_c \left(1 + \frac{2\pi\nu}{k} p_k(r) \right) + \nu\chi(S_c) \,. \tag{3.61}$$

To determine the dynamics of the k spots, we calculate $\vec{\alpha}$ in (3.29b) as

$$\vec{\alpha}_j = 2\pi \frac{S_c}{k} \nabla F(\mathbf{x}_1, \ldots, \mathbf{x}_k) \,, \qquad \nabla F(\mathbf{x}_1, \cdots, \mathbf{x}_k) = p_k'(r)\, e^{2\pi i j/k} \,.$$

Then, the dynamics (3.35) of Principal Result 3.3 is reduced to an ODE for the ring radius $r(t)$, given by

$$\frac{dr}{dt} = -\frac{2\pi\varepsilon^2}{k} \gamma(S_c) S_c\, p_k'(r) \,. \tag{3.62}$$

Therefore, we predict that the k spots remain equally distributed on a slowly evolving ring.

The function $p_k(r) \equiv \sum_{i=1}^{k} \sum_{j=1}^{k} \mathcal{G}_{ij}$ cannot be calculated analytically when G is the reduced-wave Green's function. Instead, we calculate it numerically from the explicit form for G given in (3.56). However, for $D \gg 1$, we can analytically calculate a two-term expansion for $p_k(r)$ in terms of D by using the two-term expansion (3.15) for the reduced-wave Green's function in terms of the Neumann Green's function, together with the simple explicit form for the Neumann Green's function in (3.58). We obtain for $D \gg 1$ that $p_k(r) \sim k^2 D/|\Omega| + \sum_{i=1}^{k} \sum_{j=1}^{k} \mathcal{G}_{ij}^{(N)}$, where the double sum here was calculated in Proposition 4.3 of [51]. In this way, for $D \gg 1$, we obtain that

$$p_k(r) \sim \frac{k^2 D}{\pi} + \frac{1}{2\pi} \left[-k \ln(k r^{k-1}) - k \ln(1 - r^{2k}) + r^2 k^2 - \frac{3}{4} k^2 \right] \,. \tag{3.63}$$

For $D \gg 1$, the equilibrium ring radius r_e satisfies $p_k^{'}(r) = 0$, which yields the transcendental equation

$$\frac{k-1}{2k} - r^2 = \frac{r^{2k}}{1 - r^{2k}} \,.$$

It is readily shown that there is only one root r_e to this equation for any $k \geq 2$ in the interval $r \in (0,1)$. Hence, for $D \gg 1$, there is unique equilibrium ring radius for k spots uniformly distributed on a ring. It is also readily shown from (3.63) that $p_k^{''}(r_e) > 0$. Hence, for $D \gg 1$, $p_k(r)$ has a minimum at the equilibrium radius r_e, so that r_e is a stable equilibrium point for the ODE

(3.62) when $D \gg 1$. From (3.61), this condition also implies that $S_c(r)$ has a maximum value at $r = r_e$ when $D \gg 1$.

In Fig. 3.11(a), we fix $D = 3.912$ and plot the source strength S_c as a function of the ring radius r with $k = 3$, $\mathcal{A} = 30$ (dotted curve), $k = 4$, $\mathcal{A} = 40$ (solid curve) and $k = 5$, $\mathcal{A} = 48$ (heavy solid curve). For these three patterns, the equilibrium states are respectively $(r_{e1}, S_{ce1}) = (0.55, 4.57)$, $(r_{e2}, S_{ce2}) = (0.60, 4.70)$, and $(r_{e3}, S_{ce3}) = (0.63, 4.58)$, which are marked by the solid circles in this figure. The square markers correspond to the spot-replicating threshold $\Sigma_2 \approx 4.31$, which occurs at $r_{s1} = 0.17$, $r_{s2} = 0.14$, and $r_{s3} = 0.22$, respectively. Any portion of these curves above the square markers correspond to ring radii where simultaneous spot self-replication is predicted to occur.

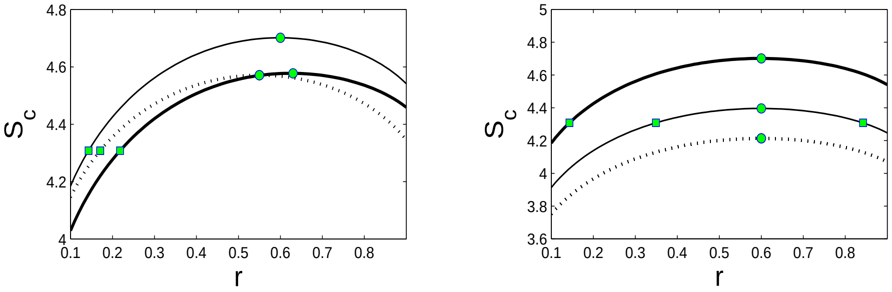

(a) S_c vs. r

(b) S_c vs. r

Figure 3.11: *Fix* $D = 3.912$. *(a)* S_c *vs.* r *with* $k = 3$, $\mathcal{A} = 30$ *(dotted curve),* $k = 4$, $\mathcal{A} = 40$ *(solid curve) and* $k = 5$, $\mathcal{A} = 48$ *(heavy solid curve). (b) Fix* $k = 4$, *we plot* S_c *vs.* r *with* $\mathcal{A} = 36$ *(dotted curve),* $\mathcal{A} = 37.5$ *(solid curve), and* $\mathcal{A} = 40$ *(heavy solid curve). The square markers indicate spot-splitting thresholds, and the solid circles mark the equilibrium states.*

In Fig. 3.11(b), we fix $k = 4$ and $D = 3.912$ and plot S_c vs. r with $\mathcal{A} = 36$ (dotted curve), $\mathcal{A} = 37.5$ (solid curve), and $\mathcal{A} = 40$ (heavy solid curve). The equilibria are at $(r_{e4}, S_{ce4}) = (0.60, 4.21)$, $(r_{e5}, S_{ce5}) = (0.60, 4.40)$ and $(r_{e2}, S_{ce2}) = (0.60, 4.70)$, respectively. In this figure we mark the spot-replicating thresholds for each case by the square markers. Note that for k spots on a ring, the maximum value of the source strength S_c is attained at the equilibrium location. Therefore, for $\mathcal{A} = 36$ and $k = 4$, since the source strength at the equilibrium state is $S_{ce5} = 4.21$, which is below the splitting threshold $\Sigma_2 \approx 4.31$, this 4-spot pattern is always stable to spot-splitting for all values of the ring radius. In contrast, on the solid curve for $\mathcal{A} = 37.5$ and

$k = 4$ if the ring radius is in the interval between the two square markers, i.e. $0.35 < r < 0.84$, we predict that all four spots will split. From the heavy solid curve for $\mathcal{A} = 40$ and $k = 4$ in Fig. 3.11(b), we predict that the four spots will split simultaneously when $r > r_{s2} = 0.14$. We now confirm this prediction with full numerical results.

Experiment 3.6: One ring pattern with $D \gg O(1)$: Spot splitting

We fix the parameters as $\mathcal{A} = 40$ and $D = 3.912$ and consider an initial 4−spot pattern with equally spaced spots lying on an initial ring of radius $r = 0.5 > r_{s2}$. Since the initial common source strength for this pattern is $S_c = 4.69$, as obtained from (3.61), we predict that all four spots will begin to split simultaneously at $t = 0$. The full numerical solution v at $t = 4.6, 70, 93, 381$, computed from the GS model (1.7), is plotted in Fig. 3.12. The numerical computations show that the four spots undergo spot-splitting in the direction perpendicular to their motion, and generate a pattern of eight equally spaced spots on a ring. This confirms our prediction based on the asymptotic analysis.

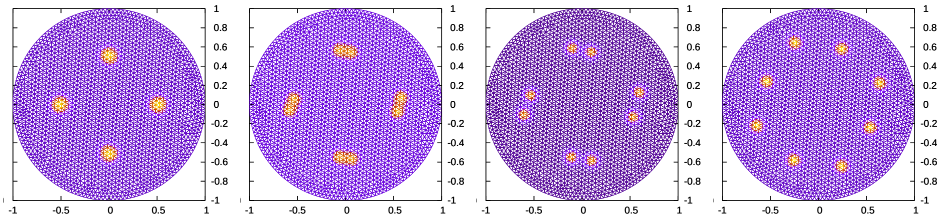

Figure 3.12: *Experiment 3.6: Fix* $D = 3.912$, $\mathcal{A} = 40.0$. *We start from an initial* 4*-spot pattern with spots equally spaced on a ring of radius* $r = 0.5$. *The common source strength is* $S_c = 4.69$. *We plot the solution* v *at* $t =$ 4.6, 70, 93, 381 *respectively, where we observe that all four spots split. This leads to an equilibrium eight-spot pattern on a ring.*

Next, we consider a different pattern whereby $k - 1$ spots are equally spaced on a ring of radius r, with an additional spot located at the center of the unit disk. The $k - 1$ spots on the ring have a common source strength S_c, while the k^{th} spot at the origin has a source strength denoted by S_k. For this pattern, the spot coordinates in complex form are

$$\mathbf{x}_j = re^{2\pi ij/(k-1)}\,, \quad j = 1, 2, \ldots, k-1\,; \qquad \mathbf{x}_k = 0\,.$$

We will analyze the dynamics of spots and the possibility of spot-splitting for this pattern for the limiting case $D \gg 1$, for which the reduced-wave

Green's function can be approximated by the Neumann Green's function.

For this special configuration, Principal Result 3.3 shows that the k^{th} spot at the center of the disk will not move. Alternatively, the motion of the remaining $k-1$ spots on the ring satisfy

$$\mathbf{x}_j' = -2\pi\varepsilon^2\gamma(S_c)\left[\left(\frac{S_c}{2}\right)\nabla_{\mathbf{x}_j}F(\mathbf{x}_1,\dots,\mathbf{x}_{k-1}) + S_k\nabla_{\mathbf{x}_j}G(\mathbf{x}_j;0)\right], \quad (3.64)$$

for $j=1,\cdots,k-1$, where

$$\nabla_{\mathbf{x}_j}F(\mathbf{x}_1,\dots,\mathbf{x}_{k-1}) = \frac{1}{k-1}p_{k-1}'(r)\,e^{2\pi i j/(k-1)}\,, \quad j=1,\cdots,k-1\,,$$

$$\nabla_{\mathbf{x}_j}G(\mathbf{x}_j;0) = \frac{1}{2\pi}\left(r-\frac{1}{r}\right)e^{2\pi i j/(k-1)}\,.$$

For $D \gg 1$, the function $p_{k-1}(r)$ is given in (3.63).

In order to calculate the equilibrium radius r_{ke} for this pattern, we need to solve a coupled system involving the source strengths S_k and S_c. We first denote $\mu = 2\pi\nu$, and then define α and β for $D \gg 1$ by

$$\alpha \equiv G(r;0) \sim \frac{D}{|\Omega|} - \frac{1}{2\pi}\ln r + \frac{r^2}{4\pi} - \frac{3}{8\pi}, \quad \beta \equiv R(0;0) = \frac{D}{|\Omega|} - \frac{3}{8\pi}\,.$$

We substitute these formulae into the nonlinear algebraic system (3.8) and set $\mathbf{x}_j' = 0$ in (3.64) for $j=1,\dots,k-1$. This leads to a three-dimensional nonlinear algebraic system for the equilibrium radius r_{ke} and the source strengths S_k and S_c given by

$$\frac{S_k}{S_c} + \frac{k-2}{2} - r^2\left(k-1+\frac{S_k}{S_c}\right) - (k-1)\frac{r^{2k-2}}{1-r^{2k-2}} = 0\,, \quad (3.65a)$$

$$\mathcal{A} = S_c\left(1+\frac{\mu p_{k-1}(r)}{k-1}\right) + \nu\chi(S_c) + \mu\alpha S_k\,, \quad (3.65b)$$

$$\mathcal{A} = (k-1)\mu\alpha S_c + \nu\chi(S_k) + S_k\left(1+\mu\beta\right)\,. \quad (3.65c)$$

In Fig. 3.13(a) and Fig. 3.13(b), we fix $D = 3.912$ and plot the source strengths S_c and S_k versus the ring radius r for $k=3, \mathcal{A}=22$ (solid curves) and $k=4, \mathcal{A}=38$ (heavy solid curves). For each pattern, there are two equilibrium states, which are marked by the solid circles. The two equilibrium ring radii for $k=3$, $\mathcal{A}=22$ are $r_{e1}=0.62$ with corresponding source strengths $(S_{c1}, S_{k1}) = (3.22, 3.31)$, and $r_{e2} = 0.49$ with $(S_{c2}, S_{k2}) = (4.50, 0.56)$. For $k=4$, $\mathcal{A}=38$, they are $r_{e1}=0.65$ with $(S_{c1}, S_{k1}) = (4.56, 4.04)$, and $r_{e2}=0.57$ with $(S_{c2}, S_{k2}) = (5.70, 0.51)$. The spot-splitting threshold Σ_2 is also marked on the curves in Fig. 3.13(a) and Fig. 3.13(b) by the square markers. On the solid curve for $k = 3$, they are at $(r, S_c) = (0.34, 4.31), (r, S_c) = (0.84, 4.31)$ and $(r, S_k) = (0.87, 4.31)$. On the heavy solid curve for $k = 4$, they are at $(r, S_c) = (0.74, 4.31)$ and $(r, S_k) = (0.68, 4.31)$.

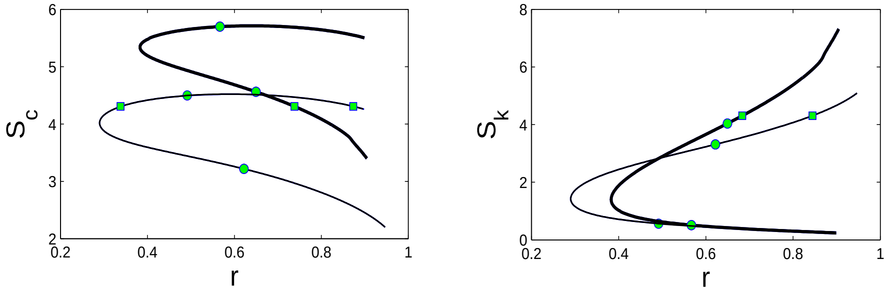

(a) S_c vs. r

(b) S_k vs. r

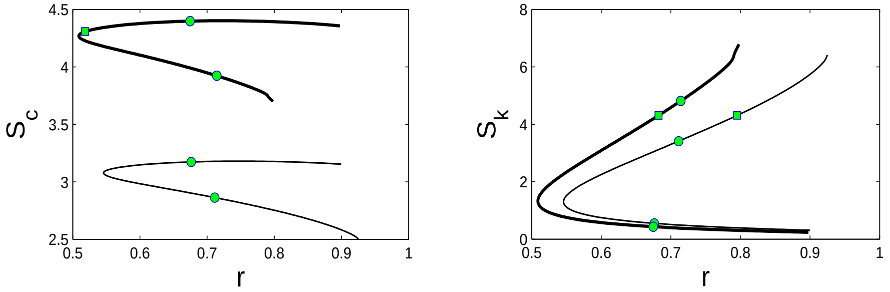

(c) S_c vs. r

(d) S_k vs. r

Figure 3.13: *Fix* $D = 3.912$. *(a)* S_c *vs.* r*; (b)* S_k *vs.* r*. The solid curves correspond to* $\mathcal{A} = 22$, $k = 3$*, the heavy solid curves correspond to* $\mathcal{A} = 38$, $k = 4$*, the square markers correspond to spot-splitting thresholds, and the solid circles correspond to equilibrium ring radii. (c)* S_c *vs.* r*; (d)* S_k *vs.* r*. The heavy solid curves correspond to* $\mathcal{A} = 82$, $k = 10$ *and the solid curves correspond to* $\mathcal{A} = 60$, $k = 10$*, the square markers correspond to spot-splitting thresholds, and the solid circles correspond to equilibrium ring radii.*

We now show how Fig. 3.13 can readily be used to predict spot-splitting behavior.

Experiment 3.7: A one-ring pattern with a center-spot for $D \gg O(1)$: Different types of spot-splitting

We fix $\mathcal{A} = 38$ and $D = 3.912$ and consider an initial pattern of one center-spot and three equally spaced spots on a ring of initial radius $r = 0.8$. We can then predict the dynamical behavior of this pattern by appealing to the heavy solid curves in Fig. 3.13(a) and Fig. 3.13(b). From the data used to plot Fig. 3.13(a) and Fig. 3.13(b), we obtain that $S_k = 5.38 > \Sigma_2$ and $S_c < \Sigma_2$ at $t = 0$. Therefore, we predict that only the center-spot will undergo spot-splitting, while the other three spots remain on a ring whose radius decreases slowly in time. For this parameter set, we show the full numerical results computed from (1.7) in Fig. 3.14 . These numerical results confirm the prediction based on the asymptotic theory.

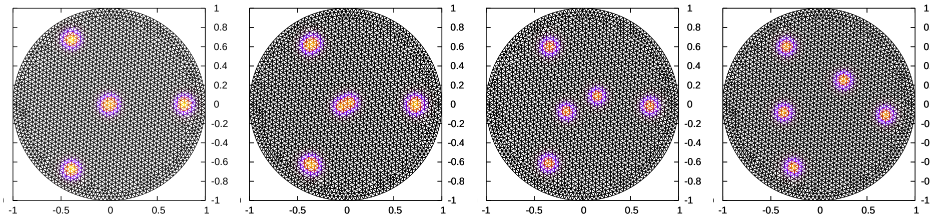

Figure 3.14: *Experiment 3.7: Fix $\mathcal{A} = 38, D = 3.912$. The numerical results computed from* (1.7) *for the initial 4-spot pattern are shown for initial ring radius $r = 0.8$. The plots (from left to right) are at times* $t = 4.6,\ 46,\ 102,\ 298$.

Alternatively, suppose that the initial ring radius is decreased from $r = 0.8$ to $r = 0.5$. Then, from the heavy solid curves in the top row of Fig. 3.13(a) and Fig. 3.13(b), we now calculate that $S_c = 4.92 > \Sigma_2$ and $S_k < \Sigma_2$ at $t = 0$. Thus, we predict that the three spots on the ring undergo simultaneous spot-splitting starting at $t = 0$, while the center-spot does not split. The full numerical results computed from (1.7), as shown in Fig. 3.15, fully support this asymptotic prediction.

Experiment 3.8: A one-ring pattern with a center-spot for $D \gg O(1)$: A triggered dynamical instability

In Fig. 3.13(c) and Fig. 3.13(d), we fix $k = 10$ and $D = 3.912$ and plot S_c and S_k versus r for $\mathcal{A} = 82$ (heavy solid curve), and for $\mathcal{A} = 60$ (solid curve). In both figures, solid circles and square markers denote the equilibrium states

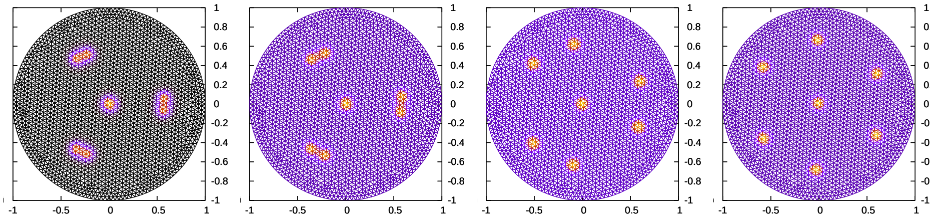

Figure 3.15: *Experiment 3.7: Fix* $\mathcal{A} = 38, D = 3.912$. *The numerical results computed from* (1.7) *for the initial 4-spot pattern are shown for initial ring radius* $r = 0.5$. *The plots (from left to right) are at times* $t = 4.6$, 56, 140, 298.

and the spot-splitting thresholds, respectively. On the solid curve for $\mathcal{A} = 60$, we have the equilibria at $r_{e1} = 0.71$ with corresponding source strengths $(S_{c1}, S_{k1}) = (2.86, 3.41)$, and $r_{e2} = 0.68$ with $(S_{c2}, S_{k2}) = (3.17, 0.55)$. In this case, only the center-spot could split, and the minimum ring radius that leads to spot-splitting is $r = 0.80$. Alternatively, on the heavy solid curve for $\mathcal{A} = 82$, we have the equilibria at $r_{e1} = 0.71$ with corresponding source strengths $(S_{c1}, S_{k1}) = (3.92, 4.81)$, and $r_{e2} = 0.68$ with $(S_{c2}, S_{k2}) = (4.40, 4.32)$. In this case, the splitting criteria are $(r, S_c) = (0.52, 4.31)$ and $(r, S_k) = (0.68, 4.31)$.

Consider an initial ring radius of $r = 0.62$. Then, from the heavy solid curve in Fig. 3.13(c) and Fig. 3.13(d), we calculate the initial source strengths as $S_c = 4.03$ and $S_k = 3.38$ at $t = 0$. Therefore, we predict that spot-splitting is not initiated at $t = 0$. However, as the ring expands slowly to approach its equilibrium state at $r_{e1} = 0.71$, the spot-splitting threshold is achieved at the ring radius $r = 0.68$ when S_k begins to exceed Σ_2, Thus, the asymptotic theory predicts that a dynamical spot-splitting instability will be triggered at this point. The predicted dynamical instability phenomenon is confirmed by the full numerical results shown in Fig. 3.16 computed from the GS model (1.7). From this figure, we observe that this pattern is stable to spot-splitting for $t < 60$, but that the center-spot eventually undergoes a dynamical spot-splitting event.

3.8 Discussion

In this chapter we have characterized the dynamics of a collection of spots for the GS model (1.7) and have provided an explicit criterion, based on a linearized stability analysis, for the initiation of a spot-splitting instabil-

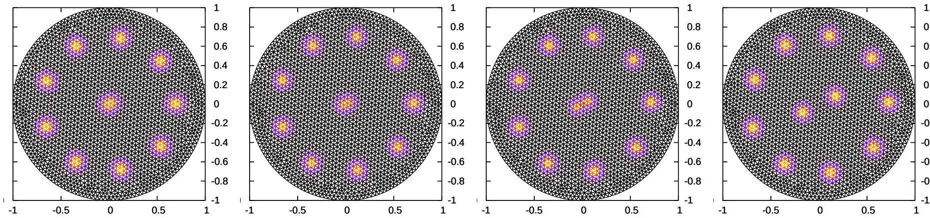

Figure 3.16: *Experiment 3.8: Fix* $\mathcal{A} = 82, D = 3.912$. *The full numerical results computed from* (1.7) *for an initial pattern with nine spots equally spaced on a ring of initial radius* $r = 0.62$ *together with a center-spot. The plots are shown at times* $t = 60$, 93, 144, 214.

ity. The analysis used in this chapter has been a combination of a formal asymptotic analysis to construct quasi-equilibrium spot patterns and to determine their dynamics, together with a numerical study of a linearized eigenvalue problem associated with a spot self-replication instability. In Principal Result 3.1, a quasi-equilibrium k-spot pattern was constructed by matched asymptotic analysis. The collective coordinates characterizing this pattern are the spatial configuration $(\mathbf{x}_1, \ldots, \mathbf{x}_k)$ of spots and their corresponding source strengths $(S_1, \ldots, S_k)$, which measure the strengths of the logarithmic growth of the local, or core, solution for u near each spot. The slow motion, with speed $O(\varepsilon^2)$, of the spots are characterized by the DAE system (3.35), where the source strengths are determined in terms of the instantaneous spatial configuration of spots by the nonlinear algebraic system (3.8). This system incorporates the interaction between the spots and the geometry of the domain mediated by the reduced-wave Green's function and its regular part, and also accounts for all logarithmic correction terms in $\nu = -1/\ln \varepsilon$. The asymptotic results for slow spot motion and the prediction of the initiation of spot self-replication have been successfully validated through some detailed comparisons with full numerical results computed from the GS model (1.7) for the unit square and the unit disk.

There are a few problems related to spot dynamics and spot-replication behavior for the GS model that should be studied. The first problem is to show that a linear instability of a spot to peanut-splitting does in fact lead to a spot self-replication event. This problem could perhaps be analyzed by performing a weakly nonlinear analysis of a localized spot to show that the initial peanut-splitting instability does not saturate in the nonlinear regime to a large, but steady-state, deformation of a single spot. The second problem is to use the equilibrium problem in Principal Result 3.4 to calculate detailed bifurcation diagrams in terms of $\mathcal{A}$ and D of steady-state k-spot patterns in arbitrary domains. The third open problem is to study the stability of the equilibrium points of the ODE's in Principal Result 3.3 describing slow spot motion. Any unstable eigenvalue of this system is small of order $O(\varepsilon^2)$ and, consequently, represents a weak, or translational instability. Based on the study of [36] of discrete interacting particles, this instability should be manifested for the unit disk when the number of equally spaced spots on a concentric ring exceeds some critical value.

Chapter 4

Competition and Oscillatory Profile Instabilities for the Two-dimensional Gray-Scott Model

In §3.2 of Chapter 3 we formulated the eigenvalue problem (3.25) to determine the stability of the core solution near each spot to localized perturbations with angular mode $m \geq 2$, which are associated with spot-splitting instabilities. In this chapter, we focus on the stability of the spot profile to the radially symmetric $m = 0$ mode, which is associated with instabilities in the amplitude of a spot. As shown below, there are two types of such instabilities; oscillatory instabilities of the spot amplitude, and competition, or overcrowding, instabilities that lead to the annihilation of a spot.

4.1 Eigenvalue Problem for the Mode $m = 0$

To determine the stability of the quasi-equilibrium solution u_e and v_e in (3.9), we introduce the perturbation

$$u(\mathbf{x}, t) = u_e + e^{\lambda\, t}\eta(\mathbf{x})\,, \qquad v(\mathbf{x}, t) = v_e + e^{\lambda\, t}\phi(\mathbf{x})\,,$$

in (1.7). This leads to the eigenvalue problem

$$\varepsilon^2\Delta\phi - (1+\lambda)\phi + 2Au_e v_e \phi + Av_e^2\eta = 0\,, \quad \mathbf{x} \in \Omega\,, \tag{4.1a}$$

$$D\Delta\eta - (1+\tau\lambda)\eta - 2u_e v_e\phi - v_e^2\eta = 0\,, \quad \mathbf{x} \in \Omega\,, \tag{4.1b}$$

$$\partial_n \phi = \partial_n \eta = 0\,, \quad \mathbf{x} \in \partial\Omega\,. \tag{4.1c}$$

In the inner region near the j^{th} spot centered at $\mathbf{x}_j$, we introduce ρ, $N_j(\rho)$ and $\Phi_j(\rho)$ in (4.1) defined by $\rho = \varepsilon^{-1}|\mathbf{x} - \mathbf{x}_j|$, $\eta = \frac{\varepsilon}{A\sqrt{D}} N_j(\rho)$, and $\phi =$

$\frac{\sqrt{D}}{\varepsilon}\Phi_j(\rho)$. Then, when τ satisfies $\tau\lambda \ll O(\varepsilon^{-2})$, we obtain that (4.1) transforms to the following radially symmetric eigenvalue problem on $0 < \rho < \infty$:

$$\Phi_j'' + \frac{1}{\rho}\Phi_j' - \Phi_j + 2U_jV_j\Phi_j + V_j^2N_j = \lambda\Phi_j \,, \tag{4.2a}$$

$$N_j'' + \frac{1}{\rho}N_j' - V_j^2N_j - 2U_jV_j\Phi_j = 0 \,, \tag{4.2b}$$

where U_j and V_j is the solution of the radially symmetric core problem (3.2) for the j^{th} spot. The boundary conditions for this system are

$$\Phi_j'(0) = N_j'(0) = 0 \,; \quad \Phi_j(\rho) \to 0 \,, \quad N_j(\rho) \to C_j \ln\rho + B_j \quad \text{as} \quad \rho \to \infty. \tag{4.2c}$$

We emphasize that as $\rho \to \infty$ we must, in general, allow N_j to grow logarithmically. This behavior is in contrast to that imposed for the eigenvalue problem (3.25) with mode $m \geq 2$ studied in Section 3.2, where we required that $N_j \to 0$ as $\rho \to \infty$. By applying the divergence theorem to (4.2b), we can identify C_j as

$$C_j \equiv \int_0^\infty (V_j^2N_j + 2U_jV_j\Phi_j)\rho \, d\rho.$$

To formulate our eigenvalue problem we must match the far-field logarithmic growth of N_j with a global outer solution for η. This matching has the effect of globally coupling the local eigenvalue problems near each spot.

Next, we determine the outer problem for η that couples the local problems near each spot. Since v_e is localized near $\mathbf{x}_j$ for $j = 1, \ldots, k$, we can use $u_e \sim \frac{\varepsilon}{A\sqrt{D}}U_j$, and $v_e \sim \frac{\sqrt{D}}{\varepsilon}V_j$ to represent the last two terms in (4.1b) in the sense of distributions as

$$2u_ev_e\phi + v_e^2\eta \sim \frac{2\pi\varepsilon\sqrt{D}}{A}\sum_{j=1}^{k}\left(\int_0^\infty (2U_jV_j\Phi_j + V_j^2N_j)\,\rho\,d\rho\right)\delta(\mathbf{x} - \mathbf{x}_j) \,.$$

Here $\delta(\mathbf{x} - \mathbf{x_j})$ is the Dirac delta function concentrated at $\mathbf{x} = \mathbf{x}_j$. Upon identifying the integral in the expression above as C_j, we then obtain that (4.1b) in the outer region becomes

$$\Delta\eta - \frac{(1+\tau\lambda)}{D}\eta = \frac{2\pi\varepsilon}{A\sqrt{D}}\sum_{j=1}^{k}C_j\delta(\mathbf{x} - \mathbf{x}_j) \,, \quad \mathbf{x} \in \Omega \,, \tag{4.3}$$

with $\partial_n \eta = 0$ for $\mathbf{x} \in \partial\Omega$. This outer solution can be represented in terms of a λ-dependent Green's function as

$$\eta = -\frac{2\pi\varepsilon}{A\sqrt{D}} \sum_{j=1}^{k} C_j G_\lambda(\mathbf{x}; \mathbf{x}_j) \,. \tag{4.4}$$

Here this Green's function $G_\lambda(\mathbf{x}; \mathbf{x}_j)$ satisfies

$$\Delta G_\lambda - \frac{(1+\tau\lambda)}{D} G_\lambda = -\delta(\mathbf{x}-\mathbf{x}_j) \,, \quad \mathbf{x} \in \Omega \,; \quad \partial_n G_\lambda = 0 \,, \quad \mathbf{x} \in \partial\Omega \,, \tag{4.5a}$$

with the following singularity behavior as $\mathbf{x} \to \mathbf{x}_j$:

$$G_\lambda(\mathbf{x}; \mathbf{x}_j) \sim -\frac{1}{2\pi} \ln|\mathbf{x} - \mathbf{x}_j| + R_{\lambda\,jj} + o(1) \,, \quad \text{as } \mathbf{x} \to \mathbf{x}_j \,. \tag{4.5b}$$

We remark that the regular part $R_{\lambda jj}$ depends on $\mathbf{x}_j$, λ, τ, and D.

The matching condition between the outer solution (4.4) for η as $\mathbf{x} \to \mathbf{x}_j$ and the far-field behavior (4.2c) as $\rho \to \infty$ of the inner solution N_j near the j^{th} spot yields that

$$-\frac{2\pi\varepsilon}{A\sqrt{D}} \left[C_j \left(-\frac{1}{2\pi} \ln|\mathbf{x} - \mathbf{x}_j| + R_{\lambda\,jj} \right) \right] - \frac{2\pi\varepsilon}{A\sqrt{D}} \sum_{i \neq j}^{k} C_i G_{\lambda\,ij} \sim \frac{\varepsilon}{A\sqrt{D}} \left[C_j \ln|\mathbf{x} - \mathbf{x}_j| + \frac{C_j}{\nu} + B_j \right] \,, \tag{4.6}$$

where $G_{\lambda\,ij} \equiv G_\lambda(\mathbf{x}_i; \mathbf{x_j})$ and $\nu = -1/\ln\varepsilon$. This matching condition yields the k equations

$$C_j \left(1 + 2\pi\nu R_{\lambda\,jj} \right) + \nu B_j + 2\pi\nu \sum_{i \neq j}^{k} C_i G_{\lambda\,ij} = 0 \,, \quad j = 1, \ldots, k \,. \tag{4.7}$$

We remark that the constants τ and D appear in the operator of the λ-dependent Green's function defined by (4.5).

Suppose that $\tau = O(1)$ and $D = O(1)$. Then, since $\nu \ll 1$, we obtain from (4.7) that to leading-order $C_j = 0$ for $j = 1, \cdots, k$. This implies that the eigenfunction $N_j(\rho)$ in (4.2) is bounded as $\rho \to \infty$, and so we can impose that $N_j'(\rho) \to 0$ as $\rho \to \infty$. Therefore, when $\tau = O(1)$ and $D = O(1)$, then to leading order in ν the eigenvalue problems (4.2) for $j = 1, \ldots, k$ are coupled together only through the determination of the source strengths $S_1, \ldots, S_k$ from the nonlinear algebraic system (3.8) of Chapter 3.

Therefore, to leading order in ν, we must compute the real part of the principal eigenvalue λ_0 of (4.2) as a function of S_j, subject to the condition that $N_j'(\rho) \to 0$ as $\rho \to \infty$. This computation is done by discretizing (4.2) by finite differences and then calculating the spectrum of the resulting matrix eigenvalue problem using LAPACK (cf. [1]). The plot of $\mathrm{Re}(\lambda_0)$ versus S_j is shown in Fig. 4.1 for the range $S_j < 7.5$, which includes the value $S_j = \Sigma_2 \approx 4.31$ corresponding to the peanut-splitting instability. We conclude that $\mathrm{Re}(\lambda_0) < 0$ for $S_j < 7.5$. In Fig. 4.2(a) and Fig. 4.2(b) we plot the corresponding eigenfunctions $\Phi_j(\rho)$ and $N_j(\rho)$, respectively, for $S_j = 3.0$ (solid curve) and $S_j = 6.0$ (dashed curve).

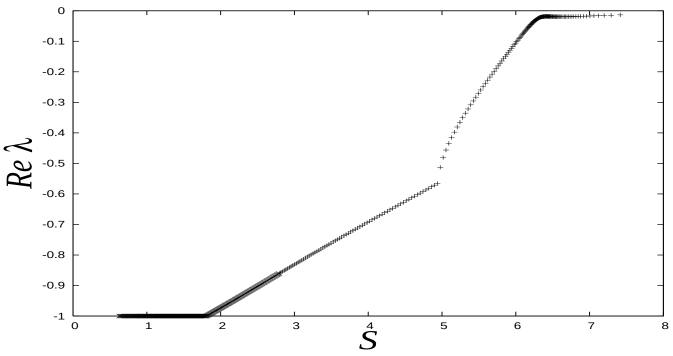

Figure 4.1: *The real part of the largest eigenvalue Re*(λ_0) *of* (4.2) *vs.* S_j *subject to the condition that* N_j *is bounded as* $\rho \to \infty$.

However, since $\nu = -1/\ln\varepsilon$ decreases only very slowly as ε decreases, the leading-order approximation $C_j = 0$ for $j = 1, \ldots, k$ to (4.7) is not very accurate. Consequently, we must examine the effect of the coupling in (4.7). Since (4.2) is a linear homogeneous problem, we introduce $\hat{B}_j$ by $B_j = \hat{B}_j C_j$, and we define the new variables $\hat{\Phi}_j$ and $\hat{N}_j$ by $\Phi_j = C_j \hat{\Phi}_j$ and $N_j = C_j \hat{N}_j$. Then, the eigenvalue problem (4.2) on $0 < \rho < \infty$ becomes

$$\hat{\Phi}_j'' + \frac{1}{\rho}\hat{\Phi}_j' - \hat{\Phi}_j + 2U_j V_j \hat{\Phi}_j + V_j^2 \hat{N}_j = \lambda \hat{\Phi}_j \,, \tag{4.8a}$$

$$\hat{N}_j'' + \frac{1}{\rho}\hat{N}_j' - V_j^2 \hat{N}_j - 2U_j V_j \hat{\Phi}_j = 0 \,, \tag{4.8b}$$

with boundary conditions

$$\hat{\Phi}_j'(0) = \hat{N}_j'(0) = 0 \,; \qquad \hat{\Phi}_j(\rho) \to 0 \,, \quad \hat{N}_j(\rho) \to \ln\rho + \hat{B}_j \,, \quad \text{as} \quad \rho \to \infty \,. \tag{4.8c}$$

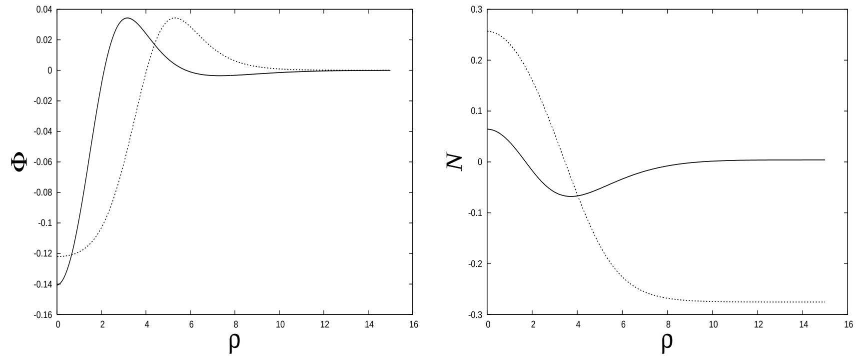

(a) Φ_j vs. ρ (b) N_j vs. ρ

Figure 4.2: *Eigenfunctions* Φ_j *and* N_j *of* (4.2) *with* N_j *bounded at infinity. Left figure:* Φ_j *vs.* ρ *for* $S_j = 3.0$ *(solid curve) and* $S_j = 6.0$ *(dashed curve). Right figure:* N_j *vs.* ρ *for* $S_j = 3.0$ *(solid curve) and* $S_j = 6.0$ *(dashed curve).*

The constant $\hat{B}_j$ in (4.8c) is a function of the, as yet unknown, complex-valued eigenvalue parameter λ. It also depends on the source strength S_j through the core solution U_j and V_j, which satisfies (3.2).

In terms of $\hat{B}_j$, the problem (4.7) transforms to the homogeneous linear system for $C_1, \ldots, C_k$ given by

$$C_j(1 + 2\pi\nu R_{\lambda\, jj} + \nu \hat{B}_j) + 2\pi\nu \sum_{i \neq j}^{k} C_i G_{\lambda\, ij} = 0\,, \quad j = 1, \ldots, k\,. \tag{4.9}$$

It is convenient to express (4.9) in matrix form as

$$\mathcal{M}\,\mathbf{c} = \mathbf{0} \qquad \mathcal{M} \equiv \mathcal{I} + \nu\mathcal{B} + 2\pi\nu\mathcal{G}_\lambda\,, \tag{4.10a}$$

where $\mathcal{I}$ is the $k \times k$ identity matrix and $\mathbf{c} \equiv (C_1, \ldots, C_k)^t$. In (4.10a), $\mathcal{B}$ is a diagonal matrix and $\mathcal{G}_\lambda$ is the λ-dependent Green's matrix defined by

$$\mathcal{G}_\lambda \equiv \begin{pmatrix} R_{\lambda\,11} & G_{\lambda\,12} & \cdots & G_{\lambda\,1k} \\ G_{\lambda\,21} & R_{\lambda\,22} & \cdots & G_{\lambda\,2k} \\ \vdots & \vdots & \vdots & \vdots \\ G_{\lambda\,k1} & G_{\lambda\,k2} & \cdots & G_{\lambda\,kk} \end{pmatrix}, \quad \mathcal{B} \equiv \begin{pmatrix} \hat{B}_1 & 0 & \cdots & 0 \\ 0 & \hat{B}_2, & \cdots & 0 \\ \vdots & \vdots & \vdots & \vdots \\ 0 & 0 & \cdots & \hat{B}_k \end{pmatrix}. \tag{4.10b}$$

Since $\mathcal{G}_\lambda$ is a symmetric matrix, then so is the matrix $\mathcal{M}$.

The condition that determines the eigenvalue λ is that there is a nontrivial solution $\mathbf{c} \neq \mathbf{0}$ to (4.10a). Hence, λ is determined by the condition that $\mathcal{M}$ is a singular matrix, i.e. $\det(\mathcal{M}) = 0$. This condition leads, effectively, to a transcendental equation for λ. The roots of this equation determine the discrete eigenvalues governing the stability of the k-spot quasi-equilibria to locally radially symmetric perturbations near each spot. We summarize our formulation of the eigenvalue problem as follows:

Principal Result 4.1: *Consider a $k-$spot quasi-equilibrium solution to the two-dimensional Gray-Scott model* (1.7). *For $\varepsilon \to 0$, with $D = O(1)$ and $\tau = O(1)$, the stability of this pattern to locally radially symmetric perturbations near each spot is determined by the condition det$(\mathcal{M}) = 0$, where $\mathcal{M}$ is defined in* (4.10). *The diagonal matrix $\mathcal{B}$ in* (4.10) *is determined in terms of S_j and λ by the local problems* (4.8) *for $j = 1, \ldots, k$. If the principal eigenvalue λ_0 of this problem is such that Re$(\lambda_0) < 0$, then the $k-$spot quasi-equilibrium solution is stable to locally radially symmetric perturbations near each spot. It is unstable if Re$(\lambda_0) > 0$.*

We remark that (4.10) couples the local spot solutions in two different ways. First, the λ-dependent terms $R_{\lambda jj}$ and $G_{\lambda ij}$ in the Green's matrix $\mathcal{G}_\lambda$ in (4.10) depend on τ, D, and λ, as well as the spatial configuration $(\mathbf{x}_1, \ldots, \mathbf{x}_k)$ of the spot locations.and the geometry of Ω. Secondly, the constant $\hat{B}_j$ in the matrix $\mathcal{B}$ depends on the eigenvalue λ and on S_j. Recall that the source strengths $S_1, \ldots, S_k$ are coupled through the nonlinear algebraic system (3.8) of Chapter 3, which involves $\mathcal{A}$, D, the reduced-wave Green's function, and the spatial configuration $(\mathbf{x}_1, \ldots, \mathbf{x}_k)$ of spot locations.

From our study of this eigenvalue problem below, there are two mechanisms through which a k-spot quasi-equilibrium pattern can lose stability. Firstly, for $k \geq 1$ there can be a complex conjugate pair of eigenvalues λ_0 that crosses into the unstable half-plane $\text{Re}(\lambda_0) > 0$. This instability as a result of a Hopf bifurcation results in an oscillatory profile instability, whereby the spot amplitudes undergo temporal oscillations. Such an instability typically occurs if τ is sufficiently large. Alternatively, for $k \geq 2$, the principal eigenvalue λ_0 can be real and enter the unstable right half-plane $\text{Re}(\lambda_0) > 0$ along the real axis $\text{Im}(\lambda_0) = 0$. This instability, due to the creation of a positive real eigenvalue, gives rise to an unstable sign-fluctuating perturbation of the spot amplitudes and initiates a competition instability, leading to spot annihilation events. This instability can be triggered if D is sufficiently large or, equivalently, if the inter-spot separation is too small.

The eigenvalue problem is rather challenging to investigate in full generality owing to the complexity of the two different coupling mechanisms in (4.10). However, for the special case when the spot configuration $(\mathbf{x}_1, \ldots, \mathbf{x}_k)$ is such that $\mathcal{G}$ is a circulant matrix, then the complexity of our eigenvalue problem reduces considerably. For this special arrangement of spot locations, the spots have a common source strength $S_c = S_j$ for $j = 1, \ldots, k$, as was discussed in Section 3.1. Hence, the inner problem (4.8) is the same for each spot. This enforces that $\hat{B}_j \equiv \hat{B}_c$ for $j = 1, \ldots, k$. where $\hat{B}_c = \hat{B}_c(\lambda, S)$ is a function of S_c and λ. Therefore, we can write $\mathcal{B} = \hat{B}_c \mathcal{I}$ in (4.10). Moreover, let v be an eigenvector of the λ-dependent Green's matrix $\mathcal{G}_\lambda$ with eigenvalue ω_λ, i.e. $\mathcal{G}_\lambda v = \omega_\lambda v$. This matrix is also circulant when $\mathcal{G}$ is circulant. Then, the condition that $\mathcal{M}$ in (4.10) is a singular matrix reduces to k transcendental equations in λ. We summarize the result as follows:

Principal Result 4.2: *Under the conditions of Principal Result 4.1, suppose that the spot locations* $(\mathbf{x}_1, \ldots, \mathbf{x}_k)$ *are such that* $\mathcal{G}$*, and consequently* $\mathcal{G}_\lambda$*, are circulant matrices. Then, the eigenvalue condition det*$(\mathcal{M}) = 0$ *for* (4.10) *reduces to the* k *nonlinear algebraic equations that*

$$1 + \nu \hat{B}_c + 2\pi \nu \omega_\lambda = 0 \,, \tag{4.11}$$

where ω_λ *is any eigenvalue of the matrix* $\mathcal{G}_\lambda$*. The eigenvectors of* $\mathcal{G}_\lambda$ *determine the choices for* $\mathbf{c}$*.*

Owing to the considerable reduction in complexity of the eigenvalue problem when $\mathcal{G}$ and $\mathcal{G}_\lambda$ are circulant matrices, we will study in detail the stability of such symmetric quasi-equilibrium spot patterns in Section §4.5.

4.1.1 Numerical Methods for the Eigenvalue Problem

The eigenvalue problem, consisting of (4.8) coupled with (4.10a), can only be solved numerically. One numerical approach would be to calculate the eigenvalue λ directly for a given set of parameters A, D, τ, and ε and for a given configuration of spots. The outline of a fixed-point iterative type method is as follows:

1. Given fixed parameter values τ, ε, A, D, $\mathcal{A} = \nu \varepsilon^{-1} A \sqrt{D}$, we first calculate $S_j, j = 1, \cdots, k$ from the algebraic system (3.8), and then compute the core solution U_j, V_j from (3.2).

2. For the n^{th} iteration, starting from a known eigenvalue λ_n, we could solve (4.8) for $\hat{B}_j$ for $j = 1, \ldots, k$.

3. Next, with $\hat{B}_j$ known for $j = 1, \ldots, k$, we could update the value of λ by requiring that the λ-dependent Green's function and its regular part be such that the matrix $\mathcal{M}$ in (4.10a) is a singular matrix. This step requires an additional inner iteration. The new approximation to the eigenvalue is denoted by λ_{n+1}.

4. We repeat step 2 using the updated λ_{n+1} until it converges to λ, with an error that is less than a given tolerance $\mathrm{Tol} = 10^{-6}$. Then λ is the eigenvalue of the coupled problem.

However, this iteration approach for λ converges very slowly, and very much relies on the initial guess. In addition, we need to study the stability for a range of values of the parameter τ, in order to determine the Hopf bifurcation threshold. Therefore, the computational cost of this simple scheme will be very large.

Instead of the former approach, we used an alternative numerical method that is based on the assumption that an instability occurs at some critical values of the parameters. For instance, in order to compute the Hopf bifurcation threshold τ_H, we assume that there is a complex conjugate pair of pure imaginary eigenvalues occurring at $\tau = \tau_H$ for which $\lambda_r \equiv \mathrm{Re}(\lambda) = 0$ and $\lambda_i \equiv \mathrm{Im}(\lambda) \neq 0$. Instead of solving for λ for each given τ, we fix $\lambda_r = 0$, and solve for the two variables τ_H and λ_i by Newton's method. A rough outline of our algorithm is as follows:

1. Given fixed parameter values ε, A, D, we first calculate the source strength S_j from (3.8) and then compute the corresponding core solution U_j, V_j from (3.2).

2. Fix $\lambda_r = 0$. Starting from the initial guess τ, λ_i, we calculate $G_{\lambda\, ij}$, $R_{\lambda\, jj}$ and their partial derivatives with respect to τ, λ_i numerically. We also calculate $\hat{B}_j$ and its derivative $\partial_\lambda \hat{B}_j$ from (4.8).

3. In (4.10a), we use Newton's method on the condition that $\det(M) = 0$ in (4.10a), to update τ, λ_i. We then go to step 2 and iterate further until reaching the specified tolerance.

Although this method is theoretically appealing, the determination of the constants τ, λ_i such that $\det(\mathcal{M}) = 0$, with $\mathcal{M}$ defined in (4.10a), is rather challenging. As such we will mainly focus on studying the instabilities of a one-spot solution and the $k-$spot symmetric patterns with $k \geq 2$, for which the Green's matrices are circulant. For this special case, Principal Result

4.2 applies. The Hopf bifurcation threshold τ_H for each of the different spot patterns considered in §4.3, §4.4, and §4.5, below were calculated by the algorithm above.

Moreover, to calculate the competition instability threshold, we fix the parameters ε, D and set $\lambda = 0$, since the principal eigenvalue enters the unstable right half-plane $\text{Re}(\lambda) > 0$ along the real axis. At some critical parameter value of D in terms of A, there could be a zero eigenvalue. The numerical computation of this critical value of D is done from the following rough algorithm:

1. Given fixed parameters ε, A, and an initial guess for D, we first calculate S_j from (3.8) and then U_j, V_j from (3.2).
2. Fix $\lambda = 0$. Starting from the initial guess for D, we calculate $G_{\lambda ij}$, $R_{\lambda jj}$ and their partial derivatives with respect to D numerically. We also calculate $\hat{B}_j$ and its derivative $\partial_D \hat{B}_j$ from (4.8).
3. In (4.10a), we use Newton's method to update D by requiring that $\det(M) = 0$. We then iterate until reaching the tolerance.

These numerical algorithms enable us to calculate the threshold parameter values for oscillatory profile instabilities and competition instabilities. Below in §4.3, §4.4, and §4.5 we demonstrate our theory by numerically computing these instability thresholds for various spot configurations in both finite and infinite domains.

4.2 Nonlocal Eigenvalue Analysis

In the previous section, we formulated a coupled eigenvalue problem associated with competition and oscillatory profile instabilities. However, in [99] and [101] a different analytical approach based on an analysis of a *nonlocal eigenvalue problem* (NLEP) was used to obtain a leading-order asymptotic theory for the existence and stability of spot patterns to the GS model (1.7), with an error of order $O(-1/\ln\varepsilon)$. In this section we summarize this theory and compare it with our quasi-steady state analysis in §3.1 and with our eigenvalue formulation in §4.1.

4.2.1 A One-spot Solution in an Infinite domain

In [99], the existence and stability of a one-spot pattern in the infinite plane $\mathbb{R}^2$ was studied. In the infinite plane, we can eliminate the parameter D by introducing $\tilde{\mathbf{x}}$ and $\tilde{\varepsilon}$ by

$$\tilde{\mathbf{x}} = \frac{\mathbf{x}}{\sqrt{D}}\,, \qquad \tilde{\varepsilon} = \frac{\varepsilon}{\sqrt{D}}\,. \tag{4.12}$$

Then, in terms of $\tilde{\mathbf{x}} \in \mathbb{R}^2$, (1.7) becomes

$$v_t = \tilde{\varepsilon}^2 \Delta v - v + Auv^2\,, \qquad \tau u_t = \Delta u + (1-u) - uv^2\,. \tag{4.13}$$

In the inner region near the spot centered at $\mathbf{x}_0$, a different scaling was used in [99] to construct the local solution near each spot. Instead of a coupled BVP system for the core problem as in (3.2), the leading-order scaling in [99] showed that the slow variable u satisfies $u \sim u_0$, where u_0 is locally constant near each spot. Moreover, from [99], the fast variable v was found to satisfy $v \sim v_0 = \frac{1}{Au_0} w(\rho)$, where $w(\rho)$ is the radially symmetric ground-state solution on $0 < \rho < \infty$ of the scalar equation

$$\Delta_\rho w - w + w^2 = 0\,; \quad w(0) > 0\,,\ w'(0) = 0\,; \qquad w \to 0\,,\ \text{as}\ \rho \to \infty\,. \tag{4.14}$$

The analysis in [99] showed, asymptotically for $\varepsilon \to 0$, that u_0 satisfies the quadratic equation

$$1 - u_0 \sim \frac{L}{u_0}, \qquad L \equiv \frac{\tilde{\varepsilon}^2}{\tilde{\nu}\, A^2} \int_0^\infty w^2(\rho)\rho\, d\rho\,, \qquad \tilde{\nu} = -1/\ln \tilde{\varepsilon}\,. \tag{4.15}$$

Therefore, the existence threshold for a one-spot equilibrium solution is that

$$L \leq \frac{1}{4} \quad \Rightarrow \quad A \geq A_f \equiv 2\tilde{\varepsilon}\sqrt{\frac{b_0}{\tilde{\nu}}}\,, \qquad b_0 \equiv \int_0^\infty w^2(\rho)\rho\, d\rho\,. \tag{4.16}$$

Define L_0 and γ by $L_0 = \lim_{\tilde{\varepsilon}\to 0} L = O(1)$ and $\gamma \equiv \tilde{\nu}\, \ln \tau = O(1)$, so that $\tau = O(\tilde{\varepsilon}^{-\gamma})$. Then, the following nonlocal eigenvalue problem (NLEP) was derived in [99]:

$$\Delta_{\mathbf{y}} \psi_0 - \psi_0 + 2w\psi_0 - \frac{2(1-u_0)(2-\gamma)}{2u_0 + (1-u_0)(2-\gamma)}\, w^2 \, \frac{\int_0^\infty w\psi_0\, \rho\, d\rho}{\int_0^\infty w^2\, \rho\, d\rho} = \lambda \psi_0\,, \tag{4.17}$$

with $\psi_0 \to 0$ as $\rho \to \infty$. An analysis of this NLEP in [99] led to Theorem 2.2 of [99], which we summarize as follows:

1. There exists a saddle node bifurcation at $L_0 = \frac{1}{4}$, such that there are two equilibrium solutions $u_0^\pm$ given by

   $$u_0^\pm = \frac{1}{2}\left(1 \pm \sqrt{1 - 4L_0}\right),$$

   for $L_0 < \frac{1}{4}$, and no equilibrium solutions when $L_0 > \frac{1}{4}$.

2. Assume that $0 \leq \gamma < 2$ and $L_0 < \frac{1}{4}$. Then, the solution branch (u_0^+, v_0^+) is linearly unstable.
3. Assume that $0 \leq \gamma < 2$. Then, the other solution branch (u_0^-, v_0^-) is linearly unstable if
$$L_0 > \frac{1}{4}\left[1 - \left(\frac{\gamma}{4+\gamma}\right)^2\right], \quad \Rightarrow \quad A < A_s \equiv A_f \left[1 - \left(-\frac{\gamma}{4+\gamma}\right)^2\right]^{-1/2}. \tag{4.18}$$
4. Assume that $\gamma = 0$ and $L_0 < \frac{1}{4}$. Then, (u_0^-, v_0^-) is linearly stable.
5. If $0 \leq \gamma < 2$, the stability of (u_0^-, v_0^-) is unknown for $A > A_s$.

We remark that the saddle-node bifurcation value of A, obtained from (4.15), has the scaling $A = O\left(\tilde{\varepsilon}[-\ln \tilde{\varepsilon}]^{1/2}\right)$ as $\tilde{\varepsilon} \to 0$. The stability results listed above from [99] also relate only to this range in A. We remark that the quasi-equilibrium spot solution constructed in §3.1 and the spot self-replication threshold of §3.2 occurs for the slightly larger value of A, with scaling $A = O\left(\tilde{\varepsilon}[-\ln \tilde{\varepsilon}]\right)$ (see (3.4) of §3.1). Consequently, the occurrence of spot self-replication behavior for the GS model (1.7) was not observed in the scaling regime for A considered in [99].

4.2.2 Multi-Spot Patterns in a Finite Domain

In [101] a related analytical approach based on the analysis of other NLEP's was used to obtain a leading-order asymptotic theory for the existence and stability of k-spot patterns to the GS model (1.7) in a bounded two-dimensional domain. In the inner region near the j^{th} spot centered at $\mathbf{x}_j$, the leading-order scaling in [101] showed that the slow variable u satisfies $u \sim u_j$, where u_j is a constant, while the the fast variable v satisfies $v \sim v_j \equiv \frac{1}{Au_j} w(\rho)$, where $w(\rho)$ is the radially symmetric ground-state solution of (4.14). For a k-spot pattern, it was shown in [101] that the u_j for $j = 1, \ldots, k$ satisfy the nonlinear algebraic system

$$1 - u_j - \frac{\eta_\varepsilon L_\varepsilon}{u_j} \sim \sum_{i=1}^{k} \frac{L_\varepsilon}{u_i}, \tag{4.19}$$

where L_ε and η_ε are defined by

$$L_\varepsilon = \frac{\varepsilon^2 2\pi b_0}{A^2|\Omega|}, \qquad \eta_\varepsilon = \frac{|\Omega|}{2\pi D\nu}, \qquad b_0 = \int_0^\infty w^2(\rho)\rho\, d\rho, \qquad \nu = -\frac{1}{\ln \varepsilon}. \tag{4.20}$$

Here $|\Omega|$ is the area of domain. Assuming that $u_j = u_0$ has a common value for all of the spots, then (4.19) is a quadratic equation. In this way, the following existence criteria for k-spot quasi-equilibria were obtained in [101] for different ranges of the parameter η_ε:

$$\begin{cases} 4kL_0 < 1, & \text{for } \eta_\varepsilon \to 0 \;\Leftrightarrow\; D \gg O(\nu^{-1}), \\ 4\eta_\varepsilon L_\varepsilon < 1, & \text{for } \eta_\varepsilon \to \infty \;\Leftrightarrow\; D = O(1), \\ 4(k+\eta_0)L_0 < 1, & \text{for } \eta_\varepsilon \to \eta_0 \;\Leftrightarrow\; D = O(\nu^{-1}) \,. \end{cases} \tag{4.21}$$

Here $L_0 = \lim_{\varepsilon\to 0} L_\varepsilon = O(1)$ and $\eta_0 = \lim_{\varepsilon\to 0}\eta_\varepsilon = O(1)$.

From (4.20), it follows that the second line in (4.21) is for the parameter range $A = O\left(\varepsilon[-\ln\varepsilon]^{1/2}\right)$ with $D = O(1)$, while the third line in (4.21) is for the range $A = O(\varepsilon)$ with $D = O(\nu^{-1})$ and $\nu = -1/\ln\varepsilon$. We emphasize that the asymptotic construction of k-spot quasi-equilibria in §3.1 is for the range $D = O(1)$ and $A = O(\varepsilon[-\ln\varepsilon])$ (see (3.4) and (3.12)). In addition, equation (3.19) derived in §3.1 pertains to the range $A = O(\varepsilon[-\ln\varepsilon])$ with $D = O(\nu^{-1})$. Consequently, the k-spot quasi-equilibrium patterns constructed in [101] do not correspond to the range $A = O(\varepsilon[-\ln\varepsilon])$ where spot self-replication occurs, as considered in our analysis.

As shown in [101], the leading order quasi-equilibrium solution $u_j \sim u_0$ in the inner region, together with the global representation for the v, have the form

$$u_0^{\pm} \sim \begin{cases} \frac{1}{2}\left(1 \pm \sqrt{1-4kL_0}\right), & \text{for } D \gg O(\nu^{-1})\,, \\ \frac{1}{2}\left(1 \pm \sqrt{1-4\eta_\varepsilon L_\varepsilon}\right) & \text{for } D = O(1)\,, \\ \frac{1}{2}\left(1 \pm \sqrt{1-4(k+\eta_0)L_0}\right), & \text{for } D = O(\nu^{-1})\,, \end{cases} \tag{4.22a}$$

$$v_0^{\pm} \sim \sum_{j=1}^{k} \frac{1}{Au_0^{\pm}}\, w\left(\varepsilon^{-1}|\mathbf{x}-\mathbf{x}_j|\right) \,. \tag{4.22b}$$

The stability analysis in [101] was largely based on the derivation and analysis of the nonlocal eigenvalue problem

$$\Delta_{\mathbf{y}}\psi - \psi + 2w\psi - \gamma\, w^2 \frac{\int_0^\infty w\psi\rho\, d\rho}{\int_0^\infty w^2\rho\, d\rho} = \lambda\psi\,, \quad 0 < \rho < \infty\,, \tag{4.23}$$

with $\psi \to 0$ as $\rho \to \infty$. In (4.23) there are two choices for γ, given by

$$\gamma = \frac{2\eta_\varepsilon L_\varepsilon(1+\tau\lambda) + kL_\varepsilon}{(u_0^2 + L_\varepsilon\eta_\varepsilon)(1+\tau\lambda) + kL_\varepsilon}\,, \qquad \text{or} \qquad \gamma = \frac{2\eta_\varepsilon L_\varepsilon}{u_0^2 + L_\varepsilon\eta_\varepsilon}\,. \tag{4.24}$$

In (4.24) it was assumed in [101] that $\tau = O(1)$.

Theorem 2.3 of [101] gives a stability result for k-spot equilibrium solution based on an analysis of the NLEP (4.23) together with certain properties of the multi-variable function $\mathcal{F}(\mathbf{x}_1, \ldots, \mathbf{x}_k)$ defined by

$$\mathcal{F}(\mathbf{x}_1, \ldots, \mathbf{x}_k) = -\sum_{i=1}^{k}\sum_{j=1}^{k} \mathcal{G}_{ij} \,. \tag{4.25}$$

Here $\mathcal{G}$ is the Green's matrix of (3.11) defined in terms of the reduced-wave Green's function. It was shown in [101] that the equilibrium spot locations for an equilibrium k-spot pattern must be at a critical point of $\mathcal{F}(\mathbf{x}_1, \ldots, \mathbf{x}_k)$. We denote by $\mathcal{H}_0$ the Hessian of $\mathcal{F}$ at this critical point.

Suppose that $4(\eta_\varepsilon + k)L_\varepsilon < 1/4$. Then, Theorem 2.3 of [101] proves that the large solutions (u^+, v^+) are all linearly unstable. For the small solutions (u^-, v^-), the following rigorous results of [101] hold for different ranges of η_ε:

1. Assume that $\eta_\varepsilon \to 0$, so that $D \gg O(\nu^{-1})$. Then,
    - If $k = 1$, and all the eigenvalues of the Hessian $\mathcal{H}_0$ are negative, then there exists a unique $\tau_1 > 0$, such that for $\tau < \tau_1$, (u^-, v^-) is linearly stable, while for $\tau > \tau_1$, it is linearly unstable.
    - If $k > 1$, (u^-, v^-) is linearly unstable for any $\tau \geq 0$.
    - If the Hessian $\mathcal{H}_0$ has a strictly positive eigenvalue, (u^-, v^-) is linearly unstable for any $\tau \geq 0$.
2. Assume that $\eta_\varepsilon \to \infty$, so that $D \ll O(\nu^{-1})$. Then,
    - If all the eigenvalues of the Hessian $\mathcal{H}_0$ are negative, then (u^-, v^-) is linearly stable for any $\tau > 0$.
    - If the Hessian $\mathcal{H}_0$ has a strictly positive eigenvalue, (u^-, v^-) is linearly unstable for any $\tau \geq 0$.
3. Assume that $\eta_\varepsilon \to \eta_0$, so that $D = O(\nu^{-1})$. Then,
    - If $L_0 < \frac{\eta_0}{(2\eta_0+k)^2}$, and all eigenvalues of $\mathcal{H}_0$ are negative, then (u^-, v^-) is linearly stable for $\tau = O(1)$ sufficiently small or $\tau = O(1)$ sufficiently large.
    - If $k = 1$, $L_0 > \frac{\eta_0}{(2\eta_0+k)^2}$, and all the eigenvalues of $\mathcal{H}_0$ are negative, then there exists $\tau_2 > 0$, $\tau_3 > 0$, such that for $\tau < \tau_1$, (u^-, v^-) is linearly stable, while for $\tau > \tau_3$, it is linearly unstable.

- If $k > 1$ and $L_0 > \frac{\eta_0}{(2\eta_0+k)^2}$, then (u^-, v^-) is linearly unstable for any $\tau > 0$.
- If the Hessian $\mathcal{H}_0$ has a strictly positive eigenvalue, (u^-, v^-) is linearly unstable for any $\tau \geq 0$.

We close this section with several remarks relating our analysis with that in [101]. Firstly, the condition of [101] that an equilibrium k-spot configuration $(\mathbf{x}_1, \ldots, \mathbf{x}_k)$ must be at a critical point of $\mathcal{F}$ in (4.25) is equivalent to the equilibrium result in Principal Result 3.4 of §3.3 provided that we replace the source strengths S_j in (3.36) by their leading-order asymptotically common value $S_c \sim \mathcal{A}$, as given in (3.13). The stability condition of [101] expressed in terms of the sign of the eigenvalues of the Hessian $\mathcal{H}_0$ of $\mathcal{F}$ is equivalent to the statement that the equilibrium spot configuration $(\mathbf{x}_1, \ldots, \mathbf{x}_k)$ is stable with respect to the slow motion ODE dynamics (3.35) in Principal Result 3.3 when we use the leading-order approximation $S_j \sim S_c$ for $j = 1, \ldots, k$ in (3.35). Therefore, the condition on the Hessian $\mathcal{H}_0$ in [101] relates to the small eigenvalues of order $O(\varepsilon^2)$ that are reflected in the stability of equilibrium points under the ODE dynamics (3.35).

Next, we relate our asymptotic parameter ranges considered for A and D with those considered in [101]. The second result of Theorem 2.3 of [101] for $\eta_\varepsilon \to \infty$, as written above, includes the range $D = O(1)$. The condition $4(\eta_\varepsilon + k)L_\varepsilon < 1/4$, together with (4.20) relating L_ε to A, shows this second result of [101] holds for the range $A = O\left(\varepsilon \left[-\ln \varepsilon\right]^{1/2}\right)$. Therefore, for this range of A and D, the analysis in [101] predicts that there is an equilibrium solution branch whose stability depends only on the eigenvalues of the Hessian matrix $\mathcal{H}_0$. Likewise, it is readily seen that the third statement in Theorem 2.3 of [101], as written above, pertains to the range $D = O(\nu^{-1})$ with $A = O(\varepsilon)$. Finally, we remark that, with the exception of the condition on the Hessian matrix of $\mathcal{F}$, the stability criteria developed in [101] can depend on the number k of spots, but does not depend on the configuration $(\mathbf{x}_1, \ldots, \mathbf{x}_k)$ of spot locations within the domain.

In our theoretical framework for the stability of k-spot quasi-equilibria solutions, as expressed in Principal Results 4.1 and 4.2, we considered the parameter range $A = O\left(\varepsilon \left[-\ln \varepsilon\right]\right)$ and $D = O(1)$. To leading-order in ν, where the k spots can be decoupled, we showed from a numerical computation of the two-component eigenvalue problem (4.2) with $N_j' \to 0$ as $\rho \to \infty$, that a k-spot quasi-equilibrium solution is always stable to $O(1)$ time-scale instabilities. This leading-order result is similar to that proved in the second statement of Theorem 2.3 of [101] for the nearby parameter range $A = O\left(\varepsilon\,[-\ln\varepsilon]^{1/2}\right)$ and $D = O(1)$. Our goal in the later sections §4.3, §4.4, and §4.5 is to go beyond this simple leading-order theory in ν and to show, specifically, that the spatial configuration $(\mathbf{x}_1, \ldots, \mathbf{x}_k)$ does have a rather significant effect on the stability of quasi-equilibrium k-spot patterns. In addition, in our stability formulation, we will are able to consider a single parameter range for A and D, i.e. $A = O\left(\varepsilon\,[-\ln\varepsilon]\right)$ and $D = O(1)$, where three separate instability mechanisms can occur: spot self-replication, oscillatory instabilities of the spot amplitudes, and competition instabilities of the spot amplitudes.

4.2.3 Comparison of the Quasi-Equilibrium Solutions

In this sub-section we show that our asymptotic construction of quasi-equilibrium k-spot solutions, as given in Principal Result 3.1 of §3.1, can be reduced to that given in [101] when $\mathcal{A} = O(\nu^{1/2})$ in (3.8). Note that when $\mathcal{A} = O(\nu^{1/2})$, then $A = O\left(\varepsilon\,[-\ln\varepsilon]^{1/2}\right)$ from (3.4), which is the key parameter regime of [101].

For $\mathcal{A} = O(\nu^{1/2})$, the nonlinear algebraic system (3.8) together with the core problem (3.2), suggest that we expand U_j, V_j, S_j, and χ, in (3.2) as

$$\begin{aligned} &\chi \sim \nu^{-1/2}(\chi_{0j} + \nu\chi_{1j} + \cdots)\,, \quad U_j \sim \nu^{-1/2}(U_{0j} + \nu U_{1j} + \cdots)\,, \\ &S_j \sim \nu^{1/2}(S_{0j} + \nu S_{1j} + \cdots)\,, \quad V_j \sim \nu^{1/2}(V_{0j} + \nu V_{1j} + \cdots)\,. \end{aligned} \tag{4.26}$$

Upon substituting (4.26) into (3.2), and collecting powers of ν, we obtain the leading-order problem

$$\Delta U_{0j} = 0\,, \qquad U_{0j} \to \chi_{0j} \quad \text{as} \quad \rho \to \infty\,, \tag{4.27a}$$

$$\Delta V_{0j} - V_{0j} + U_{0j}V_{0j}^2 = 0\,, \qquad V_{0j} \to 0 \quad \text{as} \quad \rho \to \infty\,. \tag{4.27b}$$

At next order, we obtain that

$$\Delta U_{1j} = U_{0j}V_{0j}^2\,, \qquad U_{1j} \to S_{0j}\ln\rho + \chi_{1j} \quad \text{as} \quad \rho \to \infty\,, \tag{4.28a}$$

$$\Delta V_{1j} - V_{1j} + 2U_{0j}V_{0j}V_{1j} = -U_{1j}V_{0j}^2\,, \qquad V_{1j} \to 0 \quad \text{as} \quad \rho \to \infty\,. \tag{4.28b}$$

At one higher order, we find that U_{2j} satisfies

$$\Delta U_{2j} = 2U_{0j}V_{0j}V_{1j} + V_{0j}^2U_{1j}\,, \quad U_{2j} \to S_{1j}\ln\rho + \chi_{2j} \quad \text{as} \quad \rho \to \infty\,. \tag{4.29}$$

The solution to (4.27) is simply $U_{0j} = \chi_{0j}$, and $V_{0j} = w/\chi_{0j}$, where $w(\rho)$ is the radially symmetric ground-state solution of the scalar nonlinear problem (4.14). Upon applying the divergence theorem to (4.28a), and using $U_{0j} = \chi_{0j}$ and $V_{0j} = w/\chi_{0j}$, we calculate S_{0j} in terms of χ_{0j} as

$$S_{0j} = \int_0^\infty U_{0j} V_{0j}^2 \, \rho \, d\rho = \frac{b_0}{\chi_{0j}} \,, \qquad b_0 \equiv \int_0^\infty w^2 \, \rho \, d\rho \,. \tag{4.30}$$

Next, we decompose the solution to (4.28) in the form

$$U_{1j} = \frac{1}{\chi_{0j}} \Big(\chi_{0j} \chi_{1j} + \hat{U}_{1j} \Big) \,, \qquad V_{1j} = \frac{1}{\chi_{0j}^3} \Big(-\chi_{0j} \chi_{1j} \, w + \hat{V}_{1j} \Big) \,,$$

where $\hat{U}_{1j}$ and $\hat{V}_{1j}$ are the unique solutions of

$$\Delta_\rho \hat{U}_{1j} = w^2 \,, \qquad \hat{U}_{1j} - b_0 \ln \rho \to 0 \quad \text{as} \quad \rho \to \infty \,, \tag{4.31a}$$

$$\Delta_\rho \hat{V}_{1j} - \hat{V}_{1j} + 2w \hat{V}_{1j} = -\hat{U}_{1j} \, w^2 \,, \qquad \hat{V}_{1j} \to 0 \quad \text{as} \quad \rho \to \infty \,. \tag{4.31b}$$

Similarly, by applying the divergence theorem to (4.29), we calculate S_{1j} as

$$S_{1j} = -\frac{b_0 \chi_{1j}}{\chi_{0j}^2} + \frac{b_1}{\chi_{0j}^3} \,, \qquad b_1 \equiv \int_0^\infty (w^2 \hat{U}_{1j} + 2w \hat{V}_{1j}) \, \rho \, d\rho \,. \tag{4.32}$$

The BVP solver COLSYS (cf. [2]) is used to numerically compute the ground state solution $w(\rho)$ of (4.14) and the solutions $\hat{U}_{1j}$ and $\hat{V}_{1j}$ of (4.31). Then, by using a simple numerical quadrature, we calculate $b_0 = 4.9347$ and $b_1 = 0.8706$..

Finally, upon substituting (4.30) and (4.32) into the nonlinear algebraic system (3.8) of §3.1 we obtain that $\mathcal{A} = O(\nu^{1/2})$, where

$$\mathcal{A} = \nu^{1/2} \left(\chi_{0j} + \frac{b_0}{\chi_{0j}} \right) + \nu^{3/2} \Big[\frac{b_1}{\chi_{0j}^3} + \left(1 - \frac{b_0}{\chi_{0j}^2} \right) \chi_{1j} + 2\pi \left(\frac{b_0}{\chi_{0j}} R_{jj} + \sum_{i \neq j}^{k} \frac{b_0}{\chi_{0i}} G_{ij} \right) \Big] \,. \tag{4.33}$$

For a prescribed $\mathcal{A}$ with $\mathcal{A} = \mathcal{A}_0 \nu^{1/2} + \mathcal{A}_1 \nu^{3/2} + \cdots$, we could then calculate χ_{0j} and χ_{1j} from (4.33). Since $\mathcal{A} = O(\nu^{1/2})$ corresponds to $A = O\left(\varepsilon \, [-\ln \varepsilon]^{1/2} \right)$, we conclude that it is in this parameter range that the coupled core problem (3.2) reduces to the scalar ground-state problem for the fast variable v, as was studied in [101].

Finally, we show that (4.33) reduces to the expression (4.19) used in [101]. To see this, we note that

$$\mathcal{A} = \frac{A\sqrt{D}\nu}{\varepsilon}\,, \qquad u_j = \frac{\varepsilon}{A\sqrt{D}} U_j \approx \frac{\varepsilon}{A\sqrt{D}\nu^{1/2}}\,\chi_{0j}\,.$$

Moreover, for $D \gg O(1)$, we use $R_{jj} = \frac{D}{|\Omega|} + O(1)$ and $G_{ij} = \frac{D}{|\Omega|} + O(1)$ for $i \neq j$. Then, from (4.33), we obtain

$$\frac{A\sqrt{D}\nu}{\varepsilon} \sim \frac{A\sqrt{D}\nu}{\varepsilon} u_j + \frac{b_0\varepsilon}{A\sqrt{D}\,u_j} + \frac{2\pi\nu D}{|\Omega|}\left[\frac{b_0\varepsilon}{A\sqrt{D}\,u_j} + \sum_{i\neq j}^{k} \frac{b_0\varepsilon}{A\sqrt{D}\,u_i}\right]. \quad (4.34)$$

Upon using the definitions of L_ε and η_ε in (4.20), we can write (4.34) as

$$1 - u_j = \frac{b_0\varepsilon^2}{A^2 D\nu\, u_j} + \frac{2\pi}{|\Omega|}\frac{b_0\varepsilon^2}{A^2}\sum_{i=1}^{k}\frac{1}{u_i} = \frac{L_\varepsilon\eta_\varepsilon}{u_j} + \sum_{i=1}^{k}\frac{L_\varepsilon}{u_i}\,, \quad (4.35)$$

which is exactly the same as in (4.19).

4.2.4 Comparison of the Eigenvalue Problem

Next, we show for $\mathcal{A} = O(\nu^{1/2})$ and $D = O(\nu^{-1})$ that our eigenvalue problem, consisting of (4.2) coupled to (4.7), can be reduced to the nonlocal eigenvalue problem (4.23) considered in [101]. To show this, we expand Φ_j, N_j, B_j, and C_j, in (4.2) as

$$B_j = B_{j0} + \nu B_{j1} + \cdots\,, \qquad C_j = \nu(C_{j0} + \nu C_{j1} + \cdots)\,,$$
$$N_j = N_{j0} + \nu N_{j1} + \cdots\,, \qquad \Phi_j = \nu\psi_j + \cdots\,.$$

Upon substituting these expansions, together with $U_j \sim \nu^{-1/2}\chi_{0j}$ and $V_j \sim \nu^{1/2} w/\chi_{0j}$, into (4.2b), we obtain that $N_{j0} = B_{j0}$, and that N_{j1} satisfies

$$\Delta_\rho N_{j1} = \frac{w^2}{\chi_{0j}^2} B_{j0} + 2w\psi_j\,, \quad N_{j1} \to C_{j0}\ln\rho + B_{j1} \quad \text{as } \rho\to\infty\,. \quad (4.36)$$

Upon applying the divergence theorem to (4.36) we obtain that

$$C_{j0} = \frac{b_0}{\chi_{0j}^2} B_{j0} + 2\int_0^\infty w\psi_j\rho\,d\rho\,, \qquad b_0 \equiv \int_0^\infty w^2\rho\,d\rho\,. \quad (4.37)$$

Then, we let $D = D_0/\nu \gg 1$ where $D_0 = O(1)$, and we assume that $\chi_{0j} = \chi_0$ so that to leading-order each local spot solution is the same. For

$D \gg 1$, the λ-dependent Green's function $G_\lambda(\mathbf{x}_i;\mathbf{x}_j)$ and its regular part, $R_{\lambda\, jj}$ are given by

$$G_{\lambda\, ij} \sim \frac{D}{|\Omega|(1+\tau\lambda)} + O(1)\,, \quad i \neq j\,; \quad R_{\lambda\, jj} \sim \frac{D}{|\Omega|(1+\tau\lambda)} + O(1)\,,$$

We substitute this leading-order behavior for $G_{\lambda\, ij}$ and $R_{\lambda jj}$, together with $B_j \sim B_{j0}$, $C_j \sim \nu C_{j0}$, and $D = D_0/\nu$, into (4.7). In this way, we obtain to leading-order that (4.7) reduces asymptotically to

$$C_{j0} + \frac{2\pi D_0}{(1+\tau\lambda)|\Omega|} \sum_{i=1}^{k} C_{i0} + B_{j0} = 0\,.$$

Upon substituting (4.37) for C_{j0} into this equation, we obtain that B_j for $j = 1, \ldots, k$ satisfies

$$\left(1 + \frac{b_0}{\chi_0^2}\right) B_{j0} + \frac{2\pi D_0}{(1+\tau\lambda)|\Omega|} \frac{b_0}{\chi_0^2} \sum_{i=1}^{k} B_{i0}$$
$$= -2 \int_0^\infty w\psi_j \,\rho\, d\rho - \frac{4\pi D_0}{(1+\tau\lambda)|\Omega|} \sum_{i=1}^{k} \int_0^\infty w\psi_i \,\rho\, d\rho\,. \quad (4.38)$$

Next, we define the vectors $\mathbf{p}_0$ and Ψ by

$$\mathbf{p}_0 = (B_{10}, \ldots, B_{k0})^t\,, \quad \Psi = \left(\int_0^\infty \omega\psi_1 \,\rho\, d\rho\,, \ldots\,, \int_0^\infty \omega\psi_k \,\rho\, d\rho \right)^t\,.$$

This allows us to re-write (4.38) in matrix form as

$$\left[\left(1 + \frac{b_0}{\chi_0^2}\right) \mathcal{I} + \frac{2\pi D_0}{(1+\tau\lambda)|\Omega|} \frac{b_0}{\chi_0^2} \mathbf{e}\mathbf{e}^t \right] \mathbf{p}_0 = -\left(2\,\mathcal{I} + \frac{4\pi D_0}{(1+\tau\lambda)|\Omega|} \mathbf{e}\mathbf{e}^t \right) \Psi\,,$$

where $e = (1, \ldots, 1)^t$. The matrix multiplying $\mathbf{p}_0$ is an invertible rank-one perturbation of the identity matrix. Hence, we calculate that

$$\mathbf{p}_0 = \mathcal{D}\Psi\,, \quad (4.39\text{a})$$

where the matrix $\mathcal{D}$ is defined by

$$\mathcal{D} \equiv -\left[\left(1 + \frac{b_0}{\chi_0^2}\right) \mathcal{I} + \frac{2\pi D_0}{(1+\tau\lambda)|\Omega|} \frac{b_0}{\chi_0^2} \mathbf{e}\mathbf{e}^t \right]^{-1} \left(2\,\mathcal{I} + \frac{4\pi D_0}{(1+\tau\lambda)|\Omega|} \mathbf{e}\mathbf{e}^t \right)\,. \quad (4.39\text{b})$$

We then rewrite (4.39b) in terms of L_ε and η_ε, as defined in (4.20), to get

$$\frac{b_0}{\chi_0^2} = \frac{\eta_\varepsilon L_\varepsilon}{u_0^2}\,, \qquad \frac{2\pi D_0}{(1+\tau\lambda)|\Omega|} = \frac{1}{\eta_\varepsilon}\frac{1}{1+\tau\lambda}\,.$$

Then, since the eigenvalues of matrix $\mathbf{e}\mathbf{e}^t$ are either k or 0, it readily follows that the two distinct eigenvalues r_1 and r_2 of the matrix $\mathcal{D}$ are

$$r_1 = -\frac{2\chi_0^2}{b_0}\frac{L_\varepsilon\eta_\varepsilon + \frac{kL_\varepsilon}{1+\tau\lambda}}{(u_0^2+L_\varepsilon\eta_\varepsilon)+\frac{kL_\varepsilon}{1+\tau\lambda}}\,, \qquad r_2 = -\frac{2\chi_0^2}{b_0}\frac{L_\varepsilon\eta_\varepsilon}{u_0^2+L_\varepsilon\eta_\varepsilon}\,. \tag{4.40}$$

Finally, to obtain a nonlocal eigenvalue problem we substitute $U_j \sim \nu^{-1/2}\chi_0$, $V_j \sim \nu^{1/2}w/\chi_0$, $\Phi_j \sim \nu\psi_j$, and $N_{j0} \sim B_{j0}$, into (4.2a) to obtain the vector NLEP

$$\Delta_{\mathbf{y}}\psi - \psi + 2w\psi + \frac{w^2 b_0}{\chi_0^2}\frac{\int_0^\infty \rho w \mathcal{D}\psi\, d\rho}{\int_0^\infty \rho w^2\, d\rho} = \lambda\psi\,,$$

where $\psi \equiv (\psi_1,\ldots,\psi_k)^t$. By diagonalizing this vector NLEP by using the eigenpairs of $\mathcal{D}$, we obtain the scalar NLEP problem

$$\Delta_{\mathbf{y}}\psi_c - \psi_c + 2w\psi_c + w^2\left(\frac{r_i b_0}{\chi_0^2}\right)\frac{\int_0^\infty \rho w\psi_c\, d\rho}{\int_0^\infty \rho w^2\, d\rho} = \lambda\psi_c\,, \quad i=1,2\,, \tag{4.41}$$

where r_1 and r_2 are the eigenvalues of $\mathcal{D}$ given in (4.40). Finally, by using (4.40) for r_1 and r_2, it readily follows that (4.41) reduces to the NLEP (4.23) studied rigorously in [101].

Therefore, we conclude that our eigenvalue formulation in §4.1 reduces to leading-order in ν to the NLEP problem of [101] when $A = O\left(\varepsilon\,[-\ln\varepsilon]^{1/2}\right)$ and $D = O(\nu^{-1})$.

4.3 Instabilities in an Unbounded Domain

In this section, we calculate stability thresholds for the case of the infinite planar domain $\mathbb{R}^2$. For this domain, we can eliminate the diffusivity D by scaling $\mathbf{x}$ and ε with $\sqrt{D}$ as in (4.12). Therefore, without loss of generality, we take $D=1$ in this section. For $D \neq 1$, we simply note that ε and $\mathbf{x}$ must be re-defined as in (4.12).

For the infinite-domain problem with $\Omega = \mathbb{R}^2$, the reduced-wave Green's function and its regular part satisfying (3.6) with $D=1$ is simply

$$G(\mathbf{x};\mathbf{x}_j) = \frac{1}{2\pi}K_0\left|\mathbf{x}-\mathbf{x}_j\right|\,, \qquad R_{jj} = \frac{1}{2\pi}(\ln 2 - \gamma_e)\,. \tag{4.42}$$

Here γ_e is Euler's constant, and $K_0(r)$ is the modified Bessel function of the second kind of order zero.

The construction of a k-spot quasi-equilibrium solution with spots at $\mathbf{x}_j \in \mathbb{R}^2$ for $j = 1, \ldots, k$ proceeds by the analysis in §3.1. This quasi-equilibrium solution is given in (3.9) of Principal Result 3.1, where from (3.8) and (4.42), the source strengths $S_1, \ldots, S_k$ satisfy the nonlinear algebraic system

$$\mathcal{A} = S_j\Big(1 + \nu(\ln 2 - \gamma_e)\Big) + \nu \sum_{i \neq j}^{k} S_i K_0 \left|\mathbf{x}_i - \mathbf{x}_j\right| + \nu \chi(S_j)\,, \quad j = 1, \ldots, k\,, \tag{4.43a}$$

$$\mathcal{A} = \varepsilon^{-1} \nu A\,, \qquad \nu = -1/\ln\varepsilon\,. \tag{4.43b}$$

To determine the stability of the k-spot quasi-equilibrium solution to locally radially symmetric perturbations, we must find the eigenvalues of the coupled system, consisting of (4.8) for $j = 1, \ldots, k$ together with the homogeneous linear system (4.9). The λ-dependent Green's function and its regular part, satisfying (4.5) with $D = 1$ in $\mathbb{R}^2$, are given by

$$G_\lambda(\mathbf{x}; \mathbf{x}_j) = \frac{1}{2\pi} K_0\left(\sqrt{1 + \tau\lambda}\,|\mathbf{x} - \mathbf{x}_j|\right)\,, \tag{4.44a}$$

$$R_{\lambda jj} = \frac{1}{2\pi}\Big(\ln 2 - \gamma_e - \log\sqrt{1 + \tau\lambda}\Big)\,. \tag{4.44b}$$

Since λ can be complex, we must take $\log z$ to be the principal branch of the logarithm function and choose for $z = \sqrt{1 + \tau\lambda}$ the principal branch of the square root, in order that $K_0(z)$ decays when $z \to \infty$ along the positive real axis. In terms of these Green's functions, the homogeneous linear system (4.9) becomes

$$\begin{aligned} &C_j\Big(1 + \nu(\ln 2 - \gamma_e - \log\sqrt{1 + \tau\lambda} + \hat{B}_j)\Big) \\ &\qquad + \nu \sum_{i \neq j}^{k} C_i K_0\left(\sqrt{1 + \tau\lambda}\,|\mathbf{x}_i - \mathbf{x}_j|\right) = 0\,, \quad j = 1, \ldots, k\,. \end{aligned} \tag{4.45}$$

From this formulation, in the next two subsections we consider the specific cases of one- and two-spot solutions in $\mathbb{R}^2$.

4.3.1 A One-Spot Solution

For a one-spot pattern with spot at the origin, (4.43) reduces to the scalar nonlinear algebraic equation

$$\mathcal{A} = S_1 + \nu S_1(\ln 2 - \gamma_e) + \nu\chi(S_1)\,, \quad \mathcal{A} = \varepsilon^{-1}\nu A\,, \quad \nu = -1/\ln\varepsilon\,. \quad (4.46)$$

In order that $C_1 \neq 0$ in (4.45), we require that λ satisfy

$$\hat{B}_1 + \frac{1}{\nu} + \left(\ln 2 - \gamma_e - \log\sqrt{1+\tau\lambda}\right) = 0\,. \quad (4.47)$$

Here $\hat{B}_1 = \hat{B}_1(\lambda, S_1)$ is to be computed from the inner problem (4.8) in terms of the core solution U_1 and V_1. Therefore, (4.47) is a transcendental equation for the eigenvalue λ.

We now use our numerical procedure, outlined in §4.1.1, to compute λ and to determine the threshold conditions for instability of the one-spot profile.

Experiment 4.1: One-spot solution in the infinite domain: A Hopf bifurcation

For a one-spot solution in $\mathbf{R}^2$, our computational results lead to a phase diagram in the A versus τ parameter-plane characterizing the stability of a one-spot solution. In the numerical results below we have fixed $\varepsilon = 0.02$.

Firstly, from (4.46) we compute that there is no quasi-equilibrium one-spot solution when $A \geq A_f = 0.1766$. This minimum value of A for the existence of such a solution was obtained by varying the source strength S_1 in (4.46) in the interval $S_1 \in [0.22, 7.41]$. This value $A = A_f$ is the lower horizontal dot-dashed line in Fig. 4.3(a). The peanut-splitting threshold for A, obtained from the theory in Chapter 3, is obtained by using the spot-splitting criterion $S_1 = \Sigma_2 \approx 4.3071$ and $\chi(\Sigma_2) \approx -1.783$ in (4.46), which yields $A_2 = 0.311$. This threshold value for spot self-replication is shown by the heavy dotted horizontal line in Fig. 4.3(a). Then, we use the numerical algorithm in §4.1.1 to compute a Hopf bifurcation threshold $\tau = \tau_H$ for values of A in the interval $A \in [0.1766, 0.298]$. At this Hopf bifurcation value, a complex complex conjugate pair of eigenvalues first enters the right half-plane. In Fig. 4.3(a), we plot the Hopf bifurcation value A vs. τ_H by the solid curve. The resulting parameter-plane as shown in Fig. 4.3(a) is divided into four distinct regions with different solution behavior.

The behavior of the one-spot solution in the four different regions of Fig. 4.3(a) is as follows. In Regime σ with $A < A_f$, the quasi-equilibrium solution does not exist; in Regime β enclosed by the dot-dashed line $A_f =$

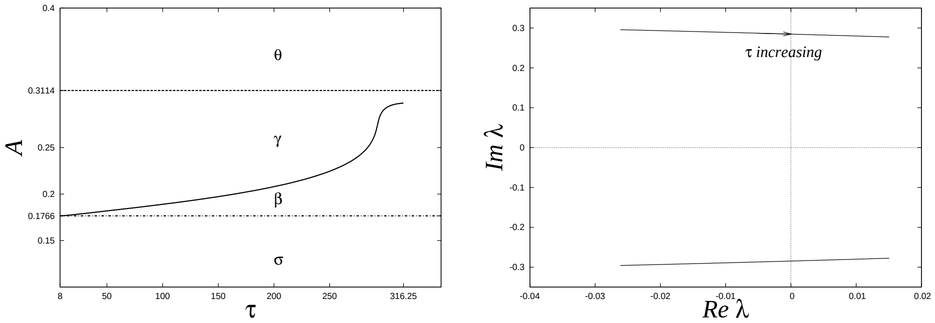

(a) A vs. τ (b) Im(λ) vs. Re(λ)

Figure 4.3: *Experiment 4.1: One-spot solution in* $\mathbb{R}^2$*. (a) Phase-diagram in the parameter plane* A *vs.* τ*. The solid curve plots the Hopf bifurcation threshold* τ_H*, the lower horizontal dot-dashed line plots the existence condition* $A_f = 0.1766$ *and the upper heavy dotted horizontal line indicates the spot-splitting threshold* $A_2 = 0.311$*. Regime* σ*: No quasi-equilibrium solution exists; Regime* β*: Oscillations in the spot amplitude; Regime* γ*: Stable one-spot solution; Regime* θ*: spot self-replication regime. (b) Fix* $A = 0.18$*, we plot the spectrum in the complex* λ *plane for* $\tau \in [30, 40]$*. At* $\tau = 30$*,* $\lambda = -0.026 \pm 0.296\,i$*. At* $\tau = 36.05$*,* $\lambda = -0.000049 \pm 0.285\,i$*. At* $\tau = 40$*,* $\lambda = 0.015 \pm 0.278\,i$*. Here* $i \equiv \sqrt{-1}$*. As* τ *increases a complex conjugate pair of eigenvalues enters the right half-plane.*

0.1766 and the solid Hopf bifurcation curve, the quasi-equilibrium solution is unstable to an oscillatory profile instability; in Regime γ it is stable; and in Regime θ, it is unstable to spot self-replication.

In Fig. 4.3(b), we fix $A = 0.18$ and plot the eigenvalue λ in the complex plane for the range $\tau \in [30, 40]$. Note that for $A = 0.18$, the Hopf bifurcation threshold $\tau_H = 36.06$ is where the complex conjugate pair of eigenvalues intersect the imaginary axis. As τ increases, we find numerically that $\text{Re}(\lambda)$ increases.

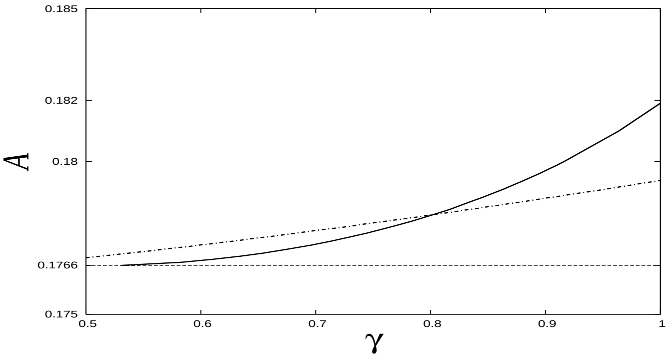

Figure 4.4: *One-spot solution in* $\mathbb{R}^2$*. In the parameter plane* A *vs.* $\gamma \equiv -\ln\tau/\ln\varepsilon$*, we plot the existence threshold* $A_f = 0.1766$ *by the thin dashed line, our Hopf bifurcation threshold* A *by the dot-dashed curve, and the stability threshold* $\tilde{A}_s$ *from the NLEP theory by the thick solid curve.*

In Fig. 4.4, we compare the stability threshold for A obtained from a numerical computation of the coupled eigenvalue formulation (4.8) and (4.47) with that obtained from the NLEP analysis of [99], summarized in §4.2.1. Recall from (4.16) and (4.18) that there are two threshold values $\tilde{A}_f$ and $\tilde{A}_s$ predicted from the leading-order (in ν) NLEP theory of [99]. For $A < \tilde{A}_f$ a one-spot quasi-equilibrium solution does not exist. For $A < \tilde{A}_s$ this solution is unstable. These threshold values, with $\tilde{A}_s$ depending on τ, are

$$\tilde{A}_f \equiv 2\varepsilon\sqrt{\frac{b_0}{\nu}}, \quad b_0 \equiv \int_0^\infty w^2(\rho)\rho\, d\rho \approx 4.9347\,, \tag{4.48a}$$

$$\tilde{A}_s \equiv \tilde{A}_f \left[1 - \left(-\frac{\gamma}{4+\gamma}\right)^2\right]^{-1/2}, \qquad \gamma \equiv -\ln\tau/\ln\varepsilon\,. \tag{4.48b}$$

For $\varepsilon = 0.02$, we compute that $\tilde{A}_f \approx 0.1757$, which agrees very well with our existence threshold value $A_f \approx 0.1766$. In Fig. 4.4 we compare the

NLEP stability threshold $\tilde{A}_s$ versus $\gamma = -\ln\tau/\ln\varepsilon$ with the Hopf bifurcation threshold A versus $\gamma = -\ln\tau_H/\ln\varepsilon$, which corresponds to the solid curve of Fig. 4.3(a). We recall from §4.2.1 that the NLEP theory predicts instability when $A < \tilde{A}_s$ for $0 \leq \tau \leq \varepsilon^{-2}$, but has no conclusion regarding stability or instability if $A > \tilde{A}_s$. Our Hopf bifurcation threshold predicts that stability changes when we cross the heavy solid curve in Fig. 4.4. Therefore, we conclude that our stability result and that predicted by the NLEP theory are only in disagreement for τ sufficiently large, after the two curves in Fig. 4.4 have crossed. This disagreement likely results from neglecting quantitatively significant logarithmic correction terms in $\nu = -1/\ln\varepsilon$ in the leading-order NLEP theory.

4.3.2 A Two-Spot Solution

Without loss of generality, we assume that the two spots are centered at $(\alpha, 0)$ and $(-\alpha, 0)$ with $\alpha > 0$ along the horizontal axis. The distance between the two spots is 2α. Since the domain is the infinite plane, the two spots always drift apart along the horizontal axis with speed $O(\varepsilon^2)$ as t increases, and there is no final equilibrium solution. However, this motion is slow compared to the possibility of $O(1)$ time-scale oscillatory or competition instabilities of the spot profile. We now numerically determine the range of parameters for these instabilities.

For this two-spot quasi-equilibrium solution, it was shown in (3.46) that the spots have a common source strength S_c, which satisfies

$$\mathcal{A} = S_c\left[1 + \nu(\ln 2 - \gamma_e) + \nu K_0(2\alpha)\right] + \nu\,\chi(S_c)\,, \quad \mathcal{A} = \varepsilon^{-1}\nu A\,, \quad \nu = -\frac{1}{\ln\varepsilon}\,, \tag{4.49}$$

where γ_e is Euler's constant. The λ-dependent Green's function is given in (4.44) and the λ-dependent Green's matrix $\mathcal{G}_\lambda$ is circulant. Therefore, Principal Result 4.2 applies. The eigenvectors V_i for $i = 1, 2$ and eigenvalues $\omega_{\lambda\,i}$ for $\mathcal{G}_\lambda$ are $V_1 \equiv (1, 1)^t$ and $V_2 \equiv (1, -1)^t$, where

$$\begin{aligned}
\omega_{\lambda\,1} &= G_{\lambda 12} + R_{\lambda 11} = K_0(2\alpha\sqrt{1+\tau\lambda}) + (\ln 2 - \gamma_e - \log\sqrt{1+\tau\lambda})\,, \quad \text{for } V_1\,,\\
\omega_{\lambda\,2} &= G_{\lambda 12} - R_{\lambda 11} = K_0(2\alpha\sqrt{1+\tau\lambda}) - (\ln 2 - \gamma_e - \log\sqrt{1+\tau\lambda})\,, \quad \text{for } V_2\,.
\end{aligned}$$

From (4.11) of Principal Result 4.2, our stability formulation is to find the roots of the two transcendental equations for λ, given by

$$1 + \nu\hat{B}_c + 2\pi\nu\omega_{\lambda\,j} = 0\,, \quad j = 1, 2\,, \tag{4.50}$$

where $\hat{B}_c(\lambda, S_c)$ is to the common value for $\hat{B}_j$ for $j = 1, 2$ in (4.8).

We will show numerically below that in some region of the A versus α parameter plane the two-spot solution becomes unstable when τ is increased due to the creation of an unstable eigenvalue λ from $\omega_{\lambda 1}$ as a result of a Hopf bifurcation. Since this oscillatory instability is associated with the eigenvector $V_1 = (1,1)^t = (C_1, C_2)^t$, it leads to the initiation of a simultaneous in-phase oscillation in the amplitudes of the two spots. In another region of the A versus α parameter plane we will also show numerically that an unstable eigenvalue λ for $\omega_{\lambda 2}$ can occur even when $\tau = 0$ if the inter-spot separation distance 2α is below some threshold. This instability results from the creation of a real positive eigenvalue. Since this instability is associated with the eigenvector $V_2 = (1,-1)^t = (C_1, C_2)^t$, it leads to the initiation of a sign-fluctuating instability in the amplitudes of the two spots, which leads ultimately to the annihilation of one of the two spots. Since this instability is triggered when 2α is sufficiently small, it is also referred to either as a competition or an overcrowding instability.

Experiment 4.2: Two-spot solution in the infinite plane: Oscillatory profile instabilities and competition instabilities

We fix $\varepsilon = 0.02$ in the computations below. In Fig. 4.5(a) the two-spot existence threshold A_f as a function of $\alpha \in [0.02, 2.02]$ is shown by the lower solid curve, while the spot self-replication threshold A_2 vs. α is shown by the top solid curve. To obtain A_f we determined the minimum value of A as S_c is varied in (4.49), while A_2 is obtained by setting $S_c = \Sigma_2 \approx 4.31$ in (4.49). In Fig. 4.5(a) the middle dotted curve is the threshold for the onset of a competition instability. These three curves separate the A versus α parameter-plane of Fig. 4.5(a) into four distinct regions. In Regime σ, the quasi-equilibrium two-spot solution does not exist. In Regime β, the two-spot quasi-equilibrium solution undergoes a competition instability for any $\tau \geq 0$. This instability ultimately leads to the annihilation of one of the spots. We note that competition threshold approaches the existence threshold when the inter-separation distance α becomes large. This is because when α is sufficiently large, the spots essentially do not interact, and there is no competition instability for a one-spot solution in $\mathbb{R}^2$. In Regime ζ, the two-spot pattern is stable to a competition instability, but becomes unstable to an oscillatory profile instability only when τ is large enough. As τ increases above a certain threshold τ_H, a Hopf bifurcation occurs and the two-spot solution is unstable to either in-phase or out-of-phase spot amplitude oscillations. The in-phase, or synchronous, oscillatory instability is the dominant of these two types. In Regime θ the two-spot quasi-equilibrium solution is unstable to spot self-replication for any $\tau \geq 0$.

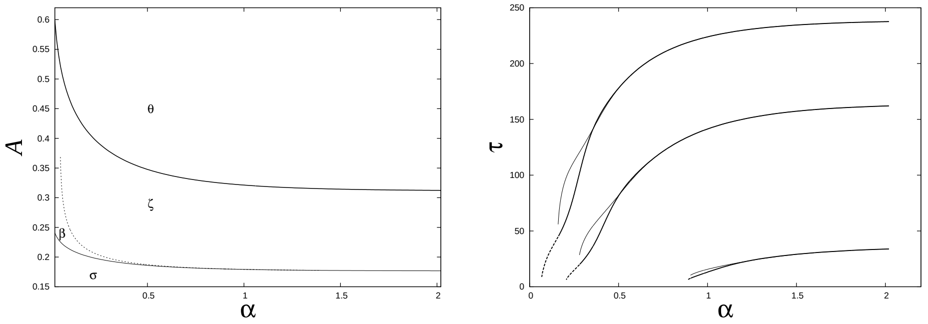

(a) A vs. α (b) τ vs. α

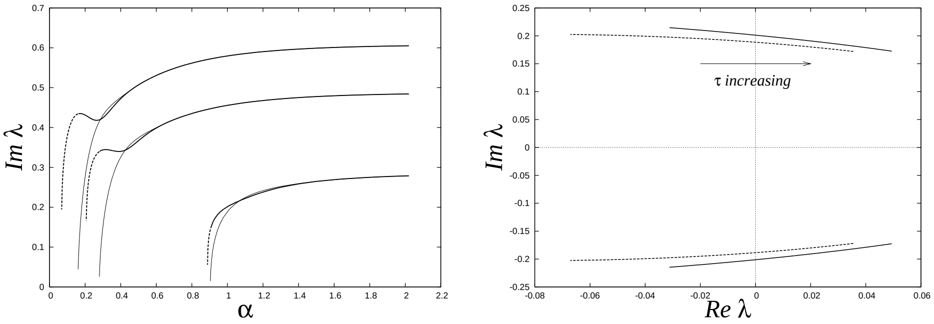

(c) λ_i vs. α (d) Im(λ) vs. Re(λ)

Figure 4.5: *Experiment 4.2: Two-spot solution in* $\mathbb{R}^2$*. (a) We plot the existence threshold* A_f *vs.* α *by the lower curve, and the spot-splitting threshold* A_2 *vs.* α *by the top curve. (b) Hopf bifurcation threshold* τ_{H1} *associated with in-phase oscillations (bottom of each pair of curves) and* τ_{H2} *associated with out-of-phase oscillations (top of each pair of curves), are plotted as a function of* α *for* $A = 0.18$ *(bottom pair),* $A = 0.2$ *(middle pair), and* $A = 0.22$ *(top pair). The dotted portions on* τ_{H1} *correspond to the parameter regime* β *in subfigure (a) where competition instabilities occur for any* τ*. (c) Imaginary part* λ_i *of* λ *versus* α *at the Hopf bifurcations thresholds for* $A = 0.18$ *(bottom),* $A = 0.2$ *(middle), and* $A = 0.22$ *(top). The heavy solid curves are the eigenvalues associated with in-phase oscillations, and the thin solid curves are the eigenvalues for out-of-phase oscillations. The dotted portions lie on* τ_{H1} *where a competition instability occurs. (d) Eigenvalue path in the complex plane for* $A = 0.18$ *and* $\alpha = 1$ *on the range* $\tau \in [10, 20]$*. The eigenvalues associated with in-phase and out-of-phase oscillations enter the right half plane at* τ_{H1} *and* τ_{H2}*, respectively.*

A a function of α and for three values of A, in Fig. 4.5(b) we plot the Hopf bifurcation thresholds τ_{H1}, associated with the eigenvector $V_1 = (1, 1)^t$ (the bottom curve in each pair of curves), and τ_{H2}, associated with eigenvector $V_2 = (1, -1)^T$ (the top curve in each pair of curves). From the bottom pair of curves to the top pair in Fig. 4.5(b), the values of A are $A = 0.18$, $A = 0.2$ and $A = 0.22$, respectively. We observe that for each fixed A, the two thresholds τ_{H1} and τ_{H2} essentially overlap when α is large enough. This is because when the two spots are far away, the interaction between them is negligible. As a consequence, when $\alpha \to \infty$, each of the two spots can be treated as a single isolated spot in the infinite plane, so that both τ_{H1} and τ_{H2} approximate the Hopf bifurcation threshold τ_H of an isolated one-spot solution.

From Fig. 4.5(b) the Hopf bifurcation curves for τ_{H1}, which each have a dotted portion, end at the values $\alpha_f = 0.888, 0.206, 0.068$ for the curves $A = 0.18, 0.2, 0.22$, respectively. At these critical values of α, the quasi-equilibrium existence condition $A > A_f(\alpha)$ is no longer satisfied. Moreover, the Hopf bifurcation threshold τ_{H2} terminates at another set of critical values $\alpha_c = 0.904, 0.28, 0.16$ for the curves $A = 0.18, 0.2, 0.22$, respectively. The reason for this disappearance is seen in Fig. 4.5(c), where we plot the imaginary part of the eigenvalues at the Hopf bifurcation thresholds for V_1 (curves with dotted portions) and V_2 (curves without dotted portions). From this figure it is clear that as $\alpha \to \alpha_c$ from above, the complex conjugate pair of eigenvalues associated with τ_{H2} merge onto the real axis at the origin, which is precisely the crossing point for the onset of a competition instability.

When the spots are two close in the sense that $\alpha_f < \alpha < \alpha_c$, then there is a positive real eigenvalue in the unstable right half-plane for any $\tau \geq 0$. If in addition, $\tau < \tau_{H1}$, it is the only unstable eigenvalue. This eigenvalue is the one associated with a competition instability. In Fig. 4.5(b) and Fig. 4.5(c), the dotted segments of the curves correspond to the range of α where this competition instability occurs.

Next, we observe from Fig. 4.5(b) that $\tau_{H1} \leq \tau_{H2}$. Therefore, the in-phase synchronous oscillatory instability of the spot amplitudes is always the dominant instability mechanism for each $\alpha > \alpha_c$ as τ is increased. Moreover, we observe that the Hopf bifurcation threshold τ_{H1} is an increasing function of spot inter-separation distance. Recall that the slow dynamics of the two spots is repulsive in the sense that α increases as t increases, with speed $O(\varepsilon^2)$ (see (3.47) of Section §3.5).. The monotone increasing nature of τ_{H1} with α eliminates any possibility of a dynamically triggered oscillatory instability for the two-spot solution. Namely, consider an initial two-spot quasi-equilibrium with initial inter-separation distance $2\alpha_0$ and with a fixed

τ with $\tau < \tau_{H1}(\alpha_0)$, where $\alpha_0 > \alpha_c$. Then, since α increases as time t increases, and τ_{H1} is monotone increasing in α, we conclude that $\tau < \tau_{H1}(\alpha)$ for any $t > 0$. Therefore, there are no dynamically triggered oscillatory instabilities for two-spot patterns on the infinite plane..

We remark that the phase diagram obtained for the two-spot quasi-equilibrium solution in $\mathbb{R}^2$ is qualitatively rather similar to the case of a two-spike solution to the one-dimensional GS model on the infinite real line in the low reed-rate regime, as was studied in [86].

Finally, we show a plot of the eigenvalue in the complex plane as τ is increased. We take $A = 0.18$ and $\alpha = 1.0$, and we vary $\tau \in [10, 20]$. The two Hopf bifurcation values are, respectively, $\tau_{H1} = 13.1$ and $\tau_{H2} = 15.6$. The paths of the eigenvalue in the complex plane as τ increases are shown in Fig. 4.5(d) for the eigenvectors V_1 (solid curves) and V_2 (dotted curves) For each of these eigenvectors, the real part of both eigenvalues λ_r increases as τ increases.

4.4 A One-Spot Solution in a Finite Domain

Next, we study the stability of a one-spot quasi-equilibrium solution in a finite domain. We will only consider the unit disk and the unit square, since it is for these domains that the reduced-wave Green's functions and its regular part, satisfying (3.6), are analytically known (see Section 3.6). We remark that for these special domains, the λ-dependent Green's function and its regular part, satisfying (4.5), can be readily obtained by replacing D with $D/(1 + \tau\lambda)$ in the formulae for the reduced-wave Green's functions given in Section 3.6. Since λ is in general complex, we require that the software for the necessary special function evaluations in Section 3.6 can treat the case of complex arguments.

4.4.1 A One-Spot Solution in the Unit Disk

Consider the unit disk $\Omega = \{\mathbf{x} : |\mathbf{x}| \leq 1\}$, and suppose that a one-spot quasi-equilibrium solution is centered at $\mathbf{x}_0$ inside the unit disk.

Experiment 4.3: One-spot solution in the unit disk: Dynamical profile instability

Let $r = |\mathbf{x}_0$ denote the distance from the spot to the center of the unit disk, so that $0 \leq r \leq 1$. The equilibrium location for the slow dynamics of the spot is at the center $r = 0$, as seen from Principal Result 3.3. We choose a value for the feed-rate parameter A such that A exceeds the existence threshold A_f for the entire range $0 < r < 1$. In Fig. 4.6(a), we plot the Hopf bifurcation threshold τ_H versus r for fixed $A = 0.16$, but for different values of the diffusivity D. The two solid curves in this figure correspond $D = 4, 5$, with the lower solid curve in this figure corresponding to $D = 4$. For these values of D, we observe from Fig. 4.6(a) that the maximum of $\tau_H = \tau_H(r)$ is obtained at the equilibrium location $r = 0$, and that τ_H decreases monotonically as r increases. Next, we plot by the dashed curves, the Hopf bifurcation thresholds for the larger values of D given by $D = 6, 7, 8$. Notice that for these larger values of D, the curves of $\tau_H = \tau_H(r)$ are concave down near $r = 0$, which yields a local minimum for τ_H at $r = 0$. Therefore, we conclude that when D is sufficiently large, we can obtain a dynamically triggered oscillatory instability in the spot amplitude. To illustrate this, suppose that $D = 8$. Then, we calculate $\tau_H(0) \approx 3.73$ and $\tau_H(0.612) \approx 3.88$. Suppose that we take $\tau = 3.8$ with the initial spot location at time $t = 0$ at $r = 0.612$. Then, since $\tau < \tau_H(0.612)$, the spot is stable at $t = 0$. However, since the motion of the spot is towards the origin and $\tau > \tau_H(0)$, it follows that a dynamically triggered oscillatory profile instability will occur before the spot reaches the center of the disk.

We did a similar numerical experiment for $A = 0.18$. For this value of A, we plot τ_H versus r in Fig. 4.6(b). The solid curves correspond to $D = 2, 3$, for which $\tau_H(r)$ has a maximum at $r = 0$. For the value $D = 4.3, 5, 6$, as indicated by the dashed curves, $\tau_H(r)$ has a local minimum at the equilibrium location $r = 0$. For these larger values of D, we can choose a value of τ and an initial spot location that will lead to a dynamical instability.

Experiment 4.4: One-spot solution in the unit disk: A profile instability observed by full numerical simulation

In this experiment we compare our numerically computed Hopf bifurcation threshold obtained from the coupled eigenvalue problem with full numerical results for the threshold as computed from the Gray-Scott PDE model (1.7). The full system was computed numerically by an explicit time-step finite element code, which was first developed and used in [50]. Given a parameter set ε, τ, A, D and an initial condition, we evolve the solution to the PDE (1.7) in time, and record the amplitude $v_m = \max\{v(\mathbf{x}) : \mathbf{x} \in \Omega\}$ of the solution component v at each time step. In Fig. 4.7, we plot v_m vs. t with fixed parameters $\varepsilon = 0.02$, $A = 0.16$, and $D = 4$ for three values of τ. This figure shows that the unstable oscillation occurs near $\tau = 3.2$, which roughly agrees with the Hopf bifurcation threshold $\tau_H \approx 3.5$ computed from our coupled eigenvalue formulation (see Fig. 4.6(a)). We remark that if

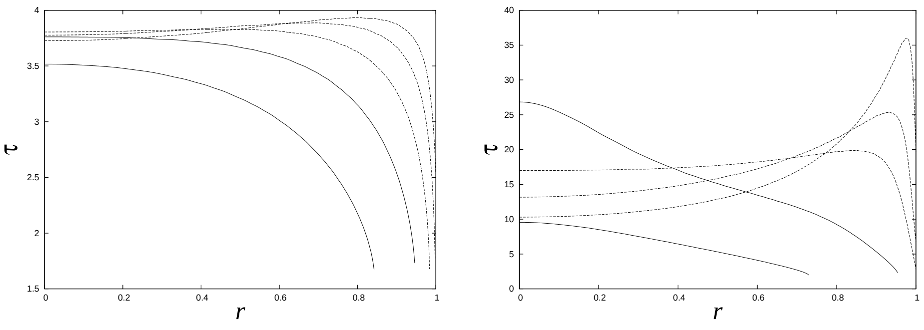

(a) τ_H vs. r $A = 0.16$ (b) τ_H vs. r $A = 0.18$

Figure 4.6: *Experiment 4.3: One-spot solution in the unit disk. Plot of* τ_H *vs.* r *for different* A *and* D*. (a) Fix* $A = 0.16$*. The solid curves are for* $D = 4, 5$*, arranged from lower to upper* $y-$*intercepts, respectively. The dashed curves are for* $D = 6, 7, 8$*, arranged from upper to lower* y*-intercepts, respectively. (b) Fix* $A = 0.18$*. The solid curves are for* $D = 2, 3$ *arranged from lower to upper* $y-$*intercepts, respectively. The dashed curves are for* $D = 4.3, 5, 6$*, arranged from upper to lower* $y-$*intercepts, respectively.*

we changed the parameters to be $A = 0.18$, and $D = 6$, then $\tau_H \approx 10.3$ (see Fig. 4.6(b)), as predicted by our coupled eigenvalue formulation. This compares reasonably well with the result $\tau \approx 9$ as observed in Fig. 4.8 and computed from the full numerical computations of (1.7).

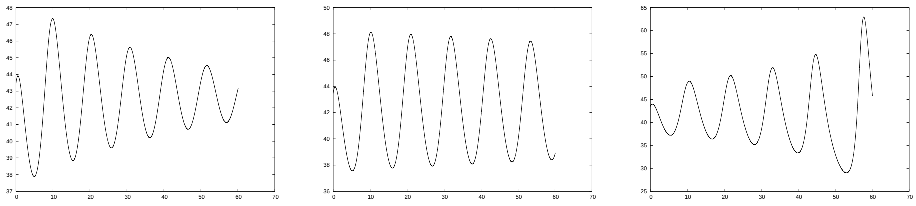

(a) $\tau = 3.0$ (b) $\tau = 3.2$ (c) $\tau = 3.4$

Figure 4.7: *Experiment 4.4: One-spot solution with spot at the center of the unit disk. We fix* $\varepsilon = 0.02$*,* $A = 0.16, D = 4$*, and plot the spot amplitude* v_m *vs.* t *for (a)* $\tau = 3$*; (b)* $\tau = 3.2$*; (c)* $\tau = 3.4$*.*

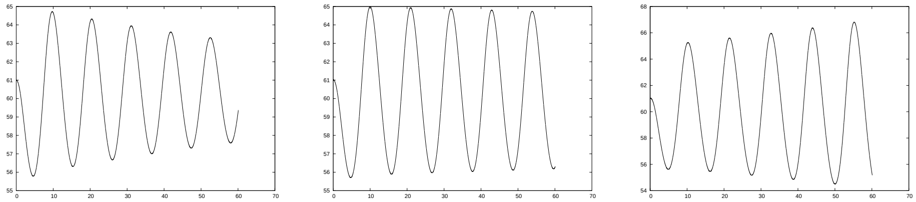

(a) $\tau = 8.5$ (b) $\tau = 9.0$ (c) $\tau = 9.5$

Figure 4.8: *Experiment 4.4: One spot solution with spot at the center of the unit disk. We fix* $\varepsilon = 0.02$*,* $A = 0.18, D = 6$*, and plot the spot amplitude* v_m *vs.* t *for (a)* $\tau = 8.5$*; (b)* $\tau = 9.0$*; (c)* $\tau = 9.5$*.*

4.4.2 A One-Spot Solution in a Square

In this subsection we compute stability thresholds for a one-spot quasi-equilibrium solution in the unit square $\Omega = [0,1] \times [0,1]$.

Experiment 4.5: One-spot solution in a square: A dynamical profile instability compared with full numerical simulations

We fix $\varepsilon = 0.02$, and we let the spot be centered on the diagonal line (x, x). From Principal Result 3.3 it follows that the spot will move slowly along this diagonal until it approaches its equilibrium location at $(0.5, 0.5)$. In Fig. 4.9(a), we fix $A = 0.28$, and plot τ_H vs. x for $D = 1$ (heavy solid curve), $D = 1.5$ (solid curve), $D = 2$ (dotted curve) and $D = 2.5$ (dashed curve) as computed from our eigenvalue problem. The last two curves show the existence of a dynamical instability, since as the spot drifts towards its equilibrium location along the diagonal of the unit square the Hopf bifurcation threshold decreases. In Fig. 4.9(b), we fix $D = 1$, and plot τ_H vs. x for four values of A. In Fig. 4.10, we plot the numerically computed spot amplitude $v_m = v_m(t)$ for a spot centered at the midpoint of the unit square. This spot amplitude was computed for three values of τ from the full GS model (1.7) by using the fortran software package VLUGR2 (cf. [7]). The estimated Hopf bifurcation value is $\tau \approx 3.3$, which compares very favorably with our prediction of τ_H as seen in Fig. 4.9(a).

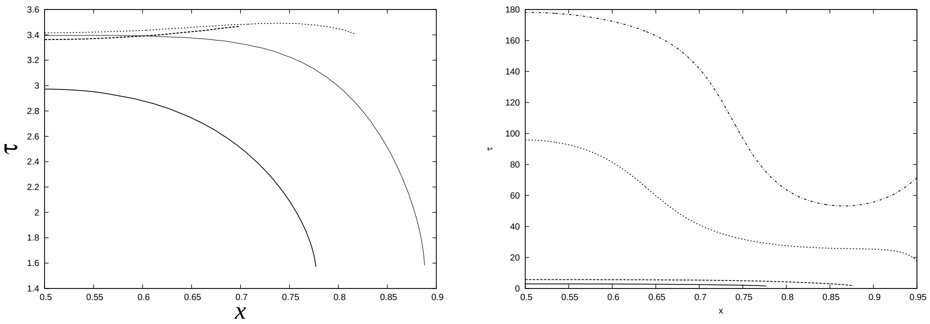

(a) τ_H vs. x (b) τ_H vs. x

Figure 4.9: *Experiment 4.5: One-spot solution centered at* (x, x) *on a diagonal of the unit square* $[0, 1] \times [0, 1]$ *(a) Fixing* $A = 0.28$, *we plot* τ_H *vs.* x *for* $D = 1$ *(lower solid curve),* $D = 1.5$ *(upper solid curve),* $D = 2$ *(dotted curve) and* $D = 2.5$ *(dashed curve). The last two curves for larger values of* D *show the existence of a dynamical oscillatory instability in the spot amplitude since as the spot drifts towards its equilibrium location along the diagonal, the Hopf bifurcation threshold decreases and has its minimum at the center of the square. (b) Fixing* $D = 1$, *we plot* τ_H *vs.* x *for* $A = 0.28$, 0.3, 0.35, 0.4, *arranged from lower to upper* $y-$*intercepts, respectively.*

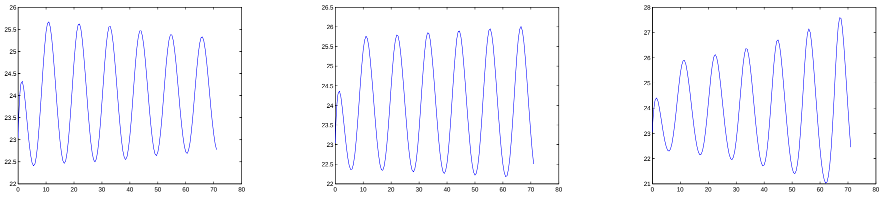

(a) $\tau = 3.2$ (b) $\tau = 3.3$ (c) $\tau = 3.4$

Figure 4.10: *Experiment 4.5: One-spot solution in a square. We fix* $\varepsilon = 0.02$, $A = 0.28, D = 1$, *and let the spot be located at its equilibrium location* $\mathbf{x} = (0.5, 0.5)$. *From the full GS model we plot the spot amplitude* v_m *vs.* t *for (a)* $\tau = 3.2$; *(b)* $\tau = 3.3$; *(c)* $\tau = 3.4$.

4.5 Symmetric $k-$Spot Patterns in a Finite Domain

Next, we consider multi-spot patterns in a finite domain. It is computationally rather intensive to numerically study our eigenvalue formulation for the general case where k spots are arbitrarily located within the domain. Therefore, we will assume that the k spots are arranged to form certain symmetric patterns. We define a spot pattern to be *symmetric* if and only if the Green's matrix $\mathcal{G}$ in (3.11) is circulant, which immediately implies that the λ-dependent Green's matrix $\mathcal{G}_\lambda$ in (4.10) is also a circulant matrix. With this special structure, our coupled eigenvalue problem reduces to that given in Principal Result 4.2. One special case where a circulant Green's matrix arises is when there are k-spots equally spaced on a ring that is concentric with the unit disk.

4.5.1 A Symmetric Circulant Matrix

We assume that the $k-$spot pattern is symmetric. We denote the first row of $\mathcal{G}$ by the row vector $\mathbf{a} = (a_1, \ldots, a_k)$. Since $\mathcal{G}$ is circulant it follows that all of the other rows of $\mathcal{G}$ can be obtained by rotating the components of the vector $\mathbf{a}$. In addition, since $\mathcal{G}$ is also necessarily a symmetric matrix it follows that $a_2 = a_k$, $a_3 = a_{k-1}$, …, and $a_j = a_{k+2-j}$ for $j = 2, \ldots, [k/2]$.

Next, we calculate the eigenvectors and eigenvalues of the λ-dependent Green's matrix $\mathcal{G}_\lambda$ as needed in Principal Result 4.2. We recall that if a matrix of size $k \times k$ is circulant, its eigenvectors V_j consist of the k^{th} roots of unity, given by

$$\kappa_j = \sum_{m=0}^{k-1} a_{m+1} e^{2\pi(j-1)m/k}\,, \qquad V_j = (1, e^{2\pi(j-1)/k}, \ldots, e^{2\pi(j-1)(k-1)/k})^t\,.$$

Here κ_j is the eigenvalue of $\mathcal{G}_\lambda$ associated with V_j for $j = 1, \ldots, k$, and a_m is the m^{th} component of the row vector $\mathbf{a}$.

For illustration, let $k = 3$. Then, the eigenpairs are $V_1 = (1, 1, 1)$ with $\kappa_1 = a_1 + a_2 + a_3$, $V_2 = (1, e^{2\pi i/3}, e^{4\pi i/3})$ with $\kappa_2 = a_1 + a_2 e^{2\pi i/3} + a_3 e^{4\pi i/3}$, and $V_3 = (1, e^{4\pi i/3}, e^{2\pi i/3})$ with $\kappa_2 = a_1 + a_2 e^{4\pi i/3} + a_3 e^{2\pi i/3}$. Then, since the matrix is also symmetric, we have $a_2 = a_3$, so that the last two eigenvalues are equal, i.e. $\kappa_2 = \kappa_3 = a_1 - a_2$, yielding one eigenvalue with multiplicity 2. Then, since any linear combination of V_2 and V_3 is also an eigenvector, we take the real part of V_2 as one such vector, and the imaginary part of V_2 as the other. In summary, we can take $V_1 = (1, 1, 1)^t$, $V_2 = (1, -0.5, -0.5)^t$ and

$V_3 = (0, \sqrt{3}/2, -\sqrt{3}/2)^t$ as the three eigenvectors of $\mathcal{G}_\lambda$ for the symmetric 3-spot pattern.

In general, the symmetry of $\mathcal{G}_\lambda$ implies that $a_j = a_{k+2-j}$ and $V_j = V_{k+2-j}$, and $V_{jm} = V_{j(k+2-m)}$ for $m = 2, \ldots, [k/2]$ and $j = 2, \ldots, [k/2]$. Since the eigenvalue is $\kappa_j = V_j \cdot \mathbf{a}$, we have $\kappa_j = \kappa_{k+2-j}$. This generates $[k/2] - 1$ eigenvalues with multiplicity 2, whose eigenvectors can be obtained by taking any linear combination of two complex conjugate eigenvectors. For instance, for the j^{th} eigenvalue κ_j the corresponding two eigenvectors can be taken as the real and imaginary parts of V_j, respectively. In summary, we know that all of the eigenvectors can be chosen to be real, but the eigenvalues in general will not be. This leads to the following general result for the spectrum of a $k \times k$ symmetric and circulant matrix whose first row vector is $\mathbf{a} = (a_1, \ldots, a_m)$:

$$\begin{cases} \kappa_1 & = \sum_{m=1}^{k} a_m, \quad V_1^t = (1, \ldots, 1), \\ \kappa_j & = \sum_{m=0}^{k-1} \cos\left(\frac{2\pi(j-1)\,m}{k}\right) a_{m+1}, \quad \text{eigenvalues with multiplicity 2}, \\ V_j^t & = \left(1, \cos\left(\frac{2\pi(j-1)}{k}\right), \ldots, \cos\left(\frac{2\pi(j-1)(k-1)}{k}\right)\right), \\ V_{k+2-j}^t & = \left(0, \sin\left(\frac{2\pi(j-1)}{k}\right), \ldots, \sin\left(\frac{2\pi(j-1)(k-1)}{k}\right)\right), \quad j = 2, \ldots, [k/2] + 1\,. \end{cases} \tag{4.51}$$

Note that if k is even, then $\kappa_{[k/2]+1} = \sum_{m=1}^{k} (-1)^{m-1} a_m$ is a simple eigenvalue with eigenvector $(1, -1, \cdots, 1, -1)^t$.

For a symmetric spot pattern, we can simply substitute (4.51) into (4.11) of Principal Result 4.2 and derive the eigenvalue problem associated with the j^{th} eigenvector V_j. This yields,

$$1 + \nu \mathrm{Re}(\hat{B}_c) + 2\pi\nu \sum_{m=1}^{k} \mathrm{Re}(a_m) V_{jm} = 0\,, \tag{4.52a}$$

$$\nu \mathrm{Im}(\hat{B}_c) + 2\pi\nu \sum_{m=1}^{k} \mathrm{Im}(a_m) V_{jm} = 0\,, \quad j = 1, \ldots, [k/2] + 1\,. \tag{4.52b}$$

Here the row vector $\mathbf{a}$ has components $a_1 = R_{\lambda\,11}$, and $a_m = G_{\lambda\,1m}$ for $m = 2, \ldots, k$, where $G_{\lambda\,1m}$ and $R_{\lambda\,11}$ are the λ-dependent Green's function and its regular part satisfying (4.5).

4.5.2 A Ring of Spots in the Unit Disk

In this subsection, we assume that all k spots are equally spaced on a ring of radius r concentric with the unit disk. The location of the spots are at

$$\mathbf{x}_j = re^{2\pi ij/k}\,, \qquad j = 1, \ldots, k\,.$$

For this special arrangement of spot locations, the Green's matrices $\mathcal{G}$ and $\mathcal{G}_\lambda$ are both symmetric and circulant.

Our goal is to compute the Hopf bifurcation threshold τ_H as a function of the ring radius r for various one-ring patterns, and to compare our stability threshold results with those computed from full numerical computations of the GS model (1.7).

Experiment 4.6: A two-spot solution in the unit disk: Dynamical oscillatory profile instability and dynamical competition instability

Suppose that there are two spots equally spaced on a ring of radius r, with $0 < r < 1$, concentric with the unit disk. The equilibrium ring radii for different values of D, representing the equilibrium point for the ODE in Principal Result 3.3, are given in Table 4.1. These equilibria do not depend on the values of A.

D	r_e	D	r_e
0.8	0.45779	2.0	0.45540
1.0	0.45703	3.0	0.45483
1.3	0.45630	4.0	0.45454
1.5	0.45596	5.0	0.45436

Table 4.1: Equilibrium ring radius r_e for a two-spot symmetric pattern in the unit disk for different values of D.

In Fig. 4.11, we fix the feed-rate parameter at $A = 0.26$, and denote by the solid curve the Hopf bifurcation threshold τ_H with $V_1 = (1,1)^t$. The dotted segment is the portion of this curve where a competition instability occurs. In Fig. 4.11(a) we plot τ_H versus r for $D = 0.8, 1.0, 1.3, 1.5$, and in Fig. 4.11(b), we plot τ_H versus r for $D = 2, 3, 4, 5$. At $r = 0.45$, the lowest curve corresponds to the largest value of D. We conclude that for $D \geq 2$, there could be a dynamical oscillatory profile instability for a two-spot symmetric pattern with $A = 0.26$. Another observation is that for $D = 5$, a competition instability occurs when $r \approx 0.568$. Upon recalling from Table 4.1 that the equilibrium ring radius is $r_e = 0.455$, we conclude that there could be a dynamical competition instability. To illustrate this, let $D = 5$ and $\tau = 1$ and suppose that we have an initial two-spot symmetric pattern with initial value $r = 0.7$ at $t = 0$. Then, as the two spots move toward each other, a dynamical competition instability will be triggered before the ring reaches its equilibrium ring radius at $r_e \approx 0.455$.

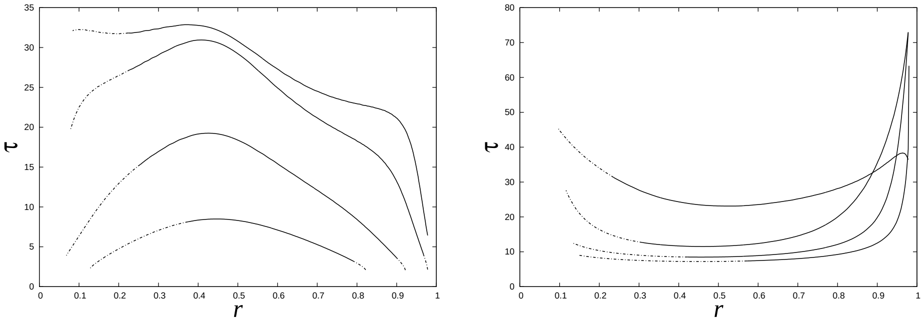

(a) τ_H vs. r (b) τ_H vs. r

Figure 4.11: *Experiment 4.6: Two spots in the unit disk. (a) Fix* $A = 0.26$*. We plot* τ_H *vs.* r *for small values of* $D = 0.8, 1.0, 1.3, 1.5$*, with the lower curves corresponding to smaller values of* D*. The solid curves correspond to regions in* r *where an oscillatory profile instability occurs, and the dotted portions of these curves correspond to where a competition instability occurs. (b)* τ_H *vs.* r *for the larger values of* D *given by* $D = 2, 3, 4, 5$*. The lower curves at* $r = 0.6$ *correspond to larger values of* D*.*

Next we fix $A = 0.26$ and $D = 3$. In Fig. 4.12(a) we plot the Hopf bifurcation thresholds τ_{H1} for in-phase oscillation $(1, 1)$ (lower solid curve) and τ_{H2} for out-of-phase oscillation $(1, -1)$ (upper solid curve). The dotted portion on τ_{H1} shows where a competition instability occurs for any $\tau \geq 0$. In Fig. 4.12(b), we fix two spots on the equilibrium ring of radius $r_e = 0.45483$, and we plot the path of the complex conjugate pair of eigenvalues in the complex plane for the range $\tau \in [3.7, 36]$. The solid curve is the eigenvalue path for in-phase oscillations with eigenvector $(1, 1)$, while the dotted curve is the eigenvalue path for out-of-phase oscillations with eigenvector $(1, -1)$. We note that as τ increases, the real parts of both pairs of eigenvalues increase. The eigenvalue for $(1, 1)$ enters the right half-plane at $\tau \approx 11.5$. Note that the imaginary eigenvalue of $(1, -1)$ becomes very close to the real axis for $\tau < 3.7$, and our numerical computation breaks down because our assumption that $\lambda_r = 0, \lambda_i \neq 0$ does not hold in this case.

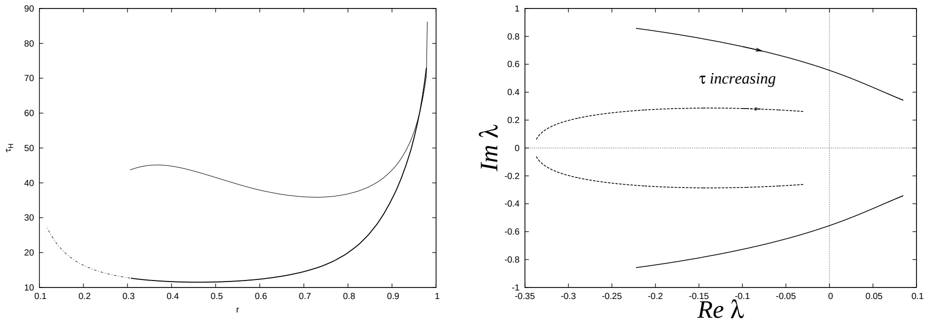

(a) τ_H vs. r (b) Im(λ) vs. Re(λ)

Figure 4.12: *Experiment 4.6: Two spots in the unit disk. Fix* $A = 0.26$ *and* $D = 3$. *(a)* τ_H *vs.* r *for in-phase oscillation* $(1, 1)$ *(lower solid curve), and* τ_{H2} *for out-of-phase oscillation* $(1, -1)$ *(upper solid curve). The dotted portions on* τ_{H1} *show where a competition instability occurs for any tau* ≥ 0. *(b) Two spots equally spaced on an equilibrium ring of radius* $r_e = 0.45483$. *Plot of* λ *in the complex plane on the range* $\tau \in [3.7, 36]$. *The solid curve is for* $(1, 1)$, *while the dotted curve is for* $(1, -1)$.

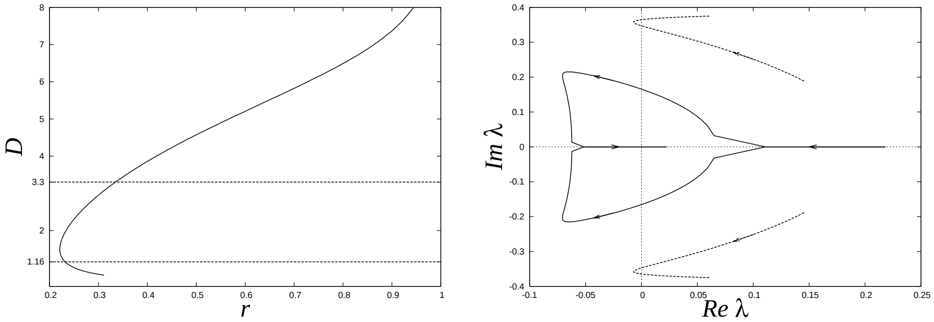

(a) D_c vs. r (b) Im(λ) vs. Re(λ)

Figure 4.13: *Experiment 4.7: Two spots in the unit disk. Fix* $A = 0.26$ *and* $\varepsilon = 0.02$ *(a) Plot of* D_c *vs. r (solid curve), where* D_c *is the critical value of* D *at which a competition instability is initiated. The region* $1.1583 < D < 3.3030$ *between the two horizontal lines is where the leading-order NLEP theory predicts that no competition instability occurs. (b) For* $\tau = 30$ *and* $r = 0.3$, *plot the spectrum in the complex plane by varying* D *in the range* $[0.8, 3]$. *The solid curve corresponds to the eigenvalues with* $(1, -1)$, *and the dotted curve corresponds to the eigenvalues with* $(1, 1)$. *The arrows show the path as* D *increases.*

Experiment 4.7: A two-spot solution in unit disk: Competition instability

Fix $\varepsilon = 0.02, A = 0.26$. In Theorem 2.3 of [101], as summarized in Section 4.2.2, the leading order NLEP analysis proves that if $D = O(\nu^{-1})$ and $L_0 < \frac{\eta_0}{(2\eta_0+k)^2}$, then the small solution u^-, v^- of (4.2.2) is stable for any τ sufficiently small. In addition, the leading-order NLEP theory predicts that if $L_0 > \frac{\eta_0}{(2\eta_0+k)^2}$, then this solution is unstable for any $\tau > 0$. From (4.20), we recall that $L_0 = \lim_{\varepsilon\to 0} \frac{\varepsilon^2 2\pi b_0}{A^2|\Omega|}$ and $\eta_0 = \lim_{\varepsilon\to 0} \frac{|\Omega|}{2\pi D\nu}$, where $b_0 = \int_0^\infty w^2\rho\, d\rho \approx 4.9347$ and w is the ground-state solution of (4.14). With $|\Omega| = \pi$ and $\nu = -1/\ln\varepsilon$, and for the other parameter values as given, this stability bound yields $0.296 < D\nu < 0.844$, or equivalently $1.158 < D < 3.303$. For this range of D, the leading order NLEP theory predicts that the solution u^-, v^- is stable for τ sufficiently small. Outside of this bound for D, the leading-order NLEP theory predicts that a competition instability.occurs for any $\tau > 0$.

We fix $\varepsilon = 0.02$ and $A = 0.26$. In Fig. 4.13(a), we plot D_c vs. r by the solid curve, where D_c denotes the critical value of D where a competition instability is initiated. To the left of this curve, oriented with respect to the direction of increasing D, we predict that a competition instability occurs for any $\tau > 0$, while to the right of this curve we predict that the solution is stable when τ is small enough. The two horizontal dotted lines with $D_1 = 1.158$ and $D_2 = 3.303$ in this figure bound a region of stability as predicted by the leading-order NLEP theory of [101]. The leading-order in ν prediction from NLEP theory does not capture the dependence of the stability threshold on the ring radius r. Our stability formulation, which accounts for all orders in $\nu = -1/\ln\varepsilon$, shows that $D_c = D_c(r)$. For $\varepsilon = 0.02$, ν is certainly not very small, and this dependence of the threshold on r, not accounted for by NLEP theory, is indeed very significant.

In Fig. 4.13(b), for $A = 0.26$, $\tau = 30$, and $r = 0.3$, we plot the spectrum in the complex plane as D varies over the range $[0.8, 3.0]$. This range of D corresponds to taking a vertical slice at $r = 0.3$ in Fig. 4.13(a) that cuts across the stability boundary at two values of D. The arrows in this figure indicate the direction of the path of eigenvalues as D is increased. The loop of spectra, corresponding to the solid curves in this figure, plot the eigenvalues associated with the eigenvector $(1, -1)$. From Fig. 4.13(a) we predict instability when D is near $D = 0.8$ or when D is near $D = 3.0$. This is clearly shown by the behavior of the closed loop of spectra in Fig. 4.13(b).

With regards to the loop of spectra (solid curves) in Fig. 4.13(b) associated with the $(1,-1)$ eigenvector, our results show that for $D = 0.8$ the eigenvalue is on the positive real axis at $\lambda = (0.218, 0)$. As D is increased above $D = 0.8$ the real eigenvalue moves along the horizontal axis to the left, and splits into a complex conjugate pair at $D \approx 0.84$. At $D = 0.84$, then $\lambda = (0.111, 0)$, while at $D = 0.85$ then $\lambda = (0.0649, 0.0322)$. For $D \approx 1.0$, λ enters the stable left half-plane $\mathrm{Re}(\lambda) < 0$. For $D = 2.89$ the eigenvalues merge onto the negative real axis. One eigenvalue then enters the right half-plane at $D \approx 2.95$. This is the value of D where a competition instability is initiated. For $D > 2.95$, there is a positive real eigenvalue associated with the $(1,-1)$ eigenvector, which generates a competition instability.

Alternatively, the dotted curves in Fig. 4.13(b) correspond to the path of eigenvalues associated with the $(1,1)$ eigenvector, representing synchronous instabilities. This path depends sensitively on the value chosen for τ. For $\tau = 30$, our computational results show that as D is increased above $D = 0.8$, the real part of these eigenvalues first starts to decrease and then crosses into the stable left half-plane at $D \approx 1.33$. The real part of these eigenvalues starts increasing when $D \approx 1.59$ and the path then re-enters the unstable right half-plane at $D = 1.89$ where stability is lost at a Hopf bifurcation corresponding to synchronous oscillations of the two spot amplitudes. This path of eigenvalues remain in the unstable right half-plane for $D > 1.89$.

We conclude that if $1.33 < D < 1.89$, this two-spot symmetric pattern is stable to both competition and synchronous oscillatory instabilities. When $D > 2.95$ there is an unstable real eigenvalue in the right half-plane associated with a competition instability in addition to a synchronous oscillatory instability associated with the complex conjugate pair of eigenvalues. On the range $1.89 < D < 2.95$ there is only a synchronous oscillatory instability. We remark that if τ is taken to be considerably smaller than our chosen value of $\tau = 30$, there would be only one unstable eigenvalue in $\mathrm{Re}(\lambda) > 0$ (located on the positive real axis) when $D > 2.95$.

We set $A = 0.26$, $D = 3$, $\tau = 30$, and consider an initial two-spot symmetric pattern with ring radius $r = 0.3$. With these parameter values and initial condition, in Fig. 4.14 we show results from a full numerical simulation of the GS model (1.7) at later times. For these parameter values, we conclude from Fig. 4.13(b) that there is an unstable real eigenvalue together with an unstable complex conjugate pair of eigenvalues. We remark that since we use the finite element method, the locations of the two spots is not exactly symmetric, which has essentially a similar effect to adding a small perturbation to the initial condition to initiate an instability. For the left spot, its amplitude is initially $v_{m1} \approx 37.5$, while the initial amplitude of the right spot is $v_{m2} \approx 40.1$. From the full numerical results shown in Fig. 4.14

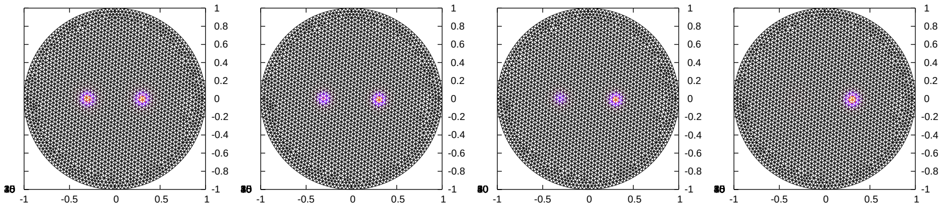

Figure 4.14: *Experiment 4.7: We fix* $D = 3.0$*,* $A = 0.26$*,* $\tau = 30$*, and* $\varepsilon = 0.02$*. The initial condition is a symmetric two-spot pattern on a ring of radius* 0.3*. The solution* v *is plotted at times* $t = 0.5$*, 8, 10, 15, respectively. The spot on the left is rather quickly annihilated.*

at $t = 0.5, 8, 10, 15$, we observe that the amplitude of the left spot decays with time, and this spot disappears after $t = 15$.

In Fig. 4.15 we plot the amplitude of the two spots. The amplitude v_{m1} vs. t of the left spot is shown by the dot-dashed curve, while the amplitude v_{m2} vs. t of the right spot is shown by the solid curve. These amplitudes were obtained by tracking the locations of spots in the numerical simulation at each time step. The amplitude of the left spot decays rapidly to zero before $t = 13$. Meanwhile, the amplitude of the right spot begins to oscillate, but the oscillation ceases after the left spot is annihilated. This is because after the left spot has been removed, the value $\tau = 30$ is below the Hopf bifurcation value for a one-spot solution.

Experiment 4.8: A two-spot solution in the unit disk: Phase diagram for different diffusion coefficients D

In Experiment 4.8, we plot the phase diagram A vs. r for different diffusion coefficients D. In Fig. 4.16, we plot the existence threshold A_f for a two-spot quasi-equilibrium solution by the solid curve. The critical value of A for the competition instability is shown by the dotted curve, and the peanut-splitting threshold A_2 by the upper heavy solid curve. The solution behavior in the four different parameter regimes in this figure is as follows. In Regime σ the quasi-equilibrium solution does not exist. In Regime β the quasi-equilibrium solution exists but is unstable to competition. In Regime ζ the solution is unstable to an oscillatory profile instability when τ exceeds a Hopf bifurcation threshold τ_H. In region θ the solution is unstable to peanut-splitting. The subfigures from left to right are plotted for: (a) $D = 0.2$; (b) $D = 1$; (c) $D = 5$. Note that when $D = 0.2 \ll 1$, the subfigure is qualitatively similar to the phase diagram shown in Fig. 4.5(a)

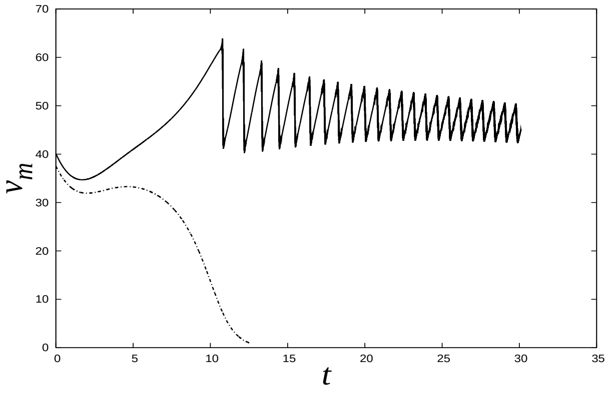

(a) v_m vs. t

Figure 4.15: *Experiment 4.7: Two spots in the unit disk. Fix* $\varepsilon = 0.02, A = 0.26$*,* $D = 3$*, and* $\tau = 20$*. The dot-dashed curve plots the amplitude of the left spot* v_{m1} *vs.* t*., the solid curve plots the amplitude of the right spot* v_{m1} *vs.* t*.*

for a two-spot solution in the infinite plane.

Experiment 4.9 k-spot solution with $k > 2$ *in the unit disk: Phase diagram*

Finally, we compute the stability phase diagram associated with k-spots that are equally spaced on a ring of radius r. We fix $D = 0.2$ and $\varepsilon = 0.02$ and plot this phase diagram in the parameter plane A versus the ring radius r for $k = 2, 4, 8, 16$. We are particularly interested in determining if there exists $k-$spot pattern with fixed parameters D and ε such that the peanut-splitting regime for $k-$spots intersects the competition regime for a pattern with $2k$-spots. If this occurs then it would be possible that a $k-$spot pattern undergoes peanut-splitting first, followed by a competition instability with $2k$ spots, leading to the annihilation of k of them, with the cycle of self-replication followed by self-destruction repeating again.

We assume that all k spots are equally distributed on a ring of radius r. Then using the techniques in Section 4.5.1 it follows readily that for $2k = 4$, the eigenvectors are $V_1 = (1, 1, 1, 1)^t$, $V_2 = (1, -1, 1, -1)^t$, $V_3 = (1, 0, -1, 0)^t$ and $V_4 = (0, 1, 0, -1)^t$. Note that the last three of these vectors have components with different signs. Moreover, the computational results show that the competition instability threshold associated with V_2 is always above that of V_3 or V_4, and so it has a larger competition instability regime in the phase diagram, and this instability occurs more readily than with V_3

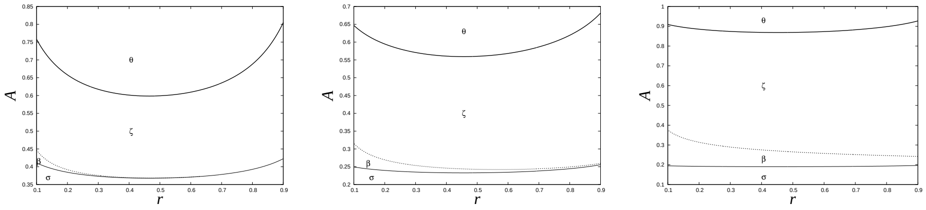

(a) $D = 0.2$ (b) $D = 1.0$ (c) $D = 5.0$

Figure 4.16: *Experiment 4.8: Two spots in the unit disk. We plot the phase diagram A vs. r. The solid curve is the existence threshold A_f for a two-spot quasi-equilibrium solution; the dotted curve is the critical value for a competition instability; the heavy solid-curve is the peanut-splitting threshold A_2. Regime σ: no solution; Regime β: the quasi-equilibrium solution is unstable to competition; Regime ζ the solution is unstable to a profile oscillation if $\tau > \tau_H(r)$; Regime θ: the solution is unstable to peanut-splitting. Subfigures from left to right are plotted for: (a) $D = 0.2$; (b) $D = 1$; (c) $D = 5$.*

and V_4. The profile oscillatory instability occurs first as τ is increased for the eigenvector V_1. Similarly for $k = 8, 16$, the instability with eigenvector of the form $V = (1, -1, 1, -1, \ldots, 1, -1)^t$ is always the dominant competition mechanism. Therefore for $2k-$spot equally distributed on a ring, if the competition instability does occur, it will lead to the annihilation of one of the two adjacent spots. For $2k$ even, half the total number of total spots will disappear leaving a $k-$spot pattern.

In Fig. 4.17, we plot the phase diagram in the A versus r plane for $k = 2, 4, 8, 16$. The computations are done for the fixed value $D = 0.2$. The thin solid curves on the bottom is the existence threshold A_f for a quasi-equilibrium solution; the dotted curves are the critical value of A for a competition instability, and the heavy solid curves on top are the peanut-splitting threshold A_2. In Regime σ the quasi-equilibrium solution does not exist. Regime β is where the quasi-equilibrium solution exists but is unstable to competition. In Regime ζ the solution is unstable to profile oscillation if $\tau > \tau_H(r)$. In Regime θ there is instability to peanut-splitting.

4.6 Discussion

In this chapter, we formulated an eigenvalue problem associated with instabilities in the amplitudes of spots. This eigenvalue problem, associated with locally radially symmetric perturbations, differs from the eigenvalue

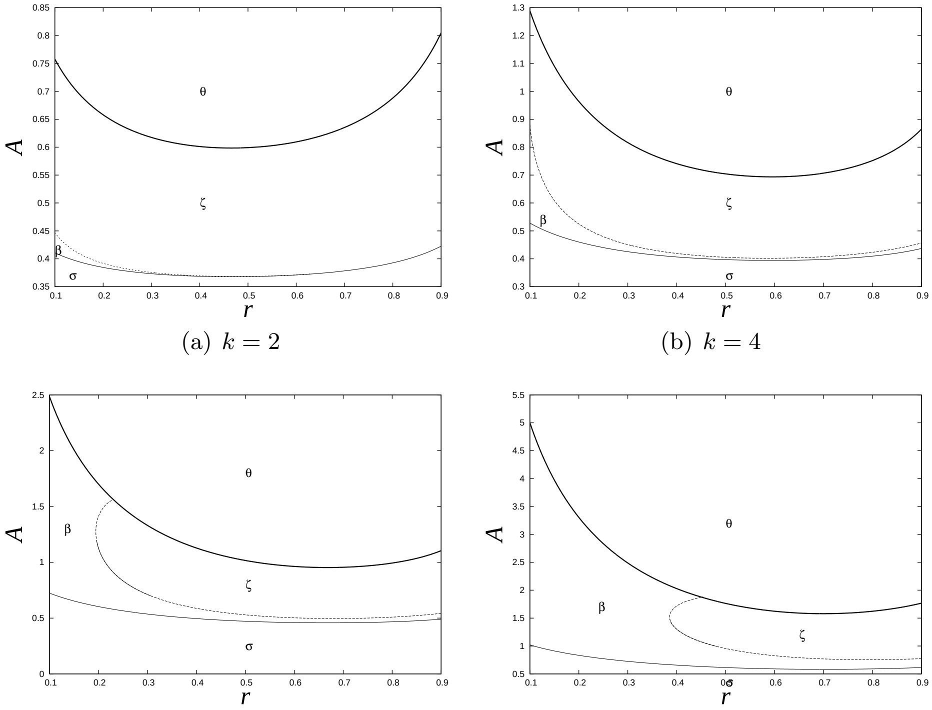

(a) $k = 2$

(b) $k = 4$

(c) $k = 8$

(d) $k = 16$

Figure 4.17: *Experiment 4.9: Symmetric k-spot pattern in the unit disk. We plot the phase diagram A vs. r with* $D = 0.2$. *The thin solid curves are the existence threshold* A_f *for the quasi-equilibrium; the dotted curves are the critical values of A for a competition instability; the heavy solid curves is the peanut-splitting threshold* A_2. *In Regime* σ *the quasi-equilibrium solution does not exist. In Regime* β *the quasi-equilibrium solution exists but is unstable to competition. In Regime* ζ *the solution is unstable to a profile oscillation if* τ *exceeds a Hopf bifurcation threshold* $\tau_H(r)$ *In Regime* θ *the solution is unstable to peanut-splitting. Subfigures from left to right are plotted for: (a)* $k = 2$; *(b)* $k = 4$; *(c)* $k = 8$; *(d)* $k = 16$.

problem of Chapter 3 in that the local eigenfunction $N_j(\rho)$ grows logarithmically as $\rho \to \infty$. This logarithmic growth has the effect of introducing a strong inter-spot coupling effect in the formulation of our eigenvalue problem governing spot amplitude instabilities. If in the complex λ-plane a real eigenvalue crosses into the unstable right half-plane $\text{Re}(\lambda) > 0$ along the real axis, then a competition instability is initiated. Alternatively, if there is a complex conjugate pair of eigenvalues entering the unstable right half-plane through a Hopf bifurcation then an oscillatory profile instability is initiated. By numerically computing discrete eigenvalues of the eigenvalue problem (4.8) and (4.10a) using the algorithms in §4.1.1, we are able to calculate both the Hopf bifurcation threshold and the critical parameter values for a competition instability. These computations allow us to plot phase diagrams in parameter space where the three different types of instabilities can occur. These instabilities are spot self-replication, an oscillatory instability in the spot amplitudes, and a competition instability of the spot amplitudes. These phase diagrams are plotted for various spatial configuration of spot patterns and for both finite and infinite domains.

There are several open problems that warrant investigation. One such problem is to derive the correction term to the leading-order NLEP theory in §4.2 to more accurately determine the threshold parameter values for spot stability in terms of the spatial configuration of spots. A second open problem is to consider a weakly nonlinear analysis around a multi-spot quasi-equilibrium solution for parameter values near the onset of either an oscillatory profile instability or a competition instability. With such a weakly nonlinear theory one could determine whether the oscillatory instability is subcritical or supercritical, and one could characterize in more detail a spot competition process in the weakly nonlinear regime. A third open problem is to investigate the stability thresholds associated with other, less symmetric, configurations of spots such as for the case of $k-1$ spots on a ring and a spot at center of the unit disk or the case of two spots arbitrarily spaced in a domain. Finally, the most interesting open problem is to try to determine a parameter range where a spot-replication \ spot-annihilation "loop" could occur. Such an attractor would consist of a continuously evolving pattern of self-organized spots undergoing repeated cycles of spot self-replication followed by spot-annihilation due to overcrowding instabilities.

Chapter 5

Conclusions and Future Work

5.1 Conclusions

In this thesis, we have presented results on the dynamics and instabilities of one-dimensional spike patterns and two-dimensional spot patterns in different parameter regimes for the Gray-Scott model, based on a combination of asymptotic and numerical methods.

With regards to the one-dimensional Gray-Scott model in the semi-strong interaction regime $D = O(1)$, we have focused on analyzing two types of oscillatory instabilities of multi-spike patterns in a finite domain, identifed in the intermediate feed rate regime $O(1) \ll \mathcal{A} \ll O(\varepsilon^{-1/2})$. The oscillatory profile instability resulting from a Hopf bifurcation of the large eigenvalues occurs in fast time t, with the spikes evolving on the slow time $\sigma = \varepsilon^2 \mathcal{A}^2 t$ in (2.12b). Therefore, we formulated a nonlocal eigenvalue problem (2.38) associated with the profile instability, based on the quasi-equilibrium solution obtained by freezing the locations of spikes. The threshold $\tau_h = O(\mathcal{A}^4)$ for the Hopf bifurcation can be calculated explicitly by Principal Results 2.4, with the threshold depending on the instantaneous configuration of spikes in the interval. In contrast, the oscillatory drift instability resulting from a Hopf bifurcation of the small eigenvalue occurs on the slow time-scale σ. For this problem, we derive and compute solutions to a Stefan-type problem (2.12) with a moving singular source. This formulation allows us to study the behavior of multi-spike pattern away from bifurcation point $\tau_{tw} = O(\varepsilon^{-2}\mathcal{A}^{-2})$ in (2.59). In particular, in Fig. 2.4(c) we have computed a large-scale oscillation in the location of the spike. According to the scalings of these two thresholds, we identified two subregimes: when $O(1) \ll \mathcal{A} \ll O(\varepsilon^{-1/3})$, $\tau_h \ll \tau_{tw}$, the oscillatory profile instability dominates; when $O(\varepsilon^{-1/3}) \ll \mathcal{A} \ll O(\varepsilon^{-1/2})$, $\tau_{tw} \ll \tau_h$, the oscillatory drift instability dominates. Therefore, in the semi-strong interaction regime, and with the feed rate $\mathcal{A}$ increasing, the primary instability mechanisms of multi-spike patterns are respectively in order: competition instability, oscillatory profile instability ($\tau > \tau_h$), oscillatory drift instability ($\tau > \tau_{tw}$) and then finally, pulse-splitting.

An open problem here is to compute the long time evolution of the oscillatory drift solutions based on the integro-differential equation (2.78), by using a numerical method similar to that used in [76] for a related, but considerably simpler, integro-differential flame-front equation. It is of interest to determine if the spike trajectories can exhibit similar chaotic behavior as was observed in the flame-front model of [76].

For the Gray-Scott model in a two-dimensional domain in the semi-strong interaction regime $D = O(1)$, we construct the quasi-equilibrium spot patterns by matched asymptotic analysis, and derive a DAE system (3.35) governing the dynamics of a collection of spots. An existence condition $A > A_f = O(\varepsilon(-\ln\varepsilon)^{1/2})$ for the quasi-equilibrium multi-spot solution is required, as a result of a saddle node bifurcation of the parameter A in (3.8). The asymptotic and numerical investigation of the eigenvalue problem (3.23) corresponding to different instability types has shown that, in the limit $A = O(\varepsilon(-\ln\varepsilon)^{1/2})$, competition and oscillatory profile instabilities can both occur. This regime is similar to the low-feed rate regime for one-dimemsional spike patterns. If the feed rate is increased to $A = O(\varepsilon(-\ln\varepsilon))$, the multi-spot pattern can be unstable to self-replication, which leads to the creation of more spots. Spot-replication criteria have been explicitly calculated in §3.2 in terms of the source strength S_j for each spot, with $\Sigma_2 \approx 4.31$, $\Sigma_3 \approx 5.44$, and $\Sigma_4 \approx 6.14$. Recall that in §3.1, there exists a critical value $S_v \approx 4.78$ such that if $S_j > S_v$, the radially symmetric solution $V(\rho)$ develops a volcano shape, as shown in Fig. 3.1(c). For example, given a large enough feed rate, if the source strength of j^{th} spot satisfies $\Sigma_4 > S_j > \Sigma_3 > S_v$, it would first expand and form a ring shape, and then break up into three spots, which is similar to the breakup instability discussed in [57] in the same semistrong interaction regime $D = O(1)$ with larger feed rate A.

In [57], the stability of stripe and ring patterns with respect to zigzag and breakup instabilities was studied. In the regimes $O(\varepsilon^{1/2}) \ll A \ll O(1)$ and $A = O(1)$, equilibrium solutions of homoclinic stripes and rings exist. For these solutions, it was shown that a band of unstable modes always occurs for both breakup and zigzag instabilities. These instabilities cannot be prevented unless the domain is with $O(\varepsilon) \ll O(1)$ thin. Note that the unstable bands for zigzag and breakup instabilities overlap in a way that a zigzag instability is always accompanied by a breakup instability.

Therefore, a ring or stripe pattern always breaks up and leads to a spot pattern. Such spot patterns have much better stability properties. Similar to the one-dimensional case, we can categorize the equilibrium solutions and instability mechanism in terms of an ascending feed-rate parameter A as follows competition of spots, profile oscillation of spots ($\tau > \tau_h$), self-replication of spots, breakup of stripes or rings and zigzag instability of stripes or rings. One remark is that while the first two instabilities reduce the number of spots, spot-replication creates more spots. Moreover, if $A \gg O(\varepsilon^{1/2})$, the equilibrium solution could be ring or stripe, although they are unstable to modes of a certain wavenumber associated with breakup and zigzag instabilities. This result agrees with our intuition from FIS reaction that with the reagents fed in a high rate, there would be more spots as a results of more intense reaction, and there would be a threshold above which larger localized regions such as stripes or rings could be formed from coagulation of spots.

In contrast, in the weak interaction regime $D = O(\varepsilon^2)$, both u and v are localized variables, stripes and rings can be unstable to a zigzag instability without undergoing breakup instability. As a result, a labyrinth pattern can be generated in this regime. Numerical studies in [57] has shown that patterns in this regime depend very sensitively on the parameters, with spots, rings, stripes and labyrinths being formed through zigzag, breakup or spot-splitting instabilities.

One open problem in two-dimensional Gray-Scott model is to compute the equilibrium bifurcation diagram for multi-spot pattern in a finite domain. Multiple equilibrium locations are possible by calculating $\mathbf{x}_j'(t) = 0,\ j = 1, \cdots, k$ in (3.35). For each steady-state, we could try to determine the set of initial conditions leading to long-time behavior that approaches this state. This basin of attraction problem is an interesting open question. Another problem is to identify a parameter range where a spot-replication \ spot-annihilation “loop” could occur. Since this continuous process of spot birth by replication and death by competition has been observed numerically in the weak interaction regime $D = O(\varepsilon^2)$ in [77]. Therefore, it would be interesting to determine whether it can be found, largely based on analytical results, in the regime $O(\varepsilon^2) \ll D \ll O(1)$, by using results for the instability thresholds of spot-replication, competition and profile oscillation, for two-particle interactions. Finally, it would be interesting to study small eigenvalue instabilities associated with the motion of spots. In particular, what instability would occur if there are too many spots on one ring? Is there a Stefan-type problem similar to the one-dimensional case for some range of τ and A?

A long term goal is to investigate generic types of instabilities of particle-like solutions to reaction-diffusion systems that have non-variational structure. We would also like to derive conditions on the kinetic $F(A,H)$ and $G(A,H)$ for a general two-component reaction-diffusion model (1.1). In the next section, we propose a few projects as potential future work.

5.2 Application to Other Systems

It should be possible to apply our theoretical framework used for the two-dimensional GS model to other reaction-diffusion systems that have numerically been shown to exhibit spot self-replication phenomena. We anticipate that our theoretical approach will still be useful in a wide context, but may have to be tailored to each particular new RD model. We now propose a few examples of possible future work in this direction.

5.2.1 Localized Patterns in Cardiovascular Calcification

Yochelis et. al.(cf. [105]) have recently modeled cardiovascular calcification by a Gierer-Mainhardt (GM) type system with saturated autocatalytic kinetics for the activator and an inhibition source term S. In dimensionless form this model is

$$u_t = D\Delta u - u + \frac{u^2 v^{-1}}{1+u^2}\,, \qquad v_t = \Delta v - Ev + S + Gu^2\,, \tag{5.1}$$

where $D = 0.005$, $G = 1$, $E = 2$, and the constant inhibition source S is the control parameter.

This problem is motivated by the results of *in vitro* experiments that vascular-derived mesenchymal stem cells can display self-organized calcified patterns such as labyrinths and spots. In these experiments, the bone morphogenetic protein 2 (BMP-2) acts as an activator, and the matrix GLA protein (MGP) acts as the inhibitor, which can be altered by external addition of MGP. In [105], a spatial dynamics approach together with numerical continuation was used to identify the primary instabilities and possible stable and unstable one-dimensional solution branches as a function of the inhibition source S. Then these results were extended to calculate the secondary instabilities and the parameter regions in S in which two-dimensional patterns, such as labyrinths, spots, stripes and mixtures of spots and stripes, can form. It has been shown numerically that labyrinthine patterns arise at lower concentrations of added MGP (corresponding to small S values), while a higher MGP concentration (larger S values) leads to spot patterns.

It would be very interesting to develop an analytical theory for the dynamics and different types of instabilities of such localized patterns by an asymptotic method that is valid in the limit $D \ll O(1)$. With regards to the spot self-replication instability, the mechanism for this instability is likely to be essentially similar to that for the GS model, as studied in Chapter 3 of this thesis. Such a study would allow for a theoretical understanding of the different types of localized patterns in the GM model (5.1), and to determine the parameter range of the inhibition source S that leads to the formation of calcified patterns.

5.2.2 The Brusselator Model with Superdiffusion

Golovin et. al. [34] have studied the effect of superdiffusion on pattern formation in a generalized Brusselator model, formulated as

$$
\begin{aligned}
u_t &= \nabla^{\alpha} u + (B-1)u - U^3 + Q^2 v + \frac{B}{Q}u^2 + 2Quv + u^2 v\,, && (5.2\text{a})\\
\eta^2 v_t &= \nabla^{\beta} v - Bu - Q^2 v - \frac{B}{Q}u^2 - 2Quv - u^2 v\,. && (5.2\text{b})
\end{aligned}
$$

Here the superdiffusion term ∇^{β} is defined by its action in Fourier space $\mathcal{F}[\nabla^{\beta}](\mathbf{k} = -|\mathbf{k}|^{\beta}\mathcal{F}[u](\mathbf{k})$. Different from normal diffusion that describes the random walk of molecules, superdiffusion models molecules that have a jump size distribution with infinite moments. Superdiffusive processes are common in plasma and turbulent flows, in surface diffusion, and in diffusion in porous media with fluid flow etc. In [34], a linear stability analysis has shown that a Turing instability can occur even when the diffusion of the inhibitor is slower than that of the activator. A set of coupled amplitude equations was formulated from a weakly nonlinear analysis, which determined the selected hexagonal and striped patterns and their stability. Moreover, these theoretical results were confirmed by full numerical simulations near stability boundaries. In the computation, a new pattern, involving self replicating spots not described by the analysis, was observed in the parameter region where hexagons and stripes are unstable. It would be interesting to try to extend our theoretical framework developed for the GS model to investigate the self-replicating spot patterns observed in the numerical computations of [34] for (5.2).

5.2.3 A Three-Component Reaction-Diffusion System

It would also be interesting to consider three-component reaction-diffusion systems, which presumably allow for more complex spatio-temporal patterns than for two-component systems such as the GS or GM models. One such system was initially introduced by Schenk et. al. [80] to model a planar semiconductor gas-discharge system. The dimensionless system is

$$\begin{aligned} U_t &= \Delta U + U - U^3 - \varepsilon(\alpha V + \beta W + \gamma)\,, && (5.3a)\\ \tau V_t &= \frac{1}{\varepsilon^2}\Delta V + U - V\,, && (5.3b)\\ \theta W_t &= \frac{D^2}{\varepsilon^2}\Delta W + U - W\,. && (5.3c) \end{aligned}$$

Here $0 < \varepsilon \ll 1$, $\tau > 0$, $\theta \ll \varepsilon^{-3}$, and α, β, γ are $O(1)$ constants. This system has two inhibitors V and W with fast diffusivities, which differ only in their reaction-time constants and diffusion scale. The activator U is only weakly coupled at $O(\varepsilon)$ to V and W.

In [5], the laboratory experiments on a planar gas discharge device have shown the occurrence of birth, death, and scattering of multiple spots in different parameter regimes. This three-component model (5.3) has been mostly studied by numerical simulations, and the dynamics exhibited by the localized patterns agree qualitatively with those seen in actual experiments.

There has been some theoretical work for (5.3) for the case of a one-dimensional spatial domain. Doelman et. al. have investigated the existence (cf. [23]) and stability (cf. [37]) of pulse and front patterns in the one-dimensional case, and they have developed an approach by which the existence and stability of front or pulse patterns of 3-component system can be established. Theses studies [23], [37] have provided a detailed mathematical analysis and obtained explicit results for various types of bifurcations such as saddle-node bifurcations and Hopf bifurcations, which result in breathing oscillations. However, there has been no comprehensive analysis for (5.3) in a two-dimensional spatial domain. It would be interesting to extend our basic approach for the GS model to asymptotically study the existence of spot solutions, the dynamics of spots (spot scattering), and their various instabilities. Based on the instabilities observed from [5], we anticipate that there will be two types of instabilities; a spot-splitting instability (spot birth) and a competition instability (spot death).

5.2.4 A General Class of Reaction-Diffusion Models

An interesting extension of this thesis would be to extend the analysis to consider localized spot patterns arising in a class of singularly perturbed reaction-diffusion models in a two-dimensional domain. For the case of a one-dimensional spatial domain, Doelman and Kaper (cf. [20]) have developed theories for the stability and dynamics of pulse solutions in the semi-strong interaction limit for a class of singularly perturbed RD system. By adopting the theoretical framework of this thesis it should be possible to extend the results of [20] to the case of spot patterns in a two-dimensional domain. The goal of this analysis would be to find certain criteria on the reaction kinetics that lead to different instability mechanisms of localized spot solutions, and to plot the phase diagram in parameter space where such instabilities could occur.

Bibliography

[1] E. Anderson et al. (1999), *LAPACK User's Guide: Third Edition*, SIAM Publications.

[2] U. Ascher, R. Christiansen and R. Russell (1979), *Collocation Software for Boundary Value ODE's*, Math. Comp. **33**, pp. 659–679.

[3] Y. Astrov, E. Ammelta, S. Teperickb and H. Purwins (1996), *Hexagon and stripe Turing structures in a gas discharge system*, Phys. Lett. A **211**, pp. 184–190.

[4] Y. Astrov and H. Purwins (2001), *Plasma spots in a gas discharge system: birth, scattering and formation of molecules*, Phys. Lett. A **283**, pp. 349–354.

[5] Y. Astrov and H. Purwins (2006), *Spontaneous division of dissipative solitons in a planar gas-discharge system with high ohmic electrode*, Phys. Lett. A **358**, pp. 404–408.

[6] R. P. Beyer and R. J. Leveque (1992), *Analysis of a one-dimensional model for the immersed boundary method*, SIAM J. Numer. Anal. **29 (2)**, pp. 332–364.

[7] J. G. Blom, R.A.Trompert and J.G.Verwer (1996), *Algorithm 758: VLUGR 2: A vectorizable adaptive grid solver for PDEs in 2D*, ACM Trans, Math. Softw. **22 (3)**, pp. 302–328.

[8] J. G. Blom and P. A. Zegeling (1994), *Algorithm 731: a moving-grid interface for systems of one-dimensional time-dependent partial differential equations*, ACM Trans. Math. Software, **20 (2)**, pp. 194–214.

[9] J. Carr (1981), *Applications of center manifold theory*, Springer-Verlag, New York, Heidelberg, Berlin.

[10] W. Chen and M. J. Ward (2009), *Oscillatory instabilities and dynamics of multi-spike patterns for the one-dimensional Gray-Scott model*, Euro. J. Appl. Math **20 (2)**, pp. 187–214.

[11] W. Chen and M. J. Ward (2009), *Self-replication of spot patterns for the two-dimensional Gray-Scott model*, submitted to SIAM J. Appl. Dyn. Syst.

[12] W. Chen and M. J. Ward (2009), *Competition and oscillatory profile instabilities of spot patterns for the two-dimensional Gray-Scott model*, submitted to SIAM J. Appl. Dyn. Syst.

[13] X. Chen and M. Kowalczyk (2001), *Dynamics of an interior spike in the Gierer-Meinhardt system*, SIAM J. Math. Anal. **33 (1)**, pp. 172–193.

[14] M. C. Cross and P. C. Hohenberg (1993), *Pattern formation outside the equilibrium*, Rev. Mod. Physcis **65 (3)**, pp. 851–1112.

[15] A. de Wit (1999). *Spatial patterns and spatiotemporal dynamics in chemical physics*, Adv. Chem. Phys. **109**, pp. 435–513.

[16] A. Doelman, W. Eckhaus and T. J. Kaper (2001), *Slowly-modulated two-pulse solutions in the Gray-Scott model I: asymptotic construction and stability*, SIAM J. Appl. Math. **61 (3)**, pp. 1080–1102.

[17] A. Doelman, W. Eckhaus and T. J. Kaper (2001), *Slowly-modulated two-pulse solutions in the Gray-Scott model I: geometric theory, bifurcations and splitting dynamics*, SIAM J. Appl. Math. **61 (6)**, pp. 2036–2062.

[18] A. Doelman, R. A. Gardner and T. J. Kaper (2000), *A stability index analysis of 1-D patterns of the Gray-Scott model*, Memoirs of the AMS **155 (737)**.

[19] A. Doelman, R. A. Gardner and T. J. Kaper (1998), *Stability analysis of singular patterns in the 1D Gray-Scott model: A matched asymptotic approach*, Physica D **122 (1-4)**, pp. 1–36.

[20] A. Doelman and T. J. Kaper (2003), *Semi-strong pulse interactions in a class of coupled reaction-diffusion equations*, SIAM. J. Appl. Dyn. Sys. **2 (1)**, pp. 53–96.

[21] A. Doelman, T. J. Kaper and K. Promislow (2008), *Nonlinear asymptotic stability of the semi-strong pulse dynamics in a regularized Gierer-Meinhardt mode*, SIAM J. Math. Anal., **38 (6)**, pp. 1760–1789.

[22] A. Doelman, T. J. Kaper and P. A. Zegeling (1997), *Pattern formation in the one-dimensional Gray-Scott model*, Nonlinearity **10**, pp. 523–563.

[23] A. Doelman, P. Van Heijster and T. J. Kaper (2008), *Pulse dynamics in a three-component system: Existence analysis*, J. Dynam. Differential Equations (in press).

[24] S. Ei (2002), *The motion of weakly interacting pulses in reaction-diffusion systems*, J. Dynam. Differential Equations **14 (1)**, pp. 85–137.

[25] S. Ei, H. Ikeda and T. Kawana (2008), *Dynamics of front solutions in a specific reaction-diffusion system in one dimension*, Japan J. Indust. Appl. Math. **25 (1)**, pp. 117–147.

[26] S. Ei, M. Mimura and M. Nagayama (2002), *Pulse-pulse interaction in reaction-diffusion systems*, Physica D **165 (3-4)**, pp. 176–198.

[27] S. Ei, M. Mimura and M. Nagayama (2006), *Interacting spots in reaction-diffusion systems*, Discrete Contin. Dyn. Sys. **14 (1)**, pp. 31–2.

[28] S. Ei and J. Wei (2002), *Dynamics of metastable localized patterns and its application to the interaction of spike solutions for the Gierer-Meinhardt system in two space dimensions*, Japan J. Indust. Appl. Math. **19 (2)**, pp. 181–226.

[29] M. Frankel, G. Kovacic, V. Roytburd and I. Timofeyev (2000), *Finite-dimensional dynamical system modeling thermal instabilities*, Physica D **137 (3-4)**, pp. 295–315.

[30] A. Garfinkel, Y. Tintut, D. Petrasek, K. Bostrom and L. Demer (2004), *Pattern formation by vascular mesenchymal cells*, Proc. Natl. Acad. Sci. USA **101**, pp. 9247–9250.

[31] A. Gierer and H. Meinhardt (1972), *A theory of biological pattern formation*, Kybernetik **12 (1)**, pp. 30–39.

[32] K. B. Glasner (2009), *Spatially Localized Structures in Diblock Copolymer Mixtures.* submitted, SIAM J. Appl. Math..

[33] M. I. Golubitsky, I. Stewart, D. G. Schaeffer (1988), *Singularities and Groups in Bifurcation Theory vol. II*, Applied Mathematical Sciences **69**, Springer, New York.

[34] A. A. Golovin, B. J. Matkowsky and V. A. Volpert (2008), *Turing pattern formation in the Brusselator model with superdiffusion*, SIAM J. Appl. Math., **69 (1)**, pp. 251–272.

[35] P. Gray and S.K.Scott (1984), *Autocatalytic reactions in the isothermal, continuous stirred tank reactor: Oscillations and instabilities in the system* $\mathbf{A} + \mathbf{2B} \rightarrow \mathbf{3B}, \mathbf{B} \rightarrow \mathbf{C}$, Chem. Eng. Sci. **39**, pp. 1087–1097.

[36] S. Gueron and I. Shafrir (1999), *On a Discrete Variational Problem Involving Interacting Particles*, SIAM J. Appl. Math., **60 (1)**, pp. 1–17.

[37] P. Van Heijster, A. Doelman and T. J. Kaper (2008), *Pulse dynamics in a three-component system: stability and bifurcations* Physica D, **237(24)**, pp. 3335–3368.

[38] T. Ikeda and Y. Nishiura (1994), *Pattern selection for two breathers*, SIAM J. Appl. Math. **54 (1)**, pp. 195–230.

[39] D. Iron and M. J. Ward (2002), *The dynamics of multi-spike solutions to the one-dimensional Gierer-Meinhardt model*, SIAM J. Appl. Math. **62 (6)**, pp. 1924–1951.

[40] D. Iron, M. J. Ward and J. Wei (2001), *The stability of spike solutions to the one-dimensional Gierer-Meinhardt model*, Physica D **150 (1-2)**, pp. 25–62.

[41] A. Kaminaga, V. K. Vanag and I. R. Epstein (2006), *A reaction-diffusion memory device*, Angew. Chem. Int. Ed. **45**, pp. 3087–3089.

[42] B. S. Kerner and V. V. Osipov (1989), *Autosolitons*, Sov. Phys.- Usp. **32 (2)**, pp. 101–138.

[43] B. S. Kerner and V. V. Osipov (1994), *Autosolitons: A new approach to problems of self-organization and turburlence*, Dordrecht: Kluwer.

[44] B. S. Kerner and V. V. Osipov (1990), *Self-organization in active distributed media: scenarios for the spontaneous formation and evolution of dissipative structures*, Sov. Phys.- Usp. **33 (9)**, pp. 679–719.

[45] J. Kevorkian, J. Cole (1981), *Perturbation Methods in Applied Mathematics*, Applied Mathematical Sciences **34**, Springer-Verlag, New York, Berlin.

[46] C. M. Kirk and W. E. Olmstead (2005), *Blow-up solutions of the two-dimensional heat equation due to a localized moving source*, Anal. Appl. (Singap.) **3 (1)**, pp. 1–16.

[47] E. Knobloch (2003), *Outstanding problems in the theory of pattern formation*, in *Nonlinear dynamics and chaos. Where do we go from here?* S. J. Hogan, et al. (Eds.), Institute of Physics Publishing, Bristol, UK, pp. 117–166.

[48] S. Koga and Y. Kuramoto (1980), *Localized patterns in reaction-diffusion systems*, Prog. Theor. Phys. **63**, pp. 106–121.

[49] T. Kolokolnikov, T. Erneux and J. Wei (2006), *Mesa-type patterns in the one-dimensional Brusselator and their stability*, Physica D **214 (1)**, pp. 63–77.

[50] T. Kolokolnikov, W. Sun, M. J. Ward and J. Wei (2006), *The stability of a stripe for the Gierer-Meinhardt model and the effect of saturation*, SIAM J. Appl. Dyn. Sys. **5 (2)**, pp. 313–363.

[51] T. Kolokolnikov, M. S. Titcombe and M. J. Ward (2005), *Optimizing the fundamental Neumann eigenvalue for the Laplacian in a domain with small traps*, European J. Appl. Math. **16 (2)**, pp. 161–200.

[52] T. Kolokolnikov and M. J. Ward (2003), *Reduced wave Green's functions and their effect on the dynamics of a spike for the Gierer-Meinhardt model*, Euro. J. Appl. Math. **14 (5)**, pp. 513–545.

[53] T. Kolokolnikov, M. J. Ward and J. Wei (2006), *Slow translational instabilities of spike patterns in the one-dimensional Gray-Scott model*, Interfaces Free Bound. **8 (2)**, pp. 185–222.

[54] T. Kolokolnikov, M. J. Ward and J. Wei (2005), *The existence and stability of spike equilibria in the one-dimensional Gray-Scott Model: The low feed rate regime*, Studies in Appl. Math. **115**, pp. 21–71.

[55] T. Kolokolnikov, M. J. Ward and J. Wei (2005), *The existence and stability of spike equilibria in the one-dimensional Gray-Scott model: The pulse-splitting regime*, Physica D. **202 (3-4)**, pp. 258–293.

[56] T. Kolokolnikov, M. J. Ward, and J. Wei (2009), *Spot self-replication and dynamics for the Schnakenburg model in two-dimensional domain*, J. Nonlinear Sci. **19 (1)**, pp. 1–56.

[57] T. Kolokolnikov, M. J. Ward, and J. Wei (2006), *Zigzag and Breakup Instabilities of Stripes and Rings in the Two-Dimensional Gray-Scott Model*, Studies in Appl. Math. **16 (1)**, pp. 35–95.

[58] S. Kondo and R. Asai (1995), *A Reaction-Diffusion Wave on the Skin of the Marine Angelfish Pomacanthus*, Nature **376**, pp. 765–768.

[59] K. Lee, W. D. McCormick, J. E. Pearson and H. L. Swinney (1994), *Experimental observation of self-replication spots in a reaction-diffusion system*, Nature **369**, pp. 215–182.

[60] M. Mimura, M. Nagayama and K. Sakamoto (1995), *Pattern dynamics in an exothermic reaction*, Physica D **84 (1-2)**, pp. 58–71.

[61] C. B. Muratov and V. V. Osipov (1996), *Scenarios of domain pattern formation in reaction-diffusion system*, Phys. Rev. E **54**, pp. 4860–4879.

[62] C. B. Muratov and V. V. Osipov (2001), *Spike autosolitons and pattern formation scenarios in the two-dimensional Gray-Scott model*, Eur. Phys. J. B **22**, pp. 213–221.

[63] C. B. Muratov and V. V. Osipov (2002), *Stability of static spike autosolitons in the Gray-Scott model*, SIAM J. Appl. Math. **62 (5)**, pp. 1463–1487.

[64] C. B. Muratov and V. V. Osipov (2000), *Static spike autosolitons in the Gray-Scott model*, J. Phys. A: Math Gen. **33**, pp. 8893–8916.

[65] C. B. Muratov and V. V. Osipov (2001), *Traveling spike auto-solitons in the Gray-Scott model*, Physica D **155 (1-2)**, pp. 112–131.

[66] J. D. Murray (2003), *Mathematical Biology II: Spatial Models and Biomedical Applications*, Interdisciplinary Applied Mathematics **18**, Springer, New York.

[67] A. C. Newell and J. A. Whitehead (1969), *Finite bandwidth, finite amplitude convection*, J. Fluid Mech. **38 (2)**, pp. 279–303.

[68] Y. Nishiura (2001), *Global bifurcational approach to the onset of spatio-temporal chaos in reaction-diffusion systems*, Meth. Appl. Anal. **8 (2)**, pp. 321–332.

[69] Y. Nishiura and H. Fujii (1987), *Stability of singularly perturbed solutions to systems of reaction-diffusion equations*, SIAM J. Math. Anal. **18**, pp. 1726–1770.

[70] Y. Nishiura and H. Mimura (1989), *Layer oscillations in reaction-diffusion systems*, SIAM J. Appl. Math. **49 (2)**, pp. 481–514.

[71] Y. Nishura, T. Teramoto and K. Ueda (2005), *Scattering of traveling spots in dissipative systems*, Chaos **15**, 047509.

[72] Y. Nishiura and D. Ueyama (1999), *A skeleton structure of self-replicating dynamics*, Physica D **130**, pp. 73–104.

[73] Y. Nishiura and D. Ueyama (2001), *Spatial-temporal chaos in Gray-Scott model*, Physica D **150 (3-4)**, pp. 137–162.

[74] J. Ockendon, S. Howison, A. Lacey and A. Movchan (2001), *Applied Partial Differential Equations*, Oxford U. Press.

[75] Q. Ouyang and H. L. Swinney (1991), *Transition from a uniform state to hexagonal and striped Turing patterns*, Nature **352**, pp. 610–612.

[76] J. H. Park, A. Bayliss, B. J. Matkowsky and A. A. Nepomnyashchy (2006), *On the route to extinction in nonadiabatic solid flames*, SIAM J. Appl. Math. **66 (3)**, pp. 873–895.

[77] J. E. Pearson (1993), *Complex Patterns in a Simple System*, Science, **216**, pp. 189–192.

[78] W. N. Reynolds, S. P. Dawson and J. E. Pearson (1997), *Self-replicating spots in reaction-diffusion systems*, Phys. Rev. E **56 (1)**, pp. 185–198.

[79] W. N. Reynolds, J. E. Pearson and S. P. Dawson (1994), *Dynamics of self-replicating patterns in reaction-diffusion systems*, Phys. Rev. Lett. **72**, pp. 2797–2800.

[80] C. P. Schenk, M. Or-Guil, M. Bode and H. Purwins (1997), *Interacting pulses in three-component reaction-diffusion systems on two-dimensional domains*, PRL **78 (19)**, pp. 3781–3784.

[81] L. A. Segel (1966), *The importance of asymptotic analysis in applied mathematics*, Am. Math. Monthly **73**, pp. 7–14.

[82] L. A. Segel (1969), *Distant side-walls cause slow amplitude modulation of cellular convection*, J. Fluid Mech. **38**, pp. 203–224.

[83] L. A. Segel and J. L. Jackson (1972), *Dissipative structure: an explanation and an ecological example*, J. Theor. Biol. **37**, pp. 545–549.

[84] L. A. Segel and M. Slemrod (1989), *The quasi-steady state assumption: a case study in perturbation*, SIAM Rev. **31 (3)**, pp. 446–477.

[85] R. Straube, M. J. Ward and M. Falcke (2007) *Reaction rate of small diffusing molecules on a cylindrical membrane*, J. Stat. Physics **129 (2)**, pp. 377–405.

[86] W. Sun, M. J. Ward and R. Russel (2005), *The slow dynamics of two-spike solutions for the Gray-Scott and Gierer-Meinhardt systems: competition and oscillatory instabilities*, SIAM J. Appl. Dyn. Syst. **4 (4)**, pp. 904–953.

[87] C. Teuscher, foreword by D. Hofstadter (2004), *Alan Turing: life and legacy of a great thinker*, Springer Press, first edition.

[88] M. S. Titcombe and M. J. Ward (2000), *An asymptotic study of oxygen transport from multiple capillaries to skeletal muscle tissue*, SIAM J. Appl. Math. **60 (5)**, pp. 1767–1788.

[89] A. K. Tornberg and B. Engquist (2004), *Numerical approximation of singular source terms in differential equations*, J.Comput.Phys., **200 (2)**, pp. 462-488.

[90] A. M. Turing (1952), *The Chemical Basis of Morphogenesis*, Philos. Trans. R. Soc. **237**, pp. 37–72.

[91] D.Ueyama (1999), *Dynamics of self-replicating patterns in the one-dimensional Gray-Scott model*, Hokkaido Math J. **28 (1)**, pp. 175–210.

[92] V. K. Vanag and I. R. Epstein (2007), *Localized patterns in reaction-diffusion systems*, Chaos **17 (3)**, 037110.

[93] H. van der Ploeg and A. Doelman (2005), *Stability of spatially periodic pulse patterns in a class of singularly perturbed reaction-diffusion equations*, Indiana Univ. Math. J **54 (5)**, pp. 1219-1301.

[94] D. Walgraef (1997), *Spatio-Temporal Pattern Formation, With Examples from Physics, Chemistry, and Materials Science*, Springer, New York.

[95] M. J. Ward (2006), *Asymptotic Methods for Reaction-Diffusion Systems: Past and Present*, Bull. Math. Biol. **68 (5)**, pp. 1151–1167.

[96] M. J. Ward, W. D. Henshaw and J. B. Keller (1993), *Summing logarithmic expansions for singularly perturbed eigenvalue problems*, SIAM J.Appl.Math. **53 (3)**, pp. 799–828.

[97] M. J. Ward and J. Wei (2003), *Hopf bifurcations and oscillatory instabilities of spike solutions for the one-dimensional Gierer-Meinhardt model*, J. Nonlinear Sci. **13 (2)**, pp. 209–264.

[98] J. Wei (1999), *On single interior spike solutions for the Gierer-Meinhardt system: uniqueness and stability estimates*, Europ. J. Appl. Math. **10 (4)**, pp. 353–378.

[99] J. Wei (2001), *Pattern formations in two-dimensional Gray-Scott model: existence of single-spot solutions and their stability*, Physica D. **148**, pp. 20–48.

[100] J. Wei and M. Winter (2003), *Asymmetric spotty patterns for the Gray-Scott model in* $\mathbb{R}^2$, Studies in Appl. Math. **110 (1)**, pp. 63–102.

[101] J. Wei and M. Winter (2003), *Existence and stability of multiple spot solutions for the Gray-Scott model in* $\mathbb{R}^2$, Physica D. **176 (3-4)**, pp. 147-180.

[102] J. Wei and M. Winter (2002), *Spikes for the two-dimensional Gierer-Meinhardt system: the strong coupling case*, J. Differ. Equ. **178 (2)**, pp. 478–518.

[103] J. Wei and M. Winter (2001), *Spikes for the two-dimensional Gierer-Meinhardt system: the weak coupling case*, J. Nonlinear Sci. **11 (6)**, pp. 415–458.

[104] J. Wei and M. Winter (2008), *Stationary multiple spots for reaction-diffusion systems*, J. Math. Biol. **57 (1)**, pp. 53–89.

[105] A. Yochelis, Y. Tintut, L. L. Demer and A. Garfinkel (2008), *The formation of labyrinths, spots and stripe patterns in a biochemical approach to cardiovascular*, New J. Phys, **10** (16pp)